Masayoshi Nakasako

# X-Ray Diffraction Imaging of Biological Cells

Springer

# Springer Series in Optical Sciences

Volume 210

**Springer Series in Optical Sciences**

The Springer Series in Optical Sciences, under the leadership of Editor-in-Chief William T. Rhodes, Georgia Institute of Technology, USA, provides an expanding selection of research monographs in all major areas of optics: lasers and quantum optics, ultrafast phenomena, optical spectroscopy techniques, optoelectronics, information optics, applied laser technology, industrial applications, and other topics of contemporary interest.
With this broad coverage of topics, the series is of use to all research scientists and engineers who need up-to-date reference books.
The editors encourage prospective authors to correspond with them in advance of submitting a manuscript. Submission of manuscripts should be made to the Editor-in-Chief or one of the Editors. See also www.springer.com/series/624

Masayoshi Nakasako

# X-Ray Diffraction Imaging
of Biological Cells

Springer

Masayoshi Nakasako
Department of Physics, Faculty of Science
    and Technology
Keio University
Yokohama, Kanagawa
Japan

Diffraction pattern from a frozen-hydrated bacterial cell taken at BL29XUL of SPring-8. Published with kind permission of Masayoshi Nakasako 2018. All Rights Reserved

# Preface

Microscopic imaging techniques satisfy our curiosity regarding events within biological cells. For instance, X-ray crystallography has revealed the three-dimensional structures of biological macromolecules. However, the method is only applicable to crystalline specimens, and the structures of many noncrystalline particles are still unknown. X-ray diffraction imaging (XDI) is one of the techniques applicable to structural analyses of biological cells and organelles, which have never been crystallized. Its feasibility for the structural analysis of noncrystalline particles was first demonstrated in 1999. Since then, several groups have been engaged in the development of the methodology. In XDI experiments, spatially isolated noncrystalline particles are illuminated with X-rays, and their diffraction patterns are recorded with a high-resolution two-dimensional detector with a large number of pixels. The two- or three-dimensional structure of the sample is reconstructed from the diffraction patterns alone using phase-retrieval algorithm. Currently, XDI is a promising technique for the structural analysis of noncrystalline particles at nanometer resolution. The development of the XDI has been accelerated by utilizing X-rays from synchrotron and X-ray free-electron laser (XFEL) facilities.

In this book, the author describes the structural analyses of biological specimens, such as cells and organelles, using XDI at the synchrotron facility Super Photon ring at 8 GeV (SPring-8) and the XFEL facility, SPring-8 Angstrom Compact free electron LAser (SACLA). At 2016, XFEL pulses with wavelength of subnanometer were available at linac coherent light source (LCLS) at Stanford and SACLA. Because the author had no experience of XDI experiments at LCLS, the pioneer works at LCLS are introduced in some sections with references. Although several XFEL facilities will be constructed after 2016, it was difficult to include their future plans and prospects in this book. In addition, because XFEL facilities are improved in every year, the comparison of their characteristics is avoided here.

This book is composed of ten chapters, each of which is divided into several sections. The unit used for physical quantities is the SI unit. In addition, throughout the book, scattering vector $S$ rather than momentum transfer $Q$ is used for the convenience to calculate the resolution between real and reciprocal space in X-ray

diffraction. In the first three sections, microscopy, X-ray diffraction, and XDI are introduced briefly. After the introduction, the remainder of this book is organized into six sections. Chapters 4–6 target diffraction apparatus, specimen preparation, and diffraction data processing in XDI experiments performed mainly at SPring-8 and SACLA in Japan. In Chap. 7, theories for obtaining the most probable electron density maps are described. In Chaps. 8 and 9, the latest experimental results from the structural analysis of biological cells and cellular organelles are presented.

The theory, techniques, and simulations introduced here will be helpful for learning how XDI experiments are conducted and what kind of structural information about noncrystalline particles is obtainable.

Yokohama, Japan                                                              Masayoshi Nakasako

# Acknowledgements

# Contents

# About the Author

**Masayoshi Nakasako** is a Professor at Keio University, whose work chiefly involves the structural analysis of soft matter. After receiving his Doctor of Science from Tohoku University in 1990, he served as a Research Associate at the University of Tokyo's Faculty of Pharmaceutical Sciences, as a Researcher at RIKEN, as a Lecturer at the University of Tokyo's Institute of Molecular and Cellular Biosciences, and as an Assistant Professor at Keio University in 2002. In 2005, he was promoted to his present position. Currently, he is also a Guest Researcher at RIKEN SPring-8 Center.

His primary research interest is in imaging protein hydration, protein structures, and cells by means of molecular dynamics simulations and various physicochemical experimental techniques including X-ray imaging using synchrotron radiation and X-ray free-electron lasers.

# Abbreviations

| | |
|---|---|
| AI | Artificial intelligence |
| CCD | Charge-coupled device |
| DAQ | Data acquisition |
| DLS | Dynamic light scattering |
| DM | Diffusion map |
| ER | Error reduction |
| FOM | Figure of merit |
| FSC | Fourier shell correlation |
| GUI | Graphical user interface |
| HIO | Hybrid input–output |
| LCLS | Linac coherent light source |
| LM | Light microscopy |
| MD | Molecular dynamics |
| MIR | Multiple isomorphous replacement |
| MPI | Message passing interface |
| PCA | Principal component analysis |
| PDI | Protein disulfide isomerase |
| PLL | Poly-L-lysine |
| PR | Phase retrieval |
| PRTF | Phase-retrieval transfer function |
| RH | Relative humidity |
| RMSD | Root-mean-square difference |
| ROI | Region of interest |
| SACLA | SPring-8 Angstrom Compact free electron LAser |
| SEM | Scanning electron microscopy |
| SPring-8 | Super Photon ring at 8 GeV |
| SRFM | Super-resolution fluorescence microscopy |

| SW | Shrink wrap |
| TEM | Transmission electron microscopy |
| XDI | X-ray diffraction imaging |
| XFEL | X-ray free-electron laser |

# Chapter 1
# Introduction

**Abstract** Biological cells are basic units in life. They are composed of a huge number of biological molecules, such as proteins, nucleic acids, lipids, sugar and organic molecules and inorganic ions. The biological macromolecules form well-organized compartments, so-called organelle. The ultimate goal of cell biology would be the complete illustration of cellular events at high spatial and temporal resolutions. To illustrate spatiotemporal events in biological cells, various methods for microscopic observation have been innovated. Here, prior to introduced X-ray diffraction imaging (XDI), typical microscopic methods are introduced for visualizing the internal structures of cells, such as light microscopy, transmission electron microscopy, and X-ray imaging techniques. In addition, possible roles of XDI in visualizing cells are described.

## 1.1 Spatiotemporal Hierarchy in Biological Cells

Biological cells that make up living organisms are evolutionarily sophisticated complex systems that are as small as 1–20 μm and contain huge numbers of proteins, nucleic acids, lipids, small organic molecules, and ions immersed in water [1]. Water is the mother liquid of life and occupies 60–70% of the volume of the cell. Inside the cells, like members of a large symphony orchestra playing a well-composed musical score, a very large number of biomolecules are engaged in complex and synchronized activities, such as catalysis, transport, and specific molecular interactions that are indispensable for the survival of the cell. One of the ultimate goals of biological science is the complete description of all cellular events at molecular and, ultimately, atomic levels.

Since the publication of "*What is life?*" by Erwin Schrödinger about 70 years ago [2], various types of experimental techniques and theories have been developed and applied in order to understand the molecular events occurring inside cells. Based on the experimental and theoretical studies carried out to date, we are now elucidating specific aspects of molecular events. For instance, proteins are activated by external physical and/or chemical stimuli, such as visible light, molecular

collisions, and interactions. Such high-energy stimuli for the cellular components excite the electronic and vibrational states of specific atom groups within a picosecond time domain. The excitations propagate inside the proteins in the time range from microseconds to milliseconds, and induce complicated dynamical motions in the nanometer scale to generate the biological functions of proteins. The activated protein molecules undergo synergetic interactions with many other molecules. These activities result in cellular events appreciable in light microscopy (LM) observations.

The current picture is still limited to segmented spatiotemporal hierarchies; this situation is similar to the analysis of a musical score by focusing separately on each section rather than the whole piece. To move towards the next stage of biological sciences based on physics and chemistry, gapless descriptions of cellular events throughout spatiotemporal hierarchies are necessary in order to understand how energy and information provided by external stimuli propagate from lower to higher hierarchies.

For instance, the following four problems concerning hierarchical structures in cells are examples, which must be elucidated by structural studies in moving to the next stage.

(1) Spatiotemporal development of physicochemical stimuli in proteins and their complexes
How do primary responses of biological macromolecules to external stimuli induce conformational changes and downstream cellular events? From current research on segmented hierarchies using spectroscopy, quantum/molecular mechanics, and time-resolved X-ray crystallography, novel concepts are necessary to bridge the gaps between segmented hierarchies.

(2) Influence of water on cellular events
Water, the matrix of life, plausibly contributes to all cellular events, from the local dynamics of proteins to the motility processes of organelles. Hydration affects protein folding and conformational dynamics. Phenomena occurring at the border between Langevin and fluid dynamics may be discussed to understand the hierarchical gaps in the dynamics of cellular events in water.

(3) Dynamics of supramolecular complexes
Supramolecular complexes of biological macromolecules are suitable to understand the spatiotemporal hierarchy in cells. The structure formation and conformational dynamics in terms of energy landscapes may be helpful to discuss the development of external physicochemical stimuli from lower to higher spatiotemporal hierarchies.

(4) Structure and dynamics of cells
Cells are too large to be visualized by transmission electron microscopy (TEM). In addition, even when using fluorescence LM, the imaging of the whole cell at resolutions comparable with TEM is still difficult. To visualize the structure and dynamics of cells and cellular components, the gap between transmission electron microscopy and light microscopy must be bridged by other imaging

techniques with resolutions better than 100 nm, without chemical and physical modification of the cell specimens (Fig. 1.1).

X-ray crystallography has been used to visualize the structures of crystallized biological macromolecules, such as proteins and nucleic acids, at atomic resolution [3]. The short wavelength of the X-rays (approximately 0.1 nm) allows us to illustrate the molecular structures at atomic resolution and to discuss the atomic details of the mechanism driving the activities of macromolecules. Small-angle X-ray scattering (diffraction) [4] provides ensemble averaged structures of macromolecules in solution. Because the crystal structures provide only a snapshot of the conformational dynamics of macromolecules confined in a crystalline state, complementary use of the techniques is necessary to discuss the conformational dynamics of macromolecules in cells. These X-ray diffraction techniques rely on the characteristics of the interaction of X-rays with matter. X-rays with short wavelengths penetrate into thick specimens without significant levels of multiple scattering due to the weak interaction between X-rays and electrons in atoms [5]. In addition, the small but significant differences in the scattering cross sections between the atoms composing biological macromolecules are necessary to identify the atom species in electron density maps [6].

TEM has contributed to visualizing the structures of macromolecules and macromolecular assemblies [7]. The strong interaction of electrons with the electrostatic potential inside biological molecules is advantageous to visualize structures by single molecule analysis. However, the strong interaction limits the penetration of electrons into specimens with thickness of more than 200 nm. In addition, multiple scattering and absorption of electrons hinder the application of the weak-phase approximation in the structure analysis. Therefore, in order to visualize cells and cellular organelles, TEM requires thin-sectioned specimens. However, sectioning may cause unwanted artifacts in the native structures of the specimens.

LM, particularly fluorescence LM, is used to visualize the localization and movement of biological macromolecules labeled by fluorescent dyes or fluorescent
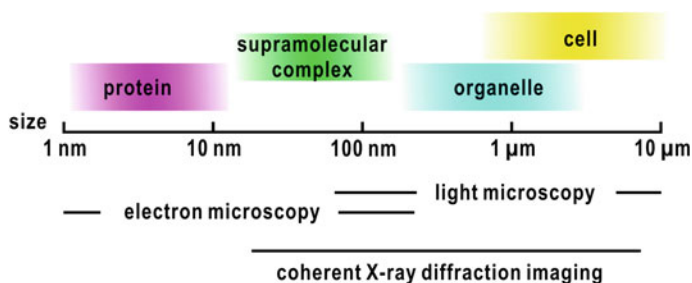


**Fig. 1.1**  Sizes of biological cells and cellular components, and the imaging techniques used to illustrate cellular structures and events of different sizes. Published with kind permission of Masayoshi Nakasako 2017. All Rights Reserved

proteins [8]. By tracking the movements of the labeled molecules in cells (live-cell imaging), LM opened a new era of cell biology in the last two decades. However, because of the wavelength of visible light, the resolutions are limited to approximately 100 nm, even when the super-resolution microscopy technique is applied. In addition, laser light used in fluorescence LM causes fatal degradation of specimens after the observation is made.

In order to visualize complicated cellular systems at a spatial resolution better than 100 nm, a novel imaging technique, namely X-ray diffraction imaging (XDI), was proposed in 1998–1999 [9, 10]. This method may contribute towards physical and chemical research on cellular events, together with sophisticated traditional techniques such as X-ray crystallography, EM, and fluorescence LM. Prior to introducing XDI, sophisticated LM and EM techniques are briefly summarized.

## 1.2  Imaging Techniques Using Lenses

As cells are small and complex, various types of microscopic imaging techniques have been applied to illustrate how the cell components work. LM and EM, which use lenses, are representative techniques that can directly provide the images of noncrystalline specimens.

The resolution limit of all microscopy is that we cannot visualize structural details significantly smaller than the wavelength of the radiation used. By the interactions of visible light or electron waves with an object, the phases of the diffracted waves shift from those of the incident waves. Then, complex interference patterns appear behind the object. The interference patterns carry information about the structures of the object in the Fourier components. Lenses work as mathematical operators to recombine the diffracted waves to the original images at a resolution limited by the size of the lenses and the wavelength of radiation used.

### 1.2.1  Light Microscopy

LM uses visible light with a wavelength in the approximate range from 400 to 800 nm. A light microscope is composed of a condenser lens, an objective lens, and an eyepiece lens (Fig. 1.2). LM observations of biological specimens in an aqueous environment at ambient temperature allow us to trace the movements and structural changes of cellular components [11, 12].

The resolution limit, at which two objects can be separately observed, depends both on the light wavelength ($\lambda$) and the numerical aperture ($NA$) of the objective lens used. The resolution limit of light microscopy $\delta$ is expressed by the Rayleigh limit [13] as
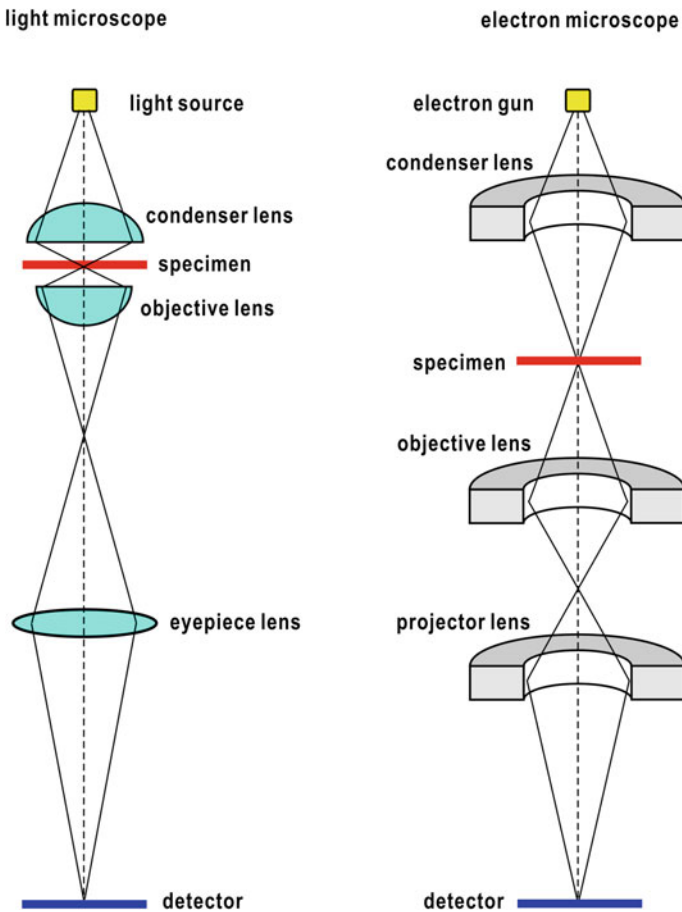
**Fig. 1.2** Schematic diagram of a light microscope (left panel) and a transmission electron microscope (right panel). Three types of lenses are used in both microscopes. The condenser lens is used to illuminate specimens. An objective lens and eyepiece lens (projector lens) collect light waves (electron waves) at the detector plane. Published with kind permission of Masayoshi Nakasako 2017. All Rights Reserved

$$\delta = \frac{A \times \lambda}{NA} \tag{1.1}$$

The parameter $A$ depends on the type of light microscope. In a typical light microscope, $A$ takes the value of 0.61. The $NA$ value depends on both the refractive index $n$ of the imaging medium and the angular width collected by the objective lens according to (Fig. 1.3)
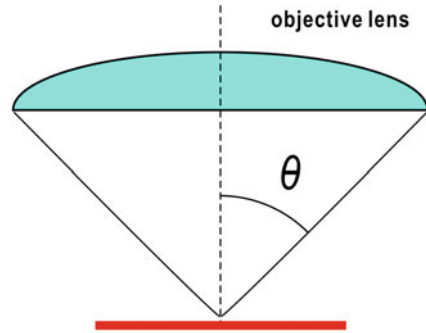
$$NA = n\sin\theta. \tag{1.2}$$

The resolution limit is approximately 200 nm for aberration-free objective lenses with $NA = 1.4$ for visible light with an average wavelength of 550 nm.

Because visible light interacts weakly with cellular components, the obtainable images are limited in contrast. One of the techniques to enhance the contrast of the cellular components is the phase-contrast microscopy. In addition, the development of fluorescent molecules with sizes of approximately 1 nm and the discovery of fluorescent proteins have opened the door to tracking molecular events in situ with diffraction limited resolution [12]. Digital techniques for acquiring and processing image data have improved rapidly in the last two decades. In particular, charge-coupled device cameras (CCD cameras) are useful and powerful devices for recording digitized image data, with a wide dynamic range of $10^3$–$10^4$ light photons/pixel. In addition, data processing techniques and algorithms, which can be installed in personal computers to control CCD devices, aid in the easy performance of microscopic observations. LM imaging thus established its role in cell biology over the past three decades.

### 1.2.1.1 Phase-Contrast Microscopy

When visible light propagates through biological cells and organelles, the phase shifts of visible light waves occur depending on the refractive indices of the specimens (Fig. 1.4a). In dense regions with large refractive indices, the phase shifts become large. The interference patterns produced by the superposition of waves propagating through different regions depend on the phase shift. If the recovery of the phase difference from the interference pattern is possible, the distribution of cellular components can be visualized in terms of the refractive index. The phase differences, i.e., the differences in refractive indices, are visualized by manipulating the interference pattern with a phase plate [13].
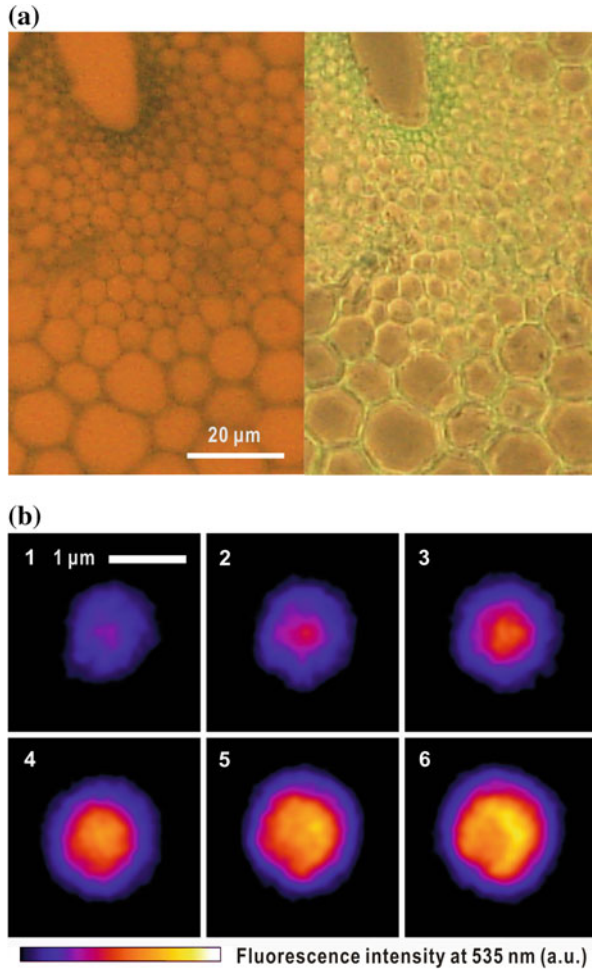
**Fig. 1.4** **a** Microscopic images of plant cells (**a**) without (left) and with (right) a phase plate (phase-contrast image). The images of the cell walls are clearly visible in the phase-contrast image. Published with kind permission of Masayoshi Nakasako 2017. All Rights Reserved. **b** Confocal microscopy images of chloroplasts from the small eukaryote *Cyanidioschyzon merolae* (schyzon). The chloroplast was stained by fluorescence dye, which has a high affinity to proteins. Images 1–6 were taken by a series of scans along the direction of incident light. The scan step was 500 nm. Photographs in panel (**b**) are reused with a modification from [62] with permission from Plant Cell Physiology, the Oxford University Press

### 1.2.1.2 Fluorescence Microscopy

Fluorescence microscopy is used to visualize the distribution of macromolecules labeled with fluorescent dyes and proteins [11, 12] (Fig. 1.4b). Then, the spatiotemporal movements of cellular components engaged in physiologically

important events are tracked at a spatial resolution of approximately 200 nm and a temporal resolution of several tens of milliseconds. Fluorescence microscopy has significantly advanced our understanding of cellular processes. One of the most striking demonstrations of this technique was the observation of the rotation of $F_1$-ATPase in the presence of adenosine triphosphate about 20 years ago [14].

Immediately after fluorescent molecules absorb visible light at a specific wavelength, they emit light with a wavelength longer than that of the absorbed light. The energy difference between the absorbed and emitted light is converted to thermal vibrations during the relaxation process of the excited fluorescence molecules after light emission. The emitted light allows us to determine the positions of fluorescent molecules bound to biological macromolecules.

Fluorescent proteins, such as the green fluorescent protein (GFP) isolated from jellyfish, are used to tag targeted proteins in living cells [15]. For instance, GFP can be used to monitor the gene expression of a targeted protein. The DNA of GFP is inserted at the beginning or end of the gene for a targeted protein to yield a fusion protein. The tagged proteins function equivalently to the untagged proteins in most cases. Then, when the targeted protein is expressed, the simultaneously expressed GFPs emit strong green fluorescence under illumination by an excitation light.

The current fashion in fluorescence microscopy is the simultaneous use of several fluorescent dyes with different absorption and emission spectra in order to distinguish molecular species in the same images of a cell [16]. The molecules have short lifetimes of emission, even under the continuous illumination of an excitation light to visualize the positions of different fluorescence dyes. Smaller fluorescent dyes with stronger intensities and faster decays of emission are more suitable for multi-color observation. The simultaneous measurement of the movements of several types of targeted molecules makes it possible to visualize the frequency of their contacts, their number density in a specified volume, and their locations. Ion-sensitive indicators, pH-sensitive molecules, and microelectrodes have also been developed and used to monitor the microscopic environment inside cells.

In confocal microscopy, every point in the focal plane of the objective lens is sequentially raster-scanned under the irradiation of the focused excitation light [17]. Then, the significantly reduced point spread gives a value of 0.37 for $A$ in (1.1). In addition to the basic arrangement of optical components similar to that of a standard fluorescence microscope, a laser is used as an excitation light for a small area of the specimen. By raster-scanning the specimen against the focused beam of the excitation laser, a very sharp two-dimensional image can be reconstructed along the focal plane of the objective lens [18]. Confocal microscopy provides three-dimensional images by shifting the position of the specimens along the direction of the optical axis of the microscope. The resolution along the optical axis is given by

$$\delta = \frac{0.67 \times \lambda}{n - \sqrt{n^2 - NA^2}}.$$

In recent years, a number of 'super-resolution' fluorescence microscopes (SRFM) have been developed from confocal laser scanning fluorescence microscopy to visualize cellular structures beyond the resolution limit given by (1.1) [19]. SRFM allows us to visualize the positions of fluorescent molecules in living cells at resolutions better than 100 nm by employing fluorophores with a nonlinear response, providing a sharper point-spread function than with ordinary LM. For instance, stochastic optical reconstruction microscopy uses photoswitchable fluorescent molecules between the excited and ground states [20]. Temporal excitation and deactivation of the fluorescence molecules allow us to map their localization at a resolution beyond the Rayleigh limit. Structural illumination microscopy increases the spatial resolution by applying a patterned illumination to the specimen. This microscopy technique doubles the spatial resolution of ordinary LM [21]. Simulated emission depletion microscopy uses a laser light to suppress the fluorescence emission from fluorophores around the targeted region to be excited [22].

The limitation of fluorescent LM, including SRFM, is that the macromolecules must be labeled with fluorescent dyes or proteins; the dye-labeled molecules are only visible. These dyes are bleached because of the finite lifetime and finite number of photons that they can fluoresce. Furthermore, the environment surrounding the labeled proteins and the vast majority of the cellular structure are invisible to the technique. Therefore, the information from fluorescence microscopy is limited to the molecules labeled by fluorescent dyes or fluorescent proteins.

## *1.2.2   Transmission Electron Microscopy*

TEM is a powerful tool to visualize the structures of small objects, such as assemblies of proteins, due to the strong interactions between electrons and the electrostatic potential inside specimens [7]. The wavelength of an electron wave ($\lambda$) depends on the velocity ($v$) according to the de Broglie relation:

$$\lambda = \frac{h}{m_e v} \sqrt{1 - \frac{v^2}{c^2}}, \qquad (1.3)$$

where $h$, $m_e$, and $c$ are Planck's constant, the electron mass, and the speed of light in vacuum, respectively. When an accelerating voltage of 200 keV is applied, the wavelength of the electron wave becomes approximately 2 pm. The motion of the electrons can be controlled by a set of electromagnetic lenses, which play the same roles as those in light microscopes. Because of the strong aberration of the electromagnetic lens, the practical resolving power of electron microscopes is 0.1 nm. Because the wavelength of the electron wave is very short, the images of the specimens obtained by electron microscopy are the map of the electrostatic

potential inside an object projected along the direction of the incident electron beam.

To avoid the absorption of the electrons by air, specimens must be set in a vacuum, as must the electron guns, electromagnetic lenses, and detectors. To prevent dehydration, biological specimens are fixed by resin or frozen-hydrated in vitreous ice. Therefore, transmission electron microscopy provides only momentary snapshots of the specimens in the preparations [23, 24].

Owing to the strong interaction of electrons with the electrostatic field produced by atoms in macromolecules, electron microscopy has been applied to the structural analyses of noncrystalline biological particles, such as viruses. In 1980–1990, the ice embedding method made it possible to observe the structures of cellular components and macromolecules in the hydrated state (Fig. 1.5).

### 1.2.2.1 Imaging of Biological Cells and Organelles

Because of the limited penetration depth of electrons arising from the strong interaction between electrons and the electrostatic potential of specimens, TEM is difficult to apply to the structural analyses of whole cells and cellular components with thicknesses larger than approximately 200 nm. To observe cells and their internal structures, specimens are sliced into a series of thin sections with a thickness of approximately 100 nm. For sectioning, specimens are fixed by resins to form a solid block, after cross-linking macromolecules with glutaraldehyde, dehydration through freeze-drying, and heavy-metal staining [25].

For appropriately sectioned specimens, TEM can provide images of the internal structures of cells with resolutions better than several tens of nanometers. However, the preparation may produce unwanted artifacts in the shape and structure of the specimens. In addition, radiation damage of the specimens by electrons is another problem in interpreting the images obtained by transmission electron microscopy.

The tomography for sliced and frozen-hydrated specimens is possible in TEM [26]. The three-dimensional structure of a specimen is reconstructed from a series of projection images taken by sequentially tilting the specimen against the direction of the incident electron beam. As the radiation damage of the specimens during irradiation by electrons is extensive, the series of irradiations must be finished within the limit of the possible electron dose. One of the applications of tomography observation is the structural analyses of large assemblies of proteins forming parts of large organelles.

### 1.2.2.2 Imaging of Biological Macromolecules

TEM has also contributed to determining the structures of large frozen-hydrated large membrane proteins and supramolecular complexes at subnanometer resolutions [7].
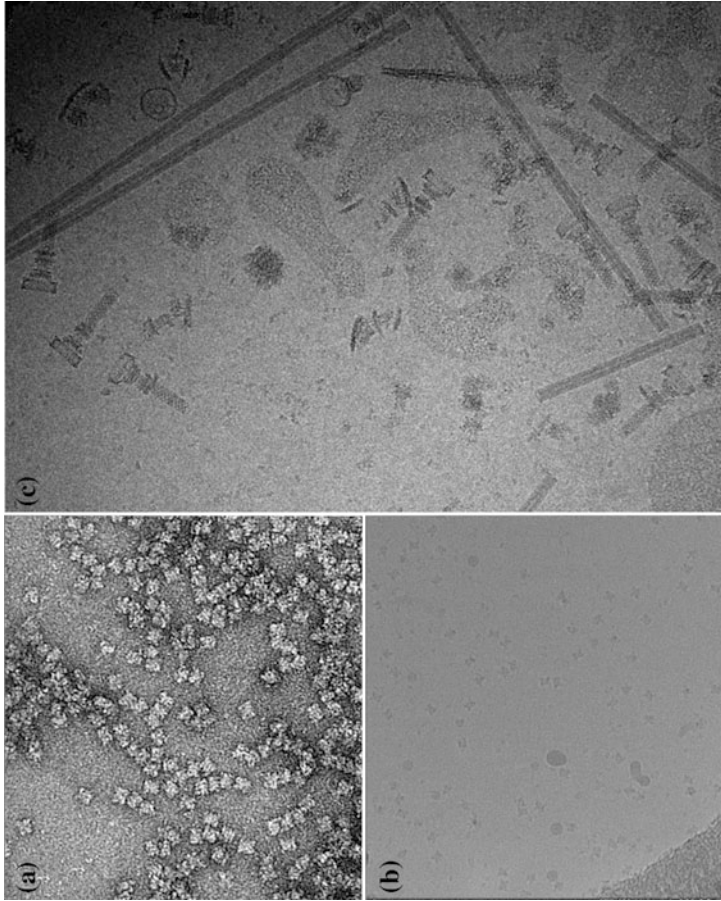
**Fig. 1.5** Electron micrographs of negatively stained (**a**) and frozen hydrated (**b**) glutamate dehydrogenase with an approximate size of 10 nm. Published with kind permission of Masayoshi Nakasako 2017. All Rights Reserved. **c** Electron micrograph of frozen-hydrated molecular motors of flagella and tobacco mosaic viruses (long sticks). The diameter of the tobacco mosaic virus is approximately 18 nm. The EM image in panel (**c**) is supplied by courtesy of Prof. Keiichi Namba. Published with kind permission of Masayoshi Nakasako 2017. All Rights Reserved

The three-dimensional structures, such as shown in Fig. 1.6, are reconstructed from millions of images by determining the orientations of individual particles against the direction of the incident electron beam, using the single particle analysis algorithms [7].

To reduce radiation damage, electron micrographs are recorded under low dose irradiation condition and at low temperature. Thus, the obtained electron micrographs have low signal-to-noise ratios. Through statistical analyses of the images of specimen particles using the correspondence analysis followed by the clustering classification method, averaged images are calculated in approximately the same orientation for the direction of the incident electron beam. From a number of averaged images, the initial three-dimensional map is reconstructed.

In the last decade, TEM has entered into a new era [27]. Direct area detectors with high detection efficiencies allow us to correct the movement of particles under electron beam irradiation using the time-resolved acquisition procedure. In addition, an algorithm that avoids overfitting and overestimation of potential maps [28] contributes to objectively refining 3D structure models reconstructed from a huge number of images of specimen particles. Subsequently, atomic resolution structures of a supramolecular complex, which has never been crystallized, such as a nuclear pore complex [29], chromatin structure [30], or spliceosome [31], have been visualized. The role of TEM in supramolecular imaging will be enormously important in structural biology.
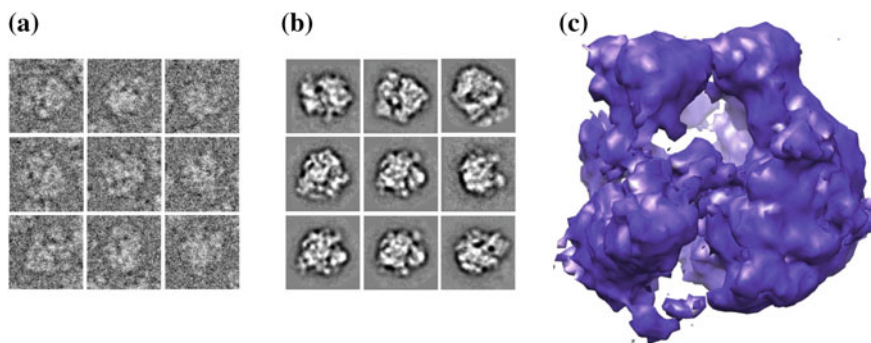


**Fig. 1.6** The 3D reconstruction of a 70S ribosome using cryo TEM at a low resolution. **a** Representative images after the correction of the aberration of the electromagnetic lenses. **b** Averaged images after classification. **c** A low-resolution three-dimensional potential map of a 70S ribosome with an approximate diameter of 20 nm. The lobes on the left and right sides are the 30S and 50S ribosomal subunits, respectively. The size of the 70S ribosomal subunit is approximately 20 nm. Published with kind permission of Masayoshi Nakasako 2017. All Rights Reserved

## 1.3 X-Ray Imaging

LM and EM have been utilized to provide structural information on the spatiotemporal hierarchies inside cells. However, it is still difficult for the two techniques to visualize whole cells and cellular components of sizes ranging from 1 to 10 μm with a resolution better than 100 nm. To move towards the next stage of imaging in biology, new imaging techniques are necessary toward gapless description of the spatiotemporal hierarchy in cells. New imaging techniques have often provided great advances in cell biology.

Imaging techniques utilizing X-rays have the potential to fill the gap inaccessible by both LM and EM. Three types of X-ray imaging techniques are currently available; X-ray microscopy, X-ray fluorescence microscopy, and XDI. In the following subsections, these techniques are briefly introduced. Because of the penetration power of the X-rays used, these X-ray imaging techniques target specimens, such as whole cells and organelles, without chemical labeling, fixation, staining, or sectioning.

### *1.3.1 X-Ray Microscopy*

The refractive index $n$ of a crystal for an X-ray with wavelength $\lambda$ is written as

$$n(\lambda) = 1 - \delta(\lambda) + i\beta(\lambda)$$
$$\delta(\lambda) = \frac{\lambda^2 r_{\mathrm{e}}}{2\pi V_{\mathrm{u}}} \sum_j \left( Z_j + f_j'(\lambda) \right)$$
$$\beta(\lambda) = \frac{\lambda^2 r_{\mathrm{e}}}{2\pi V_{\mathrm{u}}} \sum_j \left( -f_j''(\lambda) \right), \tag{1.4}$$

where $\delta(\lambda)$ and $\beta(\lambda)$ are the real and imaginary parts of the refraction index of the object, respectively, $Z_j$ is the total scattering cross section of the $j$th atom, $f_j'(\lambda)$ and $f_j''(\lambda)$ are the real and imaginary parts of the dispersion correction for the elastic scattering of X-rays by the atom, $r_{\mathrm{e}}$ is the classical electron radius ($2.818 \times 10^{-15}$ m) and $V_{\mathrm{u}}$ is the unit cell volume [5]. As both the wavelength and the classical electron radius are quite small, $\delta(\lambda)$ is in the range between $10^{-5}$ and $10^{-6}$, and the refractive index is close to 0.99999. This means that lenses to reconstruct the electron density of the specimens are difficult to fabricate. Instead of lenses, Fresnel zone plates made using microfabrication technology are used as optical elements corresponding to the condenser and objective lenses in LM. Since its first innovation, X-ray microscopy has been applied to visualize whole biological specimens using synchrotron X-rays.

X-ray microscopes use X-rays with wavelengths in the range of the so-called 'water window' between the absorption edges of carbon (4.4 nm) and oxygen (2.3 nm) [5], because X-rays in this range are absorbed by organic materials ten or more times as strongly as by water. Therefore, the water inside the cells is transparent, while organic components such as proteins, lipids, and nucleic acids are opaque. The materials composing the cells are distinguished in terms of their absorption of X-rays. The optics in transmission X-ray microscopy using X-rays in the water window are similar to those in LM. A condenser zone plate focuses X-rays onto the specimen, and then an objective zone plate focuses the transmitted X-rays onto the detector (Fig. 1.7a). Images obtained by X-ray microscopy are the projections of specimens along the direction of the incident X-ray.

By collecting images at different orientations relative to the incident X-ray beam, tomography of the specimen is possible [32]. Because a series of exposures for a single specimen takes a long period of time in a tomography experiment, it is necessary to protect the specimens from radiation damage. For instance, when measuring frozen-hydrated specimens at approximately liquid nitrogen temperature, radicals produced during the X-ray exposure are immobilized to prevent damage from occurring. Currently, cellular ultrastructures can be visualized three-dimensionally at a resolution better than 100 nm by using cryogenic X-ray tomography [33].
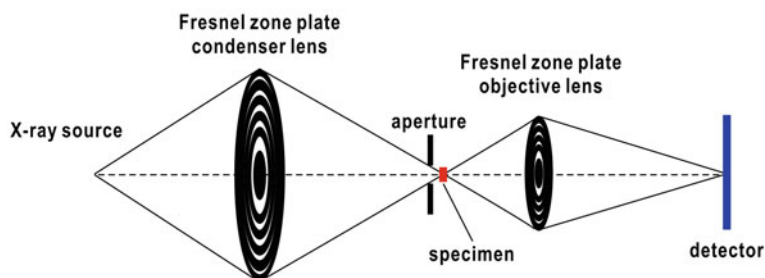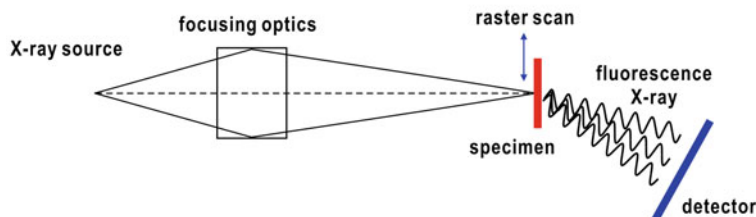


**Fig. 1.7** Schematic diagrams of X-ray microscopy (**a**) and X-ray fluorescence microscopy (**b**). Published with kind permission of Masayoshi Nakasako 2017. All Rights Reserved

## 1.3.2   X-Ray Fluorescence Microscopy

When an object is irradiated by X-rays, the intensity of the X-rays transmitted through the object is written as

$$I = I_0 \exp\left[ -\frac{\rho_\mathrm{m} N_\mathrm{A}}{M} \sigma_\mathrm{A}(\lambda) \right], \tag{1.5}$$

where $I$ and $I_0$ are the X-ray intensities observed with and without the object, respectively, and $\rho_\mathrm{m}$, $N_\mathrm{A}$, and $M$ are the mass density, Avogadro's number, and molecular mass, respectively. $\sigma_\mathrm{A}(\lambda)$ is the absorption cross-section per atom. When an atom absorbs an X-ray photon, an electron in the atom is excited from the bound state to the continuum state, as is known from photoelectric absorption. Immediately after the excitation, any electron in a higher energy state drops to the vacant lower energy state. Then, the electron emits fluorescence X-rays with a wavelength determined by the energy difference between the high and low energy states. Because the excitation of the electron is induced by X-rays with energies higher than the excitation energy, a stepwise change, referred to as absorption edges, appears in the wavelength-dependent variation of the absorption cross-section (Fig. 1.8). As the photon energies causing the absorption edges depend on elements and their ionic states, the types of elements composing an object can be identified by measuring the absorption edges in the fluorescence X-ray spectra.

X-ray fluorescence microscopy offers a quantitative mapping of the elements inside specimens (Fig. 1.7b), especially metallic trace elements indispensable for
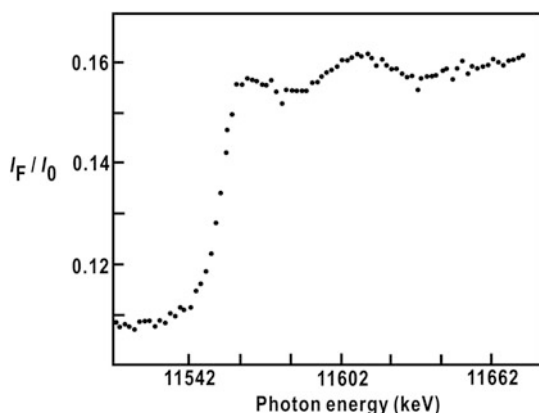


**Fig. 1.8** X-ray fluorescence spectrum measured near the $L_{III}$ absorption edge of platinum atoms bound to sulfur atoms of methionine residues in a protein crystal. The intensity of the fluorescence X-ray normalized by the incident intensity is plotted against the photon energy of the emitted fluorescence X-ray. Published with kind permission of Masayoshi Nakasako 2017. All Rights Reserved

cellular metabolism [34]. An X-ray fluorescence microscope is equipped with a high-precision scan stage and a set of detectors to measure the intensity of the fluorescence X-rays. Specimens are irradiated by microfocused and monochromatized X-rays. The X-ray fluorescence spectra are measured by changing the wavelength of the incident X-ray point by point. The fluorescence X-ray tells us what types and amounts of elements are contained at each point. By alternately carrying out raster and wavelength scans, multiple maps displaying the distribution of the trace elements are obtained [35]. In fluorescence LM, a quantitative estimation of the amount of targeted materials is difficult, as the labeling depends on the binding affinity of the fluorophores. In contrast, X-ray fluorescence microscopy can measure the amounts of elements in the irradiated area.

### 1.3.3 X-Ray Diffraction Imaging

For a long time, structural analyses of noncrystalline biological particles using X-ray diffraction have been quite difficult. In 1952, Sayre proposed a basic concept to visualize the structure of noncrystalline particles [36]. Based on this concept, Sayer and Miao proposed the phase reconstruction procedure from only a diffraction pattern using the oversampling method in 1998 [9]. In the following year, they succeeded in the experimental demonstration of the determination of the structure of a noncrystalline object [10]. These two pioneering works are the origins of the X-ray diffraction method used to visualize the structures of noncrystalline particles. This method is designated as X-ray diffraction imaging (XDI). Since then, XDI has been applied to the structural analyses of noncrystalline particles with dimensions of submicrometers to micrometers at resolutions of several tens of nanometers [37].

XDI is an imaging method that extends the basic methodology of X-ray crystallography to the structural analysis of noncrystalline specimens. XDI experiments are very simple; an isolated particle is irradiated by X-rays with high spatial coherence, and then the diffraction pattern is recorded by an area detector (Fig. 1.9a). Owing to the weak interactions between atoms and X-rays with short wavelengths, X-rays penetrate deeply into thick objects without multiple scattering. The diffraction patterns can be collected at a resolution beyond the limit of LM. While diffraction patterns from crystals are composed of sharp Bragg peaks, those from single noncrystalline particle display fine interference patterns, called speckle peaks (Fig. 1.9b).

The scattering cross-section of noncrystalline particles is far smaller than those of crystals. On the other hand, the continuously varying diffraction intensity in speckle patterns is advantageous for finer sampling than in diffraction patterns from crystals, where very small signals appear between Bragg peaks. The main problem in the lensless experiment is the loss of phase information in the detection of diffraction patterns. Owing to the large amount of diffraction intensity data sampled, the electron density map of a specimen particle can be, in principle, reconstructed from the diffraction pattern alone by applying the iterative phase retrieval algorithm [38]

**(a)**



**(b)**
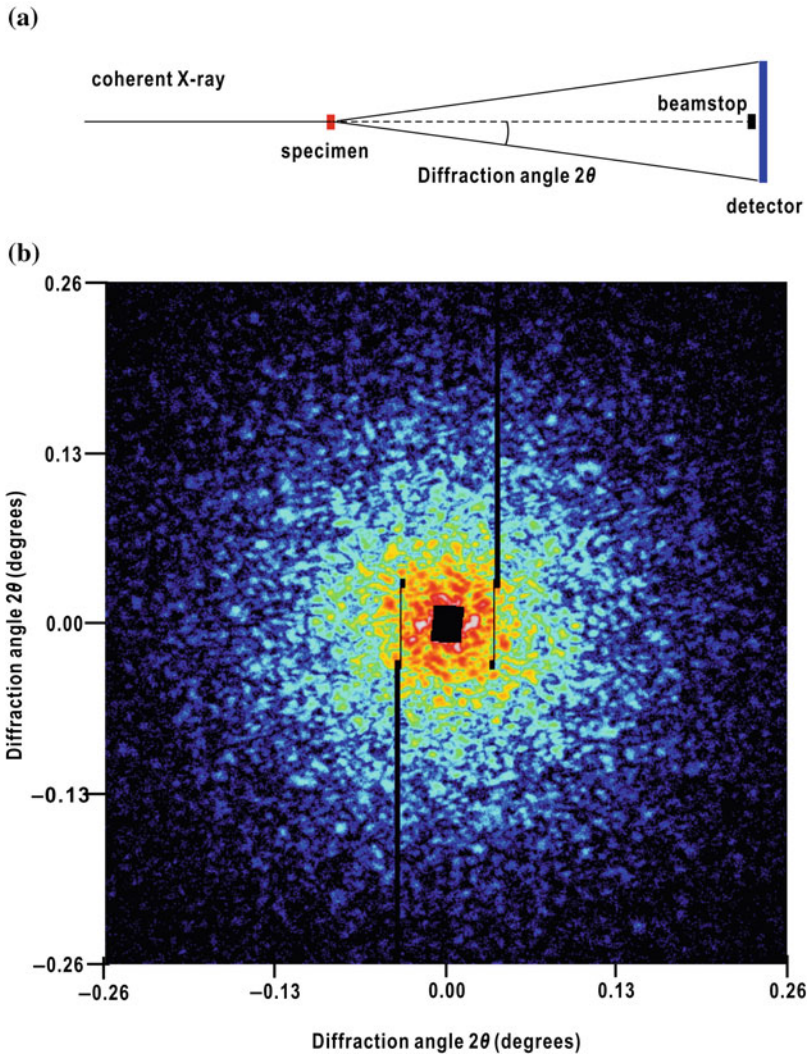


**Fig. 1.9  a** Schematic illustration of XDI experiment. **b** Diffraction pattern from a single nucleus of budding yeast (*Saccharomyces cerevisiae*) [29]. The nucleus was irradiated by a single X-ray free electron laser (XFEL) pulse with a wavelength of 0.225 nm. The diffraction pattern is composed of a number of speckle peaks. The black square at the center is the shadow of the beam stop. The black lines are the gaps between panels in the detector. Published with kind permission of Masayoshi Nakasako 2017. All Rights Reserved

under the oversampling condition [9]. The theoretical background will be described in Chaps. 2 and 3.

In the development of XDI methodology, researchers often used synchrotron X-ray radiation at the BL29XU of the SPring-8 [39] to visualize two-dimensional

projection electron density maps and three-dimensional structures of noncrystalline particles from materials science and biology [40–48]. In the first application of XDI in biology, researchers visualized the distribution of histidine-tagged fluorescence proteins to accumulate manganese inside a genetically modified *Escherichia coli* cell [41]. From the diffraction pattern of a single cell, the projection electron density map was retrieved at a resolution of 30 nm, and was consistent with the fluorescence image obtained by confocal microscopy for the same cell. The second example carried out at the Advanced Light Source is the series of XDI experiments on freeze-dried budding yeast, *Saccharomyces cerevisiae*, done using soft X-rays with a wavelength of 1.65 nm [49]. The phase-retrieved electron density maps obtained at a resolution of 30 nm have sufficient quality to discuss the locations of organelles, such as the nucleus and vacuole, inside the cell.

In the last decade, XDI experiments at synchrotron facilities have demonstrated the potential to visualize the structures of noncrystalline biological particles with micrometer dimensions. However, most of the experiments were carried out on dehydrated specimens at ambient temperature. Under these conditions, specimens suffer serious radiation damage. When specimens are kept near liquid nitrogen temperatures, the radiation damage of specimens is dramatically reduced, as demonstrated in the cryogenic X-ray crystallography of proteins [50]. To visualize the structures of hydrated biological specimens with reduced radiation damage, cryogenic XDI techniques, diffraction apparatus, and a procedure to prepare specimens in the frozen-hydrated state without any chemical staining and sectioning [51–53] were required. However, studies on the radiation damage of biological specimens predict the maximum radiation dose that a biological sample can receive before the destruction of structures and functions [54, 55]. Then, the resolution limit in structural analyses using XDI is approximately 10 nm, even for biological specimens kept under cryogenic temperatures [55].

To obtain diffraction patterns from biological specimens without radiation damage, sufficiently strong X-ray pulses of very short duration are suitable, although the specimens are destroyed after diffraction. X-ray free-electron laser (XFEL) pulses allow us to record the diffraction patterns of biological specimens without radiation damage [56]. If many copies of specimen particles with nearly the same structures are irradiated in random orientations with respect to the XFEL pulses, the three-dimensional structure of the specimen particles can be reconstructed.

In recent years, intense X-ray pulses with duration of tens of femtoseconds have been available at XFEL facilities such as the Linac Coherent Light Source (LCLS) [57] and SPring-8 Angstrom Compact free electron LAser (SACLA) [58]. Because the X-ray pulses are provided at repetition rates of 30–100 Hz, a large number of diffraction patterns can be collected in a short period of time. XFEL-XDI has been applied to the visualization of the structures of various biological samples, such as a large virus [59, 60], a cellular organelle [61, 62], and bacterial cells [63, 64]. One of weak points in XFEL-XDI is the destruction of the specimen particles at an atomic level by a single XFEL pulse. For instance, the intensity of focused XFEL pulses with wavelengths of 0.225 nm reaches $10^{10-11}$ photons/$2 \times 2$ $\mu m^2$/ pulse of 10 fs

duration at the SACLA [63, 64]. However, as the destruction of specimen particles occurs after diffraction for XFEL pulses [67, 68], we are able to collect diffraction patterns from almost radiation-damage-free particles, as demonstrated in the recent crystal structural analysis of proteins using XFEL [53].

## 1.4  A Guide to the Following Chapters

In Chaps. 2–10, the principle, experimental techniques, and examples of structural analyses for XDI will be described. To understand the structure determination by XDI, the fundamental theory of X-ray diffraction is summarized in Chap. 2. Then, the principle of XDI is introduced in Chap. 3, including the phase-retrieval algorithm, which reconstructs an electron density map from a diffraction pattern. To introduce the feasibility of XDI in biology, Table 1.1 summarizes the pros and cons of fluorescence LM, TEM, and XDI.

**Table 1.1**  The pros and cons of techniques used for cell imaging

|  | LM | TEM | XDI |
|---|---|---|---|
| Specimen | Fluorescence-labeled molecules in cells and organelles | Supramolecular complex with molecular weight larger than approximately 200 k | Cells and organelles |
| Specimen preparation | Labeling by fluorescence molecules | Sectioning and flash cooling | Flash cooling (see Chap. 5) |
| Limitation for the thickness of specimen | Several tens of μm | Less than 100 nm is better to avoid multiple scattering | 6 μm or more (see Chap. 9) |
| Imaging of whole cell | Difficult | Difficult | Possible |
| Real time observation | Partly possible | Impossible | Impossible (see Chaps. 4 and 5) |
| Object visualized | Position of labeled molecules | Electrostatic potential over the specimen | Electron density over the specimen (see Chaps. 2, 3, 7–9) |
| Radiation damage | Severe by excitation laser | Severe by electrostatic interaction between electrons and atoms | See Chaps. 4 and 9 |
| Resolution/ nm | Better than 100 in the plane normal to the optical axis, and better than 300 along the optical axis in SRFM | 10 nm or better | 20–100 nm depends on the total cross-section of specimen particle (Chaps. 8 and 9) |

XDI was proposed in 1999, and it is still a relatively new imaging technique. Therefore, diffraction apparatuses, experimental procedures, and algorithms for structural analyses using XDI are still under development. In Chap. 4, diffraction apparatuses dedicated to XDI carried out at cryogenic temperatures are described. In addition, the procedures for preparing specimens for cryogenic experiments are shown in Chap. 5. The details of the diffraction apparatuses and specimen preparation used not only for XDI but also for other measurement techniques carried out for cooled specimens are given. In XDI experiments at XFEL facilities, a large number of diffraction patterns are obtained within a short time. In Chap. 6, examples of the algorithms and procedures for processing diffraction patterns are introduced. Chapter 7 presents the algorithms and procedures used to obtain correct electron density maps from diffraction patterns. Chapters 8 and 9 provide examples of structural analyses of biological particles, such as cells and cellular organelles, to introduce the kind of structural studies that are possible using XDI. Chapter 8 is dedicated to the structural analyses for single diffraction patterns. Chapter 9 introduces how three-dimensional electron density maps necessary for discussing the entire structures of biological particles are reconstructed in XDI. Finally, current problems and future prospects are discussed in Chap. 10.

It should be noted that there exists another XDI method ([69] is cited as a typical example) applicable for specimens of sizes larger than the cross section of the incident X-ray beam; this method is outside of the scope of this book, because of the restriction from the patent of the method.

# References

1. B. Alberts, et al., *Molecular Biology of the Cell* (Garland Science, New York, 2014)
2. E. Schrödinger, *What is life? The physical aspect of living cell* (Cambridge University Press, Cambridge, 1944)
3. C.I. Blenden, J. Tooze, *Introduction to Protein Structure* (Garland Publishing Inc, New York, 1999)
4. D.I. Svergun, M.H.J. Koch, P.A. Timmins, R.P. May, *Small Angle X-ray and Neutron Scattering from Solutions of Biological Macromolecules* (Oxford University Press, Oxford, 2013)
5. J. Als-Nielsen, D. McMorrow, *Elements of Modern X-ray Physics*, 2nd edn. (Wiley, London, 2011)
6. J. Drenth, *Principles of Protein X-ray Crystallography* (Springer, New York, 1994)
7. J. Frank, *Three-Dimensional Electron Microscopy of Macromolecular Assemblies* (Oxford University Press, Oxford, 2006)
8. D.B. Murphy, M.W. Davidson, *Fundamentals of Light Microscopy and Electronic Imaging* (Wiley, New Jersey, 2012)
9. J. Miao, D. Sayre, H.N. Chapman, J. Opt. Soc. Am. A **15**, 1662 (1998)
10. J. Miao, P. Charalambous, J. Kirz, D. Sayre, Nature **400**, 342 (1999)
11. P.P. Mondal, A. Diaspro, *Fundamentals of Fluorescence Microscopy* (Springer, Berlin, 2014)
12. U. Kubitscheck (ed.), *Fluorescence Microscopy: From Principles to Biological Applications* (Wiley, New York, 2013)
13. M. Born, E. Wolf, *Principles of Optics* (Cambridge University Press, Cambridge, 1999)

14. H. Noji, R. Yasuda, M. Yoshida, K. Kinoshita Jr., Nature **386**, 299 (1997)
15. O. Shimomura, F.H. Johnson, Y. Saiga, J. Cell. Comp. Physiol. **59**, 223 (1962)
16. A. Miyawaki, Microscopy **62**, 63 (2013)
17. P. Davidovits, M.D. Egger, Nature **223**, 831 (1969)
18. J.G. White, W.B. Amos, M. Fordham, J. Cell Biol. **105**, 41 (1987)
19. B. Huang, M. Bates, X. Zhuang, Ann. Rev. Biochem. **78**, 993 (2009)
20. M.J. Rust, M. Bates, X. Zhung, Nat. Methods **3**, 793 (2006)
21. M.G.L. Gustaffson, J. Microsc. **198**, 82 (2000)
22. T.A. Klar, S.W. Hell, Opt. Lett. **19**, 780 (1994)
23. J. Dubochet, et al., Q. Rev. Biophys. **21**, 129 (1988)
24. A.M. Glauert, P.R. Lewis, *Biological Specimen Preparation for Transmission Electron Microscopy* (Princeton University Press, Princeton, 2014)
25. A.W. Robards, U.B. Sleytr, *Low Temperature Methods in Biological Electron Microscopy* (Elsevier, Amsterdam, 1991)
26. L. Gan, G.J. Jensen, Q. Rev. Biophys. **45**, 27 (2011)
27. S. Subramaniam, W. Kühlbrandtt, R. Henderson, IUCrJ **3**, 3 (2016)
28. S.H.W. Scheres, J. Struct. Biol. **180**, 519 (2012)
29. J. Kosinski et al., Science **352**, 363 (2016)
30. F. Song et al., Science **344**, 376 (2014)
31. C. Yan, et al., Science **353**, 904 (2016)
32. M.A.L. Gros, G. McDermott, C.A. Larabell, Curr. Opin. Struct. Biol. **15**, 593 (2005)
33. G. Schneider et al., Nat. Methods **7**, 985 (2010)
34. T. Paunesku, S. Vogt, J. Masr, B. Lai, G. Woloschak, J. Cell. Biochem. **99**, 1489 (2006)
35. J. Deng, Proc. Natl. Acad. Sci. USA **112**, 2314 (2015)
36. D. Sayre, Acta Crystallogr. **5**, 843 (1952)
37. J. Miao, T. Ishikawa, I.K. Robinson, M.M. Murnane, Science **348**, 530 (2015)
38. J.R. Fienup, Appl. Opt. **21**, 2758 (1982)
39. K. Tamasaku, et al., Nucl. Instrum. Methods A **467–468**, 686 (2001)
40. J. Miao, et al., Phys. Rev. Lett. **89**, 088303 (2002)
41. J. Miao, et al., Proc. Natl. Acad. Sci. USA **100**, 110 (2003)
42. J. Miao et al., Phys. Rev. Lett. **97**, 215503 (2006)
43. C. Song et al., Phys. Rev. Lett. **101**, 158101 (2008)
44. Y. Nishino, et al., Phys. Rev. Lett. **102**, 018101 (2009)
45. H. Jiang et al., Proc. Natl. Acad. Sci. USA **107**, 11234 (2010)
46. C. Song, et al., Biophys. J. **107**, 1074 (2014)
47. D. Nam et al., Phys. Rev. Lett. **110**, 098103 (2013)
48. Y. Takayama, M. Nakasako, Rev. Sci. Instrum. **83**, 054301 (2012)
49. D. Shapiro et al., Proc. Natl. Acad. Sci. U.S.A. **102**, 15343 (2005)
50. J.W. Pflugrath, Acta Crystallogr. **F71**, 622 (2015)
51. E. Lima, et al., Phys. Rev. Lett. **103**, 198102 (2009)
52. X. Huang et al., Phys. Rev. Lett. **103**, 198101 (2009)
53. M. Nakasako et al., Rev. Sci. Instrum. **84**, 093705 (2013)
54. R. Henderson, Q. Rev. Biophys. **28**, 171 (1995)
55. M.R. Howells et al., J. Electron Spectrosc. Relat. Phenom. **170**, 4 (2009)
56. K. Hirata et al., Nat. Methods **11**, 734 (2014)
57. P. Emma et al., Nat. Photon. **4**, 641 (2010)
58. T. Ishikawa et al., Nat. Photon. **6**, 540 (2012)
59. M.M. Seibert et al., Nature **470**, 78 (2011)
60. T. Ekerberg et al., Phys. Rev. Lett. **114**, 098102 (2015)
61. T. Oroguchi et al., J. Phys. B: At. Mol. Opt. Phys. **48**, 184003 (2015)
62. Y. Takayama, et al., Plant Cell Physiol. **56**, 1272 (2015)
63. T. Kimura et al., Nat. Commun. **5**, 3052 (2014)
64. G. van der Schot et al., Nat. Commun. **6**, 5704 (2015)
65. K. Tono et al., New J. Phys. **15**, 083035 (2013)

66. H. Yumoto et al., Nat. Photonics **7**, 43 (2013)
67. R. Neutze, R. Wouts, D. van der Spoel, E. Weckert, and. J. Hajdu Nat. **406**, 752 (2000)
68. H.N. Chapman et al., Nat. Phys. **2**, 839 (2006)
69. A. Diaz et al., J. Struct. Biol. **192**, 461 (2015)

# Chapter 2
# X-Ray Diffraction

**Abstract**  X-ray diffraction is the basis for understanding X-ray diffraction imaging (XDI). In this chapter, the theoretical background of X-ray diffraction is introduced starting from Maxwell's equation in the system of non-relativistic classical electromagnetism. First, fundamental equations are derived to describe electromagnetic waves emitted from accelerated electrons by solving Maxwell's equation. The theory of dipole radiation is applied to electrons bound in atoms, and then the scattering cross section for Thomson scattering is derived. By applying this theory to a system composed of two or more electrons, the interference between the diffracted waves is described as the Fourier transform of the electron density in the system. The critical importance of the phases of the diffracted waves in structural analysis is demonstrated, and then, the experimental determination of phases in protein X-ray crystallography is briefly introduced.

## 2.1  X-Rays as Electromagnetic Waves

X-rays were discovered by Röntgen in 1895 through his investigation of cathode rays. X-rays are electromagnetic waves with wavelengths in the order of $10^{-9}$–$10^{-10}$ m. The visualization of the atomic structures of materials started in 1912, when Friedrich, Knipping, and von Laue experimentally discovered the phenomenon of X-ray diffraction. Their findings implied two remarkable advances in physics [1]. The first was that X-rays are electromagnetic waves with short wavelengths; the second was that the diffraction of X-rays could be used to determine the atomic structures of materials. Von Laue formulated the theory of X-ray diffraction immediately after this discovery. Advances in mechatronics and computer technology accelerated the development of diffraction apparatuses, X-ray sources, and software for structural analysis.

Here, we use monochromatic and polarized X-ray waves to describe X-ray diffraction phenomena (Fig. 2.1) [2]. It should be noted that we use SI units for physical quantities.
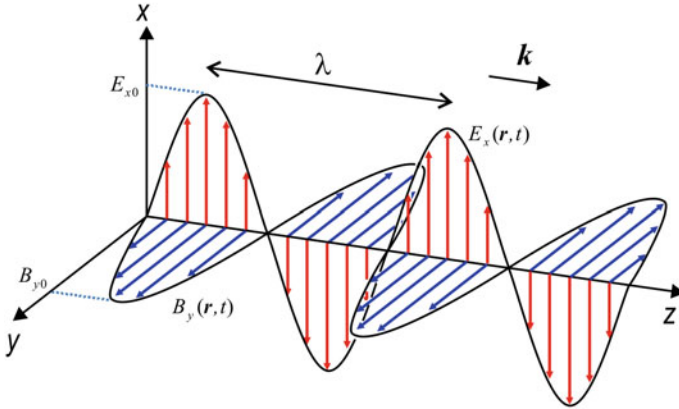
**Fig. 2.1** Schematic illustration of the propagation of a monochromatic and polarized electromagnetic wave. In this case, the electromagnetic wave propagates along the direction of the $z$-axis with the propagation vector $\boldsymbol{k}$. The electric field is polarized in the x-z plane. The electric field, magnetic induction, and direction of propagation are mutually orthogonal. Published with kind permission of Masayoshi Nakasako 2017. All Rights Reserved

A linearly polarized plane wave with wavelength $\lambda$ and angular frequency $\omega$ propagating at velocity $c$ along the $z$-axis is written as

$$\boldsymbol{E}(\boldsymbol{r},t) = \boldsymbol{E}_0 \sin\left\{\omega\left(t - \frac{z}{c}\right) + \alpha\right\},$$

$$\boldsymbol{B}(\boldsymbol{r},t) = \boldsymbol{B}_0 \sin\left\{\omega\left(t - \frac{z}{c}\right) + \alpha\right\},$$

where the magnitude of the propagation vector $\boldsymbol{k}$ is inversely proportional to the wavelength $\lambda$ and proportional to the angular frequency $\omega$ of the electromagnetic wave.

$$|\boldsymbol{k}| = \frac{2\pi}{\lambda} = \frac{2\pi v}{c} = \frac{\omega}{c},$$

where $v$ is the frequency of the wave. The magnitude of the magnetic induction is suppressed by a factor of $1/c$ compared to that of the electric field as

$$|\boldsymbol{B}(\boldsymbol{r},t)| = \frac{|\boldsymbol{E}(\boldsymbol{r},t)|}{c}.$$

## 2.2  Radiation of Electromagnetic Waves from a Charged Particle

X-ray diffraction occurs when the electrons of the atoms composing a material are in forced oscillation driven by the electric field of the X-rays propagating through the material (Fig. 2.2). When atoms in an object is irradiated by an electromagnetic
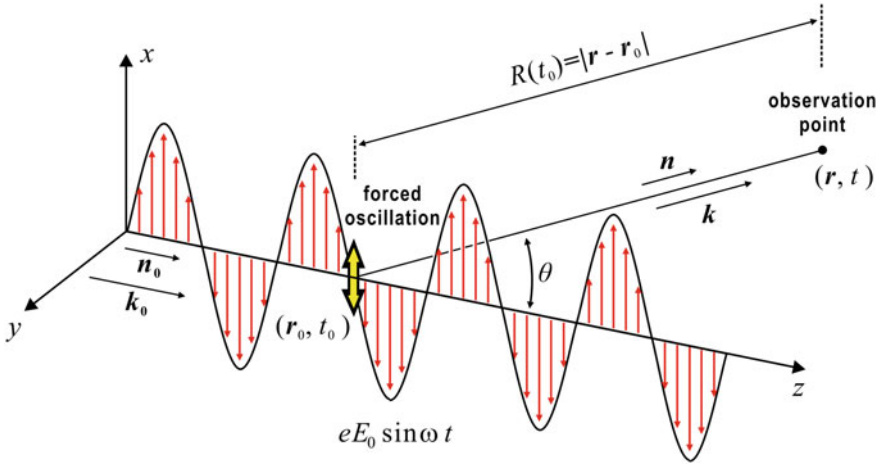
**Fig. 2.2** Schematic illustration of a fundamental process in X-ray diffraction. An electron bound in an atom is under forced oscillation driven by the polarized electric field of the monochromatic X-ray with propagation vector $\boldsymbol{k}_0$. Then, the emitted wave is observed in the direction of the propagation vector $\boldsymbol{k}$. The unit vectors along $\boldsymbol{k}_0$ and $\boldsymbol{k}$ are $\boldsymbol{n}_0$ and $\boldsymbol{n}$, respectively. The angle between the two propagation vectors is $\theta$. The distance between the electron and the observation point is $R(t_0)$. Published with kind permission of Masayoshi Nakasako 2017. All Rights Reserved

wave with the electric field $\boldsymbol{E}(\boldsymbol{r}, t)$ and the magnetic induction $\boldsymbol{B}(\boldsymbol{r}, t)$, the electrons and the nucleus are accelerated by the Lorentz force as

$$\boldsymbol{F}(\boldsymbol{r}, t) = q\boldsymbol{E}(\boldsymbol{r}, t) + qv \times \boldsymbol{B}(\boldsymbol{r}, t)$$

where $q$ is the charge of the electron or nucleus. Because the mass of the nucleus is much larger than an electron, the magnitude of the acceleration of the nucleus is negligible in comparison with that of the electron. In addition, in a non-relativistic case, where the velocity of the electron is much smaller than the velocity of light, the second term can be negligible, because of the ratio on the magnitudes of the electric field and the magnetic induction as described above. Therefore, to understand the mechanism of X-ray diffraction, we treat the electromagnetic radiation only from an electron under acceleration [2, 3]. Although deriving completely correct results for electromagnetic radiation requires quantum mechanics, the theory of classical electromagnetism is sufficient for the scope of this book.

## 2.2.1   Electromagnetic Waves from an Electron Under Acceleration

Here we discuss the electromagnetic radiation from an electron in vacuum. The electromagnetic radiation from an electron under acceleration is described by

Maxwell's equation. The acceleration induces time-dependent changes in the charge density distribution of the electron $\rho_e(\mathbf{r}, t)$. Simultaneously, the accompanying electric field $\mathbf{E}(\mathbf{r}, t)$ changes according to Gauss's law,

$$\operatorname{div} \mathbf{E}(\mathbf{r}, t) = \frac{1}{\varepsilon_0} \rho_e(\mathbf{r}, t),$$

where $\varepsilon_0$ is the permittivity of vacuum ($8.85 \times 10^{-12}$ N/V$^2$). The displacement of the electron also induces a charge current density $\mathbf{i}(\mathbf{r}, t)$ according to the continuity equation,

$$\frac{d}{dt} \rho_e(\mathbf{r}, t) + \operatorname{div} \mathbf{i}\, (\mathbf{r}, t) = 0.$$

The changes in the electric field and the charge current density simultaneously induces magnetic induction $\mathbf{B}(\mathbf{r}, t)$ according to Maxwell–Ampère's law and Faraday's law,

$$\operatorname{rot} \frac{1}{\mu_0} \mathbf{B}(\mathbf{r}, t) - \frac{\partial}{\partial t} \varepsilon_0 \mathbf{E}(\mathbf{r}, t) = \mathbf{i}(\mathbf{r}, t),$$

$$\operatorname{rot} \mathbf{E}(\mathbf{r}, t) + \frac{\partial}{\partial t} \mathbf{B}(\mathbf{r}, t) = 0,$$

where $\mu_0$ is the vacuum permeability ($1.26 \times 10^{-6}$ N/A$^2$). Thus, by combining these equations, the electric and magnetic fields can be determined by solving these differential equations in the presence of $\rho_e(\mathbf{r}, t)$ and $\mathbf{i}\,(\mathbf{r}, t)$. When the charge current density is absent, the two laws give the wave equation for an electromagnetic wave in vacuum. For instance, the electric field varies according to the wave equation,

$$\left[ -\Delta + \frac{1}{c^2} \frac{\partial^2}{\partial t^2} \right] \mathbf{E}(\mathbf{r}, t) = 0,$$

where $c$ is the velocity of light in vacuum and is defined as

$$c = \frac{1}{\sqrt{\mu_0 \varepsilon_0}}.$$

The magnetic induction and electric fields can be represented using the scalar potential $\varphi(\mathbf{r}, t)$ and vector potential $\mathbf{A}(\mathbf{r}, t)$ as

$$\mathbf{B}(\mathbf{r}, t) = \operatorname{rot} \mathbf{A}\,(\mathbf{r}, t), \tag{2.1}$$

$$\mathbf{E}\,(\mathbf{r}, t) = -\frac{\partial}{\partial t} \mathbf{A}(\mathbf{r}, t) - \operatorname{grad} \varphi(\mathbf{r}, t). \tag{2.2}$$

Then, each potential satisfies the following inhomogeneous Helmholtz-type differential equations

$$\left(\Delta - \frac{1}{c^2} \cdot \frac{\partial^2}{\partial t^2}\right) A(r, t) = -\mu_0 \, i(r, t)$$

$$\left(\Delta - \frac{1}{c^2} \cdot \frac{\partial^2}{\partial t^2}\right) \varphi(r, t) = -\frac{1}{\varepsilon_0} \rho_e(r, t),$$

using the Lorentz gauge invariance defined by

$$\text{div} A \, (r, t) + \frac{1}{c^2} \cdot \frac{\partial}{\partial t} \varphi \, (r, t) = 0.$$

There are two types of solutions for the differential equations: the advanced potential and the retarded potential. Because the advanced potential violates causality, it is discarded here. The retarded potential is written as

$$\varphi(r, t) = \frac{1}{4\pi \, \varepsilon_0} \int \frac{\rho_e(r', t - |r - r'|/c)}{|r - r'|} \, d^3 r', \tag{2.3}$$

$$A(r, t) = \frac{\mu_0}{4\pi} \int \frac{i(r', t - |r - r'|/c)}{|r - r'|} \, d^3 r', \tag{2.4}$$

$$t = t' + \frac{|r - r'|}{c}, \tag{2.5}$$

where $t$ is the time at the observation point $r$, and $t'$ is the time at the radiation point $r'$. The scalar (vector) potential at the observation point is calculated by integrating the variation of the charge density distribution (current density distribution) around the electron under acceleration. Hence, the distance from the observation point just satisfies the retardation condition (2.5).

## 2.2.2 Dipole Radiation

The term describing retardation can be modified using the Dirac delta function as

$$\delta\left((t - t') - \frac{|r - r'|}{c}\right) = \frac{1}{2\pi} \int\limits_{-\infty}^{+\infty} \exp\left\{-i\omega\left[(t - t') - \frac{|r - r'|}{c}\right]\right\} d\omega.$$

With this relation, the retarded potentials are rewritten as

$$
\boldsymbol{A}_-(\boldsymbol{r},t) = \frac{\mu_0}{4\pi} \int\limits_{-\infty}^{+\infty} dt' \frac{1}{2\pi} \int\limits_{-\infty}^{+\infty} \exp[-i\omega(t-t')]\,d\omega
$$

$$
\int \frac{\boldsymbol{i}\,(\boldsymbol{r}',t')}{|\boldsymbol{r}-\boldsymbol{r}'|} \exp\left[i\frac{\omega}{c}|\boldsymbol{r}-\boldsymbol{r}'|\right] d^3 r'
$$

$$
\varphi_-(\boldsymbol{r},t) = \frac{1}{4\pi\varepsilon_0} \int\limits_{-\infty}^{+\infty} dt' \frac{1}{2\pi} \int\limits_{-\infty}^{+\infty} \exp[-i\omega(t-t)]\,d\omega
$$

$$
\int \frac{\rho_{\mathrm{e}}(\boldsymbol{r}',t')}{|\boldsymbol{r}-\boldsymbol{r}'|} \exp\left[i\frac{\omega}{c}|\boldsymbol{r}-\boldsymbol{r}'|\right] d^3 r'
$$

The integrand in the region around the electron can be expanded in a series of multipoles as

$$
\frac{1}{|\boldsymbol{r}-\boldsymbol{r}'|}\exp\left(i\frac{\omega}{c}|\boldsymbol{r}-\boldsymbol{r}'|\right) = i\frac{\omega}{c}\sum_{i=0}^{\infty}(2\ell+1)j_\ell\!\left(\frac{\omega}{c}r'\right)h_\ell^{(1)}\!\left(\frac{\omega}{c}r\right)P_\ell(\cos\theta')
$$

$$
\frac{\omega}{c}r = \frac{2\pi}{\lambda}r = kr,
$$

where $j_\ell\!\left(\frac{\omega}{c}r'\right)$, $h_\ell^{(1)}\!\left(\frac{\omega}{c}r\right)$, and $P_\ell(\cos\theta')$ are the spherical Bessel function of the first kind, the spherical Hankel function of the first kind, and Legendre polynomial of order $l$, respectively [2].

Here we assume that the area ($r'$ ) with significant values of electron density and charge current density is very small in comparison with the wavelength ($\lambda$) of the emitted electromagnetic wave. Then, the Bessel function can be approximated by

$$
j_\ell\!\left(\frac{\omega}{c}r'\right) \underset{\frac{\omega}{c}r'\to 0}{\approx} \left(\frac{\omega}{c}\right)^\ell \frac{r'^\ell}{(2\ell+1)!!},
$$

The Hankel function is similarly approximated. Under these approximations, the retarded potentials are rewritten as [2]

$$
\varphi(\boldsymbol{r},t) = \frac{1}{4\pi\,\varepsilon_0}\sum_{\ell=0}^{\infty}\frac{(2\ell+1)}{(2\ell+1)!!}(-r)^\ell\left(\frac{1}{r}\frac{d}{dr}\right)^\ell\left[\frac{1}{r}\left\langle\rho^{(\ell)}\!\left(t-\frac{r}{c}\right)\right\rangle\right]
$$

$$
\left\langle\rho^{(\ell)}(t)\right\rangle \equiv \int r'^\ell P_l(\cos\theta')\rho_{\mathrm{e}}(\boldsymbol{r}',t)\,d^3 r'
$$

$$
\boldsymbol{A}(\boldsymbol{r},t) = \frac{\mu_0}{4\pi}\sum_{\ell=1}^{\infty}\frac{(2\ell-1)}{(2\ell-1)!!}(-r)^{\ell-1}\left(\frac{1}{r}\frac{d}{dr}\right)^{\ell-1}\left[\frac{1}{r}\left\langle\boldsymbol{i}^{(\ell-1)}\!\left(t-\frac{r}{c}\right)\right\rangle\right]
$$

$$
\left\langle\boldsymbol{i}^{(\ell)}(t)\right\rangle \equiv \int r'^\ell P_\ell(\cos\theta')\,\boldsymbol{i}(\boldsymbol{r}',t)\,d^3 r'.
$$

In these equations, the charge density and current density distribution functions are expanded in series of the multipole components. The monopole term ($\ell = 0$) does not give rise to radiation. The retarded potentials from the dipole term ($\ell = 1$) are calculated as

$$\varphi_{\ell=1}(\boldsymbol{r},t) = \frac{1}{4\pi\,\varepsilon_0}\left\{\frac{\boldsymbol{n}_0}{r^2}\cdot\boldsymbol{p}\left(t-\frac{r}{c}\right)+\frac{\boldsymbol{n}_0}{cr}\cdot\dot{\boldsymbol{p}}\left(t-\frac{r}{c}\right)\right\}, \tag{2.6}$$

$$\boldsymbol{A}_{\ell=1}(\boldsymbol{r},t) = \frac{\mu_0}{4\pi}\frac{\dot{\boldsymbol{p}}\left(t-\frac{r}{c}\right)}{r}$$
$$\dot{\boldsymbol{p}}(t) = \int \boldsymbol{r}'\,\frac{\partial\rho_{\mathrm{e}}(\boldsymbol{r}',t)}{\partial t}\,\mathrm{d}^3r' = \int \boldsymbol{i}\,(\boldsymbol{r}',t)\mathrm{d}^3r', \tag{2.7}$$

where $\dot{\boldsymbol{p}}(t)$ represents the time-dependent variation of the dipole induced by the external electric field. The unit vector $\boldsymbol{n}_0$ defines the propagation direction of the incident electromagnetic wave. By substituting (2.6) and (2.7) into (2.1) and (2.2), the electric field and magnetic induction at the observation point far from the source in the direction defined by the unit vector $\boldsymbol{n}$ is approximated as

$$\boldsymbol{E}^{\mathrm{Rad}}(\boldsymbol{r},t) \approx \frac{1}{4\pi\varepsilon_0}\left[-\ddot{\boldsymbol{p}}\left(t-\frac{r}{c}\right)\Big/c^2r + \boldsymbol{r}\left(\boldsymbol{r}\cdot\ddot{\boldsymbol{p}}\left(t-\frac{r}{c}\right)\right)\Big/c^2r^3\right]$$
$$= \frac{e}{4\pi\varepsilon_0}\frac{\boldsymbol{n}\left(t-\frac{r}{c}\right)\times\left(\boldsymbol{n}\left(t-\frac{r}{c}\right)\times\ddot{\boldsymbol{x}}\left(t-\frac{r}{c}\right)/c\right)}{c\,r}, \tag{2.8}$$

$$\boldsymbol{B}^{\mathrm{Rad}}(\boldsymbol{r},t) \approx -\frac{\mu_0}{4\pi}\left[\boldsymbol{r}\times\ddot{\boldsymbol{p}}\left(t-\frac{r}{c}\right)\Big/cr^2\right]. \tag{2.9}$$

The geometrical condition can be reworded to say that the distance between the source and the observation points is far larger than the size of the source, such as an atom. It can be demonstrated that the electric field, magnetic induction, and propagation vector of the emitted electromagnetic wave are mutually orthogonal by calculating the vector products. The emitted electromagnetic waves are polarized in the direction defined by the vector products in (2.8) and (2.9).

The Poynting vector of the electromagnetic wave is readily calculated from (2.8) and (2.9) as

$$\boldsymbol{N}(\boldsymbol{r},t) = \frac{1}{2}\boldsymbol{E}^{\mathrm{Rad}}(\boldsymbol{r},t)\times\frac{1}{\mu_0}\boldsymbol{B}^{\mathrm{Rad}}(\boldsymbol{r},t)$$
$$= \frac{\mu_0}{2(4\pi)^2c}\frac{\left|\boldsymbol{n}_0\times\ddot{\boldsymbol{p}}\left(t-\frac{r}{c}\right)\right|^2}{r^2}\vec{n}_0. \tag{2.10}$$

The radiation power is calculated by integrating the Poynting vector over the whole solid angle

$$P = \int \boldsymbol{N}(\boldsymbol{r},t)\cdot\boldsymbol{n}_0\,\mathrm{d}S = \frac{1}{12\pi}\frac{\mu_0}{c}\left|\ddot{\boldsymbol{p}}\left(t-\frac{r}{c}\right)\right|^2.$$

## 2.2.3   Thomson Scattering

Here, we consider an electron bound in an atom under forced oscillation driven by an external electric field with an angular frequency $\omega$ and an amplitude $E_0$ polarized along the $x$-axis, as illustrated in Fig. 2.2 [2]. When the energy of the X-ray is far larger than the potential energy of the electron in the atom, the motion of the electron can be treated as a free electron under forced oscillation. The dipole moment is derived from the equation of motion as

$$\ddot{p}(t) = m_e \ddot{x}(t) = -eE_0 \, \sin \omega t = eE_0 \sin(\omega t + \pi),$$

where $m_e$ and $-e$ are the rest mass and charge of electron, respectively. Then, the phase shift relative to the incident electric field is $\pi$. Therefore, according to the theory described in the previous subsection, the electron accelerated by the external electric field radiates an electromagnetic wave, the wavelength of which is the same with that of the incident X-ray. The electric field is given by

$$
\begin{aligned}
\mathbf{E}^{\mathrm{Rad}}(\mathbf{r}, t) &= \frac{e}{4\pi\varepsilon_0} \frac{e}{m_e} \frac{\mathbf{n}(t_0) \times (\mathbf{n}(t_0) \times \mathbf{E}_0 \sin[\omega t + \pi])}{c^2 R(t_0)}, \\
t_0 &= t - \frac{|\mathbf{R}(t_0)|}{c}.
\end{aligned}
\tag{2.11}
$$

The pattern of the electric field is illustrated in Fig. 2.3. It should be emphasized again that the distance $|\mathbf{R}(t_0)|$ from the electron to the observation point is much larger than the electron.



Fig. 2.3 A schematic illustration of the electric field of dipole radiation from an electron described by (2.11). The electric field of the radiated wave is illustrated by both the grey level and the contours. The yellow arrow indicates the direction of the oscillation of an electron due to an external force. Published with kind permission of Masayoshi Nakasako 2017. All Rights Reserved
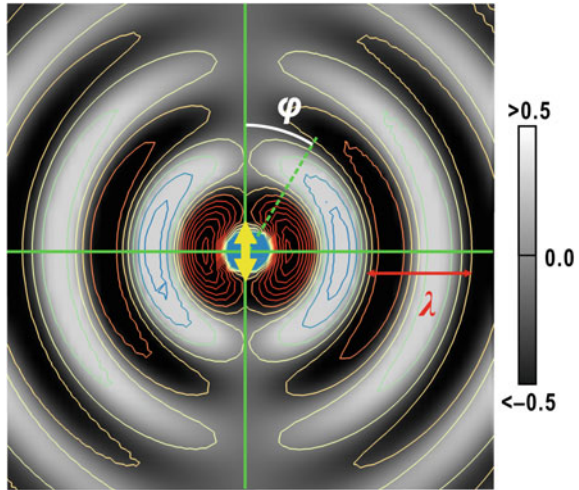
By substituting (2.11) into (2.10), the Poynting vector of the emitted wave is calculated to be

$$|\boldsymbol{N}(\boldsymbol{r})| = \frac{1}{2} \frac{1}{\mu_0 c} E_0^2 \, r_e^2 \frac{\sin^2 \varphi}{R^2}, \tag{2.12}$$

$$r_e = \left( \frac{e^2}{4\pi \, \varepsilon_0 m_e c^2} \right). \tag{2.13}$$

where $\varphi$ is the angle between the polarization direction of the incident wave ($\boldsymbol{E}_0$) and the direction of observation ($\boldsymbol{n}$). The radiation power is anisotropic as described by the angular-dependent term $\sin^2 \varphi$, and decreases in proportion to the square of the distance between the electron and the observation point. The coefficient $r_e$ is the classical electron radius, which is a very small quantity ($2.818 \times 10^{-15}$ m [4]). Thus, the electromagnetic radiation induced by the external field is very small. When the external electromagnetic wave is an X-ray with a wavelength of 0.1 nm, the energy of X-ray photon $h\nu$ is much larger than the ionization energy of the atom and influence of potential to the electron can be neglected. The radiation from the electron under this condition is called Thomson scattering.

## 2.3   Interference of X-Rays Emitted from Electrons Under Forced Oscillation

Here we consider the interference of X-rays emitted by two electrons in vacuum separated by a distance. The basic and important concept is that the solutions of the Maxwell equation can be superimposed, due to the linearity of the equation.

### 2.3.1   Interference of X-Rays Emitted from Two Electrons

Here we consider a system composed of two electrons irradiated by the plane wave of a monochromatic and polarized X-ray, as illustrated in Fig. 2.4. The plane wave has propagation vector $\boldsymbol{k}_0$, angular frequency $\omega$, and amplitude $E_0$. The two electrons are located at points A and B, and the position vector from A to B is $\boldsymbol{r}_{AB}$. The length of the position vector ranges from the size of small molecules to that of biological cells. The distance $R$ between the system and the observation point is much larger than that of the two electrons. As described in Sect. 2.2, each electron driven by the incident X-ray emits X-rays of the same wavelength as the incident X-ray [5].

The resulting electric field at the observation point is expressed as a superposition of the emitted X-ray waves from the two electrons in the direction of the propagation vector $\boldsymbol{k}$ (Fig. 2.4).
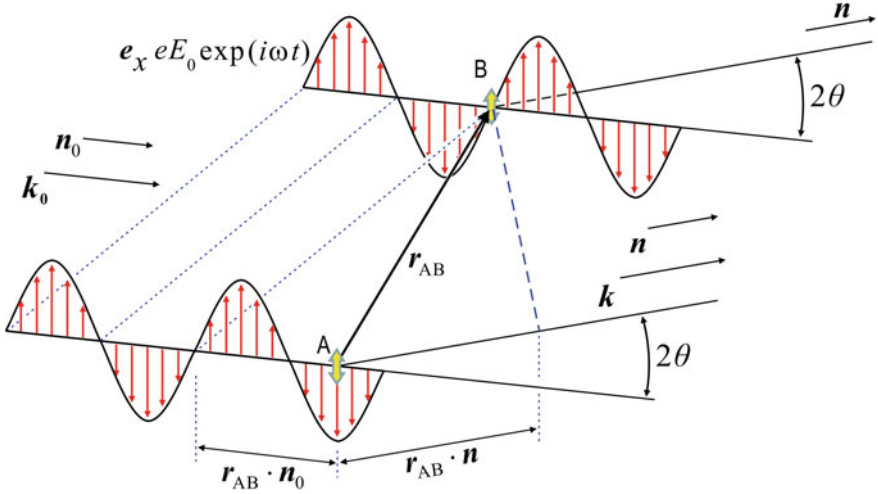
**Fig. 2.4** Schematic illustration of the electromagnetic waves emitted from a system of two electrons separated by $r_{AB}$. The angle between the incident beam and the direction of the observation point is $2\theta$. Unit vectors $n_0$ and $n$ define the propagation direction of the incident electromagnetic wave, and the direction of the observation point viewed from the system. Published with kind permission of Masayoshi Nakasako 2017. All Rights Reserved

The electric field of the X-ray emitted from the electron at point A and observed at $(r, t)$ in the direction of $k$ is

$$E_A(\mathbf{r}, t) = G \exp\left[i\omega\left(t - \frac{R}{c}\right)\right]$$
$$G = -r_e \frac{\mathbf{n} \times \mathbf{n} \times \mathbf{e}_x}{R} E_0, \tag{2.14}$$

where $n$ is the unit vector defining the direction of the observation point. $e_x$ is a unit vector defining the polarization direction of the electric field in the incident electromagnetic wave. The amplitude component defines the direction of polarization of the emitted X-ray. Because point B is separated from point A by $r_{AB}$, the X-ray wave emitted from point B is different from that emitted from point A with regard to the path length. The difference in the path length can be divided into two parts. The first is the difference caused by the projection of $r_{AB}$ onto the direction of the incident X-ray $n_0$. The second is the difference originating from the projection of $r_{AB}$ onto $n$. Hence, we have

$$E_B(\mathbf{r}, t) = G \exp\left[i\omega\left(t - \frac{R + r_{AB} \cdot n}{c}\right) + 2\pi i \frac{r_{AB} \cdot n_0}{\lambda}\right]$$
$$= G \exp\left[i\omega\left(t - \frac{R}{c}\right) - i r_{AB} \cdot (k - k_0)\right]. \tag{2.15}$$

To simplify the geometry of the observation, the scattering vector is defined as the difference between the propagation vectors in the incident and observation directions, given by

$$\boldsymbol{S} = \frac{\boldsymbol{k} - \boldsymbol{k}_0}{2\pi}, \quad |\boldsymbol{S}| = \frac{2\sin\theta}{\lambda}. \tag{2.16}$$

The length of the scattering vector is expressed in terms of the scattering angle $2\theta$ and the wavelength of the X-ray, $\lambda$.

The electric field at the observation point then results in

$$\mathbf{E}_A(\boldsymbol{S},\,t) + \mathbf{E}_B(\boldsymbol{S},\,t) = \boldsymbol{G}\,A(t)\{1 + \exp[-2\pi i\,\boldsymbol{S}\cdot\mathbf{r}_{AB}]\,\}$$
$$A(t) = \exp\left[i\omega\left(t - \frac{R}{c}\right)\right]. \tag{2.17}$$

The factor $\exp[-2\pi i\,\boldsymbol{S}\cdot\boldsymbol{r}_{AB}]$ indicates the interference caused by the phase difference between the waves from A and B. The superimposed electric field varies depending on the direction of the observation point.

## 2.3.2   Interference of X-Rays Emitted from a Many-Electron System

The results for the interference of X-rays emitted from the two electron system can be extended to an $n$-electron system. The position vector of each electron is measured from a reference electron specified as the first electron. Then, the position vector $\boldsymbol{r}_{1j}$ between the positions of the first and $j$th electrons is incorporated into the phase term of (2.17). The resulting electric field is

$$\begin{aligned}
\boldsymbol{E}(\boldsymbol{S},t) = \boldsymbol{G}A(t)\cdot\{\,& n_1 + n_2\exp[2\pi i\boldsymbol{S}\cdot\boldsymbol{r}_{12}]\\
& + \cdots + n_j\exp[2\pi i\boldsymbol{S}\cdot\boldsymbol{r}_{1j}]\\
& + \cdots + n_n\exp[2\pi i\boldsymbol{S}\cdot\boldsymbol{r}_{1n}]\}\\
= \boldsymbol{G}A(t)&\sum_{j=1}^{n} n_j\exp[2\pi i\boldsymbol{S}\cdot\boldsymbol{r}_{1j}],
\end{aligned} \tag{2.18}$$

where $n_j$ is the number of electrons located at the $j$th point [5, 6]. The last equation is known as the Fourier series. The summation is graphically illustrated in the diagram shown in Fig. 2.5.

When the electrons are continuously distributed, the Fourier series is replaced by the Fourier integral as
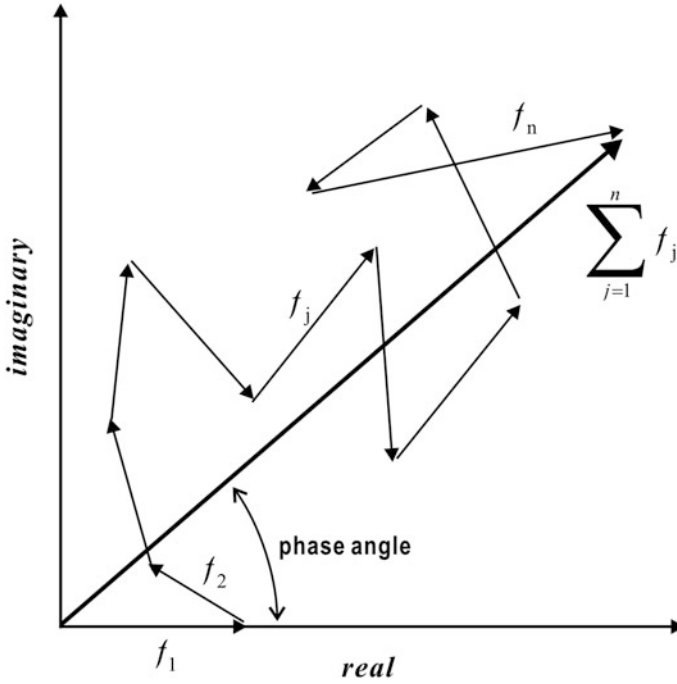
**Fig. 2.5** A diagram (Argand diagram) graphically demonstrating (2.18). Here, $f_j$ is defined as $f_j = n_j \exp\left[2\pi i S \cdot r_{1j}\right]$. Published with kind permission of Masayoshi Nakasako 2017. All Rights Reserved

$$E\left(S,t\right) = G\,A(t) \int \rho(r) \exp(2\pi\,i\,S \cdot r)\mathrm{d}^3 r. \qquad (2.19)$$

where $\rho(r)$ is the electron density, i.e., the number of electrons in volume element $\mathrm{d}^3 r$. Therefore, the resulting electric field at the observation point is the Fourier transform of the electron distribution in the system. In X-ray diffraction theory, the Fourier integral of the electron distribution is defined as the structure factor, given by

$$F(S) = \int \rho(r) \exp(2\pi\,i\,S \cdot r)\mathrm{d}^3 r = |F(S)| \exp[i\alpha\,(S)] \qquad (2.20)$$

The structure factor is a dimensionless quantity and a complex number, with amplitude and phase as illustrated in Fig. 2.5. When the structure factor is determined experimentally, we can reconstruct the electron density of the targeted object from the inverse Fourier transform (IFT) of the structure factor

$$\rho(\boldsymbol{r}) = \int F(\boldsymbol{S}) \exp(-2\pi \, i \, \boldsymbol{S} \cdot \boldsymbol{r}) \mathrm{d}^3 S. \tag{2.21}$$

The wavelengths of the X-rays used in the diffraction experiments are in the order of 0.1 nm, and the frequency of the X-rays is on the order of $3 \times 10^{18}$ Hz. Therefore, the phase term is difficult to directly measure. Only the modulus of the structure factor can be measured from the diffraction intensity. The phase term in the structure factor is lost completely in the intensity measurement.

The diffraction intensity, i.e., the number of X-ray photons, in the direction of the scattering vector $\boldsymbol{S}$ is proportional to the magnitude of the Poynting vector, i.e., the electromagnetic energy radiated to the unit area per unit time, of the radiated wave as

$$
\begin{aligned}
|N(\boldsymbol{S})| &= \frac{1}{2\mu_0 c} |\boldsymbol{G}|^2 |F(\boldsymbol{S})|^2 \left\langle A(t)^2 \right\rangle_t, \\
&= |N_0| \, r_{\mathrm{e}}^2 \, |F(\boldsymbol{S})|^2 \frac{\sin^2 \varphi}{R^2} \quad |N_0| = \frac{1}{2\mu_0 c} E_0^2,
\end{aligned}
\tag{2.22}
$$

where $|N_0|$ is the magnitude of the Poynting vector of the incident X-ray. The Poynting vector of the radiated wave is weighted by the square of the electron radius (cross section), the incident X-ray, and the square of the structure factor.

These theoretical calculations are confirmed experimentally. As an example, Fig. 2.6 shows an experimental diffraction pattern from a cuboid-shaped cuprous



Fig. 2.6 Cross-shaped diffraction pattern from a cuboid-shaped cuprous oxide particle recorded using a single-shot XFEL pulse provided from SACLA. Published with kind permission of Masayoshi Nakasako 2017. All Rights Reserved
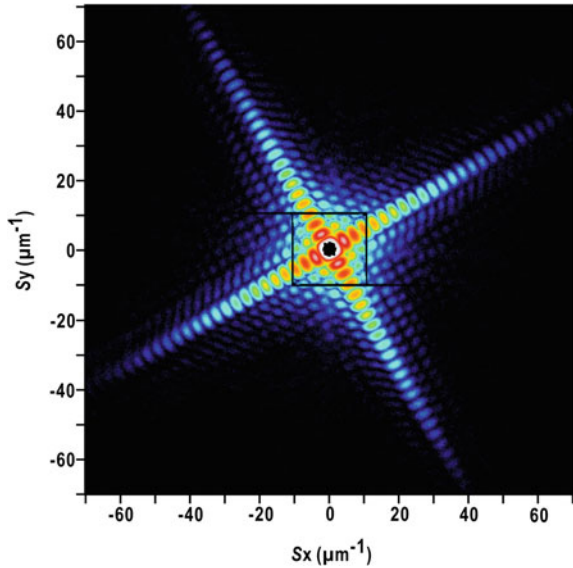
oxide particle with an approximate size of $500 \times 500$ nm. The diffraction pattern is approximated by the square of the structure factor of a cuboid shaped particle.

### 2.3.3   Resolution in X-Ray Diffraction

In X-ray diffraction experiments, the resolution in reciprocal space is mostly defined by the maximum diffraction angle $\theta_{max}$, where diffraction patterns are observed with a significant signal-to-noise ratio, given by

$$|S_{max}| = \frac{2 \sin \theta_{max}}{\lambda}$$

Then, the reciprocal of $|S_{max}|$ is defined as the shortest distance to be resolved in real space.

### 2.3.4   Diffraction by Crystals

In this subsection, we introduce the diffraction of X-rays by crystals and the method for determining the phase of diffracted X-rays. The structure factor of a crystal is calculated from the Fourier transform of the electron density, $\rho_{Xtal}(\boldsymbol{r})$, which is given by the convolution of the crystal lattice points, $L(\boldsymbol{r})$, and the electron density in the unit cell, $\rho_{UC}(\boldsymbol{r})$ [5, 6]

$$\rho_{Xtal}(\boldsymbol{r}) = \rho_{UC}(\boldsymbol{r}) * L(\boldsymbol{r}),$$
$$L(\boldsymbol{r}) = \sum_{\ell} \sum_{m} \sum_{n} \delta\left(\boldsymbol{r} - \ell\boldsymbol{a} - m\boldsymbol{b} - n\boldsymbol{c}\right) (\ell, \ m, \ n \ \in \ \text{integer}),$$

where $\boldsymbol{a}$, $\boldsymbol{b}$, and $\boldsymbol{c}$ are the unit cell vectors. The so-called crystal structure factor $F_{Cry}(\boldsymbol{S})$ is calculated as

$$F_{Cry}(\boldsymbol{S}) = F_{UC}(\boldsymbol{S}) \cdot \sum_{\ell} \sum_{m} \sum_{n} \exp[2\pi i \boldsymbol{S} \cdot (\ell\boldsymbol{a} + m\boldsymbol{b} + n\boldsymbol{c})]$$
$$= F_{UC}(\boldsymbol{S}) \frac{\sin[(2L+1)\,\pi\,\boldsymbol{S} \cdot \mathbf{a}]}{\sin(\pi\,\boldsymbol{S} \cdot \mathbf{a})} \frac{\sin[(2M+1)\,\pi\boldsymbol{S} \cdot \mathbf{b}]}{\sin(\pi\,\boldsymbol{S} \cdot \mathbf{b})} \frac{\sin[(2N+1)\pi\,\boldsymbol{S} \cdot \mathbf{c}]}{\sin(\pi\,\boldsymbol{S} \cdot \mathbf{c})},$$

where L, M, and N are the number of unit cells along the vectors $\boldsymbol{a}$, $\boldsymbol{b}$, and $\boldsymbol{c}$, respectively. Then, the time-averaged diffraction intensity is given by the square of the crystal structure factor as

$$I_{Cry}(\boldsymbol{S}) = K\, F_{UC}^*(\boldsymbol{S}) F_{UC}(\boldsymbol{S})$$

$$\times \frac{\sin^2[(2L+1)\,\pi\,\boldsymbol{S}\cdot\boldsymbol{a}]}{\sin^2(\pi\,\boldsymbol{S}\cdot\boldsymbol{a})}\frac{\sin^2[(2M+1)\,\pi\,\boldsymbol{S}\cdot\boldsymbol{b}]}{\sin^2(\pi\,\boldsymbol{S}\cdot\boldsymbol{b})}\frac{\sin^2[(2N+1)\,\pi\,\boldsymbol{S}\cdot\boldsymbol{c}]}{\sin^2(\pi\,\boldsymbol{S}\cdot\boldsymbol{c})}$$

$$K = |\boldsymbol{G}|^2 \left\langle A(t)^2 \right\rangle_t, \tag{2.23}$$

The function $\frac{\sin^2[(2N+1)\,\pi\,\boldsymbol{S}\cdot\boldsymbol{a}]}{\sin^2(\pi\,\boldsymbol{S}\cdot\boldsymbol{a})}$ is the Laue function. The peak value is proportional to the square of the number of lattices, and the half-width is approximately $1/N$ (Fig. 2.7). Therefore, the function gives sharp peaks when $\bar{\boldsymbol{S}}\cdot\bar{a}$ is an integer (the Laue condition).

The scattering vector simultaneously satisfies the Laue condition for all the unit cell vectors, that is

$$\boldsymbol{S}\cdot\boldsymbol{a} = h \text{ and } \boldsymbol{S}\cdot\boldsymbol{b} = k \text{ and } \boldsymbol{S}\cdot\boldsymbol{c} = \ell \text{ and } h, k, \ell \in \text{ integer.}$$

From this condition, we can derive the following three equations:

$$\boldsymbol{S}\cdot\left(\frac{\boldsymbol{a}}{h} - \frac{\boldsymbol{b}}{k}\right) = 0 \text{ and } \boldsymbol{S}\cdot\left(\frac{\boldsymbol{a}}{h} - \frac{\boldsymbol{c}}{\ell}\right) = 0 \text{ and } \boldsymbol{S}\cdot\left(\frac{\boldsymbol{b}}{k} - \frac{\boldsymbol{c}}{\ell}\right) = 0.$$

This equation implies that the scattering vector is normal to the plane defined by the tips of the three vectors $\frac{\boldsymbol{a}}{h}$, $\frac{\boldsymbol{b}}{k}$, and $\frac{\boldsymbol{c}}{\ell}$. This result means that the peaks in the three-dimensional Laue function appear when the angle between the incident and observation directions (diffraction angle), the X-ray wavelength, and the distance $d_{hk\ell}$ between the $(\frac{\boldsymbol{a}}{h}, \frac{\boldsymbol{b}}{k}, \frac{\boldsymbol{c}}{\ell})$ planes satisfy the Bragg condition

$$2d_{hk\ell}\sin\theta = \lambda. \tag{2.24}$$

## 2.3.5   Friedel Centrosymmetry

The structure factors at the scattering vectors $\boldsymbol{S}$ and $-\boldsymbol{S}$ are written as

$$F(\boldsymbol{S}) = \int_{-\infty}^{+\infty} \rho(\boldsymbol{r})\exp(2\pi\, i\, \boldsymbol{S}\cdot\boldsymbol{r})\mathrm{d}^3r$$

$$F(-\boldsymbol{S}) = \int_{-\infty}^{+\infty} \rho(\boldsymbol{r})\exp(-2\pi\, i\, \boldsymbol{S}\cdot\boldsymbol{r})\mathrm{d}^3r.$$

**Fig. 2.7 a** One-dimensional Laue function for a crystal composed of five (red line) and ten (blue line) lattices. **b** Precession photograph of the $(0, k, \ell)$ plane taken from a crystal of a protein. The lattice constants along the $b$ and $c$ axes are 14.6 nm and 5.6 nm, respectively. Published with kind permission of Masayoshi Nakasako 2017. All Rights Reserved
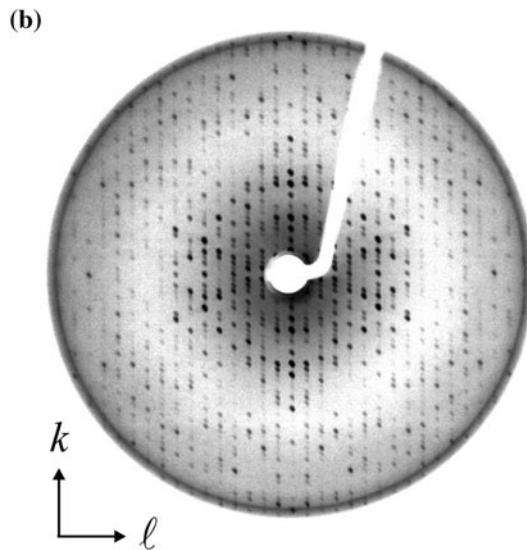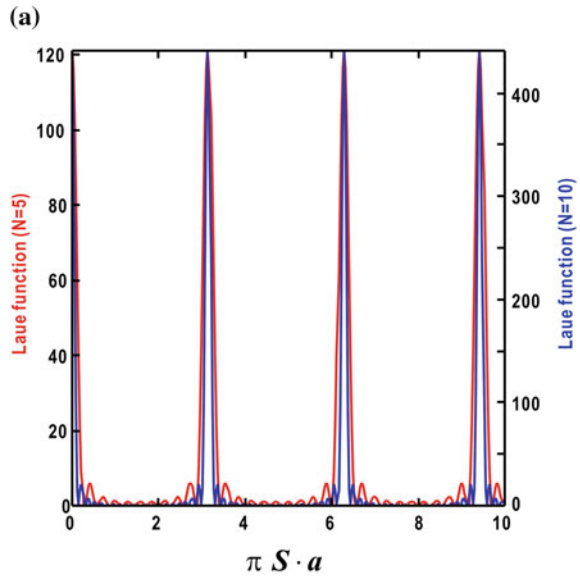


When anomalous scatterers are absent from the specimen, the electron density distribution is a real number. Then, the diffraction intensity satisfies the centrosymmetry relation as

$$I(\boldsymbol{S}) = K|F(\boldsymbol{S})|^2 = K|F(-\boldsymbol{S})|^2 = I(-\boldsymbol{S}). \qquad (2.25)$$

The centrosymmetry is called the Friedel centrosymmetry, or Friedel's law [5–7]. In the precession photograph shown in Fig. 2.7, the centrosymmetry in the diffraction intensity is clearly seen.

### 2.3.6 Ewald Sphere

The Bragg condition in (2.24) gives the simplest explanation for the diffraction spots, and can be rewritten as

$$x^2 + y^2 + \left( z + \frac{1}{\lambda} \right)^2 = \frac{4\sin^2\theta}{\lambda^2} + 2\frac{z}{\lambda} + \frac{1}{\lambda^2}, \quad \left( \frac{1}{d_{hk\ell}} \right)^2 = x^2 + y^2 + z^2.$$

where $(x, y, z)$ defines a point in space described by the scattering vector satisfying the Bragg condition. Each component of the vector has the dimension reciprocal of the length in real space. Therefore, the space described by the scattering vector is named the reciprocal space.

The $z$ coordinate of the sphere center is given by

$$z = \frac{1}{\lambda}(1 - \cos 2\theta) = -\frac{1}{\lambda} 2 \sin^2 \theta.$$

Using this equation, the Bragg condition is reduced to

$$x^2 + y^2 + \left( z + \frac{1}{\lambda} \right)^2 = \frac{1}{\lambda^2}. \tag{2.26}$$

This equation describes a sphere centered at $(x, y, z) = \left( 0, 0, \frac{1}{\lambda} \right)$ with a radius of $\frac{1}{\lambda}$, the inverse of the X-ray wavelength used in the experiment. This sphere is designated as the sphere of reflection or the Ewald sphere (Fig. 2.8) [5, 7]. Equation (2.26) means that the Bragg condition requires the contact of the reciprocal point $(x, y, z)$ with the sphere. Thus, to collect diffraction intensity data for possible reciprocal points, the crystal must be set in various orientations against the incident X-ray beam.

### 2.3.7 Autocorrelation Function

The autocorrelation function of the electron density is defined as

$$P(\boldsymbol{u}) = \int_r \rho(\boldsymbol{r}) \, \rho(\boldsymbol{r} + \boldsymbol{u}) \, \mathrm{d}^3 r = \int_S \frac{I(\boldsymbol{S})}{K} \exp[-2\pi i \, \boldsymbol{S} \cdot \boldsymbol{u}] \mathrm{d}^3 S. \tag{2.27}$$
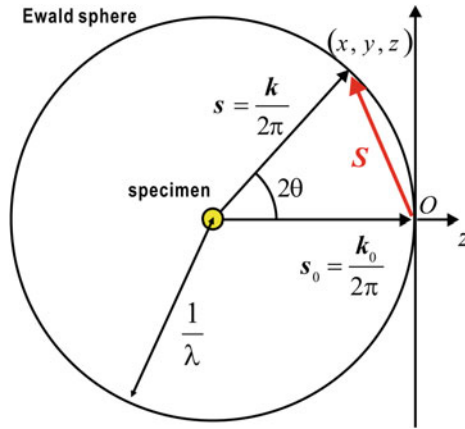
**Fig. 2.8** Illustration of the Ewald sphere in reciprocal space. Here, the point $(x, y, z)$ satisfying the Bragg condition is just on the Ewald sphere. Published with kind permission of Masayoshi Nakasako 2017. All Rights Reserved
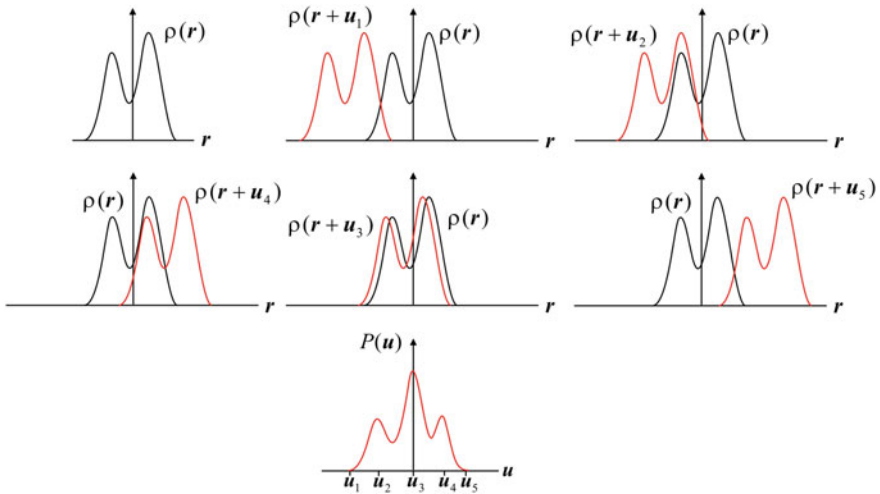


**Fig. 2.9** Schematic illustration of the auto-correlation function. According to (2.27), the sum in the overlapping region between $\rho(r)$ and $\rho(r+u)$ gives the auto-correlation function at $u$. In addition, when $u$ exceeds the maximum dimensions of $\rho(r)$, $P(u)$ become zero. Published with kind permission of Masayoshi Nakasako 2017. All Rights Reserved

This function is directly calculated from the diffraction intensity, and gives, for instance, the approximate distances between the high-density regions inside the electron density, as illustrated schematically in Fig. 2.9 [6]. For instance, when the electron density of an object is composed of a few prominent peaks, the

autocorrelation function gives the self- and cross-vectors of the peaks. These peaks illustrate the relative positions of the peaks in real space.

With regard to macromolecules or biological cells with complicated electron density distributions, it is very difficult to reconstruct their electron density maps from the auto-correlation function. However, the autocorrelation function gives the maximum dimensions of the electron density distribution as illustrated in Fig. 2.9.

## 2.4 Phase Problem in X-Ray Diffraction

The wavelength of the X-rays used for structural analysis is in the range from subnanometer to nanometer. Therefore, the frequencies of the X-rays are on the order of $10^{17}$–$10^{18}$ Hz. It is impossible to directly detect the phase of the X-rays. Only the magnitude of the Poynting vector (diffraction intensity) or the modulus of the electric field (diffraction amplitude) can be measured (2.20). To calculate the electron density distribution inside the specimen, the phase terms of the structure factors are indispensable in the inverse Fourier transform (2.21).

### 2.4.1 Importance of Phase

The structure factor is the product of the structure amplitude and phase terms (2.20). In the structure determination, i.e., the inverse Fourier transform of the structure factor, the phase term plays a crucial role in reconstructing the electron density map, as illustrated in Fig. 2.10. Because the phase term comes from the vectors specifying the positions of the electrons relative to a reference electron, the phase term reflects the distribution of the electrons inside the specimen. It is of high importance in the reconstruction of the electron density by inverse Fourier transform.

A representative method to experimentally estimate the phase terms is the multiple isomorphous replacement method developed in protein X-ray crystallography. This method is introduced here to explain how the phases of diffracted X-rays are experimentally determined.

### 2.4.2 Multiple Isomorphous Replacement Method in Protein Crystallography

The phases of the diffracted waves are lost when the diffraction intensities are measured. Theory and measurement techniques have been developed to recover the phase, known as the phase problem in X-ray structural analysis. For crystal structural analysis of small molecules, a direct method has been developed [7]. In
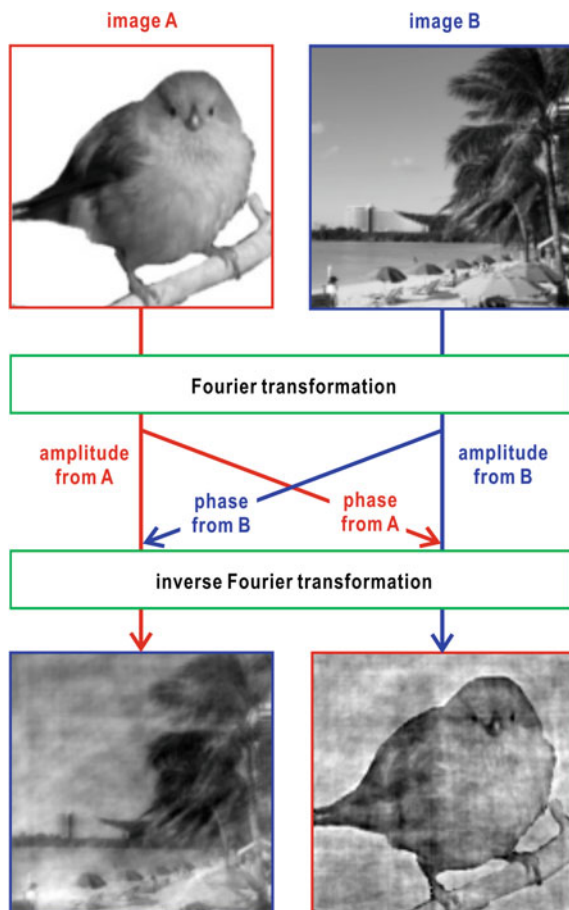
**Fig. 2.10** Simulation demonstrating the crucial role of the phase term in the inverse Fourier transform in reconstructing the electron density map. In this simulation, two photographs, a bird and a scene of a seashore, are Fourier transformed. After the amplitude and phase terms are exchanged between the two data sets, the electron density maps are reconstructed by the inverse Fourier transform. When the phase term from the photograph of the bird is combined with the amplitude term of the seashore photograph, an image close to the photograph of the bird appears, and vice versa. Therefore, most of the information crucial for the reconstruction is contained in the phase term, while the amplitude term may have little influence on the reconstructed image. The photographs in this figure are supplied by courtesy of Ms. Saki Hashimoto. Published with kind permission of Masayoshi Nakasako 2017. All Rights Reserved

protein crystallography, the diffraction signal from the protein crystals is modified by adding reagents composed of heavy atoms, such as platinum and lead, bound to specific amino acid residues exposed on the protein surfaces. The large structure factors of the heavy atoms provide a reference signal for encoding the phase information lost in the intensity measurement. It is worthy describing how the phase

problem in X-ray protein crystallography is solved by introducing the key concept of the multiple isomorphous replacement (MIR) method of using heavy atom labeling [8, 9].

The structure factor with an unknown phase is represented by a circle with a radius of amplitude in the complex plane as illustrated by Fig. 2.11a. Specific amino acid residues on the surface of the protein molecules in a crystal are labeled by heavy atoms (heavy-atom derivative). Then, it is assumed that the labeling induces only minor changes in both the conformation and the arrangement of the protein molecules in the crystal (isomorphism). To determine the phase, at least two heavy-atom derivative crystals are necessary. In the first derivative, the crystal structure factor without labeling (native crystal), $F_P(S)$, is modified by the structure factor of the heavy atoms, $F_{H1}(S)$, in the unit cell (Fig. 2.11a) as follows

$$F_{PH1}(S) = F_P(S) + F_{H1}(S), \quad S = (hk\ell),$$

where $F_{PH1}(S)$ is the structure factor of the derivative crystal at Miller indices of $(hk\ell)$ and scattering vector $S$.

Because $F_{H1}(S)$ can be estimated experimentally using the Patterson method, the circle for $F_{PH1}(S)$ is drawn after the shift of the center by $F_{H1}(S)$ from the origin of the complex plane. Then, the possible phase value for $F_P(S)$ is limited to the two points where the circles of $F_P(S)$ and $F_{PH1}(S)$ intersect each other. For the other derivative, the following relation stands

$$F_{PH2}(S) = F_P(S) + F_{H2}(S).$$
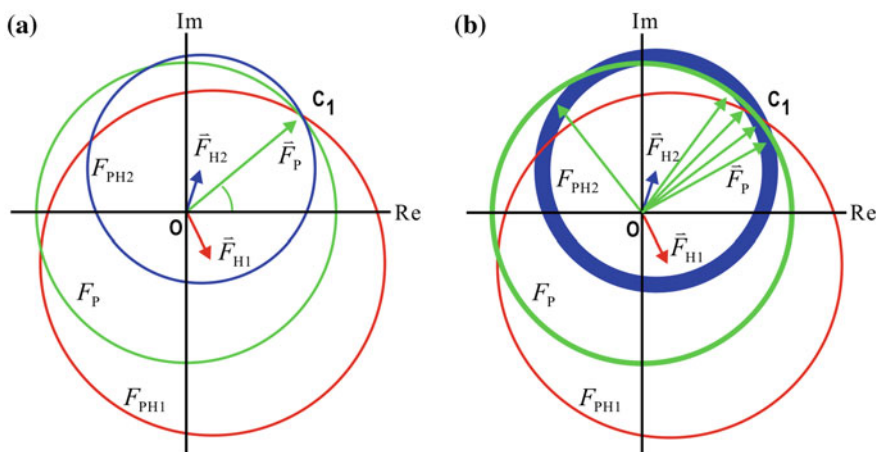


**Fig. 2.11** Diagrams used in phase determination by the MIR method. Diagrams for diffraction data **a** without and **b** with noise in measured diffraction intensities. The width of each circle reflects the errors in measuring the amplitude. Published with kind permission of Masayoshi Nakasako 2017. All Rights Reserved

Again, the circle for $F_{PH2}(S)$ is drawn after the shift of the center by $F_{H2}(S)$ from the origin of the complex (Fig. 2.11a). Ideally, the third circle intersects one of the two points suggested by the intersections of the circles of $F_P(S)$ and $F_{PH1}(S)$. Then, the phase of the diffracted wave is determined experimentally. By applying this scheme to the obtained diffraction spots, the electron density map of the asymmetric unit in the unit cell is calculated by the inverse Fourier transform of the set of amplitudes and phases.

### 2.4.3   Figure of Merit of the Estimated Phase

In experiments, because Poisson noise in the X-ray detection modifies the diffraction amplitudes, as illustrated graphically in Fig. 2.11b, it is difficult to determine single phase values. As a result, the phase is treated as a probability distribution function, $P(\alpha(S))$, instead of a single and well-defined value. Blow and Crick introduced the 'figure of merit of a phase' (FOM) to estimate the most probable phase value [9]. In the 'best inverse Fourier transform' they proposed, the phase component of the structure factor is weighted by the probability distribution function of the phase. They defined the 'best inverse Fourier transform' using FOM as

$$
\begin{aligned}
F_{\text{best}}(S) &= \int\limits_{\alpha(S)} P(\alpha(S))|F_P(S)|\exp[i\,\alpha(S)]\mathrm{d}\,\alpha(S), \\
m(S) &= \int\limits_{\alpha(S)} P(\alpha(S))\exp[i\,\alpha(S)]\mathrm{d}\alpha(S).
\end{aligned}
\tag{2.28}
$$

where $m(S)$ takes a value between 0 and 1. In this FOM-weighted inverse Fourier transform, the structure factor with a good FOM contributes to give the most probable electron density map.

Even with electron density maps obtained from the best Fourier transform, the building of the molecular structure of a targeted protein is still difficult because of the noisy density map. When the averaged FOM for all structure factors at a desired resolution is better than 0.5–0.6, the rough shape of the protein molecules in the crystal lattice may be identified using the noisy electron density map.

In protein crystallography, the electron density map obtained by the best Fourier transform is improved using density modification algorithms that modify the noisy electron density maps using the knowledge of the electron density distribution common to proteins and protein crystals (Fig. 2.12a and b). For instance, the phase set is improved to provide an electron density for solvent regions running through protein crystals as flat as possible [7]. A new electron density map is calculated using the phase set from the calculated structure factor of the modified density map and experimental structure amplitude. Then, the electron density was improved
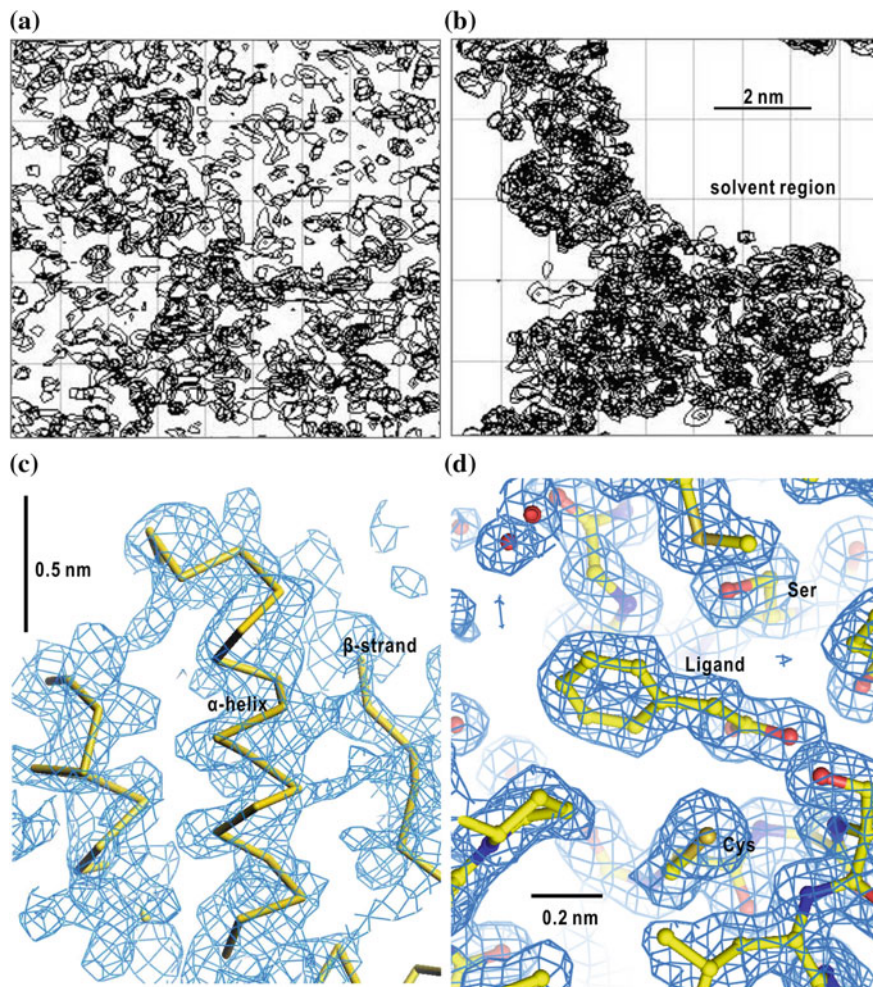
**Fig. 2.12** Electron density maps in the structural analysis of an enzyme protein. **a** Best Fourier electron density map at a resolution of 0.3 nm. The map is projected along the *c*-axis of the crystal. The FOM for all of the diffraction data (12,877 Bragg reflections) used in the inverse Fourier transform was 0.54. **b** Electron density map at a resolution of 0.3 nm obtained by applying a density modification method, which requires the solvent regions to be small values, to the best Fourier map. This method improved the FOM for all data to 0.78. **c** Magnified view of panel (**b**). The electron density map is illustrated by the blue net. The yellow sticks represent the backbones of the polypeptides modeled into the map. **d** Electron density map around the active site of the protein at a resolution of 0.14 nm after the crystallographic structure refinement. The FOM for the 35,488 Bragg peaks was 0.895 [10]. Amino acid residues and a ligand bound to the active site are illustrated as stick models. Panels are reused after modification from [11] with permission from The Physical Society of Japan

remarkably and revealed typical structures in proteins, such as α-helices and β-strands. By referring to the electron density map, the amino acid residues composing proteins are built to satisfy the stereochemistry of the peptide bonds, the electron density maps, and the observed structural amplitudes from crystallographic structure refinement [7] (Fig. 2.12c and d).

## 2.5   Small-Angle Scattering

The resolution of XDI diffraction patterns is still limited to a small diffraction angle of less than 7°. To understand what types of structural information are obtainable from small-angle diffraction and scattering, the basic theory of small-angle scattering of macromolecules in solution [12, 13] is briefly introduced (Fig. 2.13a).

In the small-angle region, the diffraction intensity is approximated by a series of scattering vectors of small length. In addition, the scattering intensity is averaged
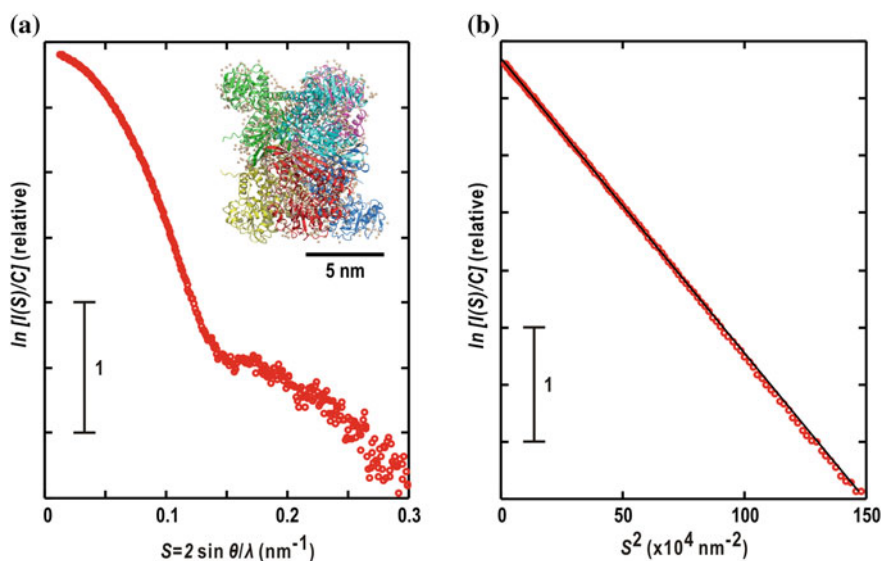


**Fig. 2.13** Small-angle scattering from a solution of glutamate dehydrogenase [14] collected at BL45XU of SPring-8. The shape of the enzyme is approximated by a cylinder with a diameter of 10 nm and a height of 10 nm. **a** The diffraction intensity in the semi-logarithmic plot decreases gradually when $S < 0.1$ nm$^{-1}$, and has a characteristic enhancement at around 0.2 nm$^{-1}$ caused by the cylindrical shape of the enzyme protein. **b** Guinier plot of the scattering profile for $S < 0.07$ nm$^{-1}$. The plot approximated by a straight line gives the $R$g value, which is calculated to be 4.3 nm. Published with kind permission of Masayoshi Nakasako 2017. All Rights Reserved

with regard to the orientation of the macromolecules with respect to the direction of the incident X-ray. Then, the small-angle scattering intensity is approximated as

$$I(S) = \frac{1}{4\pi}K \int_{\Phi=0}^{\Phi=2\pi} d\Phi \int_{\Theta=0}^{\Theta=\pi} \sin\Theta \, d\Theta \, d\Phi \int_r \int_{r'} \rho(r')\rho(r)\exp[2\pi i S \cdot (r-r')] \, d^3r \, d^3r'$$

$$S = (S\cos\Phi\sin\Theta, \ S\sin\Phi\sin\Theta, \ S\cos\Theta)$$

$$S \cdot (r-r') << \frac{1}{2\pi}$$

$$\exp[2\pi i S \cdot (r-r')] \approx \exp[0] + 2\pi i S \cdot (r-r') - \frac{1}{2}\{2\pi i S \cdot (r-r')\}^2$$

When the origin of the coordinates is set to the center of gravity for the electron density of the molecule, the scattering intensity is given by the Guinier approximation [11]

$$I(S) = I(0) \exp\left[-\frac{4\pi^2}{3}S^2 Rg^2\right], \tag{2.29}$$

where $I(0)$ and $Rg$ are the zero-angle diffraction intensity and the radius of gyration of the molecule, respectively. When the logarithm of the scattering intensity is plotted against the square of the scattering vector, the plotted data is approximated by a straight line (Fig. 2.13b) (Guinier plot). The two parameters are written in terms of the size and shape of the molecule

$$I(0) = K \int_r \int_{r'} \rho(r')\rho(r) \, d^3r \, d^3r', \tag{2.30}$$

$$Rg^2 = \frac{1}{2}\frac{\int_r \int_{r'} \rho(r')\rho(r)|r-r'|^2 \, d^3r \, d^3r'}{\int_r \int_{r'} \rho(r')\rho(r) \, d^3r \, d^3r'}. \tag{2.31}$$

The radius of gyration is the second moment of the electron density distribution in the macromolecule.

The scattering profile in the region analyzed by the Guinier approximation contains structural information regarding the size and the sum of the electrons in atoms composing the macromolecule. However, for large particles, the measurement of the small-angle region is often difficult in XDI experiments. Structural information and analysis for diffraction patterns out of the region of the Guinier approximation will be discussed in Chap. 7.

# References

1. E. Segrè, *From X-Rays to Quarks: Modern Physicists and Their Discoveries* (Freeman, San Francisco, 1980)
2. W.K.H. Panofsky, M. Philips, *Classical Electricity and Magnetism* (Addison-Wesley Publishing Company, Reading, 1978)
3. J.D. Jackson, *Classical Electrodynamics* (Wiley, New York, 1962)
4. *The NIST Reference on Constants, Units and Uncertainty*. http://physics.nist.gov/cgi-bin/cuu/Value?re
5. J. Als-Nielsen, D. McMorrow, *Elements of Modern X-Ray Physics* (Wiley, New York, 2011)
6. C.R. Cantor, P.R. Schimmel, *Biophysical Chemistry Part II: Techniques for the Study of Biological Structure and Function* (W. H. Freeman and Company, Oxford, 1980)
7. J. Drenth, *Principles of Protein X-Ray Crystallography* (Springer, New York, 1994)
8. T.L. Blundel, L.N. Johnson, *Protein Crystallography* (Academic Press, New York, 1976)
9. D.M. Blow, F.H.C. Crick, Acta Crystallogr. **12**, 794 (1959)
10. R. Obata, M. Nakasako, Biochemistry **49**, 1963 (2010)
11. M. Nakasako, M. Yamamoto, BUTSURI **70**, 702 (2015)
12. A. Guinier, G. Fournet, *Small-Angle Scattering of X-Rays* (Wiley, New York, 1955)
13. D.I. Svergun, M.H.J. Koch, P.A. Timmins, R.P. May, *Small Angle X-Ray and Neutron Scattering from Solutions of Biological Macromolecules* (Oxford University Press, Oxford, 2013)
14. M. Nakasako, et al., Biochemistry **40**, 3069 (2001)

# Chapter 3
# Theory of X-Ray Diffraction Imaging

**Abstract** X-ray diffraction imaging (XDI) is a technique for visualizing the structures of non-crystalline particles with dimensions ranging from micrometers to submicrometers. In XDI experiments, non-crystalline particles are irradiated by X-rays with high transverse coherence. Then, the Fraunhofer diffraction pattern is recorded under the oversampling condition at a desired resolution. The electron density map of the particle projected along the direction of the incident X-ray is reconstructed by applying the phase-retrieval (PR) algorithm to the diffraction pattern alone. In this chapter, the spatial coherence of X-rays, the X-ray source necessary for XDI, and the representative algorithms used for PR are introduced.

## 3.1  Outline

X-rays with short wavelengths penetrate deeply into thick objects without multiple scattering, because of the weak electromagnetic interaction with the atoms. Therefore, XDI visualizes the whole structures of thick specimens without the need for sectioning. Indeed, several XDI experiments have demonstrated the method's potential to visualize the internal structures of whole biological cells and cellular organelles [1], which have never been crystallized, at resolutions of several tens of nanometers.

Here, we consider the diffraction pattern of a spatially isolated non-crystalline specimen particle with an electron density $\rho(\boldsymbol{r})$, which is illuminated by a monochromatic plane wave of X-rays with a flux density $I_0$ and wavelength $\lambda$ (Fig. 3.1). The diffracted X-rays are detected far downstream (in the far-field) to satisfy the Fraunhofer approximation [2]. The diffraction pattern is composed of a number of intensity peaks, i.e., so-called speckle peaks, which are caused by the interference of X-rays emitted from the specimen particle. The size of each speckle is comparable to the reciprocal of the particle size.

As described in the subsequent sections, the diffraction pattern must be recorded finely to calculate the projection electron density map using the PR algorithm. The algorithm then requires a sampling of the diffraction pattern along the $x$-axis ($y$-axis) finer than the reciprocal of the product of the specimen size $a$ ($b$) with
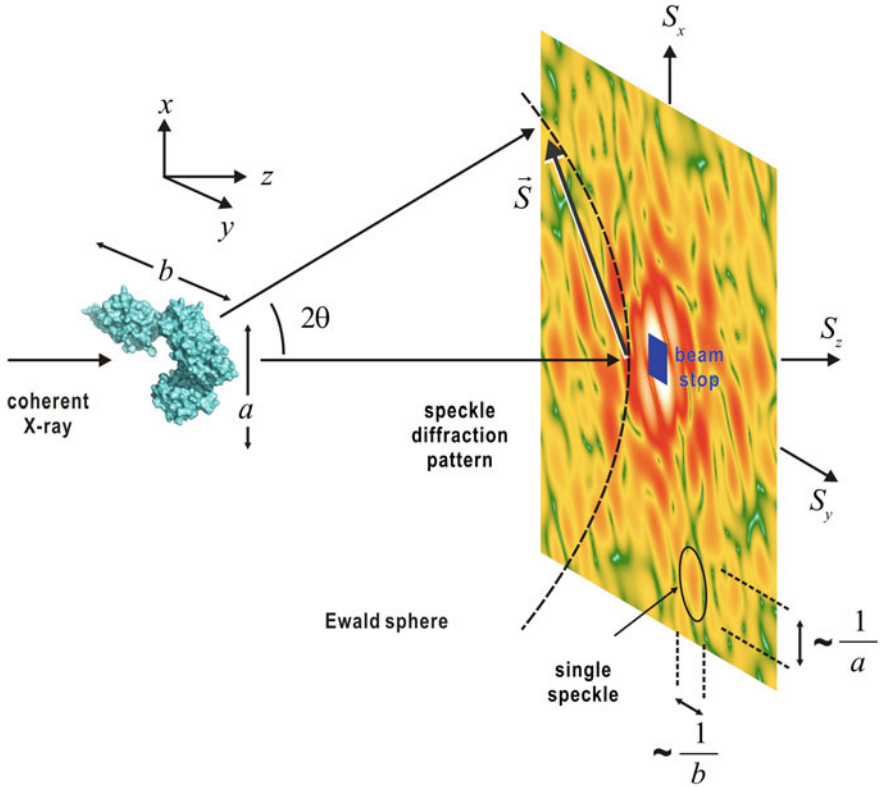
**Fig. 3.1** Schematic of an XDI experiment. The spatially isolated specimen particle is irradiated by a plane wave of monochromatic X-rays. A beamstop is placed in front of the area detector to absorb the X-ray beam passing through the particle. The diffraction patterns observed are those intersected by the Ewald sphere (see Fig. 2.8 in Chap. 2). Published with kind permission of Masayoshi Nakasako 2017. All Rights Reserved

a sampling ratio $\sigma_x$ ($\sigma_y$). On the Ewald sphere, the diffraction intensity at the scattering vector $S$ with a scattering angle $2\theta$ ($|S| = 2\sin\theta/\lambda$) is sampled in the solid angle

$$\frac{1}{\sigma_x a}\left(\frac{1}{\lambda}\right)^{-1}\frac{1}{\sigma_y b}\left(\frac{1}{\lambda}\right)^{-1}.$$

This factor is multiplied by the diffraction intensity. When using a semi-polarized X-rays, the diffraction intensity $I(S)$ measured at a distance $R$ from the specimen is written as

$$I(S) = I_0\, r_e^2\, \frac{\lambda^2}{\sigma_x\,\sigma_y\,ab}\, F(S)^*F(S)\, \frac{p}{R^2}, \tag{3.1}$$

where $p$ is the polarization factor of the incident wave (see Figs. 2.3 and (2.7) in Chap. 2). $\sigma_x \sigma_y$ is the oversampling (OS) ratio of the diffraction pattern [3], the details of which are described below; $ab$ is the projected area of the particle along the direction normal to the incident X-ray beam; $r_e$ is the classical electron radius (see 2.8); $F(S)$ is the structure factor of the particle as defined by (2.15); and $I_0$ is the intensity of the incident X-ray with complete spatial coherence.

The incident intensity $I_0$ must be large enough to record the diffraction pattern from a single non-crystalline particle with a good signal-to-noise ratio because $r_e$ is quite a small quantity. In principle, the theoretical limit of the spatial resolution of the diffraction pattern is half of the X-ray wavelength, as expected from Bragg's law (2.19) when $I_0$ is infinitely large. The intensity distribution of the observed diffraction pattern is limited to that intersecting the Ewald sphere.

In diffraction patterns, the phase terms of the structure factors are completely lost. If the phase term of the structure factor is recovered experimentally or computationally, the electron density of the specimen particle is reconstructed by the inverse Fourier transform. In principle, when we can determine the structure factor up to atomic-scale resolution, the obtained electron density map shows the locations of all the atoms in the targeted object. The phase problem has already been introduced in Chap. 2 with respect to protein crystallography. In protein crystallography, the phase problem is solved, for instance, by applying the MIR method with heavy-atom labeling of crystals. In XDI, the phase is recovered using phase-retrieval algorithms, which were developed in astronomy and information technology [4]. To understand the theoretical background of the algorithm, we have to consider the quantity of information included in a single diffraction pattern.

## 3.2 Spatial Coherence of X-Rays

An X-ray beam with high spatial coherence is necessary to conduct XDI experiments. At a synchrotron facility, X-rays with high spatial coherence are obtainable, for instance, by inserting a pinhole in the path of an X-ray beam monochromatized by the optics of the beam line for an undulator X-ray source. At the XFEL facility, X-rays with almost full spatial coherence are available. In this section, the concept of coherence is introduced [2].

### 3.2.1 Coherence

In the theory of X-ray diffraction, the incident X-ray is usually assumed to be a monochromatic plane wave produced at a point source at a far distance from the specimen. In XDI experiments, X-ray beams with almost full spatial coherence are

necessary to ensure detectable diffraction signals from small non-crystalline specimens with dimensions of sub-micrometers to micrometers.

Figure 3.2a shows a typical experimental setup to measure the spatial (transverse) coherence of light [2]. Light from source S passes through the small apertures $P_1$ and $P_2$ and produces two waves accompanying electric field of $E_1(r, t)$ and
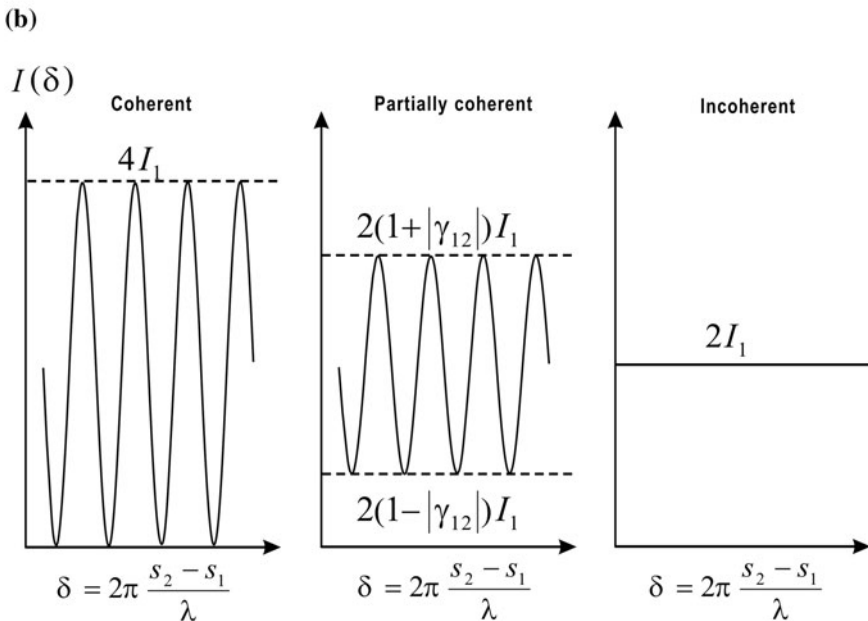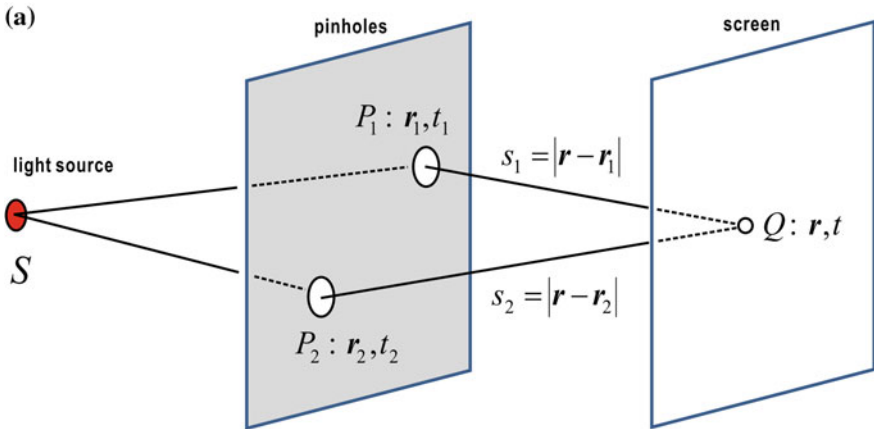


**Fig. 3.2 a** Experimental setup to estimate the spatial coherence of light by measuring the visibility of the interference pattern observed on a screen placed far from the aperture plane. **b** Intensity variation on the observation screen depending on the complex degree of coherence. Published with kind permission of Masayoshi Nakasako 2017. All Rights Reserved

$E_2(\mathbf{r}, t)$. At the position Q on the observation screen, the two waves are superimposed as

$$E_1(\mathbf{r}, t) + E_2(\mathbf{r}, t).$$

Then, the time-averaged intensity is given by

$$I(\mathbf{r}, \tau) = \frac{1}{2\mu_0 c} \left[ \left\langle |E_1(\mathbf{r}, t)|^2 \right\rangle_t + \left\langle |E_2(\mathbf{r}, t)|^2 \right\rangle_t + \mathrm{Re}\ \Gamma_{12}(\mathbf{r}, \tau) \right], \tag{3.2}$$
$$\tau = t_2 - t_1 = \frac{s_2 - s_1}{c} =, \quad t_j = t - \frac{|\mathbf{r} - \mathbf{r}_j|}{c}$$

where $\Gamma_{12}(\mathbf{r}, \tau)$ is the time-averaged cross correlation function between the two waves

$$\Gamma_{12}(\mathbf{r}, \tau) = \left\langle E_1^*(\mathbf{r}, t) E_2(\mathbf{r}, t + \tau) \right\rangle_t.$$

Because $\Gamma_{12}(\mathbf{r}, \tau)$ depends on the amplitudes of the two waves, the complex degree of coherence, $\gamma_{12}(\mathbf{r}, \tau)$, which is normalized with respect to the amplitudes, is introduced as

$$\gamma_{12}(\mathbf{r}, \tau) = \frac{\Gamma_{12}(\mathbf{r}, \tau)}{\sqrt{\Gamma_{11}(\mathbf{r}, 0)\, \Gamma_{22}(\mathbf{r}, 0)}}, \tag{3.3}$$

where $\gamma_{12}(\mathbf{r}, \tau)$ takes a value between 0 and 1. Then, the intensity of the superimposed light waves is written as

$$I(\mathbf{r}, \tau) = \frac{1}{2\mu_0 c} \left[ \left\langle |E_1(\mathbf{r}, t)|^2 \right\rangle_t + \left\langle |E_2(\mathbf{r}, t)|^2 \right\rangle_t + 2 \sqrt{\left\langle |E_1(\mathbf{r}, t)|^2 \right\rangle_t \left\langle |E_2(\mathbf{r}, t)|^2 \right\rangle_t}\ \mathrm{Re}\ \gamma_{12}(\mathbf{r}, \tau) \right]. \tag{3.4}$$

The function $\gamma_{12}(\mathbf{r}, \tau)$ is a complex function. When $|\gamma_{12}(\mathbf{r}, \tau)|$ is 1 (complete coherence), a clear interference pattern is observed on the screen. On the other hand, when $|\gamma_{12}(\mathbf{r}, \tau)|$ is 0 (complete incoherence), no interference pattern appears on the screen. For $0 < |\gamma_{12}(\mathbf{r}, \tau)| < 1$ coherence), the clarity of the interference patterns depends on this value (Fig. 3.2b).

### 3.2.2   Visibility

To experimentally evaluate the coherence of light, the visibility of the interference pattern [2] is defined as

$$V = \frac{I_{\max} - I_{\min}}{I_{\max} + I_{\min}} = \frac{2\sqrt{\left\langle |E_1(\boldsymbol{r},t)|^2 \right\rangle_t \left\langle |E_2(\boldsymbol{r},t)|^2 \right\rangle_t}}{\left\langle |E_1(\boldsymbol{r},t)|^2 \right\rangle_t + \left\langle |E_2(\boldsymbol{r},t)|^2 \right\rangle_t} |\gamma_{12}(\boldsymbol{r},\tau)|. \tag{3.5}$$

$I_{\max}$ and $I_{\min}$ are the maximum and minimum values of the interference pattern at point Q on the screen (Fig. 3.2b), and are written as

$$I_{\max} = \frac{1}{2\mu_0 c}\left[ \left\langle |E_1(\boldsymbol{r},t)|^2 \right\rangle_t + \left\langle |E_2(\boldsymbol{r},t)|^2 \right\rangle_t + 2\sqrt{\left\langle |E_1(\boldsymbol{r},t)|^2 \right\rangle_t \left\langle |E_2(\boldsymbol{r},t)|^2 \right\rangle_t} |\gamma_{12}(\boldsymbol{r},\tau)| \right]$$
$$I_{\min} = \frac{1}{2\mu_0 c}\left[ \left\langle |E_1(\boldsymbol{r},t)|^2 \right\rangle_t + \left\langle |E_2(\boldsymbol{r},t)|^2 \right\rangle_t - 2\sqrt{|E_1(\boldsymbol{r},t)| \left\langle |E_2(\boldsymbol{r},t)|^2 \right\rangle_t} |\gamma_{12}(\boldsymbol{r},\tau)| \right].$$

X-rays with high spatial coherence are used in XDI. Then, the degree of spatial coherence (or transverse coherence) of the X-rays can be estimated from the interference pattern (see Chap. 4).

## 3.3  X-Ray Sources

For XDI experiments, ideally, the incident X-ray is a monochromatic plane wave. However, such an X-ray produced by a point charge is unavailable. X-ray sources suitable for XDI experiments are as small as possible. We use two types of X-ray sources in XDI experiments; undulator light sources in synchrotron storage rings [5] (Fig. 3.3) and the XFEL light source [6, 7]. In both light sources, electrons pass through a periodic magnetic field produced by an array of magnets. Here, we briefly introduce the characteristics of the X-ray sources.
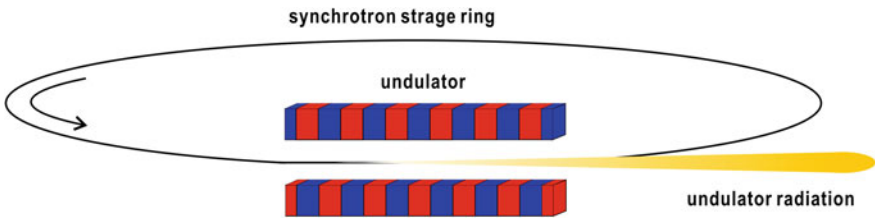


**Fig. 3.3**  Schematic of the undulator in a synchrotron storage ring. Published with kind permission of Masayoshi Nakasako 2017. All Rights Reserved

### 3.3.1 Undulator

In synchrotron storage rings, undulators are inserted in the straight sections followed by bending magnets, and work as brilliant X-ray sources. An undulator is composed of two periodic arrays of permanent magnets with mutual shifts of half the period. In the gap space between the two magnet arrays, electrons travel through magnetic induction with a sinusoidal variation produced by the magnet array (Fig. 3.4).

$$\boldsymbol{B} = \boldsymbol{e}_y \mathbf{B}_0 \sin\left(\frac{2\pi z}{\lambda_u}\right),$$

where $\lambda_u$ and $B_0$ are the period and amplitude of the field. When an electron passes through the gap, the electron is periodically deflected by the Lorentz force. The equation of motion of an electron with an energy of $E$ passing through the magnetic induction $\boldsymbol{B}$ is

$$\frac{\mathrm{d}\boldsymbol{p}}{\mathrm{d}\tau} = e\upsilon \times \boldsymbol{B}, \quad \boldsymbol{p} = \gamma m_e \boldsymbol{v}, \quad \gamma = \frac{1}{\sqrt{1 - \frac{v^2}{c^2}}}, \quad \mathrm{d}\tau = \frac{1}{\gamma}\,\mathrm{d}t.$$

$\tau$ is the time in the moving electron frame and is related to the time in the laboratory frame by using $\gamma$. The deflection parameter $K$ is defined to characterize the undulator radiation as
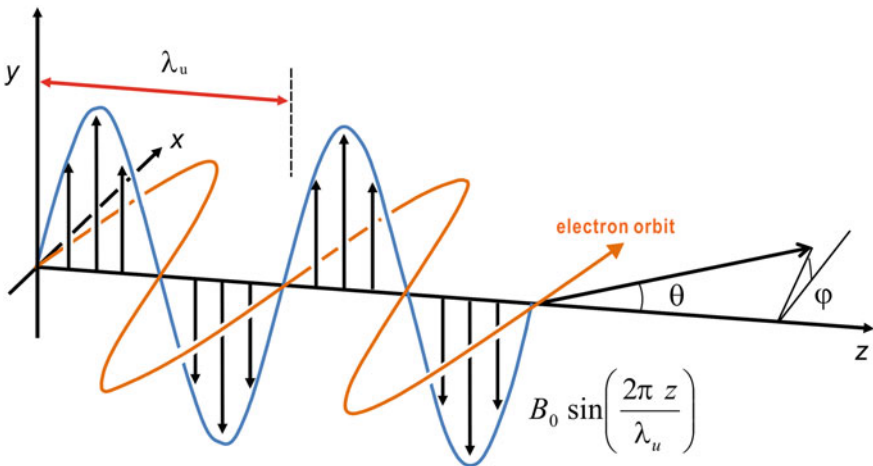


**Fig. 3.4** Schematic of the electron orbit in the magnetic field (sinusoidally varying magnetic induction) of an undulator. The angular parameters $\theta$ and $\varphi$ used in (3.7) are defined. Published with kind permission of Masayoshi Nakasako 2017. All Rights Reserved

$$K = \frac{eB_0 \, \lambda_u}{2\pi \, m_e c}. \tag{3.6}$$

The deflection of an electron at two successive crests of the sinusoidal path in the periodic field results in constructive interference between the radiations. As a result, an extremely high flux with high brilliance is emitted at specific wavelengths.

The photon flux density of undulator radiation from an electron passing through an undulator is described as a function of the angular frequency $\omega$ and solid angle $\Omega$.

$$
\begin{aligned}
\frac{\partial^2 P_k(\theta, \varphi, \omega)}{\partial \Omega \, \partial \omega} &= \frac{e^2}{4\pi\varepsilon_0} \frac{1}{c} \gamma^2 k^2 \times \left[ A_{//}^2(\gamma\,\theta, \varphi) + A_\perp^2(\gamma\,\theta, \varphi) \right] \\
&\quad \times \frac{\sin^2\left[ N\pi(\omega/\omega_1 - k) \right]}{\left[ N\pi(\omega/\omega_1 - k) \right]^2} \\
A_{//}(\gamma\,\theta, \varphi) &= \xi\left[ 2S_0 \,\gamma\,\theta\cos\varphi - K(S_1 + S_{-1}) \right] \\
A_\perp(\gamma\,\theta, \varphi) &= 2\,\xi\,S_0 \,\gamma\,\theta\sin\varphi \\
\xi &= \frac{1}{1 + (\gamma\,\theta)^2 + K^2/2} \\
S_q &= \sum_{p=-\infty}^{\infty} J_{k+2p+q}(X)\, J_P(Y) \\
X &= 2\,\xi\,\gamma\,\theta\,K\cos\varphi, \; Y = K^2\xi/4,
\end{aligned} \tag{3.7}
$$

where the index $k$ is the order of the undulator radiation; $A_{//}(\gamma\,\theta, \varphi)$ and $A_\perp(\gamma\,\theta, \varphi)$ are the amplitudes along the directions parallel and normal to the plane of the magnet array, respectively; $N$ is the number of the magnet array; $J_n(x)$ is the cylindrical Bessel function of the $n$th order; And $\omega_1$ is the fundamental angular frequency of the undulator defined as

$$\omega_1 = 4\pi \frac{c\gamma^2}{\lambda_u} \frac{1}{1 + (\gamma\theta)^2 + K^2/2}. \tag{3.8}$$

Strong radiation is produced when $\omega/\omega_1$ becomes close to $k$. Therefore, the undulator radiation is quasi-monochromatic (Fig. 3.5). The total power from the electron bunches is proportional to the current.

Undulator radiation occurs in the almost straight pathway of electron bunches along the magnet array; the apparent source size is smaller than that from the bending magnet. In addition, the intensity of undulator radiation near the fundamental angular frequency is much stronger than that of a bending magnet. Because the electrons in the electron bunches are randomly distributed, the degree of spatial coherence is too small for use in XDI experiments. As described in Chap. 4, a spatially coherent X-ray is produced by using a pinhole set in undulator radiation.

**Fig. 3.5** An example of the simulated spectra from undulator radiation. The acceleration energy is 8 GeV. The calculation assumes 2436 electron bunches circulating a storage ring with a circumference of 1435 m. The parameters are adjusted to give the fundamental radiation at 5.5 keV. The period of the magnetic array, the peak magnetic induction value of which is 0.74 T, is 32 mm, and the number of periods is 140. The peaks of the harmonics are labeled. This spectrum is calculated using the SPECTRA program suite [8]. Published with kind permission of Masayoshi Nakasako 2017. All Rights Reserved
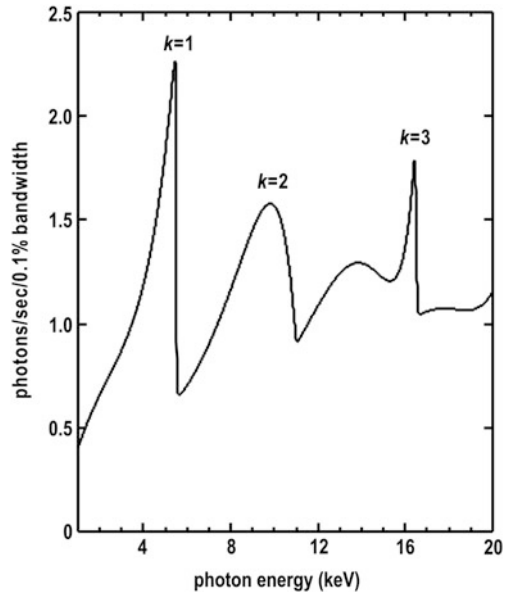


### 3.3.2 X-Ray Free Electron Laser

An ideal coherent X-ray source is a single electron, but the radiation intensity is too small. Due to the random distribution of electrons in electron bunches passing through the undulator, radiated X-rays are out of phase and almost incoherent. If electrons in a bunch can be regularly arranged into micro-bunches with a separation of the wavelength of the radiated X-rays, the radiation from one micro-bunch would be in phase with those from another.

This ideal mechanism to produce X-ray radiation is realized by the self-amplified spontaneous emission process [9] (Fig. 3.6). Each electron bunch passing through the gap between a pair of magnet arrays in an undulator is driven by the Lorentz force. After a while, a part of electrons in a bunch are bathed in the radiation emitted from other electrons downstream because the radiation travels at the speed of light, which is higher than the traveling speed of the electrons along the direction of the undulator axis. If the radiation field is sufficiently strong, the motion of the electrons is modulated over a period of the wavelength of the radiation. Then, an electron bunch is gradually modulated to be separated into microbunches with the period of the wavelength of the radiation. This modulation of the arrangement of electrons within the bunch is initiated stochastically during the travel of the bunch through a long undulator. In addition, the modulation further enhances the micro-bunch through a manner of positive feedback. Then, the radiation power of the spatially coherent X-rays increases exponentially. The duration of the XFEL pulses is in the range of several tens of femtoseconds.
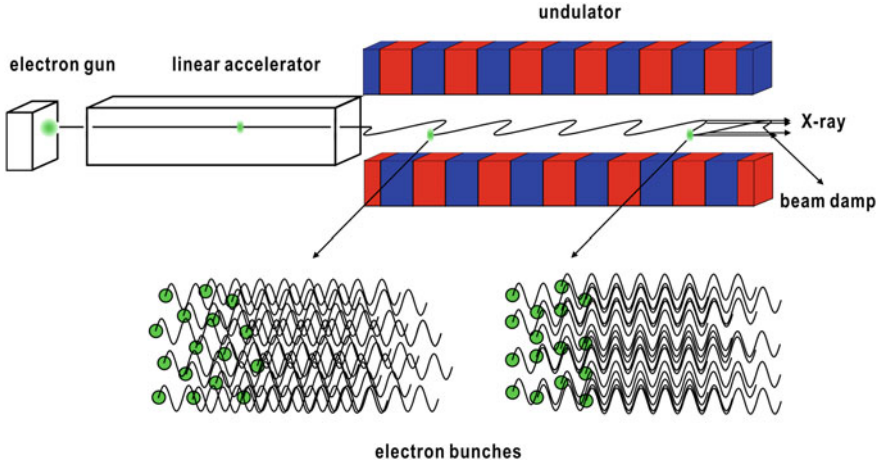
**Fig. 3.6** Schematic of the self-amplified spontaneous emission in an X-ray free electron laser. Published with kind permission of Masayoshi Nakasako 2017. All Rights Reserved

Currently, it is very difficult to realize this SASE mechanism in synchrotron storage rings. The lengths of the undulators possible in storage rings, i.e., the number of periods of magnet arrays in undulators, are insufficiently short for SASE. Although small fluctuations of the electron momenta inside bunches is highly desired in the SASE mechanism, electron bunches in storage rings suffer from transverse and longitudinal oscillation around the closed orbit. Therefore, the SASE process is now realized using linear accelerators that can produce small electron bunches with the small fluctuation of momentum required. The cutting-edge technologies in a linear accelerator, such as electron guns and high gradient acceleration tubes, ensure the quality of the electron bunch matches the level desired in SASE. Long undulators with lengths of a few hundred meters can be constructed.

The on-axis wavelength of the radiation generated by the SASE process ($\lambda_{SASE}$) is determined by the acceleration energy ($\gamma$), the undulator $K$-parameter, and the period of the magnet arrays ($\lambda_u$) as

$$\lambda_{SASE} = \frac{\lambda_u}{2\gamma^2}\left(1 + K^2/2\right). \tag{3.9}$$

This equation leads us to the idea that, when the acceleration energy reaches, for instance, 8 GeV and the period of magnet arrays in the undulator is 0.01 m, radiation with a wavelength in the hard X-ray regime can be produced by tuning the $K$-parameter of the undulator.

Rigorously, XFEL is different from an ordinary laser. A laser is composed of a gain medium and an optical feedback mechanism, such as a pair of mirrors, and provides a light with spatiotemporal coherence. In contrast, XFEL pulses generated

by the SASE process in microbunches are spatially coherent, but lack temporal coherence due to the stochastic startup process in SASE. However, the wavelength of the XFEL pulse is tunable by adjusting the acceleration energy of the electron and the $K$ value of the undulator used according to (3.9). In order to increase the temporal coherence, the seeding method is applied by using higher harmonic generation for an optical laser pulse.

### 3.3.3   X-Ray Optics

Undulator radiation has a finite bandwidth (Fig. 3.5). XFEL pulses produced by the SASE process also have a finite bandwidth, to a lesser extent than undulator radiation. A monochrometer, typically using the (111) plane of a silicon crystal, is used to obtain quasi-monochromatic X-rays from both radiation sources. From a commonly used double crystal silicon monochrometer with a fixed exit geometry, the energy resolution of the monochromatized X-ray $\Delta E/E$ is in the order of 0.1–1 eV.

For undulator radiation, the higher-order harmonics of the fundamental angular frequency are included. It is quite difficult for a monochrometer to exclude those harmonics from the radiation, as they satisfy the Bragg condition in the monochrometer. In many cases, the higher order harmonics are excluded by a pair of X-ray mirrors coated by platinum or rhodium. The critical reflection angle of the X-ray mirror is larger for X-rays with longer wavelengths. By using this characteristic of X-ray reflection, the glancing angle of the mirrors is set to pass the fundamental undulator radiation and significantly reduce the higher order harmonics.

In synchrotron experiments, a pinhole is inserted into the path of almost monochromatized X-rays to produce a plane wave. The details of the theory and application are described in Chap. 4. In the case of XFEL experiments, XFEL pulses are focused onto the irradiation area with a focal spot size of a few $\mu m^2$. The spatial coherence of the XFEL pulses is maintained as demonstrated by measurements in Chap. 4.

## 3.4   Structure Factor on the Ewald Sphere

The diffraction pattern from a specimen particle is the square of the structure factor intersecting the Ewald sphere in reciprocal space (Fig. 3.7). To understand what kind of structural information can be obtained from the diffraction pattern, it is necessary to derive a set of equations relating the structure factor on the Ewald sphere and the electron density of the particle.

The inverse Fourier transform of the structure factor $F(S)$ gives the electron density $\rho_o(r)$ as

**(a)**

Ewald sphere



**(b)**

$1\times10^{-6}$ nm

0.1 nm

0.3 nm

0.5 nm
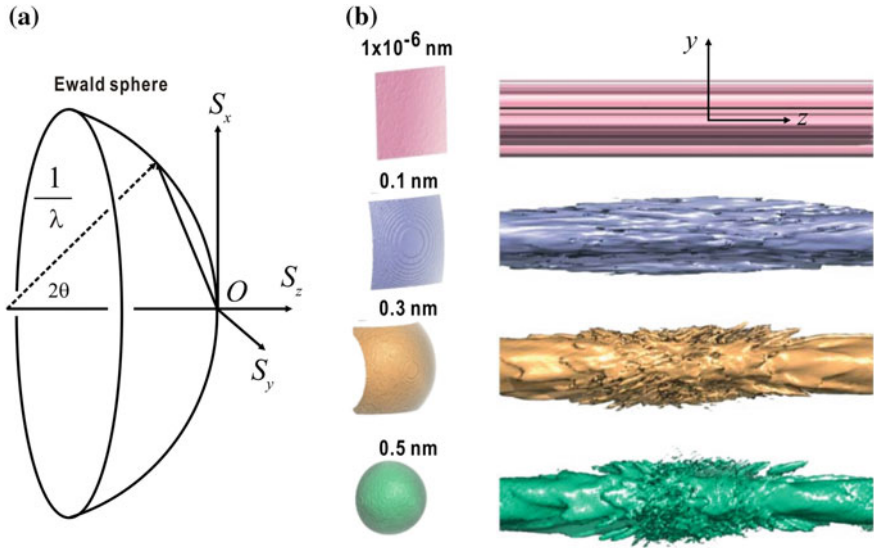


**Fig. 3.7 a** Ewald sphere. **b** Schematic of the variation of the electron density maps (right column) calculated only from the structure factors intersecting the Ewald spheres with different radii (left column). Panel (**b**) is reused from [10] after modification with permission from The Japanese Society for Synchrotron Radiation Research

$$\rho_{\mathrm{o}}(\boldsymbol{r}) = \int F(\boldsymbol{S}) \cdot \exp[-2\pi i \boldsymbol{S} \cdot \boldsymbol{r}] \mathrm{d}^3 S$$

As the inverse Fourier transform is the phase-term weighted sum of the structure factors, multiplying Dirac's δ-function by the structure factor selects only the structure factor on the Ewald sphere. It is expressed as

$$\rho_{\mathrm{Ewald}}(\boldsymbol{r}) = \int F(\boldsymbol{S}) \cdot \delta_{\mathrm{Ewald}} \left[ S_x^2 + S_x^2 + \left( S_z + \frac{1}{\lambda} \right)^2 - \frac{1}{\lambda^2} \right] \cdot \exp[-2\pi i \boldsymbol{S} \cdot \boldsymbol{r}] \mathrm{d}^3 S.$$

(3.10)

According to the convolution theorem, the product of the structure factor and the δ-function in the Fourier integral is expressed as the convolution of their Fourier transforms as

$$\rho_{\mathrm{Ewald}}(\boldsymbol{r}) = \int F(\boldsymbol{S}) \cdot \exp[-2\pi i \, \boldsymbol{S} \cdot \boldsymbol{r}] \, \mathrm{d}^3 S$$

$$* \int \delta_{\mathrm{Ewald}} \left[ S_x^2 + S_x^2 + \left( S_z + \frac{1}{\lambda} \right)^2 - \frac{1}{\lambda^2} \right] \exp[-2\pi i \, \boldsymbol{S} \cdot \boldsymbol{r}] \, \mathrm{d}^3 S$$

The Fourier transform of the δ-function is readily calculated by the substitution of $Z = S_z + \frac{1}{\lambda}$, and by using polar coordinates in reciprocal space.

$$\int \delta_{\text{Ewald}} \left[ S_x^2 + S_x^2 + Z^2 - \frac{1}{\lambda^2} \right] \exp\left[ -2\pi i \left( S_x x + S_y y + Zz - \frac{z}{\lambda} \right) \right] \, dS_x \, dS_y \, dZ$$

$$= \exp\left[ +2\pi i \frac{z}{\lambda} \right] \int \delta_{\text{Ewald}} \left( R^2 - \frac{1}{\lambda^2} \right) \exp[-2\pi i R r \cos\Theta] \sin\Theta \, d\Theta \, d\Phi \, R^2 dR$$

By using the following equation for the δ-function

$$\delta\left( R^2 - \frac{1}{\lambda^2} \right) = \frac{\lambda}{2} \left[ \delta\left( R - \frac{1}{\lambda} \right) + \delta\left( R + \frac{1}{\lambda} \right) \right], \quad R^2 = S_x^2 + S_y^2 + Z^2,$$

the integration over the solid angle can be performed analytically as

$$\exp\left[ 2\pi i \frac{z}{\lambda} \right] \frac{\lambda}{2} \frac{1}{\lambda^2} \int_{\Theta\Phi} \exp\left[ -2\pi i \frac{r\cos\Theta}{\lambda} \right] \sin\Theta \, d\Theta \, d\Phi$$
$$= \exp\left( \frac{2\pi iZ}{\lambda} \right) \frac{2\pi}{\lambda} \frac{\sin\left( \frac{2\pi r}{\lambda} \right)}{\left( \frac{2\pi r}{\lambda} \right)} \tag{3.11}$$

Finally, we obtain the relation, in which the Fourier transform of the structure factor on the Ewald sphere is expressed as the convolution of the original electron density $\rho_0(r)$ and the function in (3.13) coming from the Ewald sphere. The function is a complex number and decreases depending on the distance from the origin of the coordinates.

$$\rho_{\text{Ewald}}(r) = \rho_0(r) * \left[ \exp\left( \frac{2\pi i z}{\lambda} \right) \frac{2\pi}{\lambda} \frac{\sin\left( \frac{2\pi r}{\lambda} \right)}{\left( \frac{2\pi r}{\lambda} \right)} \right] \tag{3.12}$$

This relation depends on the curvature of the Ewald sphere, but is independent of the structure of the object. Because the equation expressed by the convolution is unsuitable for computation, it is rewritten as a set of algebraic equations as

$$\begin{pmatrix} \rho_E(r_1) \\ \rho_E(r_2) \\ \vdots \\ \rho_E(r_N) \end{pmatrix} = \begin{pmatrix} g(r_1;r_1) & g(r_1;r_2) & \cdots\cdots & g(r_1;r_N) \\ g(r_2;r_1) & g(r_2;r_2) & \cdots\cdots & g(r_2;r_N) \\ \cdots & \cdots & \cdots & \cdots \\ g(r_N;r_1) & g(r_N;r_2) & \cdots\cdots & g(r_N;r_N) \end{pmatrix} \begin{pmatrix} \rho_0(r_1) \\ \rho_0(r_2) \\ \vdots \\ \rho_0(r_N) \end{pmatrix}. \tag{3.13}$$

The vector $r$ is replaced by the distance between the $i$th and $j$th points in the object, and $g(r_i;r_j)$ is introduced to express the convolution as a matrix equation.

$$g(r_i; r_j) = \left[ \exp\left[ \frac{2\pi \, i \, z_{ij}}{\lambda} \right] \frac{2\pi}{\lambda} \frac{\sin\left(\frac{2\pi r_{ij}}{\lambda}\right)}{\left(\frac{2\pi r_{ij}}{\lambda}\right)} \right]$$

$$r_{ij} = \sqrt{\left(x_i - x_j\right)^2 + \left(y_i - y_j\right)^2 + \left(z_i - z_j\right)^2}$$

(3.14)

The matrix is nondiagonal because $g(r_i; r_j)$ and $g(r_j; r_i)$ are different and are given by

$$g(r_i; r_j) = \exp\left[ + \frac{2\pi \, i \, z_{ij}}{\lambda} \right] \frac{2\pi}{\lambda} \frac{\sin\left(2\pi \, i \, r_{ij}/\lambda\right)}{\left(2\pi \, i \, r_{ij}/\lambda\right)}$$
$$g(r_j; r_i) = \exp\left[ - \frac{2\pi \, i \, z_{ji}}{\lambda} \right] \frac{2\pi}{\lambda} \frac{\sin\left(2\pi \, i \, r_{ji}/\lambda\right)}{\left(2\pi \, i \, r_{iji}/\lambda\right)} \quad .$$

When the determinant of the matrix is nonzero, the electron density of the object can, in principle, be calculated by multiplying the inverse matrix by the electron density map calculated using the inverse Fourier transform of the structure factor on the Ewald sphere.

$$\begin{pmatrix} \rho_o(r_1) \\ \rho_o(r_2) \\ \vdots \\ \rho_o(r_N) \end{pmatrix} = \begin{pmatrix} g(r_1; r_1) & g(r_1; r_2) & \cdots\cdots & g(r_1; r_N) \\ g(r_2; r_1) & g(r_2; r_2) & \cdots\cdots & g(r_2; r_N) \\ \cdots & \cdots & \cdots & \cdots \\ g(r_N; r_1) & g(r_N; r_2) & \cdots\cdots & g(r_N; r_N) \end{pmatrix}^{-1} \begin{pmatrix} \rho_E(r_1) \\ \rho_E(r_2) \\ \vdots \\ \rho_E(r_N) \end{pmatrix}$$

(3.15)

For X-rays with a short wavelength and very small-angle diffraction, the Ewald sphere is approximated as a plane. Then, the structure factor is given by the Fourier transform of the electron density projected along the direction of the incident X-ray as

$$F\left(S_x, S_y, S_z = 0\right) = \int \rho(x, y, z) \cdot \exp\left[2\pi i \left(S_x x + S_y y\right)\right] dx \, dy \, dz$$

$$= \int \int \rho(x, y, z) \, dz \cdot \exp\left[2\pi i \left(S_x x + S_y y\right)\right] dx \, dy.$$

(3.16)

In XDI experiments, the diffraction patterns obtainable from biological specimens are limited to very small diffraction angles of less than 1°, where the Ewald sphere is approximated as a plane even when the wavelengths of the X-rays are on the order of 0.1 nm. The inverse Fourier transform of the structure factor on the 'Ewald plane' gives the low-resolution electron density map projected along the direction of the incident X-ray. To reconstruct the three-dimensional electron density distribution inside a single specimen particle, a number of diffraction patterns must be collected for the particle with different orientations with respect to the incident X-rays.

## 3.5   Phase Problem

In protein crystallography, the heavy-atom labeling method provided the basis for solving phase problems (see Sect. 2.4). In contrast to protein crystals, it is difficult to prepare heavy-atom labeled specimens with the same arrangements of molecules and components as seen in cells. Therefore, the phase problem must be solved for each specimen.

### 3.5.1   A Brief History of the Phase Problem

As described in Chap. 2, the phases of the diffracted waves cannot be directly determined. When Sayre proposed the XDI experiment, he assumed that any holographic method may be possible by placing an object with known structure in the vicinity of the specimen whose structure is unknown [11]. Later, algorithms from information technology provided a clue to solving the phase problem in XDI without any reference objects.

The iterative phase retrieval (PR) algorithm can reconstruct the phase set using only the diffraction amplitude measurements [12]. A simple algorithm was proposed by Gerchberg and Saxton to reconstruct the phase lost in intensity measurements [14]. The algorithm iterates the Fourier transform of the image of the object and the inverse Fourier transform of the structure factor with constraints in real space and reciprocal space. The constraint in real space limits the area of the object. The constraint in reciprocal space is that the experimentally obtained structure amplitude must be used in the inverse Fourier transform. The Gerchberg-Saxton algorithm was later modified by Fienup for rapid convergence of the calculations. Now the hybrid-input-output (HIO) algorithm, the details of which are described later, is used as the basis of several new algorithms proposed recently [14–17].

It was pointed out that the solutions of the phase problem are unique in two dimensions when the Fourier modulus is sampled more finely than the Nyquist interval [18]. This sampling manner is known as the oversampling method. The oversampling method compensates for the missing phase information by providing a large number of equations for the region with zero density around a specimen. A theoretical breakthrough in solving the phase problem by further sophistication of the oversampling method [19] allows for the application of X-ray diffraction to the structural analysis of noncrystalline particles of a few micrometers in size at resolutions of a few tens of nanometers. Therefore, diffraction experiments combined with the phase-retrieval algorithm have the potential to be widely used in cell biology and materials science to fill the gap between the capabilities of EM and LM.

In 1999, XDI was first applied to the imaging of a microfabricated test object using X-rays with a wavelength of 1.7 nm [20]. As a result, an object with a size of approximately 2 μm was visualized at a resolution of 75 nm. This experiment demonstrated that brilliant X-ray beams with small divergence and high intensity

are necessary for the XDI to obtain high resolution imaging. However, it also suggested that radiation-sensitive specimens must be protected from radiation damage.

In structural analysis by XDI, the phase retrieval algorithm is used to reconstruct the electron density of a specimen particle projected along the direction of the incident X-ray. Here the principle of the phase retrieval algorithm is described to understand how the electron density map of a specimen is reconstructed from only the diffraction pattern.

### 3.5.2   Oversampling of the Diffraction Pattern

The theoretical basis on the quantity of information in the signals is the Nyquist-Shannon sampling theorem [21]. This theorem states the possibility of the reconstruction of a signal after a uniform sampling. In the uniform sampling of a band-limited signal, even if all of the information in the signals between sample points is discarded, there is sufficient information for the perfect mathematical reconstruction of the original signal from only the discrete samples. This means that if a function $f(t)$ does not include frequencies higher than $W$, it is completely described by frequencies lower than $W$.

$$
\begin{aligned}
f(t) &= \frac{1}{2\pi} \int_{-\infty}^{\infty} F(\omega) \exp(i\omega t) \mathrm{d}\omega \\
&= \frac{1}{2\pi} \int_{-2\pi W}^{+2\pi W} F(\omega) \exp(i\omega t) \mathrm{d}\omega
\end{aligned}
\tag{3.17}
$$

In XDI experiments, the discrete sampling of a diffraction pattern by an area detector is required to obtain information sufficient for the reconstruction of the entire object. In addition, the highest sampling frequency in reciprocal space must be finer than the interference pattern between the diffracted X-rays from the largest dimension of the object projected along the incident X-ray beam (Fig. 3.8).

In the small-angle diffraction region, where the Ewald sphere is approximated as a plane, the structure factor is expressed as the Fourier transform of the projection of $\rho(\mathbf{r})$ along the direction of the incident X-ray beam, $\rho_P(x, y)$ (3.16). Here we consider the discrete Fourier transform for the projection electron density $\rho_P(x, y)$ described by $N_x \times N_y$ pixels with an area element of $\Delta x \Delta y$ as

$$
\begin{aligned}
&\left| F_{\mathrm{OBS}}\left(S_x, S_y, S_z = 0\right) \right| \\
&= \left| \sum_{x=0}^{Nx-1} \sum_{y=0}^{Ny-1} \rho_P(x, y) \exp\left[ 2\pi i \left( S_x \frac{x}{N_x} + S_y \frac{y}{N_y} \right) \right] \Delta x\, \Delta y \right|,
\end{aligned}
\tag{3.18}
$$
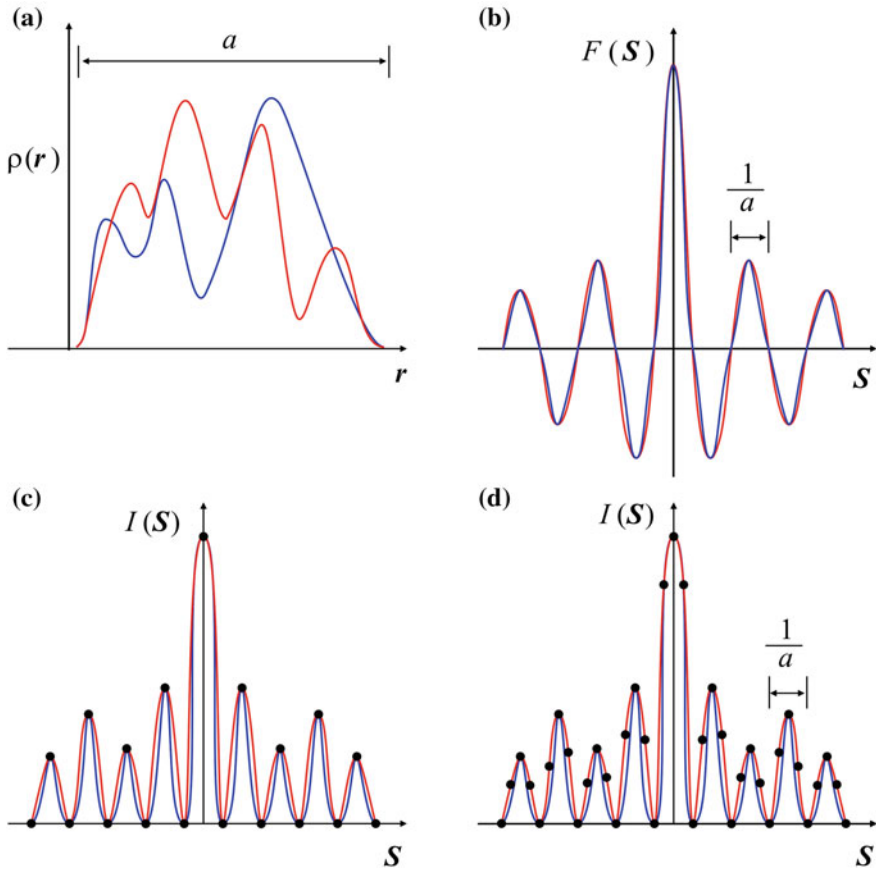
**Fig. 3.8** Schematic explanation of the sampling of diffraction patterns in XDI. **a** Two particles (blue and red lines) with the same size but different electron density distributions. **b** The structure factor of the particles. The peak width is approximated as the inverse of the size, but the profiles are different from each other because of the different electron densities. Panels (**c**) and (**d**) show the profiles of the diffraction intensity for the particles. Filled circles indicate the sampling points. **c** If the sampling interval is the reciprocal of the particle size, it is impossible to distinguish the diffraction patterns of the two particles. **d** In contrast, the two diffraction patterns can be distinguished if the sampling interval is half of the reciprocal of each particle size. Published with kind permission of Masayoshi Nakasako 2017. All Rights Reserved

where $\left| F_{\mathrm{OBS}}(S_x, S_y, S_z = 0) \right|$ is the structure factor of the projection electron density $\rho_{\mathrm{P}}(x, y)$. $N_x$ and $N_y$ must be greater than the number of pixels satisfying the sampling theorem. This set of algebraic equations regarding $\rho_{\mathrm{P}}(x, y)$ can, in principle, be solved for a set $\left| F_{\mathrm{OBS}}(S_x, S_y, S_z = 0) \right|$ observed at $N_x \times N_y$ different points (Fig. 3.9a). However, in objects without anomalous scatterers, the centrosymmetry (Friedel centrosymmetry, (2.20) in the diffraction patterns reduces the set of $\left| F_{\mathrm{OBS}}(S_x, S_y, S_z = 0) \right|$ by half as $N_x \times N_y / 2$. Then, to solve the algebraic equation,

the number of data points of observed diffraction amplitudes is required to be more than double $N_x \times N_y/2$. To increase the number of equations, we sample the diffraction pattern $\sigma_x N_x$ along the direction of $S_x$ and $\sigma_y N_y$ along the direction of $S_y$ (Fig. 3.9b). When the following relationship is satisfied, $\rho_P(x, y)$ can, in principle, be determined.

$$\sigma = \sigma_x \times \sigma_y \geq 2 \qquad\qquad (3.19)$$

The parameter $\sigma$ is the oversampling ratio [3, 19]. This requirement is the so-called oversampling condition to define the minimum number of data points
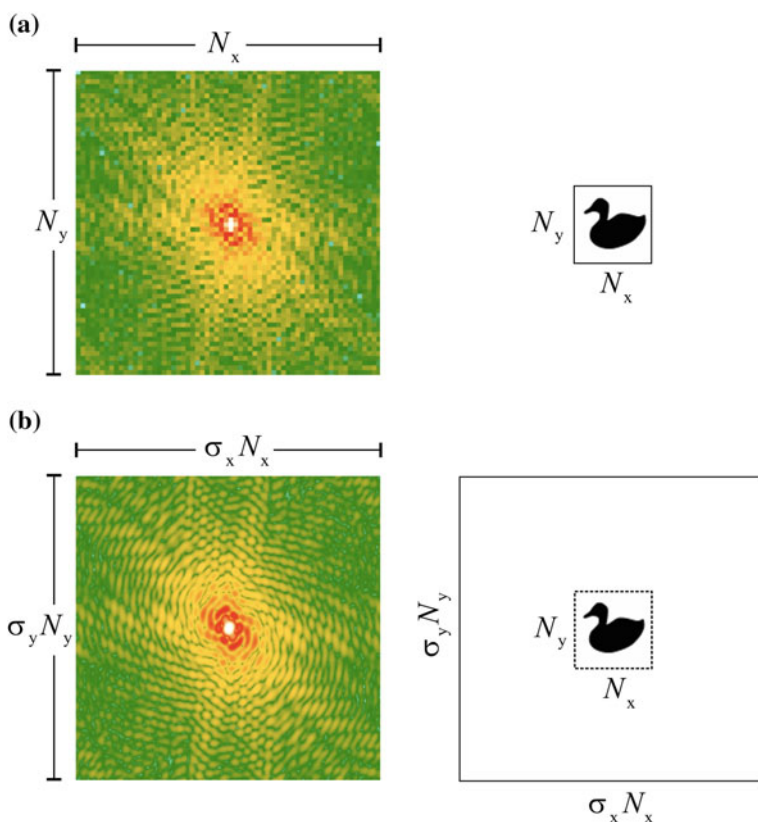


**Fig. 3.9** Schematic of the oversampling of a diffraction pattern. **a** When a diffraction pattern is sampled by $N_x \times N_y$ pixels at the Nyquist frequency, the inverse Fourier transform of the structure factor gives an electron density map of $N_x \times N_y$ pixels. **b** In contrast, when the diffraction pattern is oversampled by $\sigma_x N_x \times \sigma_y N_y$ pixels, the electron density of the object appears in the area of $N_x \times N_y$ pixels (the support) in the image of $\sigma_x N_x \times \sigma_y N_y$ pixels. The electron density in the area outside the support must be zero and is used to increase the number of algebraic equations in order to solve the phase problem. Published with kind permission of Masayoshi Nakasako 2017. All Rights Reserved

necessary to solve the set of algebraic equations. Therefore, diffraction patterns must be collected such that the number of detector pixels exceeds the oversampling ratio requested in the calculation.

## 3.6  Iterative Phase Retrieval Algorithm

### 3.6.1  Outline of the Iterative Phase Retrieval Algorithm

In practice, $\rho_P(x, y)$ is determined from the oversampled diffraction amplitude by an entirely computational procedure with the iterative PR algorithm, as outlined in Fig. 3.10 [13]. The calculation starts with a random electron density map. After the Fourier transform (FT) of the initial map, the structure amplitude of the calculated
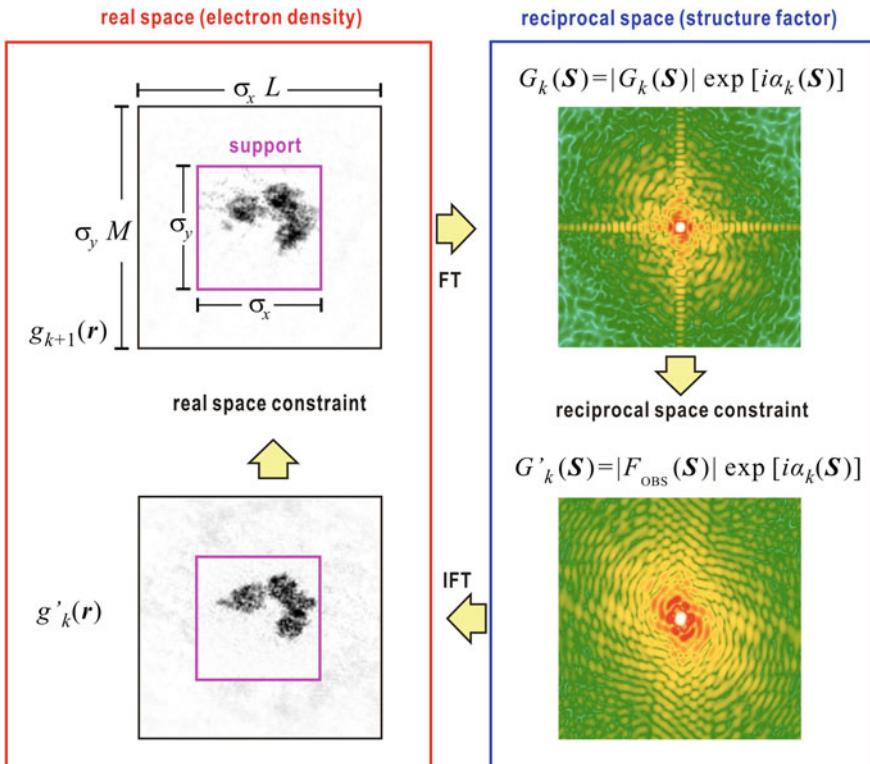


**Fig. 3.10** Schematic of iterative phase-retrieval calculation. Published with kind permission of Masayoshi Nakasako 2017. All Rights Reserved

structure factor is modified by the constraint in reciprocal space. For instance, in the $k$th iteration cycle, the amplitude of the structure factor $G_k(\boldsymbol{S})$ is replaced by the observed structure amplitude.

$$\begin{aligned} G'_k(\boldsymbol{S}) &= |F_{\text{OBS}}(\boldsymbol{S})|\exp[i\alpha_k(\boldsymbol{S})] = \frac{|F_{\text{OBS}}(\boldsymbol{S})|}{|G_k(\boldsymbol{S})|}G_k(\boldsymbol{S}) \\ G_k(\boldsymbol{S}) &= |G_k(\boldsymbol{S})|\exp[i\alpha_k(\boldsymbol{S})] \end{aligned} \tag{3.20}$$

Then, a new electron density map is obtained from the inverse Fourier transform (IFT) of the structure factor modified by the constraint in reciprocal space. The new map is modified according to the constraint specifying the electron density map for the next step (the constraint in real space). The details of the constraint in real space are described in the subsequent subsection. When the oversampling condition is satisfied, the electron density map is, in principle, retrieved by iterating the cycles.

### 3.6.2  Constraint in Real Space

Several types of iterative PR algorithms have been proposed, such as error-reduction (ER) [13], hybrid-input-output (HIO) [22], and difference maps [17] with differences regarding the constraints in real space. Among these algorithms, the classical and simplest method is the ER algorithm. This algorithm provides the basic idea for real space constraints. For the constraint in real space, the following two conditions are applied to the electron density map calculated by the inverse Fourier transform of the structure factor modified by the constraint in reciprocal space.

$$\rho_{k+1}(\boldsymbol{r}) = \begin{cases} \rho'_k(\boldsymbol{r}), & \boldsymbol{r} \in \text{support} \\ 0, & \boldsymbol{r} \notin \text{support} \end{cases} \tag{3.21}$$

In the support regions, the electron density of the specimen should appear. One of the weak points of this algorithm is the slow convergence of the calculation.

The HIO algorithm [22] was developed to avoid calculations around in fake solutions for a long time. The algorithm uses the following constraint in real space.

$$\rho_{k+1}(\boldsymbol{r}) = \begin{cases} \rho'_k(\boldsymbol{r}), & \boldsymbol{r} \in \text{support} \\ \rho'_k(\boldsymbol{r}) - \beta\rho'_k(\boldsymbol{r}), & \boldsymbol{r} \notin \text{support} \end{cases} \tag{3.22}$$

Parameter $\beta$ controls the degree of reduction of the electron density outside the support. Because the constraint for $\beta = 1$ is the same as that of the ER algorithm, the ER algorithm is a special case of the HIO algorithm.

Experimentally, due to the use of a beamstop to absorb the X-ray beam transmitting specimens, the diffraction pattern around the zero-diffraction angle is

missed; this is problematic because the missing region contains important structural information regarding the size and total number of electrons in the specimen (2.29 and 2.30 in Chap. 2). Therefore, the PR calculations for experimental diffraction patterns with such missing regions sometimes fail. In our experience, the omission of several layers of speckle patterns from the center leads to failures in any type of PR algorithms.

### 3.6.3  Shrink-Wrap Algorithm

The shrink-wrap (SW) algorithm is introduced to modify the shape and size of the support through two steps during the PR calculations [23]. In the first step, a new electron density map is generated by convolution of a Gaussian function with the standard deviation $\alpha$ as

$$\rho'(\boldsymbol{r}) = \rho(\boldsymbol{r}) * g(\boldsymbol{r}), \quad g(\boldsymbol{r}) = \frac{1}{\sqrt{2\pi}} \exp\left(-\frac{x^2 + y^2}{2\,\alpha^2}\right). \tag{3.23}$$

In the computation, the convolution for the electron density map of $N \times N$ pixels requires a calculation cost on the order of $N^4$. To reduce the cost, the convolution theorem is applied. The Fourier transforms of $g(\boldsymbol{r})$, $\rho(\boldsymbol{r})$, and $\rho'(\boldsymbol{r})$ are designated as $G(\boldsymbol{S})$, $F(\boldsymbol{S})$, and $F'(\boldsymbol{S})$, respectively. Then, $F'(\boldsymbol{S})$ is expressed as

$$F'(\boldsymbol{S}) = F(\boldsymbol{S})\,G(\boldsymbol{S}).$$

$\rho'(\boldsymbol{r})$ is calculated by applying the inverse Fourier transform to $F'(\boldsymbol{S})$. The computational cost is then reduced to the order of $N^2\,(\log N)^2$.

In the second step, for the modified map, a new support is redefined as the area with electron densities higher than a specified value empirically defined as

$$\rho''(\mathbf{r}) = \begin{cases} 1 & \text{if } \rho(\boldsymbol{r}) \geq \rho_c \\ 0 & \text{otherwise} \end{cases}. \tag{3.24}$$

where $\rho''(\boldsymbol{r})$ is used as the support shape in the subsequent PR cycles.

In practice, we apply this SW-update of the map after every 100 HIO cycles (Fig. 3.11). The standard deviation of the Gaussian is changed depending on the progress of the HIO cycles as

$$s_n = (0.99)^n s_0,$$

where $s_0$ is the initial value before applying the SW calculation. When $s_n$ falls below a defined value, the application of SW is terminated.
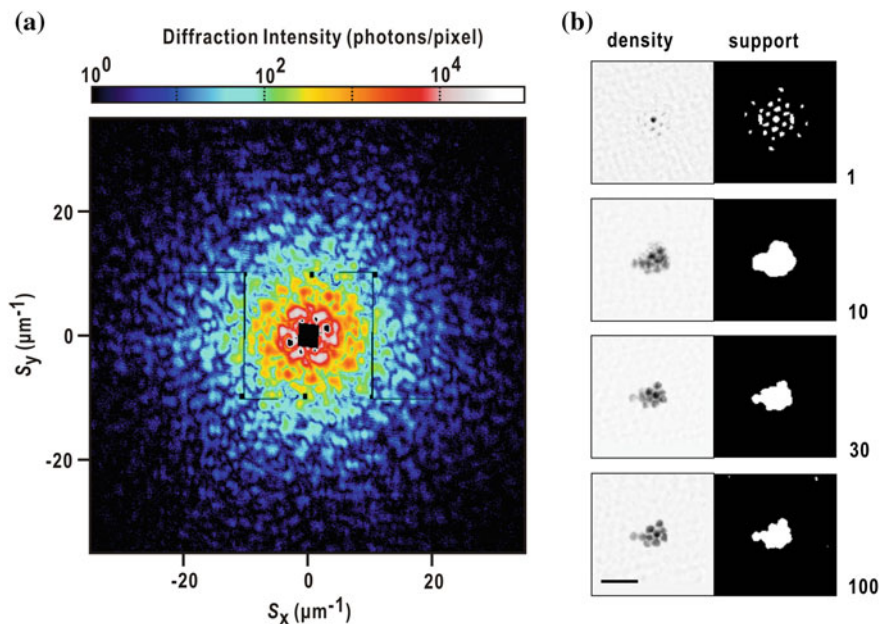
**Fig. 3.11 a** A diffraction pattern from an aggregate of ten gold colloidal particles with an approximate diameter of 250 nm. **b** SW modification of the support during the PR calculation of the diffraction pattern in panel (**a**). From the electron density maps in the left column, the support shapes are calculated for every set of 100 cycles of HIO calculations. SW cycles are indicated by the numbers on the right. Panel (**a**) is reused from [24, https://doi.org/10.1107/s1600577517008396] after modification with permission from The International Union of Crystallography. Published with kind permission of Masayoshi Nakasako 2017. All Rights Reserved

### 3.6.4  Oversampling Smoothness Algorithm

The HIO algorithm is a powerful method to retrieve the electron density maps of metal particles, the diffraction patterns of which are recorded with a good signal-to-noise ratio. In contrast, PR calculations for biological specimens using the HIO algorithm often fail, because the diffraction patterns are weak and suffer from Poisson noise due to the small scattering cross sections. Poisson noise in X-ray detection becomes more significant for higher resolution (or high frequency), because the atomic structure factor decreases monotonically at high resolution.

The oversampling smoothness (OSS) algorithm is proposed for PR of diffraction patterns with low signal-to-noise ratios [25]. In PR cycles, high frequency noises come from the region outside the support. The OSS algorithm introduces a low-pass filter to damp the diffraction intensity at high resolution in the real-space constraint. The low-pass filter works to reduce the influence from weak intensities with significant levels of Poisson noise in the high resolution, and weights the low

resolution data that is less degraded by Poisson noise. In this way, the fluctuations of the electron density map inside the support are suppressed.

The idea is implemented by the real-space constraint is described by the following equation.

$$\rho_{k+1}(\boldsymbol{r}) = \begin{cases} \rho_k'(\boldsymbol{r}), & \boldsymbol{r} \in \text{support} \\ F^{-1}\big[G_k'(\mathbf{S})\,W(\mathbf{S})\big], & \boldsymbol{r} \notin \text{support} \end{cases} \qquad (3.25)$$

where $F^{-1}$ is the inverse Fourier transform, $G_k'(\mathbf{S})$ is the Fourier transform of $\rho_k'(\boldsymbol{r})$, and $W(\boldsymbol{S})$ is a normalized Gaussian function acting as a low-pass filter.

$$W(\boldsymbol{S}) = \exp\left[-\frac{1}{2}\left(\frac{\boldsymbol{S}}{\alpha}\right)^2\right] \qquad (3.26)$$

The standard deviation $\alpha$ is gradually changed from $N$ to $\frac{1}{N}$ in the course of the PR calculations. In the initial stage of PR calculations, the OSS algorithm works with a real-space constraint similar to that of the HIO algorithm. By gradually increasing the effect of the low-pass filter, the OSS algorithm in the final stage acts as the ER algorithm. Therefore, the OSS algorithm incorporates the advantages of the HIO and ER algorithms, depending on the progress of the PR calculations.

The OSS algorithm was examined in the application to the diffraction pattern of a dehydrated single yeast cell as a representative biological specimen by comparing the average and variance of the resulting electron density maps with those obtained by other algorithms. The comparison suggests that the OSS algorithm is superior to the others in PR for weak diffraction patterns.

## 3.7 Parameters for Assessing the PR Calculation

In general, indirect imaging techniques relying on numerical optimization methods, such as the PR algorithms, stand on the following assumption: if the solution is unique, it satisfies the constraints, and therefore it must be true. Only an exhaustive search performed by running the reconstruction algorithm with different random starts can provide an opportunity to examine the uniqueness and correctness of the suggested solutions. When a number of calculations reliably converge to similar solutions, we assume that the solutions are correct. Then, we can screen failure runs and select success runs.

Experimental diffraction patterns miss the small-angle region due to the beam-stop and the saturation of the detector pixels. Diffraction patterns at high angles are modified by Poisson noise in X-ray detection. Therefore, PR calculations often fail, particularly for diffraction patterns from biological specimens. We use parameters characterizing the PR maps to examine the success of the PR calculations, namely, a parameter monitoring the convergence of the PR calculation in real space, the

crystallographic R-factor [26], the zero-angle diffraction intensity, and the effective resolution estimated by the phase-retrieval transfer function (PRTF) [27]. The details of the PRTF will be described in Chap. 7.

The necessary condition for the convergence of electron density maps is the reduction of two parameters. One is defined as

$$\gamma = \frac{\sum\limits_{\mathbf{r} \notin \text{support}} \rho(\boldsymbol{r})}{(\sigma - 1) \sum\limits_{\mathbf{r} \in \text{support}} \rho(\boldsymbol{r})} \qquad (3.27)$$

This parameter monitors the electron density outside the support. When a PR calculation gives a correct electron density map, the numerator, which is the sum of the electron densities outside the support, becomes zero [28]. The crystallographic R-factor is defined as

$$R_{\mathrm{F}} = \frac{\sum\limits_{\mathbf{S}} \left| \sqrt{I_{\text{obs}}(\boldsymbol{S})} - k\sqrt{I_{\text{cal}}(\boldsymbol{S})} \right|}{\sum\limits_{\mathbf{S}} \sqrt{I_{\text{obs}}(\boldsymbol{S})}}, \qquad (3.28)$$

where $I_{\text{obs}}(\boldsymbol{S})$ and $I_{\text{cal}}(\boldsymbol{S})$ are the observed and calculated diffraction intensities at the scattering vector $\boldsymbol{S}$, respectively. The scale factor $k$ is defined to equalize the sum of the experimental and calculated diffraction intensities. The crystallographic R-factor measures how the structure amplitudes calculated from the retrieved map are similar to the observed values, and it is conventionally used as an error function or a convergence criterion. In the calculated diffraction intensity, the zero-angle (forward) diffraction intensity $I_0$ is proportional to the squared total sum of the electron density (see 2.30). When a PR calculation fails, $I_0$ tends to become extremely large.

Figure 3.12 shows the variation of parameter $\gamma$ and the $R_{\mathrm{F}}$-factor during a PR calculation. The diffraction pattern lacks the small-angle regions due to the beamstop and the saturation of the detector pixels, but the PR calculation leads to a correct electron density map, in which the borders of ten gold colloidal particles are clearly visualized. Both $\gamma$ and $R_{\mathrm{F}}$ decreased significantly within 1000 cycles of the HIO calculation with ten SW modifications, and then maintained their values until the end of the calculation. This result suggests that both $\gamma$ and $R_{\mathrm{F}}$ can be used as a necessary condition. However, the electron density is still undergoing improvement after the first 1000 cycles, despite the small fluctuations in both $\gamma$ and $R_{\mathrm{F}}$. Therefore, the convergence of them is insufficient to judge the success of PR calculations. To extract correct electron density maps from a number of trials of PR calculations, another parameter or protocol is necessary. This point will be discussed in Chap. 7.
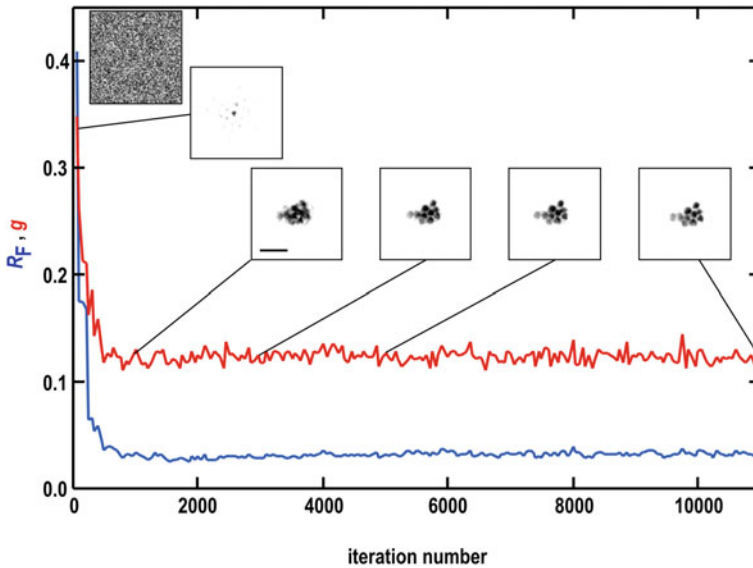
**Fig. 3.12** The variation of parameter $\gamma$ and $R_F$ during a PR calculation using the combination of the HIO and SW algorithms for the diffraction pattern in Fig. 3.9**a**. Electron density maps at the initial, 1000th, 3000th, 5000th, and 11000th (final) cycle are shown. Published with kind permission of Masayoshi Nakasako 2017. All Rights Reserved

# References

1. J. Miao, T. Ishikawa, I.K. Robinson, M.M. Murnane, Science **348**, 530 (2015)
2. M. Born, E. Wolf, *Principles of Optics* (Cambridge University Press, Cambridge, 1999)
3. J. Miao, T. Ishikawa, E.H. Anderson, K.O. Hodgson, Phys. Rev. B **67**, 174104 (2003)
4. J.R. Fienup, Appl. Opt. **21**, 2758 (1982)
5. T. Hara, et al., J. Synchrotron Rad. **5**, 403 (1998)
6. P. Emma et al., Nat. Photon. **4**, 641 (2010)
7. T. Ishikawa et al., Nat. Photon. **6**, 540 (2012)
8. T. Tanaka, H. Kitamura, J. Synchrotron Rad. **8**, 1221 (2001). (http://radiant.harima.riken.go.jp/spectra/index.html)
9. Z. Huang, K.-J. Kim, Phys. Rev. ST Accel. Beams **10**, 034801 (2007)
10. Nakasako et al., HOSYAKO **26**, 11–25 (2013)
11. D. Sayre, *Prospects for long-wavelength x-ray microscopy and diffraction* (In Imaging Processes and Coherence in Physics, Springer, Berlin Heidelberg, 1980)
12. J.R. Fienup, Appl. optics **21**, 2758 (1982)
13. R.W. Gerchberg, W.O. Saxton, Optik **35**, 237 (1972)
14. Y. Nishino, J. Miao, T. Ishikawa, Phys. Rev. B **68**, 220101(R) (2003)
15. C. Song, et al., Phys. Rev. Lett. **101**, 158101 (2008)
16. D. Luke, Russel Inverse problems **21**, 37 (2005)
17. V. Elser, J. Opt. Soc. Am. A **20**, 40 (2003)
18. R.H.T. Bates, Optik **61**, 247 (1982)
19. J. Miao, D. Sayre, H.N. Chapman, J. Opt. Soc. Am. A **15**, 1662 (1998)
20. J. Miao, P. Charalambous, J. Kirz, D. Sayre, Nature **400**, 342 (1999)

21. C.E. Shannon, Proc. IRE **37**, 10 (1949)
22. J.R. Fienup, Opt. Lett. **3**, 27 (1978)
23. S. Marchesini, et al., Phys. Rev. B **68**, 140101 (2003)
24. Y. Sekiguchi, T. Oroguchi, M. Nakasako, J. Synchrotron Rad. **23**, 312 (2016)
25. J.A. Rodriguez, et al., J. Appl. Cryst. **46**, 312 (2013)
26. J. Drenth, *Principles of Protein X-Ray Crystallography* (Springer, New York, 2007)
27. H.N. Chapman et al., J. Opt. Soc. Am. A **23**, 1179 (2006)
28. J. Miao, K.O. Hodgson, D. Sayre, Proc. Natl. Acad. Sci. U.S.A. **98**, 6641 (2001)

# Chapter 4
# Diffraction Apparatus for X-Ray Diffraction Imaging

**Abstract** To visualize the structures of frozen-hydrated non-crystalline biological particles such as cells and organelles, two types of diffraction apparatus were developed for X-ray diffraction imaging (XDI) experiments at cryogenic temperatures using synchrotron X-rays and X-ray free electron laser (XFEL) pulses. Cryogenic experiments are advantageous for the suppression of the radiation damage of specimens over the long exposure times in synchrotron experiments. In addition, frozen-hydrated biological specimens are free from dehydration and bubbling under vacuum conditions at ambient temperature. One apparatus, KOTOBUKI-1, is dedicated to cryogenic XDI experiments at the synchrotron radiation facility SPring-8. Another apparatus, named TAKASAGO-6, was developed for cryogenic XFEL-XDI experiments at SACLA. Each apparatus is equipped with a cryogenic pot mounted on a goniometer stage for the collection of diffraction data at 66–80 K. The details of the devices used in these apparatuses are introduced together with the miscellaneous devices assisting their practical use. This chapter provides examples and clues to construct a new diffraction apparatus for diffraction experiments at cryogenic temperatures, including the delivery of cooled specimens.

## 4.1 Concept Behind Cryogenic X-Ray Diffraction Experiments

In XDI experiments, because the specimen particles have a small scattering cross section, a vacuum environment is necessary to avoid scattering from the air and absorption of diffracted X-rays from particles in the air. The vacuum environment is non-hazardous for particles from material sciences. In contrast, biological specimens, which require an aqueous environment to maintain their functional structures, are degraded by drying, the boiling of water, and adiabatic expansion under vacuum conditions. In the last decade, cells and organelles have been chemically fixed [1] or dried [2] for use in XDI experiments using synchrotron X-rays. We are hesitant to accept the experimental evidence provided by such experiments. Although X-ray exposure under a high humidity environment at ambient temperature has been

proposed, it is difficult to deny the possibility that specimen particles may be
degraded by radiation damage under ambient temperature [3].

Researchers developed diffraction apparatus and specimen preparation methods
to avoid the degradation of biological specimens under vacuum conditions in
XFEL-XDI experiments, such as the liquid jet method [4], the aerosol method [5,
6], and the micro-liquid enclosure-array method [7]. These experimental methods
have been applied to the structural analyses of viruses [4, 5, 8], cellular components
[9], and bacterial cells [6, 7]. These methods are only suitable for XFEL-XDI
experiments, where the diffraction pattern of each particle is recorded by a
single-shot exposure, and are unsuitable for synchrotron experiments, where a long
exposure time of a few days is necessary.

An XDI experiment at cryogenic temperatures is proposed to visualize the
structures of frozen-hydrated biological particles without fixing or labeling. The
benefits of cryogenic experiments have been demonstrated in a pioneer study [10],
and also by recent XDI experiments in both synchrotron [11–14] and XFEL
facilities [15–17]. In this chapter, the apparatuses and devices dedicated to cryo-
genic experiments are described.

### 4.1.1   Cooled Specimens in Vacuum

In XDI experiments, specimens are set in vacuum to reduce the absorption and
scattering of the incident and diffracted X-rays by air. For instance, X-rays with a
wavelength of 0.2 nm are attenuated to approximately 77% when traveling along an
air path of 0.1 m (Fig. 4.1). The attenuation by air must be diminished to record
weak diffraction signals. To record diffraction patterns in a very small diffraction
angle, XDI experiments require a long camera distance of several meters. The total
cross section of nitrogen molecules present along a camera length of 5 m is larger
than that of a single biological specimen, and therefore diffraction signals from the
specimen would be buried in the diffraction pattern from the air. Therefore, it is
better to place specimens in vacuum. In addition, the small scattering cross sections
of biological particles require the incident X-ray beam to be as strong as possible.

In XDI, one of the important targets are non-crystalline biological specimens
such as cells and cellular organelles, as described in Chap. 1. Many XDI experi-
ments on biological specimens using synchrotron X-rays have been carried out at
ambient temperature and in vacuum [1–3, 18–20]. However, because water occu-
pies 60–70% of the volume of biological cells, biological cells and organelles
require a fully aqueous environment to maintain their functional structures. At the
molecular level, the stability of the proteins depends on the level of hydration. For
instance, protein molecules are fully hydrated on the surface in an aqueous envi-
ronment [21]. When cells are set in vacuum at ambient temperature, it is difficult to
deny the probability that the evaporation of water and/or the bubbling of water
inside the cells under low pressure will damage the functional structures. Indeed,
the dehydration of biological specimens in vacuum results in substantial structural
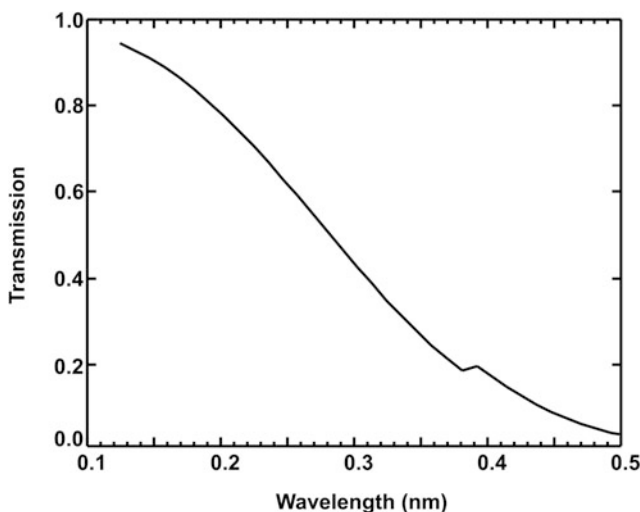
**Fig. 4.1** Absorption of X-rays with a photon energy range from 1.24 to 12.40 keV by air at 101,325 N/m² and 300 K. The path length of air is 0.1 m. In the plot, the transmission of X-rays is plotted against the X-ray wavelength. The transmission was calculated using the website of the Center for X-ray Optics Research group at the Lawrence Berkeley National Laboratory, USA (http://henke.lbl.gov/optical_constants/). Published with kind permission of Masayoshi Nakasako 2017. All Rights Reserved

differences from frozen-hydrated specimens, which are believed to retain the functional structures [22]. To avoid this destruction, some XDI experiments have used biological specimens fixed by chemical reagents [1].

Frozen-hydrated cells and cellular components would be free from damage by evaporation and bubbling even in a vacuum environment. Indeed, for electron microscopy of cellular components, specimens are frozen-hydrated in vitreous ice to withstand both a vacuum environment of approximately $10^{-4}$ Pa and radiation damage during exposure to the electron beam [23–26]. The thermal shrinkage of the cytosols inside the cells by flash cooling would be as small as that of vitreous ice frozen from water [25]. According to cryogenic X-ray protein crystallography, the linear thermal-expansion coefficients of the frozen proteins are in the order of $2.5 \times 10^5$ K$^{-1}$ [27]. Therefore, the thermal shrinkage of the cellular specimens after flash-cooling will be negligibly small.

As demonstrated through the use of cryogenic technologies developed to store biological cells at low temperatures in the medical sciences [28–30], frozen-hydrated cells and cellular organelles retain their functional structures and are still alive after being returned to the ambient temperature [31]. Cryogenic specimen preparation enables us to store frozen-hydrated specimens in liquid nitrogen until their use in experiments. As described in Chaps. 6, 8, and 9, the preparation of cooled specimens allows us to harvest a large number of biological cells and isolated unstable cellular organelles at a desired point in the cell cycle.

## 4.1.2   Radiation Damage

X-ray irradiation induces the ionization of atoms and chemical bonds primarily to degrade the structures of biological molecules in cells. The ionized atoms and molecules are frequently transformed to free radicals [32]. At ambient temperature, the diffusion of radicals inside the specimens causes secondary damage which degrades the arrangement and interactions of the biomolecules (Fig. 4.2). An irradiation dose of more than $10^5$–$10^6$ Gy/exposure is necessary to record the diffraction patterns of the biological specimens [32], because of the small total scattering cross sections of the light atoms composing the biological materials. Thus, the radiation damage of biological specimens is difficult to avoid in synchrotron XDI experiments at ambient temperature.

Data collection at near-liquid-nitrogen temperatures significantly reduces the radiation damage of biological specimens. At liquid nitrogen temperatures, free radicals causing secondary damage are immobilized. In fact, a dramatic reduction of the radiation damage of specimens near liquid nitrogen temperatures was reported from cryogenic electron microscopy [34] and cryogenic X-ray protein crystallography (Fig. 4.1a) [35]. In structural studies at cryogenic temperatures, flash-cooled biological specimens are kept in a frozen-hydrated state in vitreous ice.

However, it is difficult to completely eliminate all radiation damage using cryogenic methods [32, 36, 37]. The limit of the radiation dose was first proposed as the Henderson limit (approximately $2 \times 10^7$ Gy, 1 Gy = 1 J/1 kg) for the threshold radiation dose in structural analyses of biological specimens at a resolution of 0.2 nm [32, 36]. By summarizing experimental data from X-ray crystallography, TEM, and X-ray tomography, an empirical relation between the
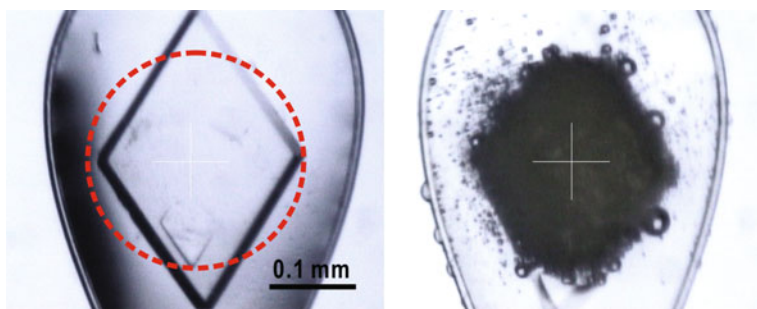


**Fig. 4.2** Photographs demonstrating the radiation damage to a protein crystal [33]. The left photograph was taken before X-ray exposure. The wavelength of the X-ray was 0.1000 nm, and the X-ray flux was $10^9$ photons/s. The red dashed circle indicates the area irradiated by the X-ray beam. After X-ray irradiation for 12 h, the cold nitrogen gas stream was closed for 10 s by a plastic plate. During the temperature increase of the protein crystal, many small bubbles appeared from the interior of the crystal (right panel). Panels are reused after modification with permission from The Physical Society of Japan

maximum tolerable dose and the resolution is proposed [32]. According to the relation, the maximum tolerable dose is roughly proportional to the real-space resolution with a coefficient of $10^8$. Therefore, to achieve structure analyses at high resolution, diffraction data are better to be collected within the tolerable dose. In X-ray crystallography, because the conformation of biological macromolecules in crystals is fixed, nearly the same diffraction data can be obtained from different crystals. Single particle analysis in TEM visualizes the 3D structures from a number of molecules in the same conformation. In contrast, in XDI tomography experiments for cells and organelles, a number of diffraction patterns must be collected from a single particle. Therefore, the maximum resolution will be limited by the maximum tolerable dose.

In experiments, the resolution of a diffraction pattern depends on the wavelength of the X-rays, the size of the specimen particle, and the incident intensity of the X-rays. To estimate the irradiation dose, a theoretical relation between the total X-ray dose, $D$, and the maximum resolution, $d$, is proposed [32] as

$$D = I_0 \, h \, v \, \frac{\mu}{\rho_m} \frac{1}{r_e^2 \, \lambda^2} \frac{1}{\rho^2} \frac{1}{d^4} \tag{4.1}$$

where $h$, $v$, $\lambda$, and $r_e$ are Planck's constant, the frequency and wavelength of the incident X-rays, and the classical electron radius, respectively. $\mu$, $\rho_m$, and $\rho$ are the mass absorption coefficient, mass density, and electron density of the specimen, respectively. $I_0$ is the number of photons. Therefore, the X-ray dose necessary to detect diffraction patterns up to a desired resolution is proportional to $d^{-4}$. This relation is consistent with the experimental diffraction data for a biological cell in the resolution range from 20 to 100 nm. From the theoretical estimation and the empirically obtained maximum tolerable dose, the maximum resolution in a to-mography XDI experiment for a single biological particle is estimated to be approximately 10 nm. Because LM and TEM are difficult to visualize the structure of the whole biological cell at a resolution of 10 nm, only tomography XDI experiments provide the detailed structures of whole cells without any physical or chemical modification of the specimens. The details of XDI tomography experiments will be described in Chap. 9.

## 4.1.3   Diffraction Apparatus

### 4.1.3.1   Diffraction Apparatus for the Use of Synchrotron X-Rays

As described in the previous two subsections, flash-cooled biological specimens are advantageous for withstanding vacuum environment and radiation damage. We prepare frozen-hydrated biological specimens as described in Chap 5.

In XDI experiments, frozen-hydrated specimens must be transferred from a storage chamber filled with liquid nitrogen to a goniometer stage in a vacuum chamber without frosting and with little increase in temperature. In addition, the temperature of a specimen set on the stage must be kept near the liquid nitrogen temperature during diffraction data collection. Transfer devices and diffraction apparatuses dedicated to XDI experiments at cryogenic temperatures are necessary in order to fulfill these requirements.

To date, two types of diffraction apparatuses have been developed for cryogenic XDI experiments targeting biological specimens by using synchrotron X-rays. The first is an in-vacuum type apparatus utilizing a commercially available cryogenic specimen holder developed for EM [24]. The cryogenic holder is inserted into a vacuum chamber on a custom-made goniometer to rotate and translate the specimen holder for tomography experiments [38, 39]. The second is a non-vacuum type utilizing the free-standing thin-film method developed for cryogenic X-ray protein crystallography [12, 13, 40]. Both techniques have demonstrated the potential of cryogenic XDI experiments to collect diffraction patterns of specimens under the significant reduction of the damage from the vacuum and X-ray radiation.

In the first type of experiments, the diffraction apparatuses used are equipped with a goniometer inside a vacuum chamber [38, 39]. In the apparatus, the goniometer accepts a specimen holder dedicated to TEM and can tilt specimens in the angular range of $\pm 80°$ with respect to the direction of the X-ray beam [39]. The frozen-hydrated specimen particles set at the tip of the holder are cooled at approximately 95 K by heat conduction to the liquid-nitrogen in the dewar of the holder. For the delivery of the cooled specimen holder into the vacuum chamber, the apparatus has a load-lock chamber. A soft X-ray diffraction imaging experiment on a frozen-hydrated budding yeast cell in vacuum demonstrated the great reduction in artifacts due to dehydration, ice formation, and radiation damage at 103 K [11]. The used of a cryogenic holder is advantageous for the positional stability of the specimen, because EM observation requires very small positional fluctuation during exposure.

Cryo-loops are convenient for performing XDI experiments at cryogenic temperatures [41]. The experimental procedure is quite simple and is standardized in protein crystallography. A small droplet of the specimen suspension is picked up by a small loop made of thin nylon fiber with a diameter of less than 100 μm. Then, the droplet is quickly flash-cooled by insertion into a stream of cold nitrogen gas, the temperature of which is adjusted to around 100 K. In this method, because the specimen particles are embedded in a thick vitreous ice, the contrast of the electron density projected along the direction of the incident X-ray is small between the specimen particles and vitreous ice. In addition, for instance, Karman vortices produced at the interface between the edge of the loop and the gas stream probably induce oscillatory movements of the loop. Subsequently, the loop in the gas stream displays positional fluctuations during X-ray exposure. Because the size of the area with good spatial coherence is limited to several micrometers in the X-ray beam produced by a pinhole (see Sect. 4.2.2.1), the positional fluctuation of the loop may frequently move specimen particles outside the area of spatially coherent irradiation

[13]. In addition, scattering and absorption by the cold nitrogen gas stream and the air around the specimen modify the diffraction patterns of the specimen particles. Although a vacuum environment is more advantageous, the combination of cold nitrogen gas flow and the loop method is difficult to apply to specimens set inside a vacuum chamber.

### 4.1.3.2   Diffraction Apparatus for the Use of X-Ray Free Electron Laser Pulses at Ambient Temperature

XDI experiments using intense and coherent XFEL pulses with a short duration allow us to collect diffraction pattern of a specimen particle before their destruction at the atomic level [42–44]. On the other hand, due to the repetition rate of the XFEL pulses, a large number of diffraction patterns can be collected within a short time. In XFEL-XDI experiments at ambient temperature, the aerosol method [5–7] was developed to collect diffraction patterns from biological specimens, such as viruses, cellular components, and bacterial cells, in vacuum. When hydrated small specimen particles are injected into a vacuum chamber, the specimens suffer from adiabatic expansion, the boiling of water inside the particles, and the vapor-diffusion of water from the buffer solution surrounding the particles. It is difficult to ensure that specimen particles are completely free from these phenomena under vacuum conditions.

The micro-liquid enclosure-array method utilizes microfabrication technology to product an array of small compartments on silicon [8]. Silicon frames are fabricated to have an array of small and shallow depressions with thin windows. After the depressions of one frame are filled with the specimen suspension, another frame is placed face-to-face to confine the small volumes of suspension into compartments. The pair of silicon frames is set in a diffraction apparatus, and each compartment is irradiated by XFEL pulses by scanning the frame. Immediately after a single XFEL pulse destroys the windows of each compartment, the buffer solution in the compartment boils. The size of the windows and the translational motion limit the efficient scanning by XFEL pulses provided at a repetition rate of 30 Hz.

### 4.1.3.3   Devices Required in Cryogenic Diffraction Experiments

Among the various methods, XDI experiments for frozen-hydrated biological specimens at cryogenic temperatures are likely most suitable for biological specimens. Frozen-hydrated biological specimens harvested at a desired state in the cell cycle provide the opportunity to conduct two types of XDI experiments. The first type is synchrotron XDI tomography for a frozen-hydrated single cell, which uses a diffraction apparatus equipped with a high-precision goniometer. The second type is the XFEL-XDI experiment to obtain the projection electron density maps of thousands of cells by using an apparatus equipped with a fast scan stage, which supplies fresh specimens to the irradiation area in sync with the repetition rate of the XFEL pulses. After conducting these two types of experiments, the projection maps

from the XFEL-XDI experiments are compared with the three-dimensional electron density maps from the XDI tomography experiments.

## 4.2   Diffraction Apparatus for X-Ray Diffraction Imaging Using Synchrotron X-Rays

Undulator radiation has a finite bandwidth around the wavelength of the harmonics, and contains higher order harmonics. For the use of undulator radiation in XDI experiments, monochromatic X-rays are selected using a monochrometer and a mirror (Fig. 4.3a). A monochrometer is composed of two silicon crystals in a fixed-exit geometry. The (111) plane of each crystal is used for selecting X-rays with a desired wavelength at an energy resolution $\Delta E/E$ of $10^{-4}$–$10^{-3}$ [45]. Here, the reason for the choice of X-ray wavelength used in XDI experiments should be noted. The X-ray wavelength for experiments is selected by considering the wavelength-dependent variations of the following three parameters: the scattering cross-section of specimen, the quantum efficiency of the detector, and the absorption of X-rays by specimen particles. Because the X-ray diffraction intensity is proportional to the second power of the X-ray wavelength (see Eq. (3.1) of Chap. 3), X-rays with longer wavelengths (lower energy) are advantageous for collecting diffraction patterns with better signal-to-noise ratios. In contrast, the absorption of X-rays by water, which occupies 60–70% of the volume of biological cells and organelles, becomes larger for X-rays with longer wavelengths.

Because the exclusion of higher order harmonics is difficult in a monochrometer, a pair of mirrors in a fixed-exit geometry are used to significantly reduce the harmonics by adjusting the glancing angle. The refractive index of an object without anomalous scatters against X-rays with wavelength $\lambda$ in the order of 0.1 nm is given by

$$n = 1 - \delta, \quad \delta = \frac{N_\rho\, e^2\, \lambda^2}{2\pi\, m_e c^2}$$

where $N_\rho$ is the number of electrons in the unit volume. The value of $\delta$ is very small in the order of $10^{-5}$–$10^{-6}$. Therefore, the refractive index is approximately 0.99999. When the glancing angle $\theta_g$ of the incident X-ray beam to the object is small as $2\sin^2(\theta_g/2) \leq \delta$, the total reflection of the incident X-ray occurs at the surface of the object. The critical angle $\theta_c$ for total external reflection depends on the density $\rho$ and X-ray wavelength $\lambda$ as

$$\theta_c \approx \sqrt{2\delta} \propto \lambda\sqrt{\rho}. \tag{4.2}$$

The reflectivity of the mirrors to X-rays decreases for shorter wavelengths and larger glancing angles [45] (Fig. 4.3b). After selecting X-rays with a desired wavelength, a spatially coherent X-ray beam is produced using a pinhole inserted into the path.

**Fig. 4.3 a** Schematic of the arrangement of the monochrometer, mirror, and pinhole in XDI experiments. A specimen particle is placed between a pair of slits and a beamstop. **b** The variation of the reflectivity of a silicon mirror with an assumed surface roughness in the order of 0.1 nm for X-rays with photon energies ranging from 4 to 16 keV. The reflectivity was calculated by using the website of the Lawrence-Berkley Laboratory (http://henke.lbl.gov/optical_constants/mirror2.html). Published with kind permission of Masayoshi Nakasako 2017. All Rights Reserved
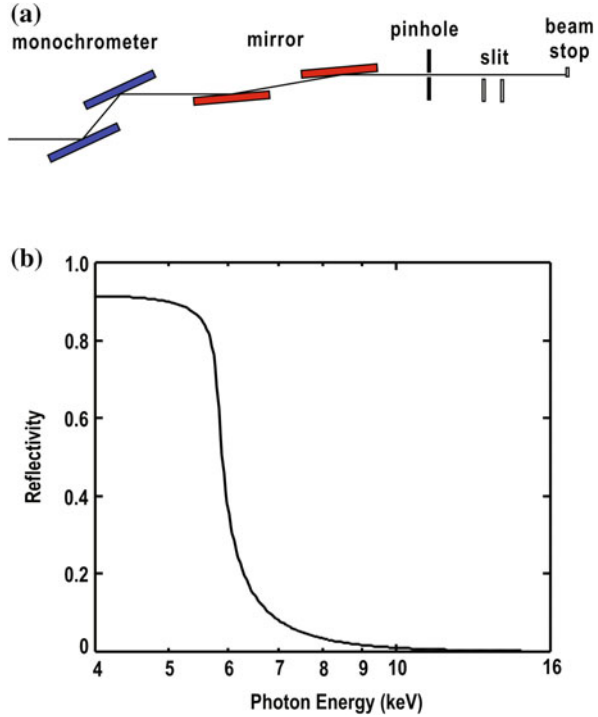


## 4.2.1 Production of Spatially Coherent X-Rays with a Pinhole

Because the electron bunches circulating in the synchrotron emit almost incoherent light, a spatially coherent X-ray beam with the wavelength $\lambda$ is produced using the diffraction pattern from a pinhole (Fig. 4.4a). When the distance $s_0$ between the pinhole (the radius $a$) and the specimen is insufficient to satisfy the Fraunhofer diffraction condition $(a^2/s_0\lambda \ll 1)$, the Fresnel-Kirchhoff integral equation [46] gives the amplitude $|E(s)|$ and the phase $\alpha(s)$ at the direction of $\boldsymbol{s} = (s_x, s_y, s_0)$

$$E(\boldsymbol{s}) = |E(\boldsymbol{s})|\exp[i\,\alpha(\boldsymbol{s})]$$
$$= -\frac{i}{2\lambda}E_{\text{in}}\int_0^a \int_0^{2\pi} \frac{\exp(iks)}{s}(1+\cos\theta)\,\eta\mathrm{d}\eta\,\mathrm{d}\varphi \tag{4.3}$$
$$s = \sqrt{s_0^2 + (\eta\,\cos\varphi - s_x)^2 + (\eta\,\sin\varphi - s_y)^2}, \quad \cos\theta = -\frac{s_0}{s}$$

where $E_{\text{in}}$ is the amplitude of the electric field of the incident beam.

**(a)** $s_{0y}$  pinhole

$s_{0x}$  $s_y$

$\eta$  $\varphi$

$s$

$a$

$s_0$

$s_x$

0

screen

normalized amplitude

phase (rad)

position (μm)

**(b)**

intensity (arbitrary unit)

10 μm

vertical position (pls)

intensity (arbitrary unit)

10 μm

vertical position (pls)

**(c)**  diffraction intensity (photons/pixel)

$10^0$        $10^2$        $10^4$

$S_y$ (μm$^{-1}$)

$S_x$ (μm$^{-1}$)

Detector pixel

Intensity (x10$^{-2}$ photons/pixel)

Intensity (x10$^{-2}$ photons/pixel)

Detector pixel
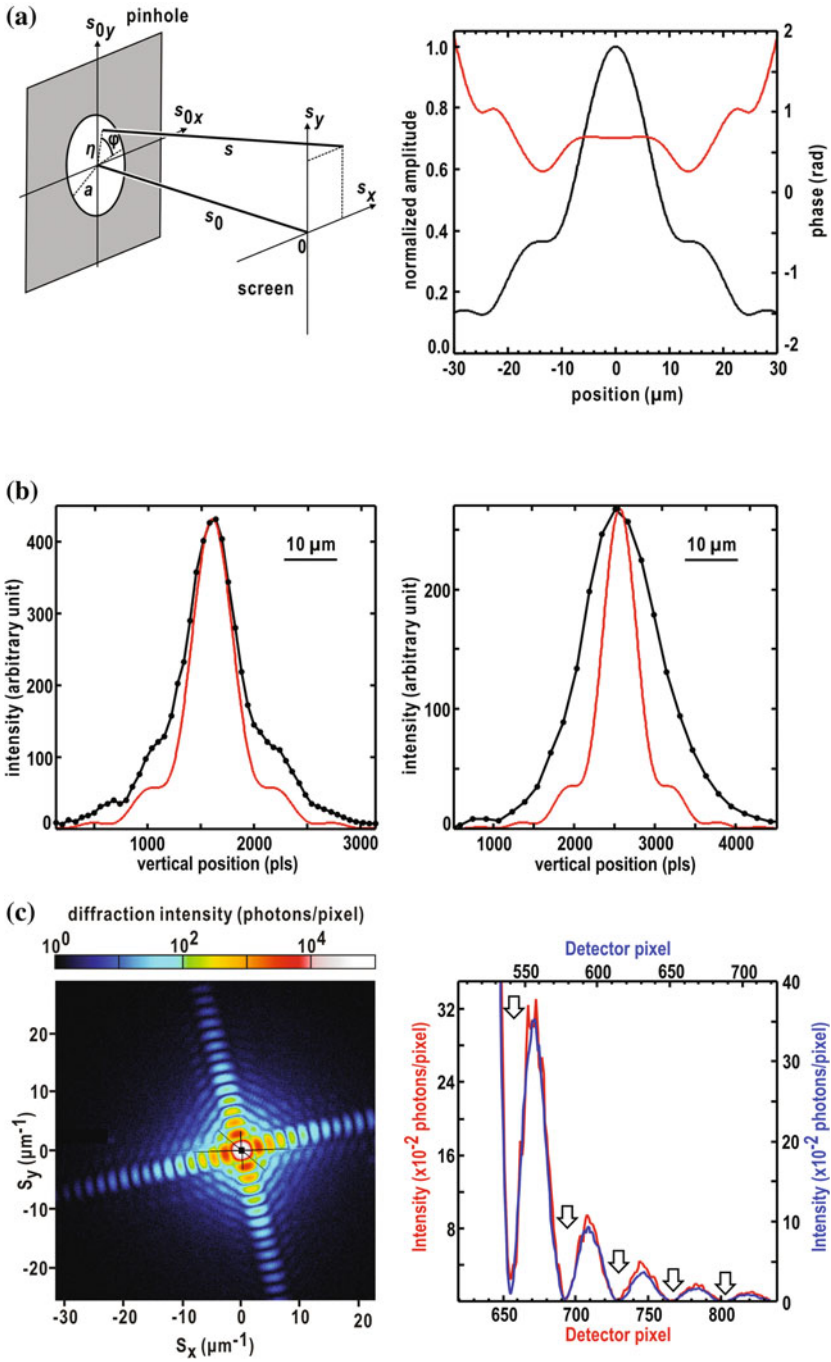
◄**Fig. 4.4  a** An example of Fresnel-Kirchhoff integration for a pinhole. The left panel is an illustration defining the parameters in (4.2). The right panel shows the variation of the amplitude (black line) and phase (red line) in a plane normal to the direction of the incident X-ray at the specimen position. The wavelength of the X-ray is 0.225 nm. The radius of the pinhole is 19 μm. The distance from the pinhole to the specimen position is 1.965 m. **b** Line profiles of an X-ray beam from a pinhole with a radius of 19 μm (black lines) are compared with theoretical values (red lines) in panel (a). The left and right panels are the profiles along the vertical and horizontal directions, respectively. The profiles were measured at the specimen position using the knife-edge scan method. X-rays with a wavelength of 0.225 nm irradiated the pinhole located 1.956-m upstream of the specimen. **c** The left panel displays a diffraction pattern from a cuboid-shaped cuprous oxide particle [47] recorded in a XDI experiment at SPring-8. The pattern is approximated by the Fraunhofer diffraction from a rectangular shaped aperture. The right panel shows line profiles along the strong interference patterns. The arrows indicate the valleys, where the diffraction intensities are almost zero. Published with kind permission of Masayoshi Nakasako 2017. All Rights Reserved

Figure 4.4a shows the variation of the diffraction intensity and phase angle within the central disk of the diffraction pattern from a pinhole with a radius of 19 μm, when the pinhole is placed at approximately 2 m upstream the specimen position. In this case, the phase angles are almost constant in the central region of the diffraction pattern. On the other hand, this result indicates that a positional shift of only 8 μm from the center causes a change in the phase angle of more than 0.01 rad. Therefore, the positional stability of the specimen is of great importance in designing a diffraction apparatus, to ensure the exposure of the specimens to spatially coherent illumination over a long period of time.

As an example, Fig. 4.4b shows the profiles of X-ray beams produced by a pinhole with a radius of 19 μm compared with those from theoretical calculations (Fig. 4.4a). The profile along the vertical direction is similar to the theoretical one with respect to the width and enhancement at around 15 μm from the beam center. In contrast, the measured profile along the horizontal direction has a width approximately 1.5 times larger than the theoretical one. The difference is mainly caused by the apparent divergence of electron bunches passing through the undulator.

According to the theoretical simulation and the measured profile, X-rays within a radius of 8 μm from the center are assumed to be nearly in the same phase. Therefore, to ensure spatially coherent illumination of the whole specimen, a specimen particle with a size less than approximately 16 μm is placed at the beam center. When this condition is satisfied, a diffraction pattern with good visibility will appear. As an example, Fig. 4.4c shows a cross-shaped diffraction pattern from a cuboid-shaped cuprous-oxide particle with an approximate edge length of 500 nm. This pattern is approximated by the Fraunhofer diffraction of a rectangular aperture. In the profiles of the diffraction intensity along the cross pattern, the valleys between the peaks are almost zero, indicating that the visibility of the pattern is almost one (see Fig. 3.2 of Chap. 3).

## 4.2.2   Diffraction Apparatus

In XDI experiments using synchrotron X-rays, specimens should be cooled to reduce radiation damage over a long exposure time. In diffraction experiments of protein crystals at cryogenic temperatures, flash-frozen crystals held in small loops are kept in a stream of cold nitrogen gas at around 100 K. When applying this method to XDI experiments, specimen particles display positional fluctuations as large as several tens of μm induced by the flow of cold nitrogen gas as mentioned in 4.1.3.1. Such positional fluctuations make it difficult to ensure the exposure of the specimen particle to the small spatially coherent area of the X-ray beam. One of the devices to suppress the positional fluctuation of specimen particles against the incident X-ray beam is a cryogenic pot mounted on a high-precision goniometer.

A diffraction apparatus named KOTOBUKI-1 is developed for the use in synchrotron XDI experiments at cryogenic temperatures (Fig. 4.5a) [47]. The apparatus is composed of three major components: a vacuum chamber equipped with a cryogenic pot connected to a goniometer (Fig. 4.5b), a set of devices to transfer frozen-hydrated specimens to the pot, and an alignment table for the chamber and the transfer device. In addition, a suite of miscellaneous devices aids in the easy transfer of frozen-hydrated specimens from a liquid nitrogen bath under atmosphere to the cryogenic pot in vacuum with minimal water/ice contamination. The following subsections briefly introduce the key devices necessary to perform cryogenic experiments. The performance of the diffraction apparatus will be described in Chaps. 8 and 9.

### 4.2.2.1   Cryogenic Pot and Goniometer

In XDI experiments using synchrotron X-rays, the positional fluctuation of the specimen is suppressed as much as possible in order to keep the position of the specimen within the area of spatially coherent irradiation (Fig. 4.3). Therefore, the popular Gifford-McMahon type of refrigerator is difficult to use because of the mechanical oscillations produced by the thermodynamic cycle.

The KOTOBUKI-1 apparatus is equipped with a cryogenic pot, an innovation from the field of low-temperature physics [48], to maintain the temperatures of specimens without positional fluctuation (Fig. 4.5). The cryogenic pot dedicated to tomography XDI experiments has a shape allowing for more than $\pm 170°$ rotation with respect to the direction of the incident X-ray. The pot is made of oxygen-free copper and coated with gold to avoid staining. The pot is machined to have a chamber with a volume of approximately 8 mL. Liquid nitrogen is supplied to the chamber from a storage dewar through a high impedance capillary made of an annealed cupronickel. The dewar with a volume of 7 L is mounted at the top of the vacuum chamber. The flow rate of liquid nitrogen depends on the inner diameter and the length of the capillary. The chamber is connected to a vacuum pump through a flexible exhaust pipe. When the pot is evacuated to a pressure of less than
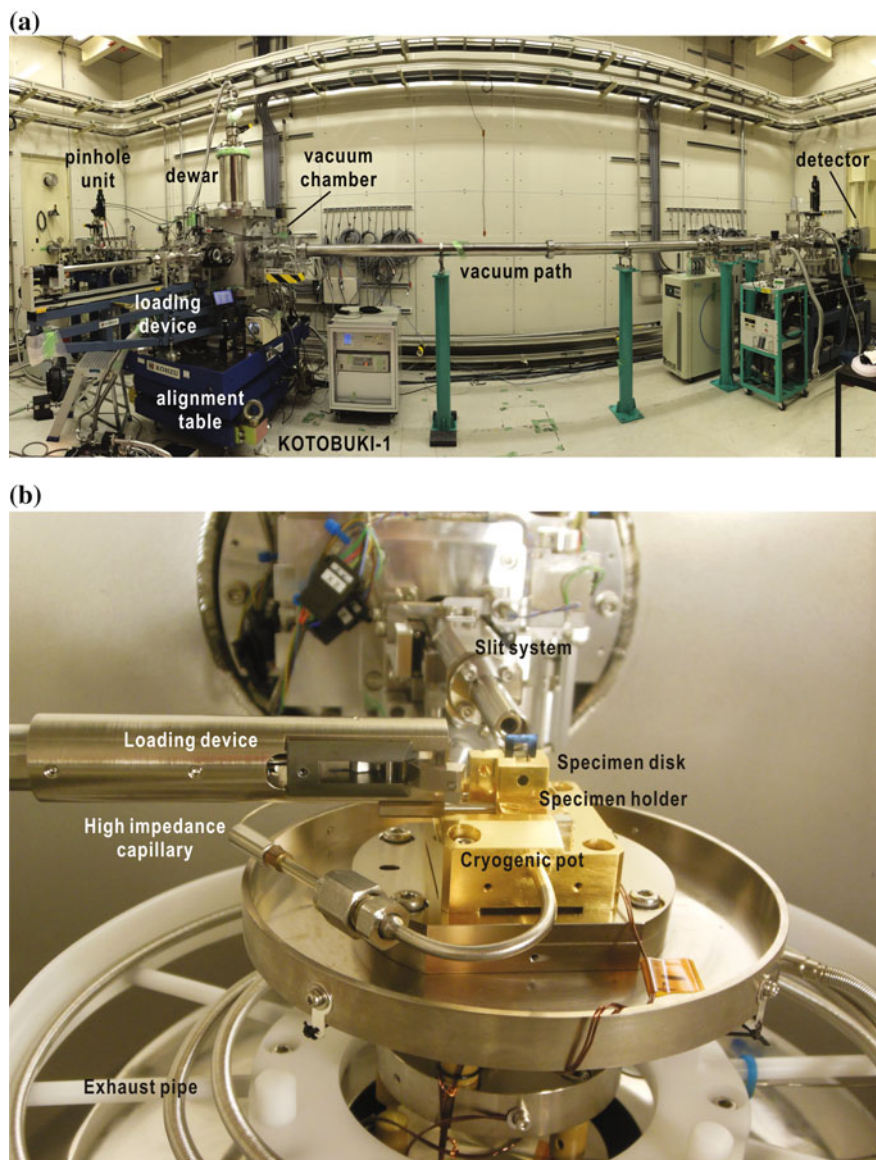
**Fig. 4.5  a** A photograph of the experimental setup of the KOTOBUKI-1 diffraction apparatus in the second experimental hutch of BL29XUL in SPring-8. The height of the apparatus, from the bottom to the top of the storage Dewar, is 2.5 m. Along the direction of the X-ray beam, the length of the alignment table is 1.1 m. A pinhole unit is located approximately 2 m upstream from the specimen position inside the apparatus in order to provide a spatially coherent X-ray beam to the specimen. An Eiger detector (DECTRIS, Switzerland) records the diffraction patterns approximately at 5 m downstream from the specimen position. **b** A photograph of the cryogenic pot used in tomography experiments. A specimen holder is delivered to the pot by the transfer device. Published with kind permission of Masayoshi Nakasako 2017. All Rights Reserved

1 Pa, the temperature of the pot subsequently reaches 66 K due to the evaporation cooling of the liquid nitrogen inside the pot. The temperature of the pot is measured by a resistance thermometer, which is fixed to its surface. The consumption of liquid nitrogen is approximately 6 L/h. Both the capillary and the exhaust pipe are circularly arranged around the rotation stage to minimize mechanical stress to the rotation. Subsequently, the cryogenic pot at 66 K can be smoothly rotated in an angular range of $\pm170°$ with respect to the direction of the incident X-ray beam. The temperature of the specimen holder placed on the pot is kept at 66–80 K through thermal contact with the pot.

Polymer rods with low thermal conduction connect the pot stage and the goniometer. The rods have a narrow waist at the middle to reduce thermal conduction from the goniometer to the pot. In fact, the temperature of the lower half of the polymer rods is above 280 K, even when the temperature of the pot is at 66 K. The rods also work as vibration isolators in addition to the flexible high-impedance capillary and the exhaust port.

The goniometer is composed of three translational stages mounted on a rotation stage. Each translational stage provides a motion of 3 mm with a resolution of 25 nm and a positional reproducibility of approximately 200 nm. The rotation stage works in the range from $-170°$ to $+170°$ with an angular resolution of 0.004°. The sphere of confusion of the rotation stage is estimated to be less than 10 μm per 360°. Therefore, in tomography experiments, the position of the specimen is adjusted to coincide with that of the incident X-ray beam after every rotation of the specimen.

The nominal positional fluctuation of the specimen on the pot filled by liquid nitrogen is smaller than 0.4 μm. The positional fluctuations of the specimens mounted on the cryogenic pot satisfy the requirement for spatially coherent irradiation.

An alignment table accurately and stably locates the rotation center of the goniometer by using two motorized vertical axes and one horizontal axis. The vertical axes located at the front and back edges of the table adjust the height of the specimen. Through independent operation of the two vertical axes, the table can be inclined in order to ensure the orthogonality of the rotation axis of the goniometer with the incident X-ray beam.

### 4.2.2.2 Devices for Delivering Specimens

To deliver fragile specimen disks from a liquid nitrogen bath to the cryogenic pot in the vacuum chamber, several devices have been designed. First, a cooled specimen disk is set on a specimen holder made of oxygen-free copper, using a workstation in a liquid nitrogen bath. Then, to ensure thermal contact, the disk is sandwiched between the wall of the holder with neodymium magnets and a small stainless block. The specimen holder is transferred from the liquid nitrogen bath to the load-lock chamber using a carrier shown in Fig. 4.6. The carrier has a hanger frame for the specimen holder and a cover for the hanger frame to shut out moist air.

Immediately after the carrier is set on the load-lock chamber, the chamber is evacuated to less than 1 Pa. Then, the cover of the carrier and the gate valves of the chamber are opened to allow access to a long transfer rod, which brings the holder to the pot within 5 s. The transfer rod has a pair of claws at the tip to catch and release the specimen holder. After mounting the holder on the pot, the transfer rod returns to its waiting position, and the gate valves are closed. When diffraction data collection is finished, the transfer rod returns the specimen holder to the frame of the carrier.

### 4.2.3 Experimental Procedures

The KOTOBUKI-1 diffraction apparatus is placed in an experimental hutch of BL29XUL [49] located approximately 70 m from the undulator light source of the beamline. At BL29XUL, a double-crystal monochrometer with fixed-exit geometry provides monochromatic X-rays with an energy resolution better than 1 eV. X-ray photons with an energy of 5.5 keV, corresponding to a wavelength of 0.225 nm, are used in most of our XDI experiments. Higher-order harmonics of the X-rays coming from the monochrometer are excluded using a pair of flat mirrors set at a glancing angle of 5 mrad in the fixed-exit geometry (Fig. 4.3a).

A pinhole with a radius of 19 μm is illuminated by an X-ray beam from the upstream optics. At approximately 1.8 m upstream from the pinhole, parasitic scattering is reduced by a slit system composed of two pairs of silicon frames with beveled edges. The frames work as guard corners to minimize the parasitic and background scattering from the upstream X-ray optics. This slit system is necessary to collect diffraction patterns in a very small-angle region. One pair is located at approximately 7 mm upstream from the specimen position; the other is placed at 200 mm upstream. Diffraction patterns are recorded by a pixel array detector (Eiger detector, DECTRIS, Switzerland) [50] placed 5 m downstream from the specimen position. The detector with a wide dynamic range is suitable for counting X-ray photons scattered by specimens.

In order to ensure spatially coherent illumination, a specimen particle is carefully placed within the central area of the diffraction peak from the pinhole by monitoring the diffraction intensity. In addition, the Friedel centrosymmetry in the diffraction patterns of the small-angle region is a good index for determining the appropriate particle position. This iterative and time-consuming procedure is necessary for the spatially coherent illumination of specimens. Prior to cryogenic XDI experiments for biological specimens, diffraction patterns from a cuboid-shaped cuprous oxide particle with a sub-micrometer size [51] are collected to examine whether specimens are within the spatially coherent illumination (Fig. 4.4b). Under the appropriate alignment of the pinhole and slits, the speckle peaks should be visible beyond a resolution of 60 nm with very weak intensities in the valleys between peaks, indicating a good visibility attained by the spatially coherent illumination.
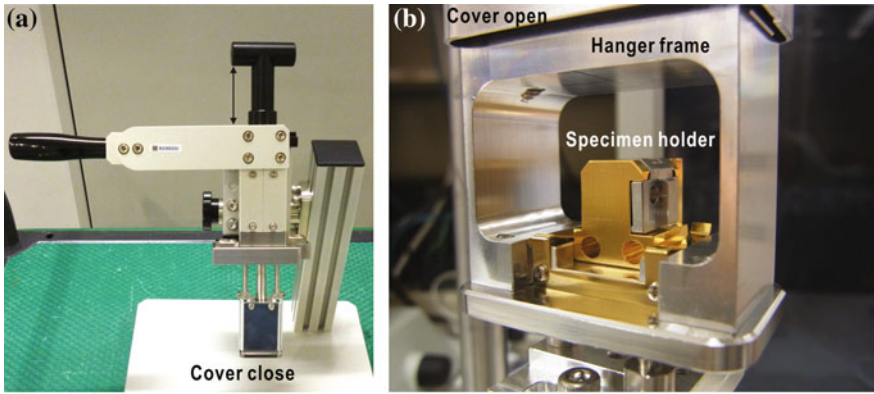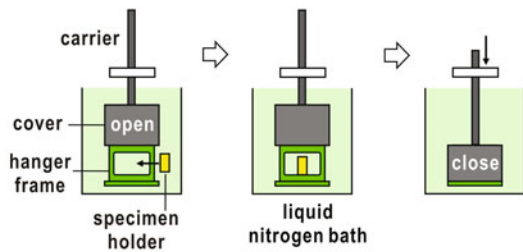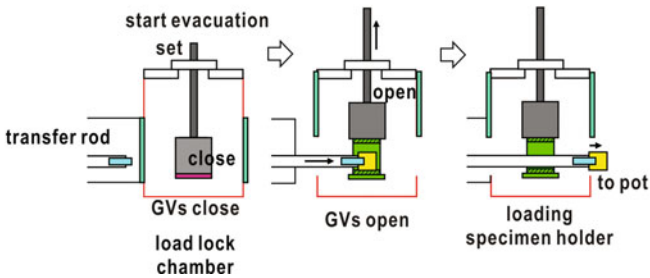
Fig. 4.6 **a** A photograph of a carrier to deliver the cooled specimen holder from a liquid nitrogen bath to the load lock chamber of the diffraction apparatus. **b** A magnified view of the hanger frame of the carrier with a specimen holder. Published with kind permission of Masayoshi Nakasako 2017. All Rights Reserved. **c** A schematic showing how the carrier works in delivering the specimen holder from the liquid-nitrogen bath to the vacuum chamber of the diffraction apparatus. (upper panel) Both the hanger frame and cover are cooled in liquid nitrogen. After setting the specimen holder onto the hanger frame, the cover is closed to shut out moist air. (right panel) When placing the device in the load-lock chamber, the transfer rod catches and moves the holder to the cryogenic pot on the goniometer stage. Panel (**a**) is reused from reference [16] with permission from IOP publishing. Panel (**c**) is reused from reference [47] with permission from AIP publishing

A set of motorized devices in the KOTOBUKI-1 diffractometer are controlled by the IDATEN program suite coded using the LabVIEW language (National Instruments, USA) through the GPIB or RS-232C interface [52]. The suite consists of four sub-programs working independently. The first subprogram drives the stepping motors of the alignment table, the slits, the goniometer, and the two telescopes used to monitor the position of specimen disk on the pot. The subprogram operates the automatic movement of the pot between the positions for receiving the specimen holder and for X-ray exposure. The second subprogram is operated using a specially designed touch panel to automatically load the specimen holder from the load-lock chamber to the cryogenic pot. The third subprogram is used to adjust the position of the specimen holder by touching the images displayed on a monitor. For diffraction data collection, the fourth subprogram controls the goniometer and sends start/stop commands through a server to the detector for data acquisition.

## 4.3   Diffraction Apparatus for X-Ray Diffraction Experiments Using X-Ray Free Electron Laser Pulses

### 4.3.1   Outline

Brilliant X-ray pulses with duration of several tens of femtoseconds have been available at SACLA [53] since 2012. The SACLA accelerator provides XFEL pulses at a repetition rate of 30 Hz. Therefore, it is now possible to collect a large number of diffraction patterns within a short period of time. In XFEL experiments, diffraction from a specimen occurs before a single X-ray pulse destroys the specimen particle at the atomic level, due to the short duration of the XFEL pulses in the range of approximately several tens of femtoseconds [53]. The structures of the specimens are then visualized without radiation damage, as demonstrated by X-ray crystal structural analyses [44]. To collect diffraction patterns pulse by pulse, it is necessary to supply fresh specimen particles into the irradiation areas.

For instance, at BL3 of SACLA [54], XFEL pulses produced by a SASE process are quasi-monochromatic X-rays with a small but finite bandwidth. A monochrometer in a fixed exit geometry is used to select the X-ray beam with a desired wavelength with an energy resolution $\Delta E/E$ of $10^{-4}$. In addition, undulator radiation occurring prior to the SASE process enters into the beamline. Higher order harmonics passing through the monochrometer are reduced by using a pair of X-ray mirrors, as in synchrotron XDI experiments. Monochromatized XFEL pulses are focused to provide an intensity of $10^{10}$–$10^{11}$ photons per $2 \times 2$ μm$^2$ (FWHM) per 10 fs pulse [55] at approximately 1.5 m downstream from the middle of the mirror unit. The intensity of the focused XFEL pulse is sufficient to destroy the specimen particles at the atomic level.

For XFEL-XDI experiments, we modified the protocol and experimental procedures developed for cryogenic XDI experiments using synchrotron X-rays to follow the repetition rate of the XFEL pulses. We perform the structural analysis of frozen-hydrated biological specimens with dimensions smaller than the cross sections of focused XFEL. To follow the repetition rate of the XFEL pulses, a thin membrane is scanned, on which the specimen particles are dispersed. However, due to the tail regions of the focused X-ray pulses, specimen particles located within 10 μm of the beam center are degraded. Therefore, it is necessary to scan the membranes at a speed higher than 20 μm per pulse, in order to supply fresh specimen particles into the irradiation area at the repetition rate of the XFEL pulses.

A diffraction apparatus named TAKASAGO-6 [56] was developed to collect single shot diffraction patterns from frozen-hydrated biological specimens with XFEL pulses provided at a repetition rate of 30 Hz (Fig. 4.7). The apparatus is equipped with a high-speed translation stage with a cryogenic pot for raster-scanning at a maximum speed of 50 μm/33 ms. In addition, the performance in diffraction experiments is supported by several devices for assisting the transfer of cooled specimens from a liquid nitrogen bath to the cryogenic pot in the vacuum chamber of the diffraction apparatus. In the current experimental procedure, the apparatus enables us to use approximately 310,000 XFEL pulses within 1 h. The following subsections briefly introduce some of the key devices of the apparatus.

### 4.3.2   Devices Used in the Diffraction Apparatus

#### 4.3.2.1   Cryogenic Pots and High-Speed Translation Stage

To reduce the number of times to exchange specimen holders must be exchanged, the TAKASAGO-6 apparatus uses a cassette container carrying 12 specimen holders at once. Because the cassette container is kept near liquid nitrogen temperatures, the apparatus is equipped with two cryogenic pots (designated as pot A and pot B) made of oxygen-free copper with gold coating (Figs. 4.8 and 4.9). Pot A maintains the temperature of the cassette container, and is fixed to translation stage A via a thick plate of epoxy glass for the prevention of heat conduction. Pot B, which is mounted on the high-speed translation stage by four rods of epoxy glass, maintains the temperature of the mounted specimen holder during diffraction data collection.

Each pot has a chamber of more than 7 mL to store liquid nitrogen, supplied by a dewar mounted on the vacuum chamber through a flow-impedance capillary made of annealed cupronickel. A scroll pump evacuates the chambers of the pots to $10^{-1}$ Pa through the exhaust pipes connected to their outlet ports. The temperatures of the pots are maintained at 66 K by the evaporation cooling effect of liquid nitrogen. The temperatures of the cassette container and mounted specimen disks are kept below 90 K through thermal contact with the pots. The liquid nitrogen is consumed
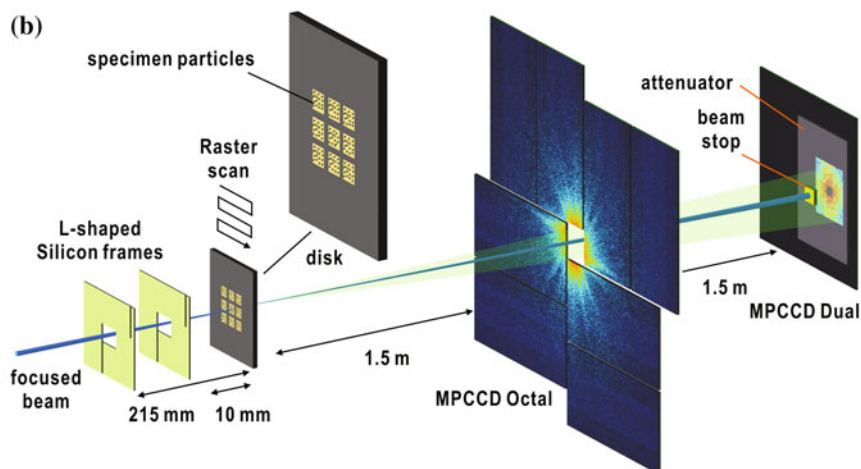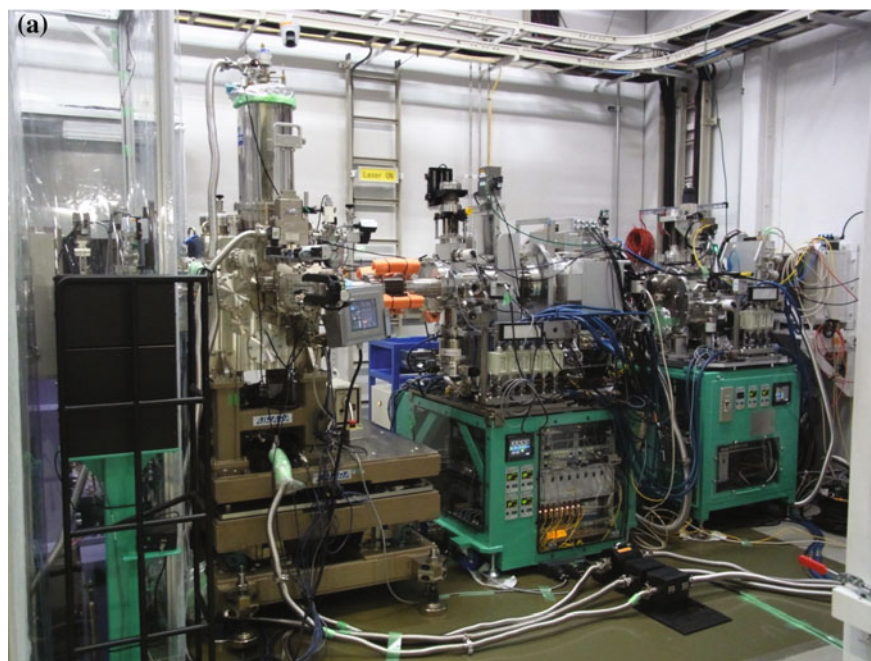
**Fig. 4.7 a** A photograph of the TAKASAGO-6 diffraction apparatus [56] installed together with two MPCCD detectors [57] at experimental hutch 4 of beamline 3 [54] in SACLA. **b** A schematic of the arrangement of the devices used in XFEL-XDI experiments. A pair of slits near the focal spot reduces parasitic and background scattering coming from the upstream optics. Because XFEL pulses destroy specimens at an atomic level, the specimen disk is raster-scanned according to the 30 Hz repetition rate of XFEL pulses. Panels are reused with modification from reference [56] with permission from AIP publishing
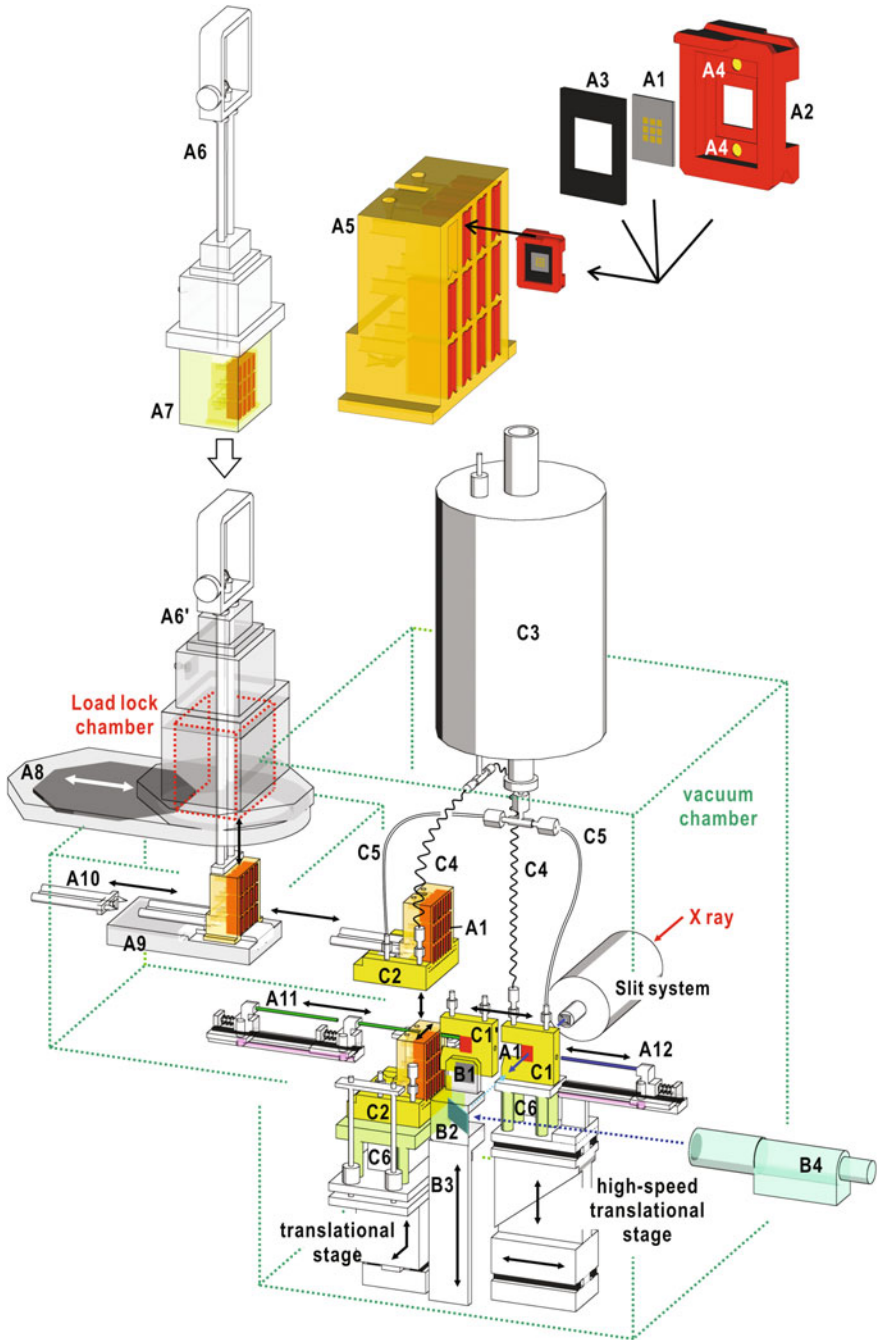
◄**Fig. 4.8** An illustration showing the arrangement of devices inside the vacuum chamber of the TAKASAGO-6 diffraction apparatus. The devices used in delivering a specimen disk (labeled as A1) are the specimen holder (A2), frame for holding the disk (A3), neodymium magnets (A4), cassette container (A5), carrier (A6), cover for the carrier (A7), gate valve (A8–A10), translational stage to move the cassette container, transfer rod used to mount the specimen holder (A11), and a second transfer rod used to dismount the specimen holder from the pot to (A12). The devices for maintaining the temperature of the mounted specimen holder are cryogenic pot A (C2), pot B (C1), the dewar (C3), high-impedance capillaries (C4), exhaust pipes (C5), and epoxy-glass rods (C6). The position of the specimen disk on pot B (C1) is adjusted using a PIN photodiode (B1) and a Mirror (B2) mounted on a vertical translational stage (B3), and a telescope outside the vacuum chamber. This figure is reused with modification from reference [56] with permission from AIP publishing
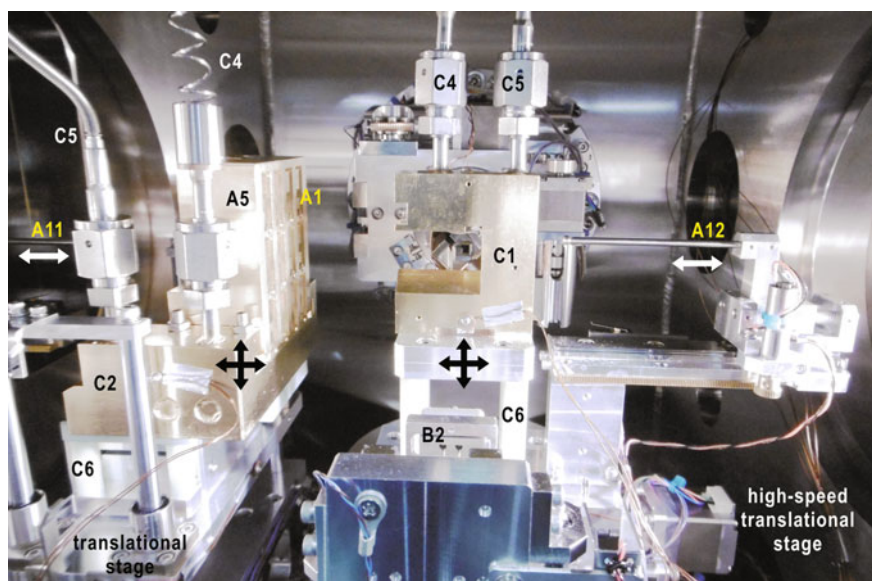


**Fig. 4.9** A photograph showing the arrangement of the devices around cryogenic pot B. The labels are the same as those in Fig. 4.8. This photograph is reused with modification from reference [56] with permission from AIP publishing

at approximately 0.45 L/h. The temperatures of the pots are measured by thermocouples fixed to the surfaces of the pots.

In a raster scan of a specimen disk mounted on pot B, a series of stop-and-go motions are carried out in sync with the repetition of the XFEL pulses (Fig. 4.8). A high-speed translation stage can shift specimen disks with a maximum speed of 50 μm per 33 ms in the plane normal to the direction of the incident XFEL pulses. The stroke of the motion is more than 30 mm with a positional resolution of 0.2 μm. A flat-top wedge stage generates the vertical translation of 10 mm with a positional resolution of 0.27 μm.

As well as the KOTOBUKI-1 diffraction apparatus, an alignment table mounting the vacuum chamber adjusts the center of the specimen disk on the high-speed translation stage into the focal spot of the XFEL pulses. Two motorized vertical translation axes can move the chamber by more than 40 mm with a resolution of 0.3 μm. The horizontal motion of the chamber normal to the X-ray beam is driven by a horizontal translation axis with a stroke of more than 40 mm and a resolution of 1 μm. A rotation axis, which provides a rotation of more than 4° with a resolution of 0.0001°, tunes the orthogonality between the X-ray beam and the horizontal axis of the high-speed translation stage.

### 4.3.2.2    Devices for Delivering Frozen-Hydrated Specimens

Specimen particles dispersed onto the membrane windows of the specimen disks are flash-cooled using liquid ethane as described in Chap. 5. Flash-cooled disks are fixed to a custom-made specimen holder with two neodymium magnets by a stainless-steel frame (Fig. 4.8). To deliver frozen-hydrated specimens from the nitrogen bath to pot B inside the vacuum chamber of the diffraction apparatus, we use a cassette container and a carrier to prevent specimens from frosting and warming (Fig. 4.8). The cassette container has slots for carrying 12 specimen holders at once to reduce the number of specimen exchanges. The carrier lifts the cassette container from the liquid-nitrogen bath into its cover, which shuts out moist air.

Immediately after setting the carrier on the load-lock chamber, the interior of the chamber is evacuated. The cassette container is moved to the transfer stage in the load-lock chamber after opening the gate valve. Next, a transfer rod brings the cassette container to pot A on translation stage A.

For mounting the specimen holder onto pot B from the container, translation stages A and B move to adjust both sliding rails of a slot of a container and pot B. Transfer rod A, located behind the cassette container, pushes the specimen holder in the slot to pot B. Translation stage B moves to the position for raster scans. After the completion of the raster scans, translation stage B carries pot B to the container. Then, transfer rod B, located behind pot B, pushes the holder into the slot of the container. These procedures are iterated until all the windows of the 12 disks are raster-scanned.

A PIN photodiode mounted on a vertical translation stage measures the intensity of the attenuated XFEL pulses during the positional adjustment of the high-speed translation stage by knife-edge scans of thin wires set on pot B. A mirror on the vertical translation stage is used to observe each specimen window from a telescope located outside the vacuum chamber. The telescope provides images with a resolution better than 7 μm.

### 4.3.2.3   Control

The TAKASAGO-6 diffraction apparatus is controlled by a program suite named *SENJU*, written in the LabVIEW language [56]. The suite is composed of four subprograms. One subprogram controls the alignment table, the slit system, the vertical translation stage mounting the PIN photodiode and the mirror, and the magnification of the telescope. The other three subprograms control the motions of the translation stages by operating two programmable logic controllers (PLCs). The two PLCs have their own central processing units, which execute programs written in the ladder language for the direct operation of the motorized stages. One PLC controls the delivery of specimen disks from the load-lock chamber to pot B. The other PLC controls a series of stop-and-go motions of the high-speed translation stage in the raster scans. When each stop-and-go motion is controlled step-by-step by PC, PC-driver communication limits the speed of the raster scans. This is why the PLC directly operates the high-speed translation stage.

For each raster scan, a user defines a set of scan steps and area by inspecting the telescope view of a membrane window in the specimen disk mounted on pot B. Then, the subprogram generates a set of coordinates for the scan, and transfers the set to the PLC for raster scan. A raster scan starts in sync with the event trigger signals provided by the linear accelerator. Raster scans of the specimen disks are then possible at a speed of 25–50 μm/33 ms and a positional accuracy better than a few μm (Fig. 4.10).

## 4.3.3   Experimental Procedures

### 4.3.3.1   Reduction of Parasitic Scattering from Upstream Optics

Cryogenic XFEL-XDI experiments are carried out at experimental hutch 4 of BL3 in SACLA. The X-ray wavelength is chosen by considering the wavelength dependence of the scattering cross-section of the specimen, the quantum efficiency of the detector used, and the absorption of X-rays by specimen particles as well as synchrotron XDI experiments (see 4.2).

Kirkpatrick-Beatze type mirror optics focus the X-rays with a wavelength of 0.225 nm (5.5 keV) to provide an intensity of $10^{10}$–$10^{11}$ photons per $2 \times 2$ μm$^2$ full width half maximum (FWHM) per 10 fs pulse [55]. The TAKASAGO-6 apparatus is placed such that the specimen is within the focal spot of the X-rays, which has a depth of approximately 10 mm along the direction of the incident X-rays. A Foucault knife-edge test with a thin gold wire on the specimen holder allows us to examine whether the focal spot overlaps with the specimen position. Then, the position of the focal spot along the direction of the incident X-rays is finely tuned by adjusting the glancing angles of the focusing mirrors through monitoring the horizontal and vertical profiles of the focused X-ray pulses measured by the knife-edge scan of the thin tungsten wire (Fig. 4.11a).
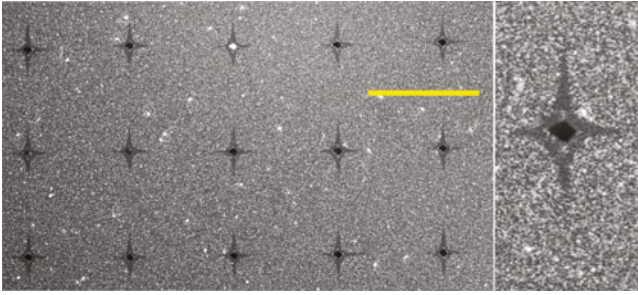
**Fig. 4.10** SEM images of a SiN membrane adsorbing gold colloidal particles with diameters of 50 nm (small white dots) after a raster scan at a speed of 50 μm per 33 ms. The scale bar is 50 μm. The right panel is a magnified view of an area irradiated by a single XFEL pulse. The center area of the cross-shape is destroyed at the atomic level. In the cross-shape, gold colloidal particles are probably dissociated from the membrane surface due to the repulsion between the membrane and the particles charged by the tail region of the focused XFEL pulse. Published with kind permission of Masayoshi Nakasako 2017. All Rights Reserved

The positions and the profiles of the focused X-ray pulses are sensitive to small deformations in the mirror housing caused by the variation in temperature inside the experimental hutch. Temperature fluctuations inside the experimental hutch were maintained at less than 0.1 K by removing heat sources from the experimental hutch. Subsequently, the reduced variation in temperature dramatically improved the positional fluctuation of the focused XFEL pulses to within 0.4 μm and reduced the time-dependent deformation of the profiles.

The TAKASAGO-6 apparatus has a slit system composed of two pairs of L-shaped silicon frames with a thickness of 500 μm (Fig. 4.11b). Each silicon frame has a low scattering power, but absorbs X-rays with a wavelength of 0.225 nm. The beveled edges with an angle of approximately 35° work as guards to eliminate parasitic and background scattering from the X-ray optics upstream. In each pair, two silicon frames are placed orthogonally. One pair is located within the focus depth along the direction of the incident X-rays, and the other is placed 215 mm upstream from the specimen position. When the edges of the frames were set at 200–300 μm away from the X-ray path, the parasitic scattering from the upstream optics can be reduced to 100 photons per detector pixel around the beamstop (Fig. 4.11c). This intensity is negligibly small in comparison with that in the small-angle diffraction from specimen particles, which exceeds sometimes $10^4$ photons per pixel.

#### 4.3.3.2  Multi-port CCD Detector

Diffraction patterns are recorded by two multi-port charge coupled device (MPCCD) detectors composed of sensor panels with $512 \times 1024$ pixels of
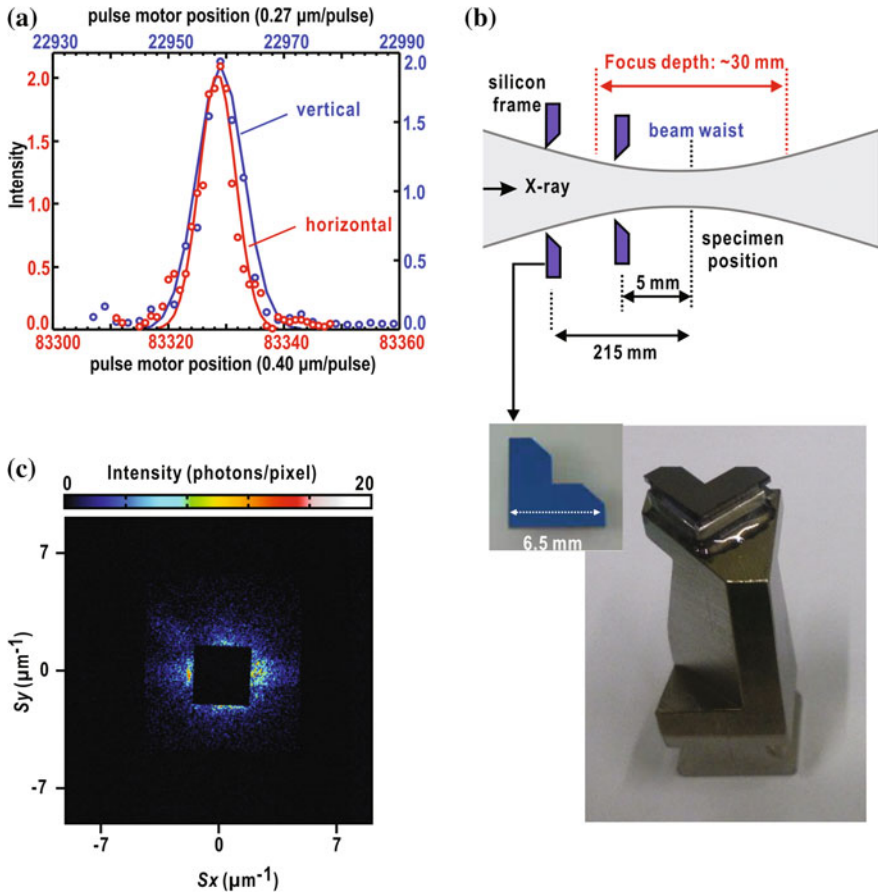
**Fig. 4.11 a** Horizontal (red circles) and vertical (blue circles) intensity profiles of two-dimensionally focused and attenuated XFEL pulses measured by knife-edge scans using a tungsten wire with diameters of 50 μm mounted on pot B filled by liquid nitrogen. The solid curves are Gaussians approximating the profiles. Tungsten wires glued to a sample holder were scanned at a step of 0.4 μm against the XFEL pulses with a repetition rate of 30 Hz. **b** A schematic illustration showing the positions of the L-shaped silicon frames near the beam center along the direction of the incident X-rays. The lower panel shows views of silicon frames glued on a block to be mounted on the slit system. A part of panel (**b**) is reused with modification from reference [56] with permission from AIP publishing. **c** Patterns of parasitic scattering in the small diffraction angle region around the beamstop after the adjustment of the positions of the L-shaped silicon frames. Panels (**a**) and (**c**) are published with kind permission of Masayoshi Nakasako 2017. All Rights Reserved

$50 \times 50 \ \mu m^2$ [57]. One detector composed of eight CCD sensors (MPCCD-Octal) (Fig. 4.12) is placed approximately 1.5 m downstream from the specimen position to record diffraction patterns in the resolution range of approximately 6–190 nm. The synchronous sliding movements of the four panels composed of two CCD

sensors change the central aperture from 3.5 to 8.0 mm. The other detector composed of two CCD sensors (MPCCD-Dual) is placed approximately 3.0 m downstream from the specimen to record the diffraction patterns in the resolution range from 150–500 nm. A beamstop with dimensions of $2.5 \times 2.5$ mm$^2$ is placed in the path to absorb the direct beam. A set of eight aluminum attenuators with thicknesses from 15–100 μm are inserted between the beamstop and the MPCCD-Dual detector.

The X-ray intensity is read out from the analog-to-digital unit, $C_{ADU}$, by the MPCCD detectors. For data processing, the $C_{ADU}$ count is converted to the number of X-ray photons, $N_{ph}$, using the following equation

$$N_{ph} = \frac{C_{ADU} \cdot G_{sys}}{E_{ph}/E_0}, \tag{4.4}$$

where $G_{sys}$ is a system gain with a typical value of 18 e$^-$/count, $E_{ph}$ is the energy of the X-ray photon, and $E_0$ is the energy necessary to create an electron-hole pair in silicon (3.65 eV/e$^-$).
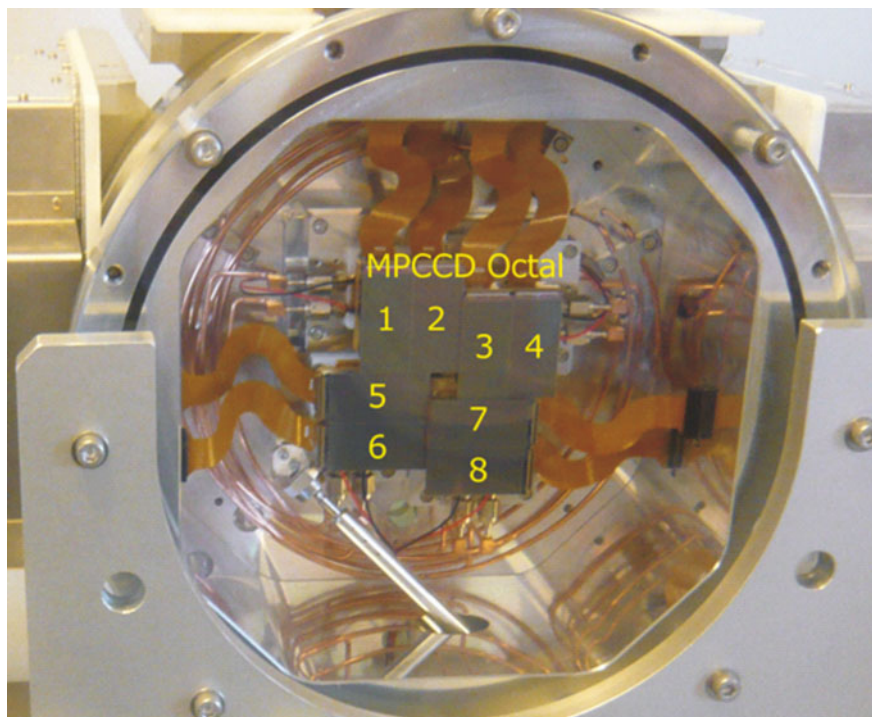


**Fig. 4.12** A photograph of an MPCCD Octal detector with eight CCD panels [57]. The photograph is supplied by courtesy of Dr. Takashi Kameshima. Published with kind permission of Masayoshi Nakasako 2017. All Rights Reserved

The saturation limit of each CCD panel is approximately $2.5 \times 10^3$ X-ray photons with an energy of 5.5 keV per pixel ($50 \times 50$ μm$^2$). When speckle patterns appear with resolutions higher than 30 nm, the total intensity in the small-angle regions frequently exceeds $10^7$–$10^8$ photons per pixel. Even when inserting an aluminum attenuator of an appropriate thickness in front of the MPCCD Dual detector, many detector pixels are saturated. Diffraction patterns in the small-angle region contain structural information regarding the sizes and overall shapes of the specimen particles. The lack of small-angle diffraction patterns is one of the factors preventing the success of PR of the projection maps of specimen particles. Therefore, the dynamic range of the MPCCD-Dual detector prevents the collection of high-quality diffraction patterns.

### 4.3.3.3 Spatial Coherence of Focused X-Ray Pulses

Prior to diffraction data collection for biological specimens, the spatial coherence of the XFEL pulses is estimated by applying visibility speckle spectroscopy [58, 59] to the diffraction patterns. The speckle contrast is defined as

$$C = \frac{\langle I^2 \rangle_T - \langle I \rangle_T^2}{\langle I \rangle_T^2}, \tag{4.5}$$

where $\langle I \rangle_T$ is the averaged diffraction intensity in a specified period of time in a region of interest.

The speckle contrast of each XFEL pulse can be measured from diffraction patterns obtained by scanning a silicon nitride membrane with uniformly dispersed gold colloidal particles (Fig. 4.13a) [60]. When XFEL pulses are ideally focused, the values of the speckle contrast are more than 0.99 (Fig. 4.13b). Then, the diffraction patterns show clear contrast between the peaks and valleys, as demonstrated in the diffraction pattern from a cuboid-shaped cuprous oxide particle. In contrast, when mirrors are out of the ideal tuning range, the speckle contrast is in the range from 0.75 to 0.80. Therefore, the spatial coherence of focused XFEL pulse is measured frequently during experiments to examine whether the spatial coherence of the focused XFEL pulses is maintained for a long time, particularly when the mirror unit is sensitive to the temperature variation inside the experimental hutch.

Before starting diffraction data collection from the biological specimens, the diffraction patterns of cuboid-shaped cuprous oxide particles are recorded to check the coherence of the focused X-ray pulses (Fig. 4.13b). The line profile with valleys dropping almost to zero intensity at a high diffraction angle is a good measure to examine coherent illumination.

#### 4.3.3.4 Performance of the Diffraction Apparatus

Figure 4.14 shows the cumulative number of XFEL pulses used for diffraction data collection over 3.5 days of beam-time in February 2016. To examine the quality of the spatial coherence, every day the profiles of the XFEL pulses were measured by
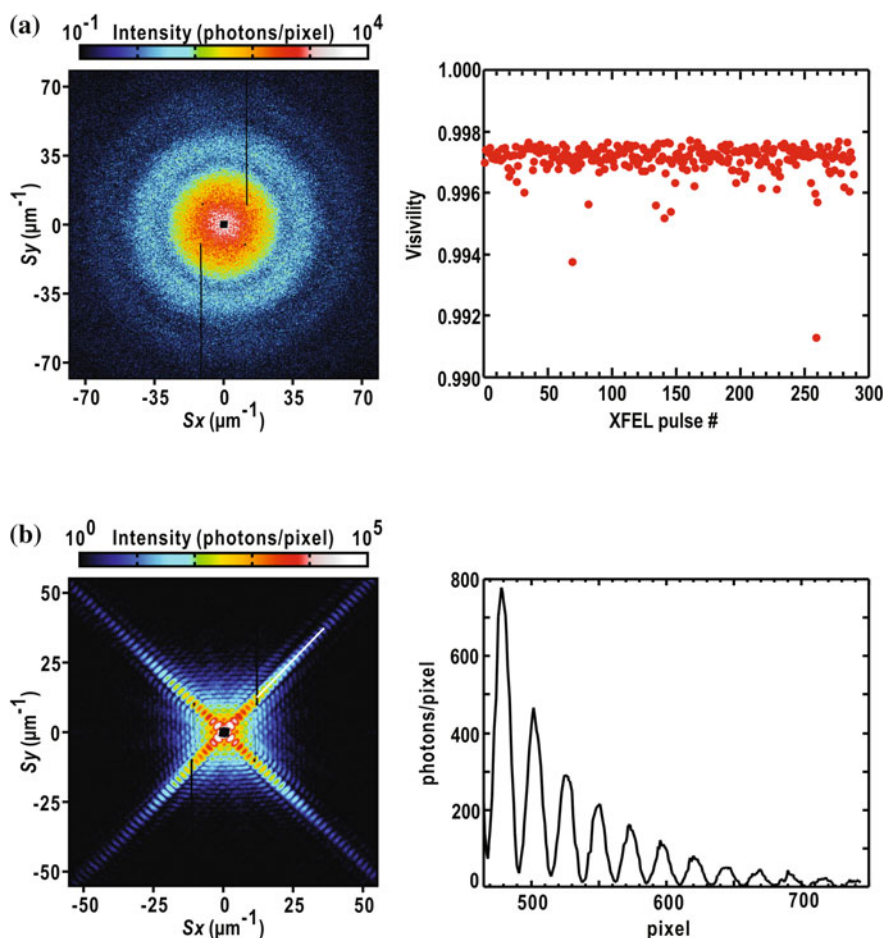


**Fig. 4.13  a** The left panel shows a single-shot diffraction pattern from densely dispersed gold colloidal particles with diameters of 20 nm. The right panel shows a shot-by-shot variation of the visibility of the XFEL pulses. The visibility is calculated as the square root of the speckle contrast [60]. **b** The diffraction pattern from a cuboid-shaped cuprous oxide particle. In the line profile along the crossed pattern (right panel), the intensities in the valleys are close to zero because of the almost complete spatial coherence of the focused XFEL pulse. Published with kind permission of Masayoshi Nakasako 2017. All Rights Reserved
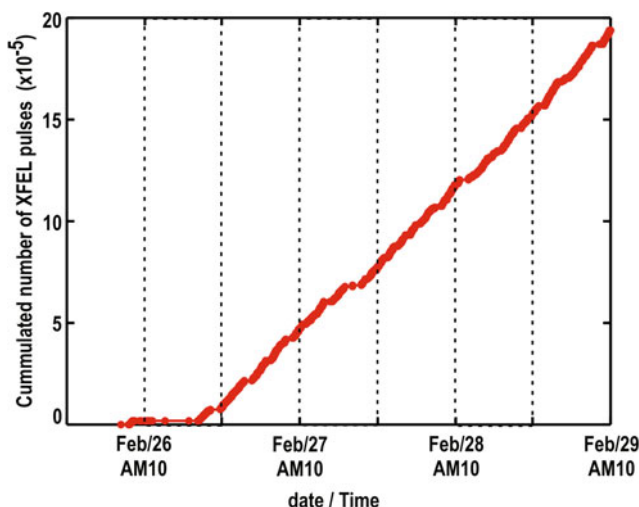
**Fig. 4.14** The cumulative number of XFEL pulses used over the beam-time in February 2016. The cryogenic XFEL-XDI experiment started in the evening of the 26th. The number of XFEL pulses used per hour was approximately 31,000. The total number of XFEL pulses used in the experiment was 1,938,225. This corresponds to approximately 30% of the total number of XFEL pulses provided by the SACLA accelerator within 60 h. Published with kind permission of Masayoshi Nakasako 2017. All Rights Reserved

a knife-edge scan (Fig. 4.11a). After the measurements of the profiles, the diffraction patterns from densely dispersed gold colloidal particles were measured to evaluate the spatial coherence and the shape of the focused XFEL pulses (see Fig. 4.11a). In addition, to maintain the temperature of the cryogenic pots, approximately 6 L of liquid nitrogen was supplied to the dewar every 6 h.

Subsequently, diffraction data collection took 60 h, including the time necessary for the exchange of specimen holders inside the vacuum chamber and the cassette container from a liquid nitrogen bath to the vacuum chamber. Of the XFEL pulses supplied at a repetition rate of 30 Hz, approximately 2,000,000 pulses were used for diffraction data collection (Fig. 4.14). Immediately after the completion of each raster scan, the diffraction patterns were processed by an automated data processing software suite, the details of which will be described in Chap. 6. The number of diffraction patterns tentatively worth analyzing by PR calculations were 354,588.

# References

1. H. Jiang et al., Proc. Natl. Acad. Sci. U.S.A. **107**, 11234 (2010)
2. Y. Nishino et al., Phys. Rev. Lett. **102**, 018101 (2009)
3. C. Song et al., Biophys. J. **107**, 1074 (2014)

4. S. Kassemeyer, *Ultrafast coherent diffractive imaging of nanoparticles using X-ray free-electron laser radiation* (Doctoral dissertation, Fachbereich Physik der Freien Universität Berlin) (2014)
5. M.M. Seibert et al., Nature **470**, 78 (2011)
6. T. Kimura et al., Nat. Commun. **5**, 3052 (2014)
7. T. Ekeberg et al., Phys. Rev. Lett. **114**, 09810 (2015)
8. G. van der Schot et al., Nat. Commun. **6**, 5704 (2015)
9. M.F. Hantke et al., Nat. Photon. **8**, 943 (2014)
10. D. Shapiro et al., Proc. Natl. Acad. Sci. U.S.A . **102**, 15343 (2005)
11. X. Huang et al., Phys. Rev. Lett. **103**, 198101 (2009)
12. E. Lima et al., Phys. Rev. Lett. **103**, 198102 (2009)
13. E. Lima et al., J. Microscopy **249**, 1 (2013)
14. Y. Takayama, M. Nakasako, Rev. Sci. Instrum **83**, 054301 (2012)
15. Y. Takayama et al., Plant Cell Physiol. **56**, 1272 (2015)
16. T. Oroguchi et al., J. Phys. B: At. Mol. Opt. Phys. **48**, 184003 (2015)
17. H. Kameda et al., J. Biochem. (Tokyo) **161**, 55 (2017)
18. J. Miao et al., Proc. Natl. Acad. Sci. U.S.A. **100**, 110 (2003)
19. C. Song et al., Phys. Rev. Lett. **101**, 158101 (2008)
20. D. Nam et al., Phys. Rev. Lett. **110**, 098103 (2013)
21. M. Nakasako, Philos. Trans. R. Soc. London, Ser. B **359**, 1191 (2004)
22. E. O'Toole, G. Wray, J. Kremer, and J. R. McIntosh, J. Struct. Biol. **110**, 55 (1993)
23. S. B. Hayward, R. M. Glaeser, *Ultramicroscopy* **4**, 201 (1979)
24. A.W. Robards, U.B. Sleytr, *Low Temperature Methods in Biological Electron Microscopy* (Elsevier, Amsterdam, 1991)
25. J. Dubochet et al., Quart. Rev. Biophys. **21**, 129 (1988)
26. R.A. Grassucci, D. J. Taylor, J. Frank, Nat. Protoc. **2**, 3239 (2007)
27. M. Nakasako, J. Mol. Biol. **289**, 547–564 (1999)
28. C. Chen, Lancet **1**, 884 (1986)
29. O. Schwartz, Int. J. Oral Maxillofac. Surg. **15**, 30 (1986)
30. C.M.O. Medeiros, F. Forell, A.T.D. Oliveira, J.L. Rodrigues, Theriogenology **57**, 327 (2002)
31. L.F. Gibson, J.T. Khoury, Let. Appl. Microbiol. **3**, 127 (1986)
32. M.R. Howells et al., J. Electron Spectrosc. Relat. Phenom. **170**, 4 (2009)
33. M. Nakasako, M. Yamamoto, BUTSURI **70**, 702 (2015)
34. R.B.G. Ravelli, E.F. Garman, Curr. Opin. Struct. Biol. **16**, 624 (2006)
35. M. Adrian, J. Dubochet, J. Lepault, A.W. McDowall, Nature **308**, 32 (1984)
36. R. Henderson, Quart. Rev. Biophys. **28**, 171 (1995)
37. B. Ziaja et al., New J. Phys. **14**, 115015 (2012)
38. J. Maser et al., J. Microscopy **197**, 68 (2000)
39. T. Beetz et al., Nucl. Instrum. Methods Phys. Res., Sect. A **545**, 459 (2005)
40. J.A. Rodriguez et al., IUCrJ **2**, 575 (2015)
41. T.-Y. Teng, J. Appl. Cryst. **23**, 387 (1990)
42. R. Neutz, et al., Nature **406**, 752 (2000)
43. H.N. Chapman et al., Nat. Phys. **2**, 839 (2006)
44. K. Hirata et al., Nat. Methods **11**, 734 (2014)
45. J. Als-Nielsen, D. McMorrow, *Elements of Modern X-ray Physics* (Wiley, New York, 2011)
46. M. Born, E. Wolf, *Principles of Optics* (Cambridge University Press, Cambridge, 1999)
47. M. Nakasako et al., Rev. Sci. Instrum. **84**, 093705 (2013)
48. L.E. Delong, O.G. Symko, J.C. Wheatley, Rev. Sci. Instrum. **42**, 147 (1971)
49. K. Tamasaku et al., Nucl. Instrum. Meth. A **467–468**, 686 (2001)
50. A. Casanas et al., Acta Crystallogra. D**72**, 1036 (2016)
51. C.H. Kuo, C.H. Chen, M.H. Huang, Adv. Funct. Mater. **17**, 3773 (2007)
52. Y. Sekiguchi, T. Oroguchi, Y. Takayama, M. Nakasako, J. Synchrotron Rad. **21**, 600 (2014)
53. T. Ishikawa et al., Nat. Photon. **6**, 540 (2012)
54. K. Tono et al., New J. Phys. **15**, 083035 (2013)

55. H. Yumoto et al., Nat. Photon. **7**, 43 (2013)
56. A. Kobayashi et al., Rev. Sci. Instrum. **87**, 053109 (2016)
57. T. Kameshima et al., Rev. Sci. Instrum. **85**, 033110 (2014)
58. C. Gutt et al., Phys. Rev. Lett. **108**, 024801 (2012)
59. F. Lehmkühler et al., Sci. Rep. **4**, 5234 (2014)
60. A. Kobayashi et al., Sci. Rep. **8**, 831 (2018)

# Chapter 5
# Specimen Preparation for X-Ray Diffraction Imaging Experiments at Cryogenic Temperature

**Abstract** X-ray diffraction imaging (XDI) experiments at cryogenic temperatures allows us to analyze the internal structures of frozen-hydrated biological cells and cellular organelles. As biological specimens are easily degraded by drying, a humidity-controlled chamber is developed to maintain a moist atmosphere during specimen preparation. In the chamber, specimen particles are dispersed onto windows of thin silicon nitride membranes. Next, the particles are flash-cooled to a frozen-hydrated state using liquid ethane. This cryogenic method of specimen preparation allows us to harvest a large number of biological cells and isolated cellular organelles at desired periods in the cell cycle. Subsequently, the prepared specimens can be stored in liquid nitrogen until the use. In this chapter, the methods and devices developed for preparing frozen-hydrated biological specimens are described. In addition, the characteristics of frozen-hydrated specimens are described.

## 5.1 Specimen Preparation Methodology

Figure 5.1 illustrates the procedure used for preparing frozen-hydrated biological specimens for cryogenic XDI experiments. The procedure is developed by referring to the sophisticated specimen preparation techniques used in cryogenic electron microscopy [1, 2] and cryogenic protein X-ray crystallography [3]. For synchrotron XDI tomography experiments at cryogenic temperatures, the diffraction patterns from a single specimen particle are collected at every rotation angle with respect to the direction of the incident X-ray [4]. In XFEL-XDI experiments, fresh particles are supplied to the irradiation area by raster scanning thin membranes that have absorbed many specimen particles, in sync with the repetition rate of the XFEL pulses, because the specimen particles are destroyed at the atomic level by a single XFEL pulse [5, 6]. In both types of experiments, support membranes, freezing devices, and procedures suitable for XDI experiments must be developed and need to be sufficiently sophisticated for the easy preparation of frozen-hydrated specimens [5–8]. In particular, a humidity-controlled chamber equipped with a
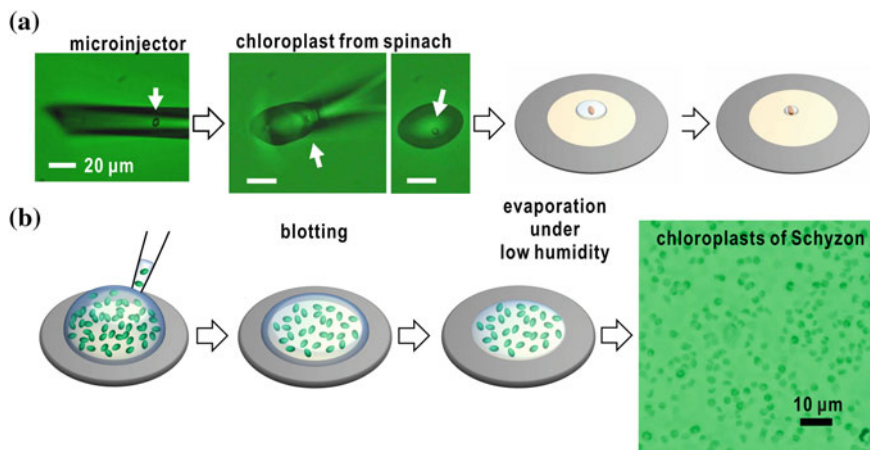
**Fig. 5.1** Sample preparation procedures for noncrystalline particles under humidity-controlled conditions for XDI experiments [7]. **a** For synchrotron XDI experiments, a specimen particle picked up by a microcapillary is set on a thin membrane. **b** For XFEL-XDI experiments, a droplet of suspension containing a number of particles is dropped onto a membrane. In both cases, excess amounts of buffer solution around the particle are removed using the tip of the microcapillary and/ or a tip of wick paper. The membranes adsorbing particles are flash-cooled using liquid ethane. Panels are reused with modification from [7] with permission from AIP publishing

micromanipulator is necessary to handle biological specimens under moist air conditions [7, 8]. The quality of the prepared specimens is examined using diffraction experiments. The materials, devices, and procedures necessary for preparing frozen-hydrated biological specimens are then introduced.

## 5.2   Membrane Support

In the preparation of frozen-hydrated specimens, particles are dispersed onto thin membranes attached to a support disk under moist conditions (Fig. 5.2a) [7, 8]. By plunging the disk into liquid ethane, specimen particles are flash-cooled to a frozen-hydrated state. The membranes and support disks must tolerate the rapid change in temperature during flash-cooling. In addition, the diffraction intensities from the membranes must be negligible in comparison to those from specimen particles. Thin silicon nitride ($Si_3N_4$) membranes with silicon frames satisfy the requirements described above. In our experience, when a $10 \times 10$ mm$^2$ silicon nitride membrane with a thickness of 100 nm is supported by a silicon frame of $30 \times 30$ mm$^2$ (Fig. 5.2a), the membrane and frame withstand flash-cooling by liquid ethane. The large membrane size allows us to rotate particles in a wide angle range with respect to the incident X-ray beam in XDI tomography experiments.
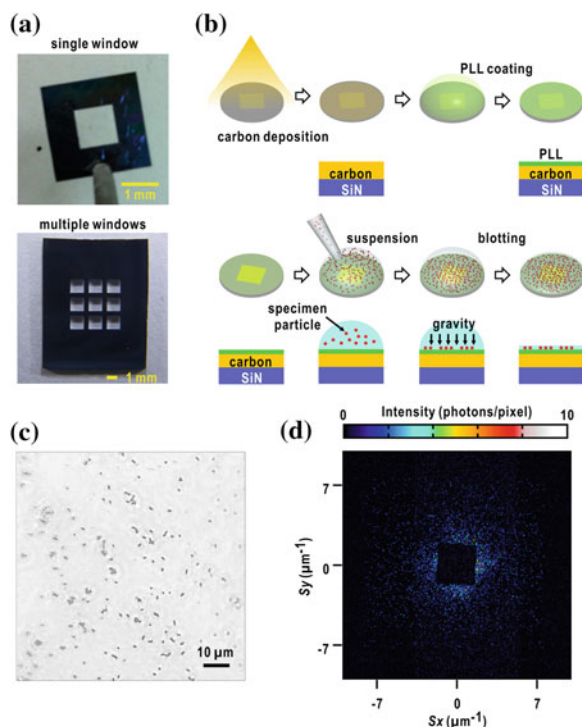
**Fig. 5.2 a** Photographs of two types of silicon disks. (Upper panel) A commercially available 3 mm$^2$ silicon disk with a single $1 \times 1$ mm$^2$ window. (Lower panel) A custom-made $10 \times 8$ mm$^2$ silicon disk with nine $1 \times 1$ mm$^2$ windows. **b** Schematic of the carbon and poly-L-lysine (PLL) coating of the silicon nitride membranes. **c** Phase-contrast LM image of cyanobacteria cells dispersed on a PLL-coated silicon nitride membrane. **d** Parasitic scattering from optics upstream and diffraction from a silicon nitride membrane with a thickness of 100 nm around the beamstop. The wavelength of the X-ray is 0.225 nm. Panels are reused from [8, https://doi.org/10.1107/s1600577516007736] after modification with permission from The International Union of Crystallography

In XFEL-XDI experiments, a larger membrane window is more suitable for collecting a large number of diffraction patterns, and is more advantageous to reduce the number of times in specimen exchange [6, 8]. On the other hand, silicon nitride membranes are occasionally cracked by the irradiation of a single XFEL pulse. Therefore, specimen disks with several membrane windows are preferable for the efficient performance of XFEL-XDI experiments. A silicon disks with $3 \times 3$ array of $1 \times 1$ mm$^2$ silicon nitride membrane windows are designed and developed for the collection of a large number of diffraction patterns in XFEL-XDI experiments (Fig. 5.2a). When a membrane window is raster-scanned with an interval of 25 μm between the irradiation spots, each window provides $38 \times 38$ points for exposure. Subsequently, one specimen disk can be used for 12,996 XFEL pulses.

Biological specimens are difficult to adsorb onto silicon nitride membranes due to the hydrophobicity. To improve the affinity, the surface of a silicon nitride membrane is coated with a carbon layer with a thickness of approximately 15 nm at first, using a vacuum evaporator (Fig. 5.2b). The thickness of the carbon membrane is controlled by monitoring the degree of carbon deposition on filter paper placed near the membrane. Next, the carbon-coated silicon nitride membrane is covered with poly-L-lysine (PLL) molecules with an approximate molecular weight of 300 k by placing a droplet of PLL solution on the carbon layer for approximately 30 min. Unbound PLL molecules are washed away with distilled water. This treatment dramatically improves the affinity of the membrane to biological specimens such as cells and organelles (Fig. 5.2c).

The diffraction pattern from the PLL-treated silicon nitride membrane is negligible in comparison to the parasitic scattering from the upstream optics, as demonstrated in Fig. 5.2d. When being irradiated by an XFEL pulse with $10^{10}$–$10^{11}$ X-ray photons with an energy of 5 keV per $2 \times 2 \ \mu m^2$, the diffraction intensities from the PLL-treated silicon nitride membranes are less than 5 X-ray photons per pixel in the small-angle regions of $S < 3 \ \mu m^{-1}$, and almost zero beyond $S > 5 \ \mu m^{-1}$ [the scattering vector length is defined as in (2.11)]. Therefore, the diffraction intensity is negligibly small in comparison to that from the biological specimens, which exceeds $10^3$ X-ray photons per pixel even in the presence of the attenuator.

If PLL spots with 2 μm diameters are regularly arrayed on a carbon-coated silicon nitride membrane, biological specimens are adsorbed only onto the spots [8]. Such a membrane can be fabricated by electro-spraying a PLL solution onto carbon-coated silicon nitride membranes masked by a holey silicon plate with regularly arrayed pinholes of 3 μm in diameter (Fig. 5.3a). Biological particles are adsorbed only onto the spots (Fig. 5.3b). In addition, the hydrophobicity of the carbon layer is advantageous for the exclusion and removal of excess amounts of buffer solution from the membrane surface by blotting.

High quality diffraction patterns suitable for structural analysis display a high signal-to-noise ratio up to a resolution of 50 $\mu m^{-1}$. When specimen particles are randomly dispersed at a number density of 7–10 per 100 $\mu m^2$, the efficiency with which high quality diffraction patterns are obtained is 1.2% of the XFEL pulses used. In contrast, regularly arrayed particles recorded a yield rate of 2.4%. This tiny difference in the number of high quality diffraction patterns obtained is significant, particularly when millions of XFEL pulses are used in a beam-time. In addition, diffraction patterns from specimens covered by thick vitreous ice are rarely observed for the membranes with regularly arrayed PLL spots, probably because the hydrophobic surfaces of the membranes exclude the buffer except at the locations of the PLL spots.
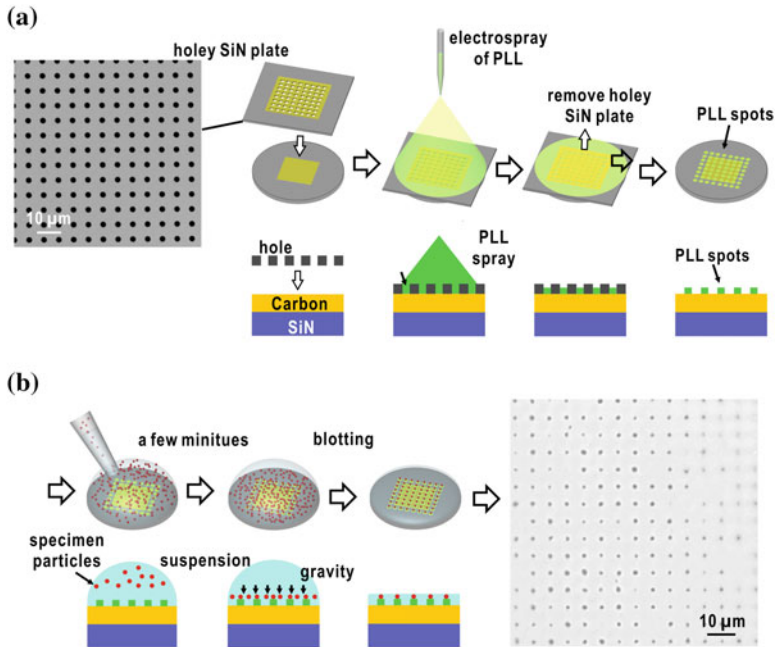
**Fig. 5.3** **a** Schematic of the procedure to fabricate regularly arrayed PLL spots on carbon-coated silicon nitride membranes (SiN). PLL molecules are electro-sprayed onto the carbon-coated silicon nitride membranes through a holey silicon nitride plate. **b** Schematic of the adsorption of biological particles onto a membrane with regularly printed PLL spots. The right panel shows a phase-contrast LM image of cyanobacteria cells adsorbed onto the regularly arrayed PLL spots after blotting. Panels are reused from [8, https://doi.org/10.1107/s1600577516007736] after modification with permission from The International Union of Crystallography

## 5.3   Specimen Preparation Under a Humidity-Controlled Atmosphere

### 5.3.1   Production of Moist Air

A moist-air generator is used to maintain the aqueous conditions of the specimen particles before flash-cooling [7, 9]. A moist-air generator produces air flow with a desired relative humidity (RH) by mixing dry and moisture-saturated air (Fig. 5.4a). The fluctuation in the RH of the moist air can be controlled by maintaining the temperature of the transfer tube to prevent dew formation. When the temperatures of the chamber and the transfer tube are kept at 303 K, RH-controlled air flow can be provided at $98 \pm 2\%$rh.

**Fig. 5.4** **a** Schematic of an RH-controlling apparatus composed of a moist-air generator, a transfer tube warmed with a film heater, and sensors measuring the temperature and RH. The flow rate was 300–450 mL/min. **b** Changes in the lattice constants *a* (orange symbols) and *c* (green) of a tetragonal crystal of hen-egg-white lysozyme under the gradual variation of the RH (blue line). **c** Representative diffraction patterns taken at stages I–IV in panel (**b**) are displayed for a quarter of the detector. The red-dotted circles indicate the resolution [9]. Panels are reused with modification from [9] with permission from Elsevier
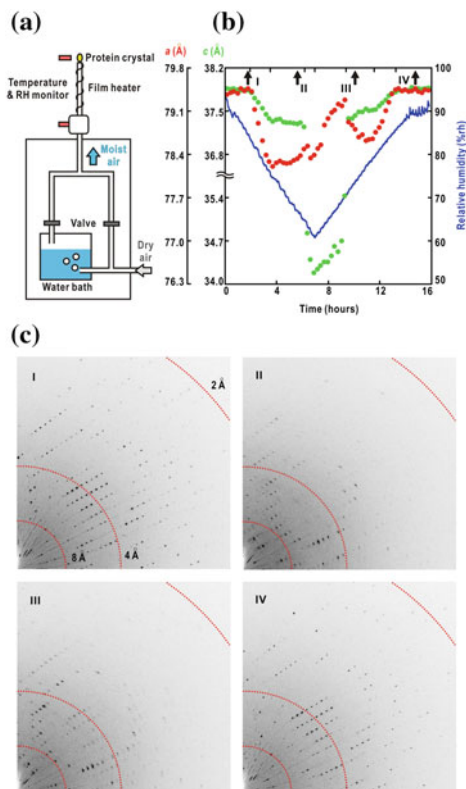


To examine the feasibility and accuracy of a moist-air generator in controlling the RH around a small specimen, the diffraction patterns of a tetragonal crystal of hen-egg-white lysozyme are recorded during the variation of the environmental RH [9]. The crystallinity of protein crystals is sensitive to the RH of the atmosphere, because 35–90% of the volume of the protein crystals is occupied by water. Protein crystals easily lose their crystalline order under low humidity conditions, and display degraded diffraction patterns [10].

The crystal diffracted X-rays beyond a resolution of 0.2 nm during the reduction of the RH from 94 to 83%rh. The reduction of the RH from 83 to 76%rh caused significant shrinkage of the unit cell along the *a*-axis (Figs. 5.4b, c). Further reduction from 76 to 65%rh degraded the crystalline order, as indicated by the appearance of broadening in the Bragg spots, with resolution limited to 0.8 nm. In the RH range of 61–65%rh, the unit cell collapsed along the *c*-axis by approximately 0.3 nm as compared to that at 94%rh. When increasing the RH to rehydrate the crystal, the unit cell displayed a sudden expansion along the *c*-axis at 71%rh. In

the RH range from 71 to 79%rh, the crystalline order was recovered, as indicated by the gradual improvement in the highest resolution of the diffraction patterns to 0.2 nm along with the sharpening of the Bragg spots. During the increase of the RH from 79 to 85%rh, the unit cell swelled in the *a–b* plane. Finally, the diffraction patterns and lattice constants return to those seen at the initial stage during the increase of the RH from 85 to 92%rh.

A series of RH-controlled diffraction experiments demonstrated the feasibility of the moist-air generator and the transfer tube with a heating device for use in controlling the RH of a several-mL volume. Subsequently, a humidity-controlled chamber based on this system is developed to prepare specimens for XDI experiments.

## 5.3.2   Humidity-Controlled System for Specimen Preparation

### 5.3.2.1   Devices Composing the System

The specimen preparation procedure for XDI experiments is conducted in three steps. A droplet of a suspension of specimen particles is set onto a thin silicon nitride membrane with a PLL layer. After the adsorption of particles onto the membrane, excess amounts of buffer solution are removed by blotting and evaporation under low RH conditions, in order to reduce the background scattering and absorption in XDI experiment. Finally, the membrane adsorbing particles are flash-cooled by a cryogen.

An RH-controlling system suitable for performing a three-step procedure was developed [7, 8] (Fig. 5.5). The system is composed of a moist-air generator equipped with an RH-controlling chamber, a transfer tube with a heating device, a microinjector mounted on a motor-controlled micromanipulator, and a specimen preparation chamber set on the sample stage of an optical microscope. The temperature and RH in the chamber are monitored using humidity sensors.

The chamber is divided into three parts (Fig. 5.5a): a main chamber that is fixed to the specimen stage of a light microscope, a pincette box to hold a pincette which catches a specimen disk, and a specimen loader to supply the specimen suspension into the main chamber. The pincette box and specimen loader are removable from the main chamber. The pincette box is separated into two parts to allow for quick flash-cooling of the specimen disk.

The RH around the specimen disk can be controlled in the range from 20–94%rh with a fluctuation of 0.5%rh under $296 \pm 0.3$ K for more than 15 min. Careful operation of air conditioners in an experimental room is advantageous to reduce the fluctuations in temperature. Prior to the specimen preparation, the RH-dependent reversible changes in the volume of the buffer droplet are examined to ensure stable performance during specimen preparation (Fig. 5.5b).
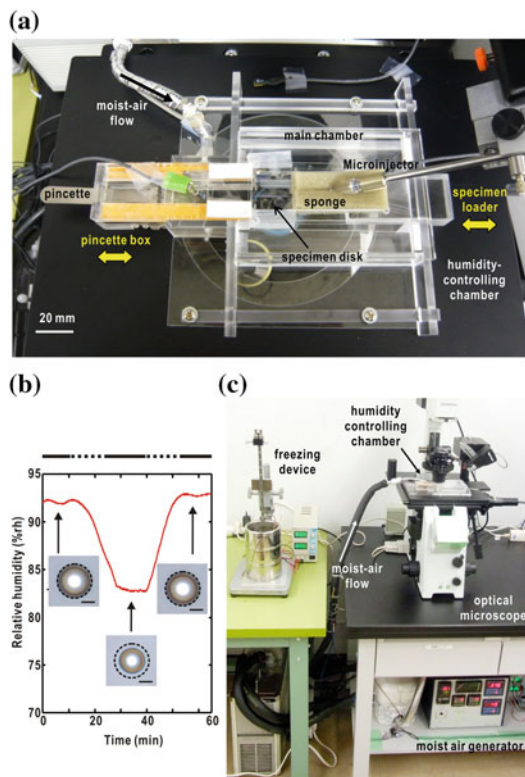
**Fig. 5.5** **a** Photograph of the specimen preparation chamber. **b** Example of the performance of the system to control the volume of a droplet (50 fL) from a buffer solution by changing the RH. When the RH of moist air is ramped down from 92.5 to 83%rh, the volume of a droplet became the half of the initial. When the RH of moist air is increased, the volume change is reversed and returns to its initial. The volume changes little under a constant RH. **c** Photograph of a specimen preparation system composed of a moist-air generator, a specimen preparation chamber mounted on a light microscope, and a liquid-ethane freezing device. Panels (**a**) and (**b**) are reused with modification from [7] with permission from AIP publishing. Panel (**c**) is reused with modification from [8] with permission from AIP publishing

### 5.3.2.2 Specimen Preparation for Experiments Using Synchrotron X-Rays

For synchrotron XDI experiments, the procedure for specimen preparation is somewhat complicated [7]. Prior to preparation, the equilibrium RH of a specimen buffer is experimentally determined by gradually changing the RH. Because the evaporation and adsorption of water vapor at the buffer-air interface are in balance at the equilibrium RH, the volume of the droplet is kept nearly constant.

When aspirating a single specimen particle into the microcapillary from a specimen suspension, the tip of the microcapillary is exposed to a low RH

atmosphere of approximately 85%rh. Subsequently, the particle is moved toward the buffer-air interface at the tip by evaporation-coupled flow inside the microcapillary. When the tip of the microcapillary contacts PLL-coated the membrane, a small droplet containing a single specimen particle contacts with the membrane. The microcapillary system can locate a specimen particle to a desired position on the membrane with a positional accuracy of approximately 1 μm. Then, the RH around the disk is adjusted to the equilibrium RH of the specimen buffer. An excess amount of the buffer around the particle is removed by blotting with a wick paper and/or vapor diffusion under 85%rh.

### 5.3.2.3   Specimen Preparation for Experiments Using X-Ray Free Electron Laser Pulses

In XFEL-XDI experiments, the number density of specimen particles in a suspension is an important factor for the efficient adsorption of particles onto the PLL-coated silicon nitride membrane [8]. After centrifugation, the concentration of specimen particles in a suspension is adjusted to yield a number density of approximately 7–10 particles per $10 \times 10$ μm$^2$ on the membrane [6, 11]. A 1–2 μL droplet of the suspension is applied onto the membrane of a specimen disk under the equilibrium RH atmosphere of the specimen buffer. After a moment, specimen particles are adsorbed onto the PLL layer of the membrane.

The suspension remaining on the membrane results in diffraction patterns composed of small speckles. In addition, due to the large cross-section of suspension in the irradiation area, most diffraction patterns have total diffraction intensities of 10–1000 times higher than those from single biological particles embedded in a thin layer of suspension. Therefore, the excess amount of suspension is blotted off by wick papers under inspection by an optical microscope. Furthermore, the few tens of femtoliters of buffer liquid sometimes remaining around the sample particles is evaporated by the moist air flow of the low RH.

## 5.4   Flash-Cooling

### 5.4.1   Cryogens for Flash-Cooling

Protein crystallography at cryogenic temperatures was developed to reduce the radiation damage to protein crystals during diffraction data collection by intense synchrotron X-rays [3]. Sophisticated flash-cooling procedures have been developed in the last two decades. The most popular procedure is the flash-cooling of protein crystals using cold nitrogen gas at 100 K. Prior to flash-cooling, protein crystals are embedded in a crystallization buffer containing an anti-freezing reagent sufficient to prevent the growth of hexagonal ice.

**Table 5.1**  Thermal properties of cryogens

| Cryogen | Melting point/K | Boiling point/K | Specific heat/J/gK |
|---|---|---|---|
| Liquid nitrogen | 63 | 67 | 2.0 |
| Ethane | 90 | 184 | 2.7 |
| Propane | 84 | 231 | 1.9 |

**Table 5.2**  Comparison of cooling rate

| Cryogen | Thermocouple diameter/μm | Cooling rate/K/ms |
|---|---|---|
| Liquid nitrogen | 150 | 1200 |
| Liquid nitrogen | 800 | 1200 |
| Liquid ethane | 150 | 10 |
| Liquid ethane | 800 | 60 |

However, anti-freezing reagents at a high concentration degrade cells and cellular organelles by osmotic pressure. When the amount of anti-freezing reagent is insufficient, rapid cooling of the specimens is necessary, done by using any cryogen with a high cooling rate (Table 5.1). Although liquid nitrogen is the most useful cryogen for storing biological specimens at low temperatures, it is unsuitable for rapid cooling. When an object at room temperature is plunged into liquid nitrogen, boiling of the liquid nitrogen on the surface of the injected object prevents the thermal contact necessary for efficient heat conduction at the interface. Subsequently, it takes 1.2 s to cool specimens from room temperature to liquid nitrogen temperature (Table 5.2). Because of the boiling, the cooling time is independent of the size of the specimen. In contrast, cold nitrogen gas at around 100 K is suitable for freezing a few microliters of crystallization buffers containing 20–25% (w/v) of glycerol to the vitreous ice state within a few hundred milliseconds.

In cryogenic EM, liquid ethane is known as the most effective cryogen for freezing biological specimens dispersed onto holy carbon membranes [12]. Little boiling occurs when an object at room temperature is plunged into liquid ethane. In addition, the specific heat and heat transfer rate of liquid ethane are advantageous for freezing buffer solutions of a few picoliters into the vitreous state. The cooling speed depends on the size of the specimens, as demonstrated by the measurements of cooling times necessary for thermocouples of different sizes (Table 5.2). In addition to liquid ethane, liquid propane may also be used as a cryogen for flash-cooling. Because liquid ethane and propane are inflammable, they should be safely handled by using draft chambers in the laboratory. In addition, safety glasses for eye protection are essential.

## 5.4.2 Flash-Cooling Procedure

For the flash-cooling of the specimen disk, the pincette box is removed from the main chamber of the humidity-controlled chamber and attached to the plunging unit of the flash-cooling device [7, 8] (Fig. 5.6a). This procedure is performed quickly, within 5 s, and the decrease in the RH inside the box is only approximately 2%rh under the RH of 40–60%rh at 296 K. Immediately after the removal of the pincette box, the specimen disk at the tip of the pincette is dropped into a liquid ethane bath, kept at 95 K by using a film heater. The flash-cooled disks are transferred to a
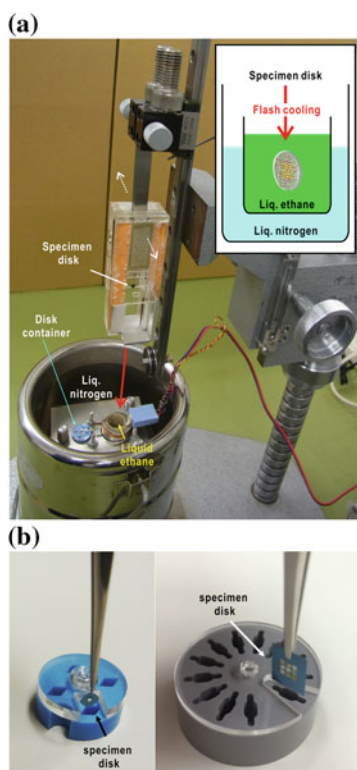


**Fig. 5.6 a** Photograph of the flash-freezing device. Liquid ethane is produced by blowing ethane gas to the wall of an aluminum cap, which is cooled by liquid nitrogen. The temperature of the liquid ethane is kept above the melting point using a film heater [7, 8]. **b** Photographs of the disk containers used to store flash-frozen specimen disks in liquid nitrogen. The container in the left panel is used for specimen disks for synchrotron XDI experiments. The right panel shows a container storing specimen disks for XFEL-XDI experiments. Panel (**a**) is reused with modification from [7] with permission from AIP publishing. Panels (**b**) and (**c**) are reused with modification from [8, https://doi.org/10.1107/s1600577516007736] with permission from The International Union of Crystallography

specially designed case kept below 100 K and stored in liquid nitrogen until their use in diffraction experiments (Fig. 5.6b).

If the temperatures of the specimens were higher than the glass transition temperature of the specimen buffer (most likely to be around 150–180 K), a large number of hexagonal or cubic ice crystals would grow. Although both types of ice crystals give rise to intense and characteristic diffraction patterns, patterns from hexagonal and/or cubic ice crystals are rarely observed. Therefore, the procedure allows us to prepare frozen-hydrated biological specimens almost free from ice crystals.

### 5.4.3  Structures of Flash-Cooled Specimens

Do the flash-cooled specimens keep their structure intact? In cryogenic X-ray crystallography, the structures of the macromolecules at around 100 K are almost the same as those at ambient temperature, as indicated by the very small thermal expansion coefficient [13]. In addition, the hydration structures of proteins at cryogenic temperatures agree with those expected from the hydrogen bond patterns of water molecules and polar protein atoms [14, 15].

Frozen-hydrated cells and cellular organelles are expected to keep their functional structures. As demonstrated in the cryogenic techniques used in the field of medical science [16, 17], frozen-hydrated cells likely maintain their functional structures, because they are still alive after returning to ambient temperatures. To examine whether frozen-hydrated cells retain the same structures as seen at ambient temperature, the reconstructed projection density maps of the prepared specimens are compared with the structures visualized by other microscopic techniques with regard to both the overall shape and size and the internal fine structures.

The projection structures of spinach chloroplasts as large as 7 μm are studied with cryogenic XDI using synchrotron X-rays [4]. The overall shape and size are consistent with the image observed by light microscopy. In addition, fine structures inside the chloroplast, such as grana, are preserved in the frozen-hydrated samples. This fact suggests that the overall and internal structures of spinach chloroplasts are probably tolerant both of the small osmotic pressure changes accompanying the RH control and rapid change of temperature in flash-cooling.

As a preliminary examination of the issue described above, the projection electron density maps of frozen-hydrated cyanobacterial cells were retrieved from diffraction patterns recorded in a cryogenic XFEL-XDI experiment. In the phase-retrieved maps with effective resolutions better than 150 nm, frozen-hydrated cyanobacterial cells displayed overall globular shapes as observed by LM (Fig. 5.7a). The sizes were consistent with those observed by dynamic light scattering (DLS) and LM. A C-shaped high-density region appeared with an approximate diameter of 500 nm. The C-shaped regions can be interpreted as stacks of thylakoid membranes, and are consistent with those observed in the tomography
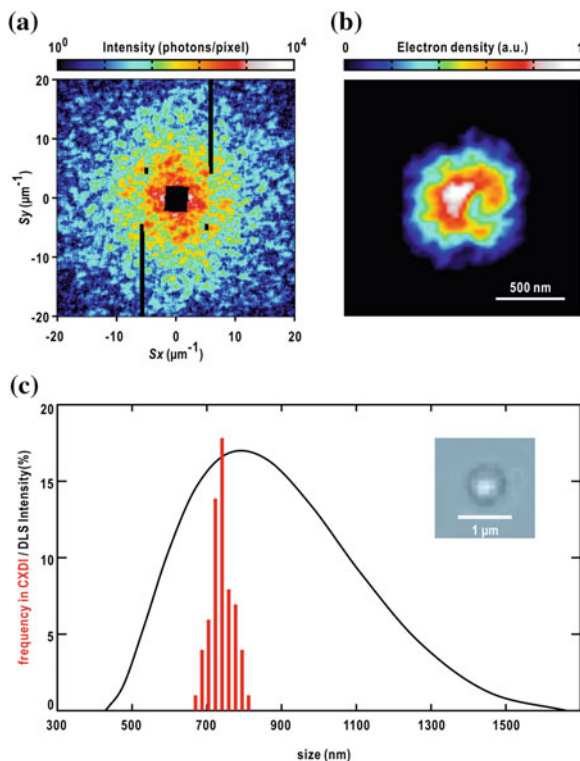
**Fig. 5.7 a** Diffraction pattern from a single frozen-hydrated cyanobacterial cell of the *Prochlorococcus* strain NIES-2087. Speckle peaks were visible beyond resolutions of 20 $\mu m^{-1}$. The pattern displayed good centrosymmetry. **b** Most probable electron density map retrieved from the diffraction pattern in panel (**a**). **c** Size distribution of cyanobacterial cells obtained from 63 retrieved electron density projection maps (red histogram), and size distribution measured by DLS (black line). The inset is an image of a cyanobacterial cell taken by a light microscope. Panels are reused from [8, https://doi.org/10.1107/s1600577516007736] after modification with permission from The International Union of Crystallography

study of a frozen-hydrated cyanobacterial cell using cryogenic TEM [18]. Therefore, the overall shape and structure of the cyanobacterial cells is maintained in vitreous ice.

Figure 5.8a shows a diffraction pattern from a semi-dried cyanobacterial cell, which was prepared as a reference for the frozen-hydrated cells. The PR map displayed an ellipsoid shape with long (300 nm) and short (90 nm) axes less than the half of those observed by dynamic light scattering. In addition, the shape and size are inconsistent with those observed by TEM. The total diffraction intensities are far smaller than those for frozen-hydrated cells, and the most frequently observed maximum resolution is approximately 100 nm. These findings indicate that the evaporation of water from the cells causes shrinkage and decreases the total cross-section for X-rays.

**Fig. 5.8** Schematic illustrations regarding the electron density contrast of biological cells in vacuum (**a**) and in solvent or vitreous ice (**b**). The upper and middle panels compare electron density distributions. The lower panels show the diffraction patterns of cyanobacteria cells under a semi-dried condition and in vitreous ice. Panels are reused from [8, https://doi.org/10.1107/s1600577516007736] after modification with permission from The International Union of Crystallography
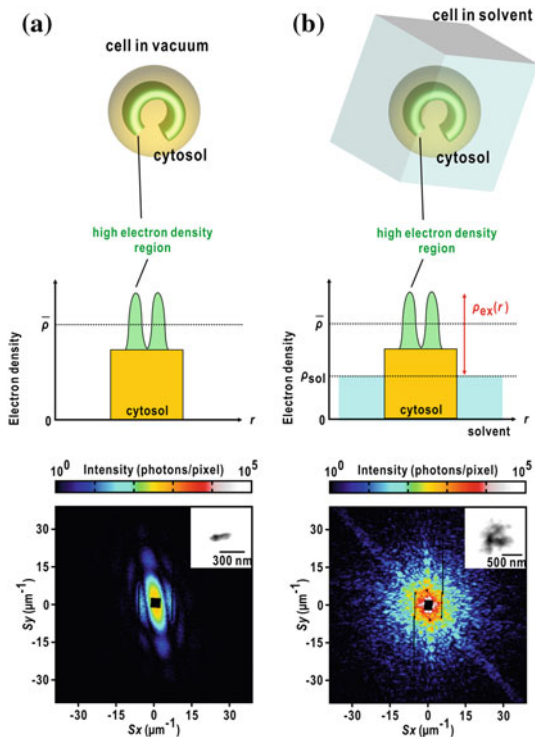


The size distribution of the specimen particles is useful experimental data for discussing the influence of flash-cooling on the overall structures of the specimen particles. DLS [19] is used to measure the size of specimen particles in solution before flash-cooling for cryogenic XDI experiments. From the DLS spectrum for a suspension of cyanobacteria, the size distribution displayed the maximum at approximately 780 nm, with a standard deviation of 230 nm (Fig. 5.7c).

In cryogenic XFEL-XDI experiments, the size distribution of cyanobacterial cells is constructed by directly measuring the diameter of each projection map retrieved from the diffraction pattern of a single cyanobacterial cell (Fig. 5.7c). The distribution has a peak at 775 nm with a standard deviation of 38 nm. The average size in the distribution is close to the peak value in the size distribution from DLS, and comparable with the low-resolution images observed using LM. The width of this distribution is narrower than that from DLS. DLS estimates the size distribution of the particles by analyzing the Brownian motion of the particles with the auto-correlation function and Stokes law. The analysis methods and assumptions sometimes result in a large uncertainty in the estimation of the size distribution. Therefore, the frozen-hydrated cyanobacteria will retain their size and likely the structure too, as observed at ambient temperature.

## 5.5   Electron Density Contrast in Electron Density Projection Maps

In cryogenic XDI experiments, projection electron density maps of specimen particles embedded in vitreous ice are retrieved from their diffraction patterns. In these maps, the fine structures inside specimen particles are clearly visualized, rather than just their outer shapes. In contrast, the overall shapes are clear in the projection maps retrieved from the diffraction patterns of semi-dried specimens under vacuum conditions. This substantial difference between the PR maps of specimens in-vacuum and in-vitreous ice can be explained in terms of electron density contrast (Fig. 5.8) [20, 21].

For a particle embedded in vitreous ice, the excess electron density $\rho_{EX}(\boldsymbol{r})$ from the uniform electron density of the solvent (or vitreous ice), $\rho_{v-ice}$, is expressed as

$$\rho_{EX}(\boldsymbol{r}) = \Delta\rho\,\rho_C(\boldsymbol{r}) + \rho_F(\boldsymbol{r}), \quad \Delta\rho = \overline{\rho} - \rho_{v-ice}, \tag{5.1}$$

where $\rho_C(\boldsymbol{r})$ represents the shape (support) of the particle at the average electron density $\overline{\rho}$, and is equal to one inside the particle and zero outside the particle. For instance, the $\overline{\rho}$ values of water, proteins, and nucleic acids are 330, 420, and 550 electrons $nm^{-3}$, respectively. $\rho_F(\boldsymbol{r})$ shows the spatial fluctuation of $\rho_{EX}(\boldsymbol{r})$ from $\overline{\rho}$. $\Delta\rho$ is the electron density contrast between solute and solvent. Because of the reciprocity between the particle size and the scattering vector, X-rays diffracted by vitreous ice with the size irradiated by the incident X-ray beam propagate into a very small-angle region hidden by a beam stop.

The diffraction intensity $I(\boldsymbol{S})$ at a scattering vector $\boldsymbol{S}$ is written as

$$\begin{aligned} I(\boldsymbol{S}) \propto\;& \Delta\rho^2\,|F_C(\boldsymbol{S})|^2 + \Delta\rho\,F_C^*(\boldsymbol{S})\,F_F(\boldsymbol{S}) \\ & + \Delta\rho\,F_F^*(\boldsymbol{S})\,F_C(\boldsymbol{S}) + |F_F(\boldsymbol{S})|^2, \end{aligned} \tag{5.2}$$

where $F_C(\boldsymbol{S})$ and $F_F(\boldsymbol{S})$ are the structure factors of $\rho_C(\boldsymbol{r})$ and $\rho_F(\boldsymbol{r})$, respectively. For particles in vacuum, $\rho_{v-ice}$ is almost zero. The diffraction intensity is then dominated by $F_C(\boldsymbol{S})$, reflecting the overall shapes of the specimen particles. In contrast, for specimen particles in vitreous ice or solvent, the contribution of $F_C(\boldsymbol{S})$ is reduced depending on $\Delta\rho$. When $\Delta\rho$ becomes small as the biological particles embedded in vitreous ice, $F_F(\boldsymbol{S})$ dominates the diffraction intensity rather than $F_C(\boldsymbol{S})$. This is one of the benefits of using cryogenic XDI to extract information on the internal structures.

## 5.6    Preparation of Standard Specimens

As described in Sect. 4.3.3.3, the spatial coherence of the XFEL pulses is measured by the visibility speckle spectroscopy [22, 23] for diffraction patterns from uniformly dispersed gold-colloidal particles with diameters of approximately 50 nm (Fig. 4.13a). The electrospray method is suitable to uniformly disperse gold colloidal particles onto silicon nitride membranes without aggregates. In the method, a charged droplet is electrostatically driven from a suspension in a thin capillary tube (Fig. 5.9a). The charged droplet is immediately exploded into small mists due to electrostatic repulsion. Finally, gold colloidal particles are adsorbed on silicon nitride membranes after the evaporation and electric breakup of water from the small mist particles. Subsequently, gold colloidal particles in distilled water are
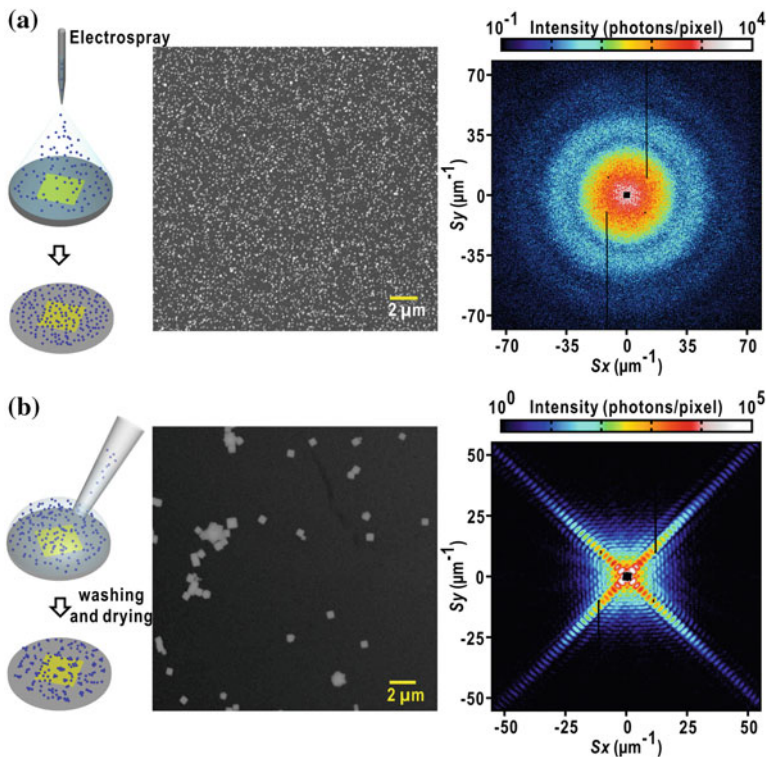


**Fig. 5.9  a** An electrospray device helps to make a layer of uniformly dispersed gold colloidal particles on a silicon nitride membrane. The diffraction pattern is used for determining the spatial coherence of XFEL pulses. **b** Cuboid shaped cuprous oxide particles are dispersed on a silicon nitride membrane with a micro pipette. From the characteristic cross-shaped diffraction pattern, the camera parameters are determined. Panels are reused from [8, https://doi.org/10.1107/s1600577516007736] after modification with permission from The International Union of Crystallography

uniformly dispersed onto a silicon nitride membrane at the number density of approximately 40 particles $\mu m^{-2}$. The diffraction pattern is composed of concentric rings with small speckle peaks. The concentric ring pattern comes from the overall shape of each gold colloidal particle, and then interference of the X-rays diffracted by particles in the irradiation area results in the small speckle peaks.

Prior to diffraction data collection, camera parameters are determined by analyzing diffraction patterns from a single cuprous oxide particle [24] (Fig. 5.9b) (see Chap. 6). In contrast to gold colloidal particles in distilled water, the electrospray device is difficult to apply to uniformly disperse copper-oxide particles, which are produced and stable in solution with a high salt concentration. Instead, cuprous oxide particles are dispersed on silicon nitride membranes in the same manner as is done for biological specimens. A microliter droplet of a suspension of cuprous oxide particles is put onto a silicon nitride membrane. After the adsorption of cuprous oxide particles to the membrane, suspension is washed out by distilled water. Finally, the membrane is air-dried under atmosphere. Diffraction patterns from single copper-oxide particles are stochastically obtained at a hit rate of approximately 11% of the total number of XFEL pulses on single or clusters of particles during a raster scan.

# References

1. A.W. Robards, U.B. Sleytr, *Low Temperature Methods in Biological Electron Microscopy* (Elsevier, Amsterdam, 1991)
2. J. Dubochet et al., Quart. Rev. Biophys. **21**, 129 (1988)
3. D.W. Rodgers Methods Enzymol. **276**, 183 (1997)
4. A. Rodriguez et al., IUCrJ **2**, 575 (2015)
5. M. Nakasako et al., Rev. Sci. Instrum. **84**, 093705 (2013)
6. A. Kobayashi et al., Rev. Sci. Instrum. **87**, 053109 (2016)
7. Y. Takayama, M. Nakasako, Rev. Sci. Instrum. **83**, 054301 (2012)
8. A. Kobayashi et al., J. Synchrotron Rad. **23**, 975–989 (2016)
9. Y. Takayama, M. Nakasako, Biophys. Chem. **159**, 237 (2011)
10. Y. Rayment, Methods Enzymol. **114**, 136 (1985)
11. Y. Takayama et al., Plant Cell Physiol. **56**, 1272 (2015)
12. A.M. Glauert, P.R. Lewis, *Biological Specimen Preparation for Transmission Electron Microscopy* (Princeton University Press, Princeton, 2014)
13. M. Nakasako, J. Mol. Biol. **289**, 547–564 (1999)
14. M. Nakasako, Philos. Trans. R. Soc. London, Ser. B **359**, 1191 (2004)
15. D. Matsuoka, M. Nakasako, J. Phys. Chem. B **113**, 11274 (2009)
16. C. Chen, Lancet **1**, 884–886 (1986)
17. C.M.O. Medeiros, F. Forell, A.T.D. Oliveira, J.L. Rodrigues, Theriogenology **57**, 327 (2002)
18. R.A. Grassucci, D.J. Taylor, J. Frank, Nat. Protoc. **2**, 3239 (2007)
19. B.J. Berne, R. Pecora, *Dynamic Light Scattering with Applications to Chemistry, Biology and Physics* (Dover, New York, 2000)
20. K. Ibel, H.B. Stuhrmann, J. Mol. Biol. **93**, 255 (1975)

21. D.I. Svergun, M.H.J. Koch, P.A. Timmins, and R.P. May, *Small Angle X-ray and Neutron Scattering from Solutions of Biological Macromolecules* (Oxford University Press, 2013)
22. C. Gutt et al., Phys. Rev. Lett. **108**, 024801 (2012)
23. A. Kobayashi et al. Sci. Rep. **8**, 831 (2018)
24. C.H. Kuo, C.H. Chen, M.H. Huang, Adv. Funct. Mater. **17**, 3773 (2007)

# Chapter 6
# Processing of Diffraction Patterns Obtained from X-Ray Diffraction Imaging Experiments Using X-Ray Free Electron Laser Pulses

**Abstract** In X-ray diffraction imaging (XDI) experiments using X-ray free electron laser (XEFL), X-ray pulses provided at a repetition rate of more than 30 Hz enable us the collection of a large number of diffraction patterns within a short period of time. Diffraction patterns with good signal-to-noise ratios are stochastically obtained depending on the positional coincidence of the XFEL pulses and particles dispersed onto membranes. Because of the large number of diffraction patterns exceeding 31,000 per hour, automatic processing is necessary to efficiently extract those patterns worth analyzing, for instance, through selection regarding signal-to-noise ratio and merging patterns simultaneously recorded by two detectors. Here, a software suite for XFEL-XDI experiments is introduced. The algorithms and the procedures will be helpful for developing data processing software for automatically treating a large amount of two-dimensional data.

## 6.1 Outline of the Data Processing Procedure

XFEL-CXDI experiments using the apparatus described in Chap. 4 provide a large amount of diffraction [1]. Diffraction patterns worth analyzing are obtained by either scanning the specimen disk or injecting suspensions into the irradiation area. In addition, while using more than two detectors to ensure the dynamic range, the diffraction patterns collected are merged into single files. Because of the rate of diffraction data collection, it is very difficult to manually process the diffraction patterns within a short time. Program suites to automatically process the collected data are therefore necessary. Here, a program suite developed for the XFEL-XDI experiments described in Chap. 4 is introduced. The scheme and algorithms used in this suite would be useful to develop any other program suite for XFEL data processing dealing with a large number of diffraction patterns.

As illustrated in Fig. 6.1, XFEL-CXDI data collection using the diffraction apparatus TAKASAGO-6 is initiated by the start signal sent from the control PC of the apparatus to the data acquisition (DAQ) system. The high-speed translation
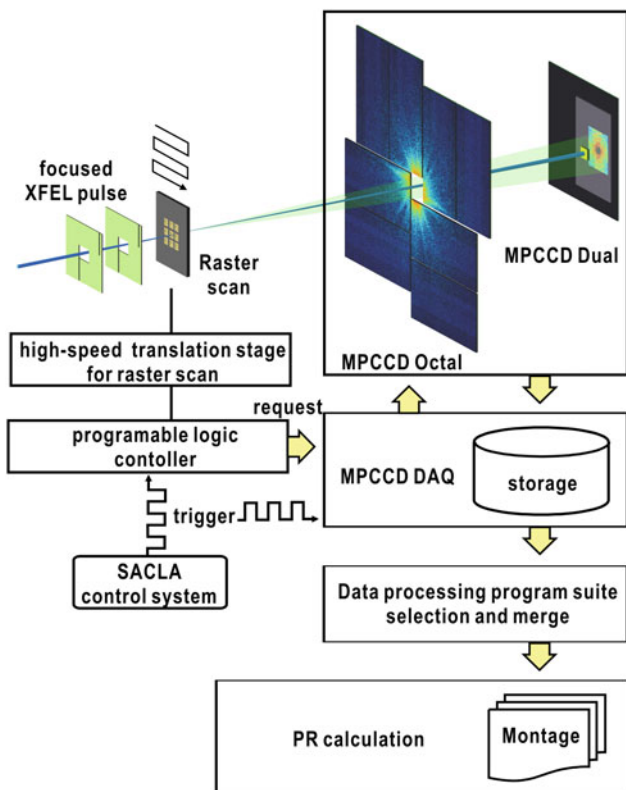
**Fig. 6.1** Outline of the data processing procedure for the diffraction patterns collected in XFEL-XDI experiments. Published with kind permission of Masayoshi Nakasako 2017. All Rights Reserved

stage scans the specimen disk at the repetition rate of the XFEL pulses. The DAQ system reads out the diffraction patterns from the two MPCCD detectors and transfers the image to its storage.

Within 5 s after the completion of a raster scan, a data processing software suite starts to process the diffraction patterns worth analyzing through the following four steps: background subtraction, determination of the beam center positions for the two detectors, merging of the diffraction patterns from the two detectors, and PR calculations [2, 3]. The program suite is composed of four subprograms, each of which carries out one of four steps.

The first program selects the diffraction patterns worthy of analysis from those obtained in the raster scans by applying threshold values relevant to the effective resolution. Currently, artificial intelligence (AI) is introduced to select high-quality diffraction patterns. The second determines the beam center positions of the two detectors and evaluates the centrosymmetry of each diffraction pattern in a

small-angle region, where the Ewald sphere is approximated as a plane. The third subprogram merges the diffraction patterns from the two detectors using the parameters determined by the second subprogram. Finally, the fourth subprogram retrieves the projection electron density maps of the specimen particles projected along the direction of the incident X-ray beam. Manual operation of the subprograms is inconvenient and unsuitable for efficiently processing a large number of diffraction patterns in a short period of time. In addition, a graphical user interface (GUI)-assisted subprogram is developed to report the progress of the automatic processing and the statistics in a set of diffraction patterns. The data processing program suite is written in the FORTRAN90 language. The GUI front-end is coded using the C++ language with the Qt GUI toolkit. In order to visualize the diffraction patterns and retrieved electron density maps, the ImageJ program is used.

At every 5 s interval, G-SITENNO monitors the status of the raster-scan data collection by running a background script, which submits a query to the DAQ system as to whether a raster scan has finished. When the DAQ system reports the completion of the scan, the script automatically invokes the first subprogram.

## 6.2   Background Subtraction, Reconstruction, and Extraction of Diffraction Patterns

### 6.2.1   Background Subtraction

By adjusting the positions of silicon frames, which significantly reduces parasitic scattering from upstream optics (Fig. 4.11b), the diffraction patterns are almost free from parasitic scattering and background scattering from the upstream optics of the beamline. Scattering from the membrane support is also negligible (Fig. 4.11c). Therefore, only the thermal and read-out noise in the detectors are taken into account. Before every raster scan for data collection, 100 noise patterns are recorded for the two detectors without X-ray beams under the same operation conditions used in data collection. The noise patterns are averaged and subtracted from the diffraction patterns in the raster scan (Fig. 6.2).

After subtracting the background noise, the first subprogram reconstructs the diffraction pattern of a single file from two detectors (Fig. 6.2), and extracts diffraction patterns which display a signal-to-noise ratio better than the user-defined threshold value at a user-defined resolution (Fig. 6.2). In most cases, the resolution is defined as the edge of the resolution shell, where the signal-to-noise ratio of the maximum diffraction intensity ($I/\sigma$) is larger than 2. For biological specimens, diffraction patterns worthy of analysis require speckle patterns of $I/\sigma > 2$ at a resolution better than 14.3 $\mu m^{-1}$ (corresponding to a resolution of 70 nm in real space).

**Background subtraction in every detector panel**



**Reconstruction of diffraction patterns recorded in 10 CCD panels**



**Extraction of diffraction patterns for structure analysis**
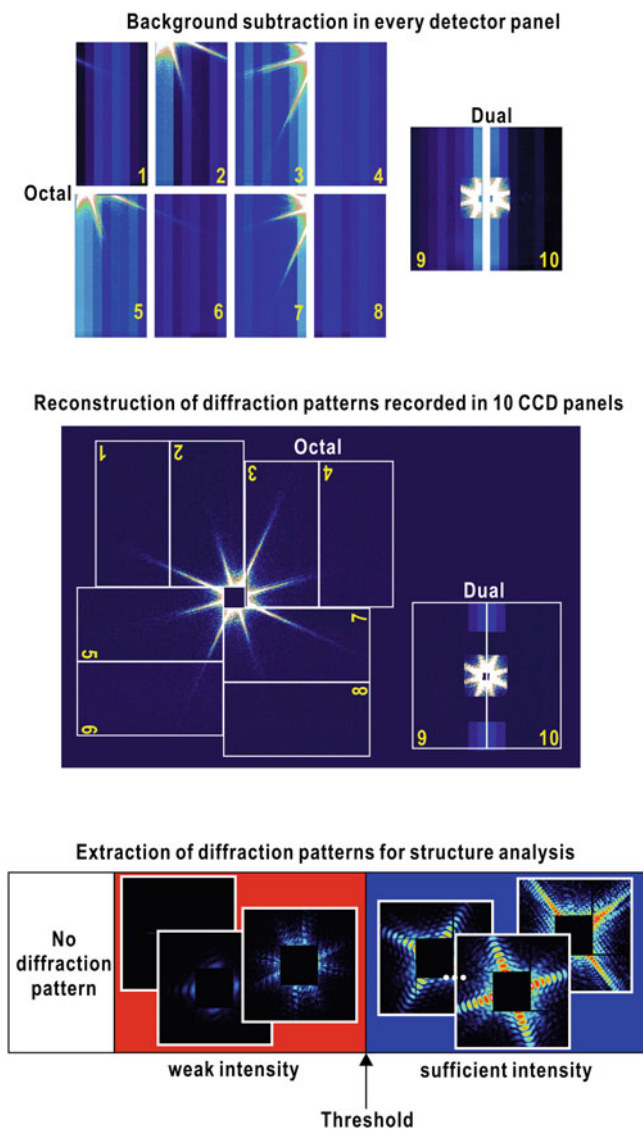


**Fig. 6.2** Flowchart showing the data processing procedure by the first subprogram. After the reconstruction of a diffraction pattern by merging ten background-subtracted CCD images, diffraction patterns with intensities above the user-defined threshold are extracted for subsequent data processing. Panels are reused from [2, https://doi.org/10.1107/s1600577514003439] after modification with permission from The International Union of Crystallography

### 6.2.2  Signal-to-Noise Ratio

The signal-to-noise ratio in diffraction pattern is an important factor for structural analyses. According to the Rose criterion [4], the signal-to-noise ratio is used to distinguish the signal and noise in the image. This corresponds to 25 photons/pixel in diffraction intensity. However, the diffraction amplitude is used in the phase retrieval (PR) calculation. When taking the Poisson noise in X-ray detection into consideration, the lower limit is 6 photons/pixel [5].

We sometimes use the signal-to-noise ratio defined as

$$R_{S/N} = \frac{1}{n_{pixel}} \sum_{x,y \in shell} \frac{I(x,y)}{\sqrt{I(x,y)}},  \tag{6.1}$$

where $n_{pixel}$ is the number of pixels located between the specified maximum and minimum scattering vector lengths, i.e., the so-called resolution shell. $R_{S/N}$ is an average ratio between the diffraction intensity $I(x,y)$ and the standard deviation of the Poisson noise $[I(x,y)]$ over the resolution shell. For the experimental diffraction patterns examined thus far, $R_{S/N}$ values of 3–4 may suggest a limit for successfully reconstructing electron density maps at the requested resolution [5].

### 6.2.3  Extraction of Diffraction Patterns Worth Analyzing

Because specimen particles are dispersed on specimen disks, high quality diffraction patterns are collected stochastically, only when a particle is bathed in the central area of a focused XFEL pulse. The probability depends on the size of the specimen particles and the number density. The probability of obtaining high quality patterns is currently less than 2%. Therefore, high quality patterns must be extracted from the collected set of diffraction patterns. Figure 6.3 displays examples of the various types of diffraction patterns. The miss-hit patterns can be excluded by measuring the intensity in a region of interest (ROI). In addition, weak diffraction patterns are also discarded when the summed diffraction intensity and signal-to-noise ratio is smaller than the requested threshold level.

However, several types of diffraction patterns are difficult to exclude using the scheme relying on the summed intensity and signal-to-noise ratio [6]. For instance, XFEL pulses sometimes cause cracks over silicon nitride membranes. In this case, strong streak patterns appear from the narrow cracks as in Fig. 6.3b. Failures in specimen preparation with regard to cooling speed, number density, and low humidity result in the formation of small hexagonal ice particles (Fig. 6.3c), aggregates of specimen particles (Fig. 6.3d), and dried particles (Fig. 6.3e). Small hexagonal ice particles give characteristic speckle patterns originating from the hexagonal shapes. The diffraction patterns from aggregates of specimen particles are composed of speckle patterns with sizes smaller than those expected from a single specimen particle. In contrast, the speckle sizes from dried particles are larger

**Fig. 6.3** Typical diffraction patterns from **a** a support membrane (miss-hit), **b** a cracked membrane, approximated as the Fraunhofer diffraction of a narrow slit with a width of 100 nm, **c** a hexagonal ice crystal with sub-micrometer dimensions with the retrieved electron density map, **d** an aggregate of particles or a cluster of vitreous ice, **f** a semi-dried cyanobacteria cell, which shrinks significantly, and **e** a frozen hydrated cyanobacteria cell. Panels are reused from [6, https://doi.org/10.1107/s1600577516007736] after modification with permission from The International Union of Crystallography
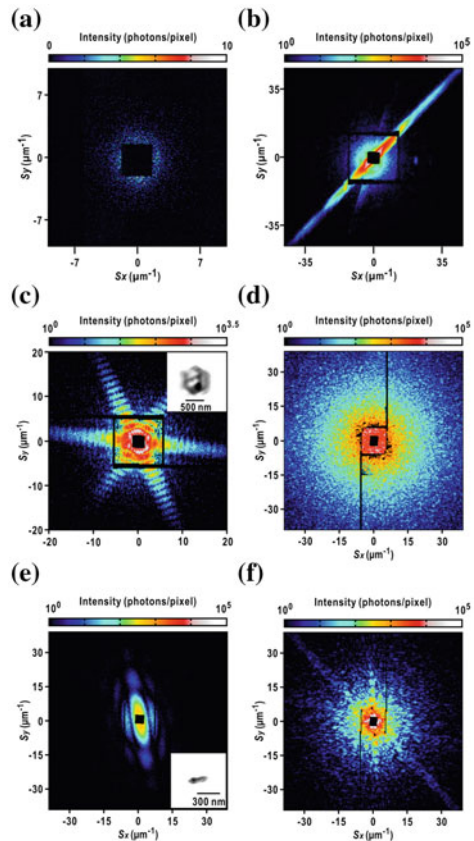


than those of frozen-hydrated particles. The patterns from specimens with inappropriate preparations can be manually identified. However, they are difficult to exclude using the criteria regarding the diffraction intensity and signal-to-noise ratio. If the total number of those diffraction patterns collected in a beam-time is in the order of $10^4$–$10^5$, manual inspection is still possible. However, the exclusion of diffraction patterns is practically difficult when the number goes above $2 \times 10^6$. Thus, a different scheme is needed to automatically extract high-quality diffraction patterns.

Artificial intelligence (AI) is now widely used in the classification of various types of images. An AI is composed of several layers of neural networks, and each layer is an assembly of a number of nodes (Fig. 6.4). The variable input to each node is a sum of parameters ($x_i$) characterizing the diffraction patterns as

$$u = \sum_{i=1}^{N} w_i x_i + b$$

**Fig. 6.4** Schematic of the AI used for extracting the desired diffraction patterns. Published with kind permission of Masayoshi Nakasako 2017. All Rights Reserved
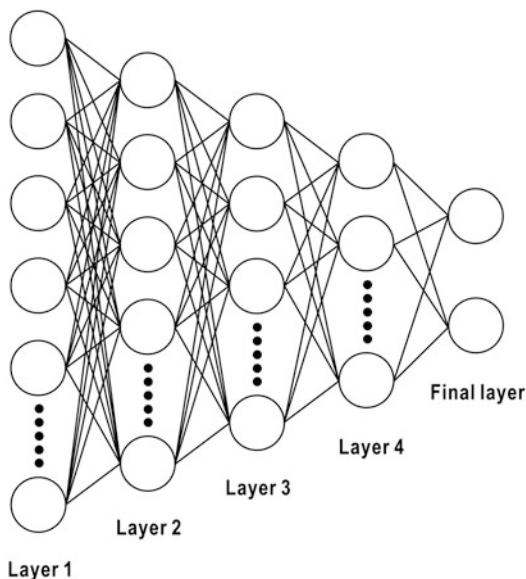
where $w_i$ is the weight for the $i$th parameter, and $b$ is a constant called the bias. The values of $w_i$ and $b$ are optimized by mechanical learning for a large amount of data. Each node outputs the value of the sigmoid function defined as

$$f(u) = \frac{1}{1 + \exp(-u)}$$

The final layer judges whether a diffraction pattern is suitable or not using the softmax function as

$$f(u_1) = \frac{\exp(u_1)}{\exp(u_1) + \exp(-u_2)}$$
$$f(u_2) = \frac{\exp(u_2)}{\exp(u_1) + \exp(-u_2)}$$

An AI constructed for selecting diffraction patterns learns how the users distinguish the quality of diffraction patterns by using a large set of diffraction patterns. The set is comprised of diffraction patterns manually selected by users. In the mechanical learning process, the AI acquires the capability to exclude the diffraction patterns depicted in Figs. 6.3b–e and to extract patterns as users do.

A diffraction pattern with $N \times N$ pixels is expressed as a one-dimensional string. Then, an AI in which the pixels are assumed to be input nodes in the first layer is constructed. The number of nodes is reduced in the next layer using the sigmoid function. The final layer provides an answer to the question of whether an input diffraction pattern is worth analyzing. For instance, after the parameters are adjusted

by mechanical learning for a set of approximately 45,000 diffraction patterns, the AI can select more than 80% of diffraction patterns to be extracted in the other set of diffraction patterns, which are not used in mechanical learning. Simultaneously, the AI can find more than 90% of the patterns to be discarded in the set. As a large number of diffraction patterns can be collected using the TAKASAGO-6 diffraction apparatus, these figures suggest that the AI is feasible for practical use in XFEL-XDI experiments.

## 6.3   Determination of Direct-Beam Position

When using two detectors as described in the previous sections, the simultaneously recorded diffraction patterns are merged into a single file [2]. The parameters necessary to merge the patterns are the direct beam position in each detector, and both the relative rotation angle and the ratio of the pixel size between the two detectors placed at different camera distances.

Two different methods are implemented for merging diffraction patterns in the second subprogram. The first method assumes that XFEL pulses arrive at the same position throughout the experiment. Then, the direct-beam position, which is common for all diffraction patterns, is determined using a diffraction pattern from a cuboid-shaped cuprous oxide particle with dimensions of approximately 250–500 nm [7] (Fig. 6.5). When a face of the particle is normal to the incident X-ray, the diffraction intensity $I$ at a scattering vector $(X, Y)$ is approximated by the Fraunhofer diffraction of a rectangular-shaped aperture with edge lengths of $2A$ and $2B$ [8] as

$$
\begin{aligned}
I(X, Y) &= C \left[ \frac{\sin(2\pi AX)}{2\pi AX} \right]^2 \left[ \frac{\sin(2\pi BY)}{2\pi BY} \right]^2 \\
\begin{pmatrix} X \\ Y \end{pmatrix} &= \begin{pmatrix} \cos\Theta & \sin\Theta \\ -\sin\Theta & \cos\Theta \end{pmatrix} \begin{pmatrix} \alpha(x - x_0) \\ \beta(y - y_0) \end{pmatrix},
\end{aligned}
\tag{6.2}
$$

where $(x, y)$ is the position of the detector pixel. $(x_0, y_0)$ is the direct-beam position. $C$ is a scale factor between the observed and calculated diffraction patterns. The origin-shifted pixel position $(x - x_0, y - y_0)$ is converted to the scattering vector $(X, Y)$ by camera-length dependent parameters $\alpha$, $\beta$ and the angle $\Theta$ between the detector edge and the $X$ axis. The two parameters are calculated using the camera distance $L$, the wavelength of X-ray $\lambda$ and the detector pixel size $D$ as

$$
\alpha = \beta = \frac{2 \sin\{\tan^{-1}(D/L)\}}{\lambda}
$$

A high-quality diffraction pattern from a single copper-oxide particle is selected from those obtained by scanning of a membrane with adsorbed particles
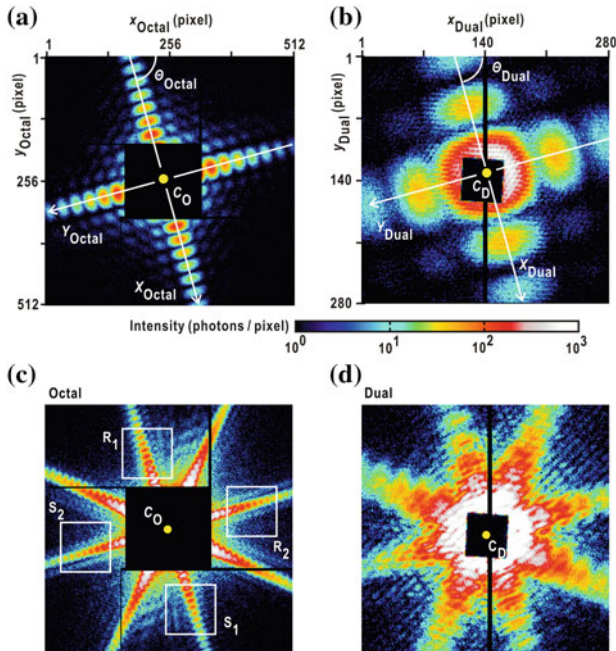
**Fig. 6.5** Determination of camera parameters by applying (6.1) to the diffraction pattern of a cuboid-shaped copper-oxide particle simultaneously recorded by the MPCCD-Octal (**a**) and MPCCD-Dual (**b**) detectors. The parameters and coordinates used in the calculation are indicated. In the second method, by applying (6.2), ROIs are used to search for the beam center position that maximizes the $C_{sym}$ score for the diffraction pattern in the MPCCD-Octal detector (**c**) and MPCCD-Dual (**d**) detectors. Panels are reused from [2, https://doi.org/10.1107/s1600577514003439] with permission from The International Union of Crystallography

(Figs. 6.5a, b). First, the beam center position, ($c_0^{Dual} = \left(x_0^{Dual}, y_0^{Dual}\right)$, the inclination angle $\Theta_{Dual}$, the scale factor, and the particle size ($A$ and $B$) are determined for the MPCCD-Dual detector. Next, a set of parameters for the MPCCD-Octal detector ($c_0^{Octal} = \left(x_0^{Octal}, y_0^{Octal}\right)$, $\Theta_{Octal}$, and a scale factor) are determined by using the estimated size of the particle.

In most cases, the positions of the diffraction maxima predicted from the particle size and the direct-beam position are consistent with those observed. In addition, the in-plane rotation of the MPCCD-Dual detector relative to the MPCCD-Octal detector is less than approximately 7 mrad. The accuracies of the beam center positions and the inclination angle are approximately 25 μm and 1 mrad, respectively.

The Ewald sphere is approximated as a plane in the small-angle region (see Sect. 2.3.6 in Chap. 2). When atoms displaying anomalous dispersion are absent from the specimens, Friedel centrosymmetry is satisfied in the diffraction patterns (see Sect. 2.3.5 in Chap. 2). Ideally, the diffraction patterns of the ROIs related by

centrosymmetry are identical. A score is introduced to evaluate the degree of centrosymmetry in the diffraction pattern [2] as

$$
\begin{aligned}
C_{\text{sym}} &= \frac{E^2 - O^2}{E^2 + O^2} \\
E &= \frac{1}{2} \sum_{x,y} \left[ I_0(x, y) + I_{\text{sym}}(-x, -y) \right] \\
O &= \frac{1}{2} \sum_{x,y} \left[ I_0(x, y) - I_{\text{sym}}(-x, -y) \right],
\end{aligned}
\tag{6.3}
$$

where $I_0(x, y)$ is the intensity of the targeted ROI and $I_{\text{sym}}(-x, -y)$ is that of its centrosymmetry mate. ROIs composed of more intense speckle peaks with smaller Poisson noise give better $C_{\text{sym}}$ scores. The $C_{\text{sym}}$ score has its maximum value, which is ideally one, when a pixel assumed to be the center-of-symmetry coincides with the direct-beam position in the diffraction pattern. Therefore, (6.2) can be used to find the direct-beam position of any diffraction pattern composed of clear and intense speckle peaks with a good signal-to-noise ratio, even when the positions of the XFEL pulses fluctuate shot-by-shot.

For diffraction patterns with good $C_{\text{sym}}$ scores, a pixel assumed to be the center-of-symmetry can be located within 1–2 pixels around the direct-beam position in the MPCCD-Octal detector, and within 2–4 pixels in the MPCCD-Dual detector. By assuming centrosymmetry with regard to the direct-beam position, one of subprograms generates diffraction patterns for symmetry-related areas lacking diffraction pattern data due to gaps between the detector panels or overlaps of the panel edges.

The fluctuation of the direct-beam position can be used as a diagnostic for the shot-by-shot fluctuation of the averaged momentum of the X-ray photons radiated from electron bunches (Fig. 6.6). The apparent direct-beam position in the MPCCD-Octal detector estimated using the $C_{\text{sym}}$ score is stable within approximately one pixel ($50 \times 50~\mu\text{m}^2$) for several hours. This finding is consistent with the stability of the direct-beam position reported within the range of 19 μm in the vertical and 40 μm in the horizontal direction upstream from the experimental hutch.

## 6.4   Merging Diffraction Patterns from Different Detectors

The third subprogram merges the diffraction patterns recorded simultaneously by the two MPCCD detectors. When merging the diffraction patterns of the two detectors, in addition to the beam center positions, another necessary parameter is the number of pixels in the MPCCD-Dual detector that correspond to one pixel in the MPCCD-Octal detector. The diffraction pattern of the MPCCD-Dual detector is converted to a pixel array virtually generated at the MPCCD-Octal plane. The coordinates of the four corners of each pixel in the MPCCD-Octal detector placed at a camera length $L_O$ are converted to the coordinates in the MPCCD-Dual detector at $L_D$ by the following equation (Fig. 6.7a)
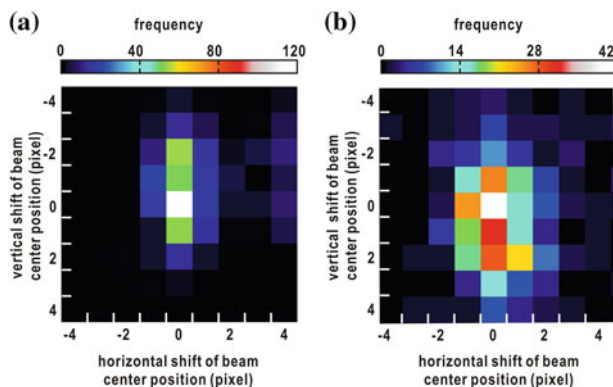
**Fig. 6.6** Fluctuation of the beam center positions in the MPCCD-Octal (**a**) and MPCCD-Dual (**b**) detectors during data collection. The size of the detector pixel is 50 μm. Panels are reused from [2, https://doi.org/10.1107/s1600577514003439] with permission from The International Union of Crystallography
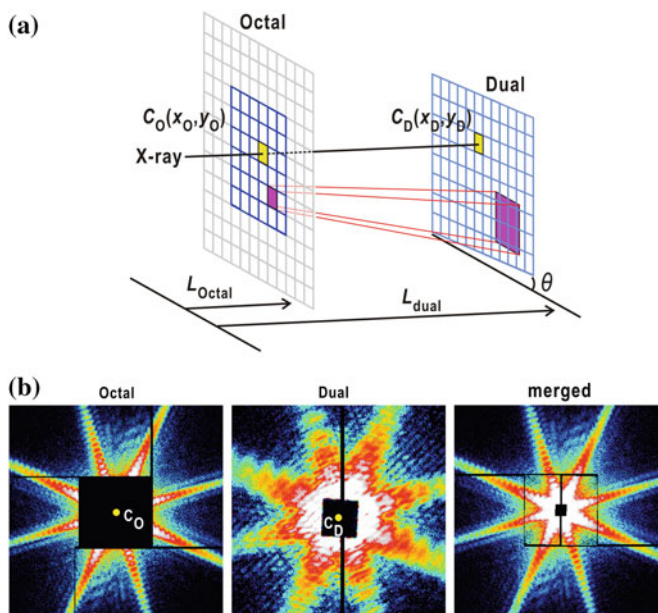


**Fig. 6.7** **a** Geometrical parameters necessary to merge the diffraction patterns recorded by two different detectors placed at different camera lengths. **b** Example of a merged diffraction pattern. Panels are reused from [2, https://doi.org/10.1107/s1600577514003439] with permission from The International Union of Crystallography

$$\begin{pmatrix} x_{iD} \\ y_{iD} \end{pmatrix} = \begin{pmatrix} x_D \\ y_D \end{pmatrix} + \frac{L_D}{L_O} \begin{pmatrix} \cos\theta & \sin\theta \\ -\sin\theta & \cos\theta \end{pmatrix} \begin{pmatrix} x_{iO} - x_O \\ y_{iO} - y_O \end{pmatrix}, \qquad (6.4)$$

where $(x_{iO}, y_{iO})$ and $(x_{iD}, y_{iD})$ are the positions of the $i$th corner in the pixel coordinate systems of the MPCCD-Octal and MPCCD-Dual detectors, respectively. $(x_O, y_O)$ is the beam-center position of the MPCCD-Octal detector, and $(x_D, y_D)$ is that of the MPCCD-Dual detector. The angle $\theta$ is the rotation angle of the edge line of the MPCCD-Dual detector relative to that of the MPCCD-Octal detector, and is calculated as the difference between $\Theta_O$ and $\Theta_D$ shown in Fig. 6.5.

The algorithm smoothly connects the diffraction patterns of the two detectors at the borders (Fig. 6.7b), and displays a good signal-to-noise ratio, providing summed intensities greater than $5 \times 10^5$ photons and a $C_{sym}$ larger than 0.7 for a ROI in the small-angle region.

## 6.5   Phase Retrieval Calculation

### 6.5.1   Outline of the PR Calculation

The fourth subprogram is developed for PR calculation through simulation studies of structural analyses [9, 10]. This subprogram implements the HIO algorithm in combination with the SW algorithm.

For PR calculations during XFEL-XDI experiments described in Chap. 4, a diffraction pattern is trimmed to a size of $256 \times 256$ pixels (corresponding to a resolution of 54.7 nm in real space), and then reduced to a size of $128 \times 128$ pixels by a $2 \times 2$ binning. Although the binning reduces the oversampling ratio to a quarter of that of the original, a better signal-to-noise ratio is more important for the success of the PR calculations.

The initial support used is calculated by the auto-correlation function, which is a Fourier transform of the diffraction pattern. In the HIO cycle, the weight $\beta$ in the real space constraint (3.22) is kept at 0.9 throughout. In the SW update, the parameter $\alpha$ in (3.23) is set to 1.5 or 3.0 pixels at the initial stage, and is gradually reduced to 0.990–0.995 of its value in the previous update. Once $\alpha$ reaches a value less than 0.90, its value is fixed at 0.90. After the update of the PR map by the SW algorithm, areas with densities less than 5% of the highest density are excluded from the support shape (3.24).

Each PR run is conducted over 10,000 iterations of the HIO cycle with a support update by SW for every 100 HIO cycles. After the iterations are completed, an additional 1000 HIO cycles are applied. The progress and convergence of the calculation are monitored by the parameter $\gamma$ (3.27) and the crystallographic $R_F$-factor (3.28). The oversampling ratio of the PR map, the zero-angle diffraction intensity, $\gamma$,

and $R_F$ suggest necessary conditions for the success or failure of PR calculations. The fourth subprogram outputs PR maps as binary image data. A scheme to address the success of PR calculations will be presented in Chap. 7 [11, 12].

## 6.5.2  Two-Dimensional Fast Fourier Transform

The fourth subprogram is parallelized for efficient and fast calculations using a supercomputer. For its execution, a two-dimensional fast Fourier transform program is developed to efficiently utilize several cores ($N_{core}$) by reducing the number of memory accesses and the computational costs of the two-dimensional fast Fourier transform [11].

A two-dimensional electron density map $\rho(x, y)$ is divided into $N_{core}$ parts with respect to $x$. The $i$th strip is processed on the $i$th core. A function calculated by the one-dimensional fast Fourier transform with respect to $y$ for the part on the $i$th core is further divided into $N_{core}$ blocks. The $j$th block on the $i$th core is exchanged with the $i$th block on the $j$th core using the message passing interface of the computer system. Then, the function appearing on the $i$th core becomes

$$F\left(1 \leq x \leq N_{pixel}, (i-1)\frac{N_{pixel}}{N_{core}} < v \leq i\frac{N_{pixel}}{N_{core}}\right).$$

Through the one-dimensional fast Fourier transform with respect to $x$ in the $i$th core, the structure factor is calculated as

$$F\left(1 \leq u \leq N_{pixel}, (i-1)\frac{N_{pixel}}{N_{core}} < v \leq i\frac{N_{pixel}}{N_{core}}\right).$$

This process is also applied to the inverse two-dimensional fast Fourier transform to transform structure factors into density maps. A PR calculation utilizing this protocol on 12 cores is approximately ten times faster than that performed by an ordinary Fourier transform on a single core.

For diffraction patterns of $128 \times 128$ pixels, the scalability of the speed of the PR calculation protocol is almost linear in each 12-core node. In addition, to maximize the performance in the on-the-fly analysis of the huge number of diffraction patterns, the fourth subprogram automatically submits jobs to idling nodes by monitoring the status of the nodes.

## 6.6 Performance and Output

### 6.6.1 Performance

Data processing and PR calculations are carried out immediately after data collection. The performance of subprograms in processing 1000 diffraction patterns are summarized in Table 6.1. The three subprograms for raw data processing deliver several files to indicate the progress of the calculations.

The data processing program suite outputs a macro file instructing ImageJ to compile a set of the observed diffraction patterns, PR maps, and diffraction patterns calculated from the maps. The compiled file, called "montage," is helpful to inspect which diffraction patterns are worth further analysis (Fig. 6.8) [3].

The performance was measured on a supercomputer composed of 960 Intel(R) Xeon(R) CPU X5690 cores (3.47 GHz/core).

### 6.6.2 Graphical User Interface

The data processing program suite is equipped with its own graphical user interface to display the progress of the data processing and the statistics of parameters used to evaluate the quality of data for each raster scan. The GUI is composed of two panels (Fig. 6.9). One panel displays the status of data processing for the diffraction patterns of every raster-scan run and the number of diffraction patterns extracted by the first subprogram. The other panel presents the quality of the processed data and the reconstructed projected electron densities. Frequency distributions of the total intensity, effective resolution, and centrosymmetry of the diffraction patterns are displayed after the completion of the four-step processing procedure (Fig. 6.9). The frequency distribution of the beam center position in the MPCCD-Octal detector is also displayed.

**Table 6.1** Performance of subprograms on a supercomputer

| Subprograms | Number of used cores | CPU time for processing 1000 diffraction patterns (s) |
|---|---|---|
| 1 | 48 (4 nodes/core) | 30 |
| 2 and 3 | 48 (4 nodes/core) | 100 |
| 4 | 48 (4 nodes/core) | 1587 |
| Total | | 1717 |
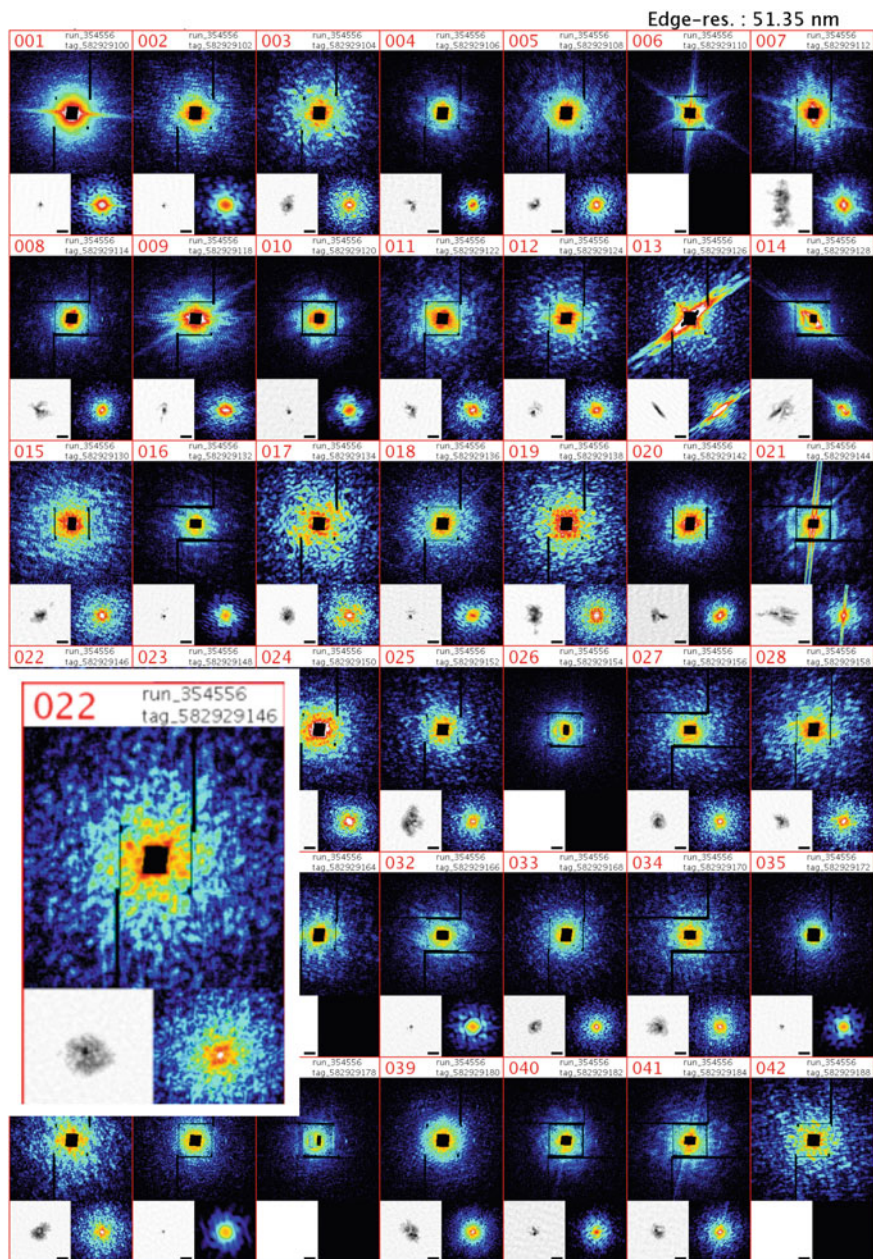
**Fig. 6.8** An example of a montage compiling diffraction patterns from biological specimens. The 22nd diffraction pattern is magnified with the phase retrieved electron density map (lower left in the magnified view) and the diffraction pattern calculated from the density map (lower right). Published with kind permission of Masayoshi Nakasako 2017. All Rights Reserved

**(a)**



**(b)**



**Fig. 6.9** Graphical user interface of the data processing program. **a** Panel reporting the status of data processing. **b** Statistics of the processed diffraction data in a raster scan, including diffraction intensity, maximum resolution, centrosymmetry score, estimated diameter of the particles, crystallographic R-factor, γ-factor, and oversampling ratio. The density map on the right shows the frequency distribution of the beam-center positions of the XFEL pulses estimated by (6.2) during a raster scan. Published with kind permission of Masayoshi Nakasako 2017. All Rights Reserved

# References

1. A. Kobayashi et al., Rev. Sci. Instrum. **87**, 053109 (2016)
2. Y. Sekiguchi et al., J. Synchrotron Rad. **21**, 600 (2014)
3. Y. Sekiguchi et al., J. Synchrotron Rad. **21**, 1378 (2014)
4. A. Rose, Advances in Electronics and Electron Physics **1**, 131 (1948)
5. Starodub et al., J. Synchrotron Rad. **15**, 62 (2008)
6. A. Kobayashi et al., J. Synchrotron Rad. **23**, 975–989 (2016)
7. C.H. Kuo, C.H. Chen, M.H. Huang, Adv. Funct. Mater. **17**, 3773 (2007)
8. M. Born, E. Wolf, *Principles of Optics* (Cambridge University Press, Cambridge, 1999)
9. T. Oroguchi, M. Nakasako, Phys. Rev. E **87**, 022712 (2013)
10. W. Kodama, M. Nakasako, Phys. Rev. E **84**, 021902 (2011)
11. Y. Sekiguchi, T. Oroguchi, M. Nakasako, J. Synchrotron Rad. **23**, 312 (2016)
12. Y. Sekiguchi et al., J. Synchrotron Rad. **24**, 1024 (2017)

# Chapter 7
# Phase Retrieval of Diffraction Patterns

**Abstract** In the phase retrieval (PR) calculations of experimentally obtained diffraction patterns, it is not easy to find the correct electron density maps due to the lack of diffraction patterns around the zero-scattering angle and the Poisson noise in detecting the X-ray photons. In this chapter, we present some approaches to obtain the correct electron density maps from experimental diffraction patterns. The first is the multivariate analysis of a large number of PR maps. The second is the introduction of a similarity score to extract the correct electron density maps. The third is the dark-field PR method applied to diffraction patterns with missing small-angle regions. The algorithms presented would be helpful in solving the phase problem in the structural analyses of non-crystalline particles.

## 7.1 Success and Failure in PR Calculations

One of the difficulties in XDI structural analysis is the reconstruction of the electron density maps of specimen particles from diffraction patterns which lack phase information. In X-ray protein crystallography, phase values can be estimated experimentally by inspecting changes in the diffraction intensities caused by heavy-atom labeling and/or anomalous dispersion of atoms in protein molecules [1] (see Sect. 2.4.2 in Chap. 2). In contrast, phase estimation in XDI is entirely performed by a computational procedure, without using experimental information [2, 3].

PR algorithms have the potential to reconstruct correct electron density maps from experimentally obtained diffraction patterns. However, one serious issue is the frequent failure of PR calculations for experimental diffraction patterns.

As the direct beam is very strong and causes fatal damage in the detector, a beamstop is placed in front of the detector to block the direct beam in any X-ray diffraction experiment [4, 5]. To collect the diffraction patterns from the small-angle region, parasitic scattering from the upstream optics and the size of the beamstop must be reduced as much as possible (see Chap. 4). In addition, the diffraction intensities in the small-angle region are considerably strong; therefore, the detector pixels are sometimes saturated and cannot record diffraction pattern [6]. The saturation

of detector pixels is particularly severe in structural analyses in XFEL-XDI experiments. As a single XFEL pulse destroys a specimen particle, the diffraction pattern of the particle is recorded only once.

Diffraction patterns in the very small-angle region contain structural information on the overall shape and total electrons of the specimen particles (Sect. 2.5 in Chap. 2). In addition, the success of the PR calculations also depends on the signal-to-noise ratio. The Poisson noise in X-ray detection modifies the considerably weak diffraction patterns and causes the breakdown of Friedel centrosymmetry. The absence of diffraction patterns in the small-angle region and the Poisson noise make it difficult to obtain a unique solution for the electron density maps of specimen particles.

Figure 7.1 demonstrates that PR calculations do not always provide the correct electron density maps [7]. For a diffraction pattern from an aggregate of ten gold colloidal particles, 1000 independent PR calculations are conducted starting from different random electron density maps. As we know the shapes of the gold colloidal particles, we can determine which electron density maps are correct. Among 1000 PR calculations, 487 gave maps in which the ten gold colloidal particles are identified, while electron densities assignable as colloidal particles are absent or unclear in the maps from 513 calculations. Parameter $\gamma$ (3.27) and the OS ratio can monitor the convergence of PR calculations in real space. However, the convergence is insufficient to indicate the success of each PR. For instance, although parameter $\gamma$ is ideally close to zero, the values in failed PR calculations are smaller than those in the successful calculations. OS ratios are difficult to use an indicator of which calculations are successful (Figs. 7.1c, d). The crystallographic $R_F$-factor (3.28), which indicates how close the structure amplitudes calculated from a PR map are to those observed in reciprocal space, is also difficult to use for evaluating which calculations are successful, because the values of the failed maps are frequently better than those of the correct maps (Fig. 7.1e). From the zero-angle diffraction intensities, it would be possible to distinguish correct and incorrect electron density maps. However, the relevant threshold is case dependent (Fig. 7.1f).

To date, the most probable maps are extracted from hundreds of PR calculations by referring to particle images from LM and/or EM. However, LM and EM images provide little with regard to the internal fine structures of thick specimens. Conventional parameters monitoring the convergence of PR calculations give incomplete confirmation of the accuracy of PR maps. In order to establish XDI as a useful tool for the structural analysis of biological specimens, protocols or methods are necessary to objectively extract the most probable PR maps for given diffraction patterns without any information or reference from other imaging techniques.

Here, we will give an account of three approaches to extract the most probable PR maps from experimental diffraction patterns. In the first approach, multivariate analysis, including principal component analysis (PCA) and the K-means clustering method, is introduced [8]. The second approach uses the similarity score to determine the correct electron density maps in phase-retrieval (PR) calculations from
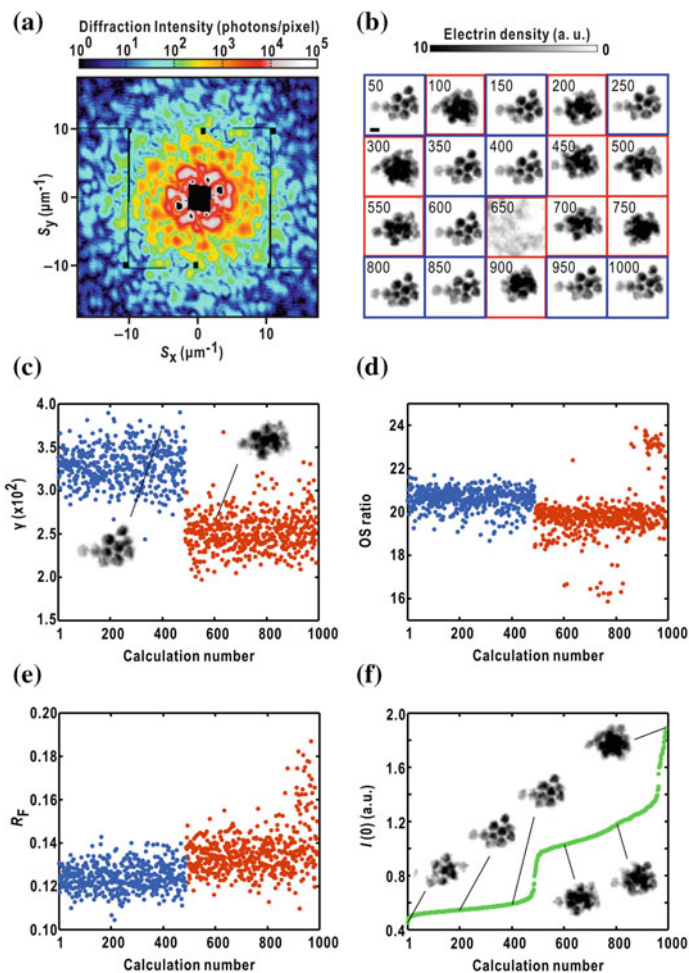
**Fig. 7.1  a** Diffraction pattern from an aggregate of ten gold colloidal particles with diameters of 250 nm. The resolution at the edge is 17.4 $\mu m^{-1}$ (corresponding to a resolution of 57.4 nm in real space). **b** PR electron density maps selected from every 50 trials of 1000 independent PR calculations starting from initial maps with different random noise. The successful and failed PR calculations are indicated by blue and red boxes, respectively. **c** parameter $\gamma$, **d** OS ratio, and **e** $R_F$-factor are plotted for 1000 PR runs. Red dots indicate the values from failed PR runs, while blue dots are used for the results from successful calculations. The OS ratio is the ratio between the number of pixels in the final updated support and that of the map. **f** Zero-angle diffraction intensity plotted after sorting. In panels (**c**) and (**f**), some representative PR maps are inset. Panels are reused from [7, https://doi.org/10.1107/s1600577517008396] after modification with permission from The International Union of Crystallography

diffraction patterns [7]. The third approach is the dark-field PR method with the constraint of Friedel centrosymmetry for diffraction patterns which are heavily lacking around the zero-scattering angle [9]. These approaches will contribute to the improved reliability of PR calculations without any experimental information on phase sets.

## 7.2   Multivariate Analysis

Here, a protocol is proposed to objectively extract the most probable maps from a large number of PR maps [8]. In this protocol, each PR map composed of $J$ pixels is treated as a point in a $J$-dimensional space, as in the single particle analysis in TEM [9, 10]. PCA allows us to characterize the distribution of the maps in $J$-dimensional space [11]. When a small number of principal axes can describe the variation in the distribution, the K-means clustering method [12] classifies the PR maps into a small number of groups and helps to extract the most probable PR maps. This subsection presents the details of the protocol and the application to the structural analysis of biological specimens.

### 7.2.1   Principal Component Analysis and Clustering

From a diffraction pattern, a large number of maps ($N$) composed of $J$ pixels are retrieved starting from different initial maps with random electron densities. In each PR map, the electron density of the $i$th pixel is regarded as the value of the $i$th axis
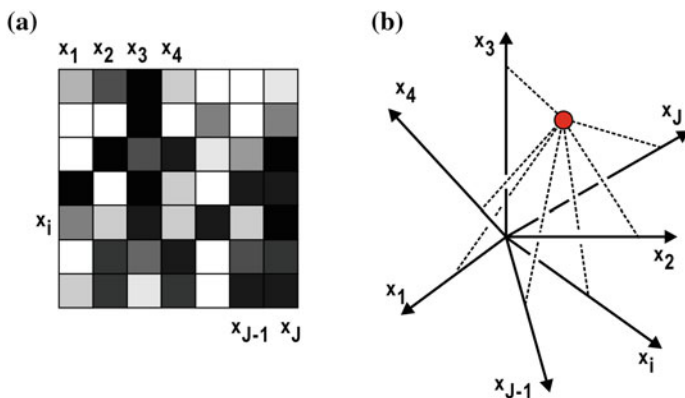


**Fig. 7.2** Electron density map composed of $J$ pixels (**a**) is expressed as a point in $J$-dimensional space (**b**). Published with kind permission of Masayoshi Nakasako 2017. All Rights Reserved

in $J$-dimensional space. Therefore, as schematically illustrated in Fig. 7.2, each electron density map is represented as a point in $J$-dimensional space.

In the protocol, before applying PCA, two preparation steps for manipulating the PR maps are necessary. First, the PR maps are superimposed by their centroids with an accuracy of better than 1 pixel, because the diffraction pattern loses the information on the absolute position of the specimen particle. In addition, because of the Friedel centrosymmetry in the diffraction pattern (2.22), a map generated by a $\pi$-rotation of a PR map is also acceptable. Either the 0- or $\pi$-rotation is selected, depending on which gives a larger correlation coefficient against the reference map. After these manipulations, each map is represented as a point in $J$-dimensional space.

It is difficult to inspect the distribution of maps in $J$-dimensional space. Therefore, PCA is applied to examine whether the distribution can be illustrated in a lower-dimensional space with minimal loss of information [13, 14]. For PCA, a matrix $\mathbf{X}$ to describe the set of $N$ electron density maps comprised of $J$ pixels is defined as

$$\mathbf{X} = \begin{pmatrix} x_{11} - \langle x_1 \rangle & x_{12} - \langle x_2 \rangle & \cdots & x_{1J} - \langle x_J \rangle \\ x_{21} - \langle x_1 \rangle & x_{22} - \langle x_2 \rangle & \cdots & x_{2J} - \langle x_J \rangle \\ \vdots & \vdots & \ddots & \vdots \\ x_{N1} - \langle x_1 \rangle & x_{N2} - \langle x_2 \rangle & \cdots & x_{NJ} - \langle x_J \rangle \end{pmatrix} \tag{7.1}$$

where $x_{ij}$ is the electron density at the $j$th pixel of the $i$th map. $\langle x_j \rangle$ is the averaged electron density of the $j$th pixel among the $N$ maps. From the covariance matrix given by the product of the matrix and its transpose ($X^t$), $\mathbf{D} = X^t X$, the eigenvalue $\lambda$ and eigenvectors $\mathbf{u}$ of $\mathbf{D}$ are given by solving the equation $\mathbf{D}\mathbf{u} = \lambda\mathbf{u}$.

The eigenvalues are the indices informing the variance of the distribution of the PR maps in $J$-dimensional space. For instance, the eigenvector for the largest eigenvalue gives the principal axis approximating the distribution of the $N$ PR maps in $J$-dimensional space. Each eigenvector has $J$ elements and is represented as an image with $J$ pixels. If the eigenvectors up to the $L$th largest eigenvalue ($L \ll J$) have a significant contribution to the variance, the distribution in $J$-dimensional space can be visualized as a projection onto the space spanned by the $L$ eigenvectors, with minimal loss of information from the distribution in $J$-dimensional space. The projections onto the $L$ axes are given mathematically by the inner product of the $J$-dimensional maps and the $L$ eigenvectors.

Next, the maps projected onto the $L$-dimensional space are classified by the K-means clustering method. The method classifies the maps into a limited number of groups ($M$) by minimizing the sum of the squared distances between the maps and the centroids of the classes defined by

$$T = \sum_{m=1}^{M} \sum_{\mathbf{y}_{im} \in m} (\mathbf{y}_{im} - \langle \mathbf{y}_m \rangle)^2, \tag{7.2}$$

where $\boldsymbol{y}_{im}$ is the $L$-dimensional vector indicating the position of the $i$th map belonging to the $m$th class. $\langle \boldsymbol{y}_m \rangle$ is the centroid of the $m$th class [12].

In practice, PCA is first applied to maps superimposed with regard to their centroids and the 0-/π-rotation. In many cases, the eigenvectors with the first and second largest eigenvalues contribute significantly to illustrate the distribution of the maps in $J$-dimensional space. Then, the maps are projected onto the plane spanned by the two principal components and are classified by the K-means clustering method, assuming 10 or more groups. As classification by the K-means clustering method depends on the distribution of the initial random centroids given for the assumed groups, the result giving the minimum $T$ is selected from 100 independent clustering trials.

## 7.2.2   Phase-Retrieval Transfer Function and the Figure of Merit

To assess the consistency of the phase values, i.e., electron density maps, within the groups classified by K-means clustering, we define the average of the phase terms at scattering vector $\boldsymbol{S}$ as

$$\langle \varphi(\boldsymbol{S}) \rangle = \frac{\left| \sum_{j=1}^{M} \exp\left[ i\varphi_j^{\text{cal}}(\boldsymbol{S}) \right] \right|}{M} \tag{7.3}$$

where $M$ is the number of maps included in the class and $\varphi_j^{\text{cal}}(\boldsymbol{S})$ is the phase value at the scattering vector $\boldsymbol{S}$ calculated from the $j$th map in the class. The radial average of $\langle \varphi(\boldsymbol{S}) \rangle_{\text{rad}}$ gives the phase-retrieval transfer function (PRTF), which assesses the effective resolution of a map calculated by averaging a set of PR maps from an experimental diffraction pattern [13]. The effective resolution is given as the inverse of the scattering vector length at which the PRTF first drops to 0.5 or 0.368 ($1/e$).

In X-ray crystallography and transmission electron microscopy, the reliability of an experimentally determined phase set is assessed by using the figure of merit (FOM) (Sect. 2.4.3 in Chap. 2) [14] defined as

$$FOM(\boldsymbol{S}) = \frac{\left| \sum_k P(\varphi_k(\boldsymbol{S})) \exp[i\varphi_k(\boldsymbol{S})] \right|}{\sum_k P(\varphi_k(\boldsymbol{S}))}, \tag{7.4}$$

where $P(\varphi_k(\boldsymbol{S}))$ is the experimentally estimated phase probability distribution function for the $k$th phase angle at a scattering vector $\boldsymbol{S}$. FOM is an important index to assess the quality of experimentally estimated phase values, i.e., the quality of maps. For instance, in X-ray protein crystallography, the electron density maps can be utilized to build molecular models, when the FOM averaged radially in a resolution shell becomes larger than 0.5 [15, 16]. In single-particle analysis of

cryogenic TEM, the effective resolution of the reconstructed three-dimensional electrostatic potential map is defined as that where the FOM averaged radially in a resolution shell drops to 0.5 [17].

Here we consider the correlation between PRTF and FOM to consider a more objective threshold to address the effective resolution of PR maps. When $P(\varphi_k(S))$ is finely measured, the sum of the phase shifts in PRTF can be approximated as

$$\sum_{j=1}^{N} \exp\left[ i\varphi_j^{\text{cal}}(S) \right] \approx \sum_{k} P(\varphi_k(S)) \exp[i\varphi_k(S)]$$

where $P(\varphi_k(S))$ is normalized as $\sum_k P(\varphi_k(S)) = M$. Then, the PRTF is related to the figure of merit as

$$\langle \varphi(S) \rangle_{\text{rad}} \approx FOM(S). \tag{7.5}$$

Therefore, based on (7.5) and the threshold levels of FOM in crystallography and cryo TEM on proteins, the resolution where the PRTF decreases to 0.5 can be defined as the effective resolution of an averaged map in the multivariate analysis protocol.

### 7.2.3   Application to Structural Analysis of Biological Specimens

The feasibility of the protocol is examined in the application to the structural analyses of noncrystalline particles in material sciences and biology [7]. As a demonstration of the application to biological particles, a structural analysis of a chloroplast isolated from the small eukaryote *Cyanidioschyzon merolae* is shown (Fig. 7.3a) [18]. The chloroplast provided a diffraction pattern with a good signal-to-noise ratio of greater than 3 up to a resolution of 17.4 $\mu m^{-1}$ (corresponding to a resolution of 57.4 nm in real space). Speckle peaks arranged into concentric ring patterns indicate that the overall shape of the chloroplast is globular. The protocol consisted of two steps. In the first step, the most probable support shape is selected. Subsequently, the most probable internal structure is proposed under the constraint of the support shape from the first step.

In the first step, PCA was applied to 1000 PR maps calculated by the combination of the HIO and SW algorithms (Sect. 3.6 in Chap. 3 and Sect. 6.5.1 in Chap. 6). The first two principal components described 45% of the total variance in the distribution of the PR maps in the $50 \times 50$-dimensional space. The K-means clustering roughly classified the maps into three groups (Fig. 7.3b). The largest group was composed of five clusters and distributed in a wide range along the two principal component axes. Taking the number density and the effective resolution from each class, the class with the largest number and located at the center of the
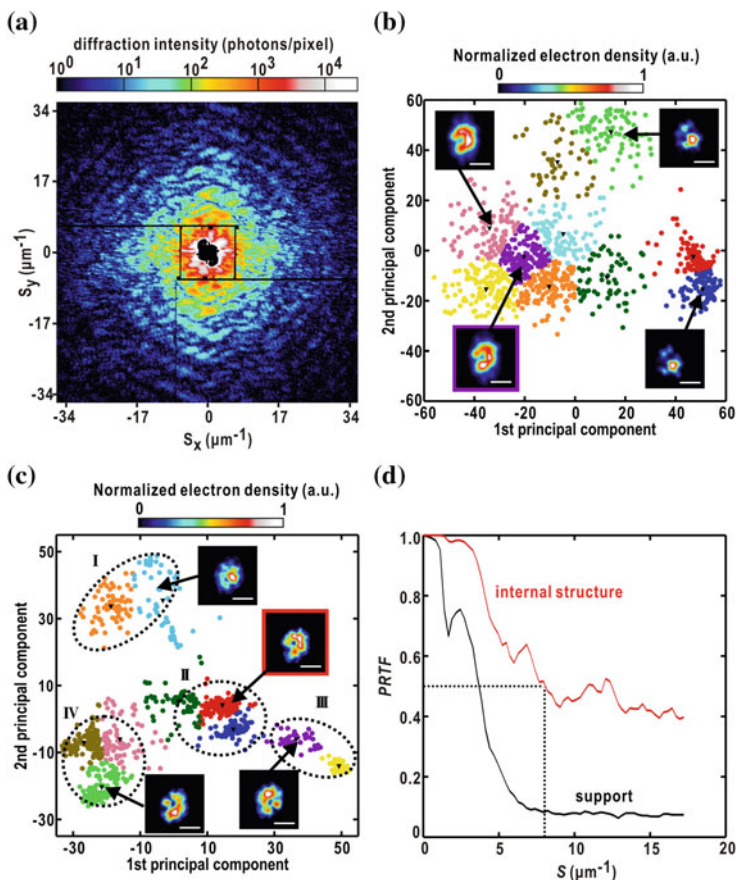
**Fig. 7.3** **a** Diffraction pattern from a chloroplast of *C. merolae*. **b** Distribution of the 1000 PR maps, which are retrived from the diffraction pattern in panel a, is displayed in the plane spanned by the two eigenvectors of the first and second largest eigenvalues after the PCA. Dots with different colors indicate the positions of maps in ten classes separated by the K-means clustering. Inserts show the averaged maps of a few clusters with a scale bar of 500 nm. The map with the colored box is the most probable. **c** Distribution of 1000 OSS maps after PCA illustrated as in panel (**b**). **d** Plots showing the PRTFs for maps in selected clusters composed of the most probable maps in the first (black line) and second (red line) steps of the protocol. Panels are reused from [8, https://doi.org/10.1107/s1600577515018202] after modification with permission from The International Union of Crystallography

group was selected as the most probable support shape. The selected support shape was globular, as expected from the concentric diffraction pattern, and had a maximum dimension consistent with that expected from the auto-correlation function of the diffraction pattern.

In the second step, PCA was carried out for 1000 maps, which were retrieved using the OSS algorithm [24] for the most probable support shape selected in the

first step. The first and second principal components explained 42% of the total variance among the 1000 PR maps. The maps on the plane spanned by the two principal components were distributed into one major cluster and three minor clusters (Fig. 7.3c). Only maps belonging to the major cluster were consistent with that of the most probable map in the first step. The K-means clustering revealed that the major cluster was composed of three subclusters. The averaged map from the most heavily populated subcluster displaying $R_F$ values of 0.36 was selected as the most probable projection structure of the chloroplast. The averaged map had a C-shaped internal structure at an effective resolution better than 12 $\mu m^{-1}$ (corresponding to 83 nm) (Fig. 7.3d). The objectively-extracted most probable map with a C-shaped internal structure was consistent with the low-resolution images observed using phase-contrast LM (see Sect. 8.2.2 in Chap. 8).

## 7.3   Similarity Score

### 7.3.1   Variation of the Phase Values During Phase Retrieval Calculations

Figure 7.4a, b show the representative variations of the phase values of the structure factors in the small-angle region of the diffraction pattern in Fig. 7.1a during the progress of PR calculations. In successful PR calculations which give a clear image of the aggregate of ten gold colloidal clusters, the phase values tended to fluctuate around a value. In contrast, phase values varied significantly in failed calculations, in which the images of the gold colloidal particles were unclear. The frequency distributions of the phase values during the PR calculations clearly demonstrate these differences (Fig. 7.4c). The frequency distributions in successful calculations had narrow maxima around a single value, while the phase values in failed calculations were distributed in a wide range. The different tendencies in the variation of the phase values between successful and failed calculations are useful to address which calculation runs provide the correct PR maps.

In order to parameterize these tendencies, in analogy with the FOM of phases in protein crystallography (see 2.23) and TEM, the centroid of the frequency distribution $\langle \alpha(S) \rangle$ is defined as

$$\langle \alpha(S) \rangle = \frac{\left| \sum_k^N P(k, S) \exp[i\alpha_k(S)] \right|}{\sum_k^N P(k, S)} \tag{7.6}$$

where $P(k, S)$ is the frequency distribution in the $k$th bin of the phase angle at scattering vector $S$. Ideally, $\langle \alpha(S) \rangle$ is close to one when the PR calculations rapidly converge to any electron density map, although it is unclear whether the map is correct. On the other hand, $\langle \alpha(S) \rangle$ is close to zero when the PR calculation diverges.

**(a)**



**(b)**



**(c)**
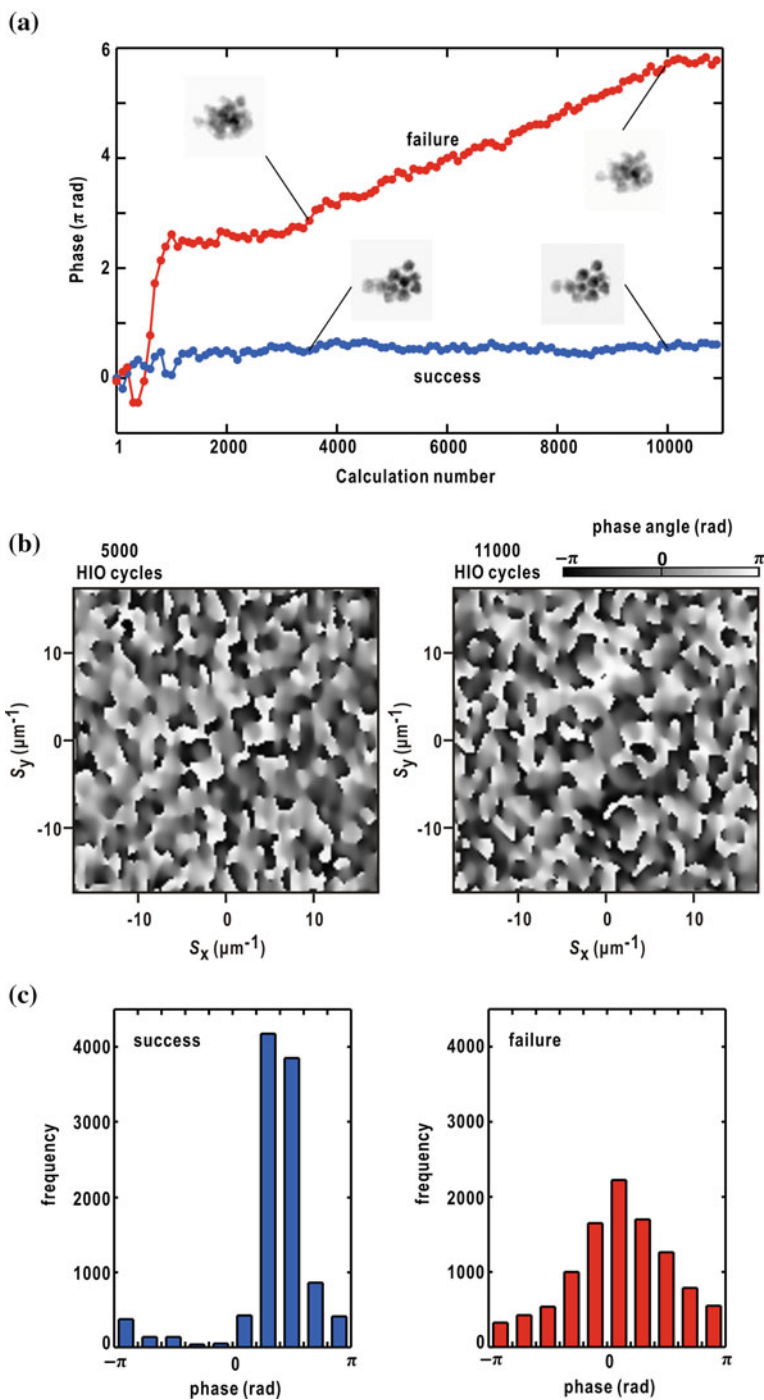
◄**Fig. 7.4  a** Plot showing the variation of the phase values in a pixel located in the small-angle region of the diffraction pattern in Fig. 7.1a during successful (blue line) and failed (red line) PR calculations. The PR maps at the 3500th and 10000th HIO cycles are shown. **b** Phase values of the diffraction pattern at the 5000th and 11,000th HIO cycles of a successful calculation. **c** Frequency distributions of the phase values at a pixel accumulated during 11,000 HIO cycles in a successful (left) and failed (right) PR calculation. Panels are reused from [7, https://doi.org/10.1107/s1600577517008396] after modification with permission from The International Union of Crystallography

In the small-angle regions of diffraction patterns, the number of pixels ($N_\alpha$) with $\langle\alpha(S)\rangle$ values exceeding a threshold value, empirically 0.5, tends to be larger in the case of successful PR calculations than that in failure cases. The threshold is in correlation with those used in experimental estimations of phase sets in single particle cryo-electron microscopy [17] and X-ray protein crystallography [15, 16], where an averaged FOM better than 0.5 is the major threshold for obtaining interpretable maps.

In successful PR calculations for the diffraction pattern in Fig. 7.1a, the values of $N_\alpha$ ranged from 300 to 3500, while those in the failed calculations were less than 2000. Therefore, $N_\alpha$ can act as an index to determine whether PR calculations succeed or fail. In addition, a PR calculation with the highest value of $N_\alpha$ can be assumed to succeed in the reconstruction of a map that is closely similar to the true one.

### 7.3.2   Similarity Score

Out of 1000 independent PR calculations, the maps similar to "the best map" with the highest $N_\alpha$ value would be correct. However, when the phase values (PR maps) converge to the correct values in the final stages of a PR calculation, the $N_\alpha$ values are as small as those in failed calculations. This is a weak point of using $N_\alpha$ values as indices to extract the correct PR maps.

A score which evaluates how similar a PR map is to the best map helps to extract the correct map [8]. The score is defined as

$$T_\mathrm{j} = \frac{\sum_{x,y}\left|\rho_1(x,y) - \rho_\mathrm{j}(x,y)\right|}{\sum_{x,y}\left|\rho_1(x,y) + \rho_\mathrm{j}(x,y)\right|} \tag{7.7}$$

where $\rho_1(x,y)$ is the electron density at the point $(x,y)$ in the best map, and $\rho_j(x,y)$ is that of the $j$th electron density map. The score is the normalized version of the Manhattan distance [19], and is sensitive to pixel-by-pixel variation between two images.

Figure 7.3 shows representative examples to demonstrate the usefulness of the similarity score to extract maps of successful PR calculations in reference to the best map. For a diffraction pattern from an aggregate of gold colloidal particles (Fig. 7.5a),

1000 HIO/SW calculation were carried out independently. Approximately 150 calculations gave maps that were difficult to interpret. The best map was composed of the electron densities of six gold colloidal particles with clear edges (Fig. 7.5c). PR maps displaying $T_j$ scores less than 0.2 had electron density distributions closely similar to the best map. The averaged map, which was calculated for approximately 530 maps with $T_j$ values of less than 0.2, was composed of six images of gold colloidal particles as well as the best map with a standard deviation of less than 0.5% of the highest density. In contrast, maps with $T_j$ scores larger than 0.2 lost the details of gold colloidal particles.

Figure 7.5d shows an application of $N_\alpha$ and the $T_j$ scores to a diffraction pattern missing parts of small-angle region due to the saturation of the detector pixels (Fig. 7.5b). For more than 650 PR maps, the $T_j$ scores are less than 0.15. The majority of the incorrect maps have $T_j$ scores larger than 0.2. Although a small number of incorrect electron density maps are included in the averaging, the maximum value of the standard deviation for the averaged electron density maps is less than 0.5% of the highest density.

If the best map is correct, the combination of the $N_\alpha$ and $T_j$ scores would be useful to determine which electron density maps are correct rather than only relying on the conventional parameters, i.e., $\gamma$, $R_F$, and the oversampling ratio. However, a high $N_\alpha$ score is still insufficient to determine whether the retrieved density map is correct or incorrect, as described below. In fact, we rarely encounter cases where the best maps are incorrect. In those cases, the same protocol with a slight modification is applicable to find the correct maps.

Through many PR calculations in structural analyses, the correct maps are included in PR maps with the 100th highest $N_\alpha$ scores. Another score to examine the cross-similarity between a number of PR maps is defined [8] as

$$T_{ij} = \frac{\sum_{x,y} \left| \rho_i(x,y) - \rho_j(x,y) \right|}{\sum_{x,y} \left| \rho_i(x,y) + \rho_j(x,y) \right|} \tag{7.8}$$

where $\rho_i(x,y)$ is the $i$th reference electron density map and $\rho_j(x,y)$ is the targeted map for examining the similarity to the reference. By changing the reference PR map from the highest to the 100th highest $N_\alpha$ score, the correct maps can be sought

out. The $T_{ij}$ scores empirically tend to be less than 0.2 when both the reference and target maps are correct. In contrast, a pair made up of a correct and incorrect map or a pair of incorrect maps have scores larger than 0.4. These clear differences in the $T_{ij}$ score ensure the extraction of the correct maps.

For the success in the extraction of PR maps by using the $N_a$, $T_j$, and $T_{ij}$ scores, the following tendencies are necessary in the variation of the phase values during the progress of the PR calculations, and in the similarities among PR maps: (i) Phase values in many successful PR calculations converge in the early stages of the PR cycles, while those in failed calculations continuously vary cycle-by-cycle. (ii) PR maps from successful calculations are similar to each other, while those of failed cases are mutually different. (iii) A reference map closely similar to the true one in the similarity analysis gives the largest number of maps with scores less than 0.2.

### 7.3.3   Practical Use of Similarity Score

Although various types of PR algorithms have been proposed to obtain the most probable maps from the PR calculations [2, 20–23], protocols to find the correct maps are still the subject of much discussion. Because a large number of diffraction patterns can be collected within a short time in XFEL-XDI experiments, automatic, reliable, and efficient extraction of maps from successful PR calculations is necessary without reference to images from other microscopic observation methods. Although the multivariate analysis described in the previous subsection provides opportunities for more objective assessment of PR maps, the protocol requires manual inspection of the results from analyses. In contrast, the combination of the $N_a$ and $T_{ij}$ score is more suitable for automatically and efficiently extracting maps from successful calculations, without time-consuming manual inspection. Of course, because of the much smaller computational costs of the $T_j$-score search as compared to the $T_{ij}$ score search, the $T_j$-score search is the first choice. However, for the automated extraction of the correct maps, the $T_{ij}$ search is better when the computational costs are ignored.

For the purpose of automatic extraction of the correct maps, it is of great interest to compare the correct maps in the similarity analysis and those from the multivariate analysis described in the previous section. In many structural analyses, a group of maps with similarity factors of less than 0.2 overlaps the distribution of the clusters of the most probable maps on the plane spanned by the two principal eigenvectors with the largest and second largest eigenvalues in multivariate analysis. Therefore, maps with similarity scores smaller than 0.2 would be the most probable maps. In the near future, an on-the-fly analysis might dramatically reduce computational costs by monitoring the phase variations to terminate calculations after a confirmation of success in retrieving the correct maps.

## 7.4  Dark-Field Phase-Retrieval Method

In XFEL-XDI experiments, the saturation of the detector pixels frequently occurs in the small-angle region due to strong diffractions from specimen particles with large scattering cross-sections. The dark-field PR method was proposed to reconstruct electron density maps from diffraction patterns, which were considerably lacking patterns in the small-angle regions. In the preliminary version of the dark-field PR method [24], a part of the diffraction pattern from the high-angle regions is extracted by multiplying Gaussian masks for use in PR calculations.

The Friedel centrosymmetry of the diffraction patterns (2.20) works as a powerful constraint in the dark-field PR method. The dark-field PR method with the centrosymmetry constraint functions successfully in the PR calculation for experimental diffraction patterns with significant quantities of missing data in the small-angle region [25].

### 7.4.1  Theoretical Background

Let us consider a diffraction pattern from a non-crystalline particle with a real number electron density $\rho(\boldsymbol{r})$. In the dark-field PR method [24], a diffraction pattern in a high-angle region, where the diffraction intensities are recorded without the saturation of the detector pixels, is extracted by multiplying a Gaussian mask defined as

$$M(\boldsymbol{S}) = \exp[-(\boldsymbol{S} - \boldsymbol{\alpha})^2 \chi^2 / 2] \tag{7.9}$$

where $\boldsymbol{S}$ is a scattering vector. The vector $\boldsymbol{\alpha}$ and parameter $\chi$ represent the peak position and the spatial extent of the mask, respectively. The two parameters reduce the diffraction intensity around the missing area to almost zero.

The map $\rho_{\text{dark}}(\boldsymbol{r})$, called the "dark image," is a complex number expressed by the convolution of $\rho(\boldsymbol{r})$ and the inverse Fourier transform of the complex point-spread function $M(\boldsymbol{S})$, as

$$\rho_{\text{dark}}(\boldsymbol{r}) = \exp\left(-\frac{2\pi^2 r^2}{\chi^2}\right) \exp(-2\pi\, i\, \boldsymbol{r} \cdot \boldsymbol{\alpha}) \otimes \rho(\boldsymbol{r}) \tag{7.10}$$

The components of $\rho(\boldsymbol{r})$ with high spatial frequencies are enhanced significantly.

Friedel centrosymmetry appears in the small-angle diffraction pattern from an object free from anomalous dispersion up to a resolution $S_{\text{max}}$, defined as

$$S_{\text{sep}} = \frac{1}{\lambda} - \left(\frac{1}{\lambda^2} - S_{\text{max}}^2\right)^{\frac{1}{2}} < \frac{1}{d} \tag{7.11}$$

where $d$ is the dimension of the particle in the direction along the incident X-ray. $S_{sep}$ is the distance between point $S_{max}$ on the Ewald sphere and the plane, which intersects the origin of reciprocal space and is normal to the incident X-ray.

Friedel centrosymmetry in diffraction patterns can be used as a constraint for density maps in the dark-field PR method [25]. A mask $M_{sym}(S)$ with centrosymmetry is comprised of a pair of symmetry-related single masks, $M(S)$ and $M(-S)$, written as

$$
\begin{aligned}
M_{sym}(S) &= M(S) + M(-S) \\
&= \exp\left[-(S - \boldsymbol{\alpha})^2 \chi^2/2\right] + \exp\left[-(S + \boldsymbol{\alpha})^2 \chi^2/2\right]
\end{aligned}
\tag{7.12}
$$

Then, the dark image $\rho_{dark}^{sym}(\boldsymbol{r})$ is described as the convolution of $\rho(\boldsymbol{r})$ and a point-spread function as

$$
\rho_{dark}^{sym}(\boldsymbol{r}) = 2\exp\left(-\frac{2\pi^2 \boldsymbol{r}^2}{\chi^2}\right)\cos(2\pi \boldsymbol{r} \cdot \boldsymbol{\alpha}) \otimes \rho(\boldsymbol{r})
\tag{7.13}
$$

Due to the centrosymmetry of $M_{sym}(S)$, $\rho_{dark}^{sym}(\boldsymbol{r})$ must be a real number as well as the point-spread function, the inverse Fourier transform of $M_{sym}(S)$.

A larger mask is more advantageous for increasing the number of data points of the diffraction data used in the PR calculation. An annular shaped mask $M_{annular}(S)$ (Fig. 7.6a) suitable to provide a number of data points is defined by two parameters as

$$
M_{annular}(S) = \int_{\alpha_{min}}^{\alpha_{maxn}} \int_{0}^{2\pi} \exp\left[-\frac{(S - \boldsymbol{\alpha})^2 \chi^2}{2}\right] \alpha \, d\alpha \, d\varphi
\tag{7.14}
$$

Because Poisson noise in the X-ray detection modifies the diffraction patterns in the high diffraction angle region, the extension of the mask is determined by inspecting the resolution-dependent variation of $C_{sym}$ reflecting the degree of Friedel centrosymmetry [see (6.2)].

The dark-field PR calculation constrained by Friedel centrosymmetry provides the dark images as a real number. Any residuals of the imaginary part of the dark image $\rho_{dark}^{sym}(\boldsymbol{r})$ must be constrained to be zero. A dark image appears as a convolution of a point-spread function and the electron density map of the targeted particle. Therefore, a map calculated by a deconvolution of the dark image can be used as an initial model for the subsequent PR calculation of the diffraction pattern without masks.
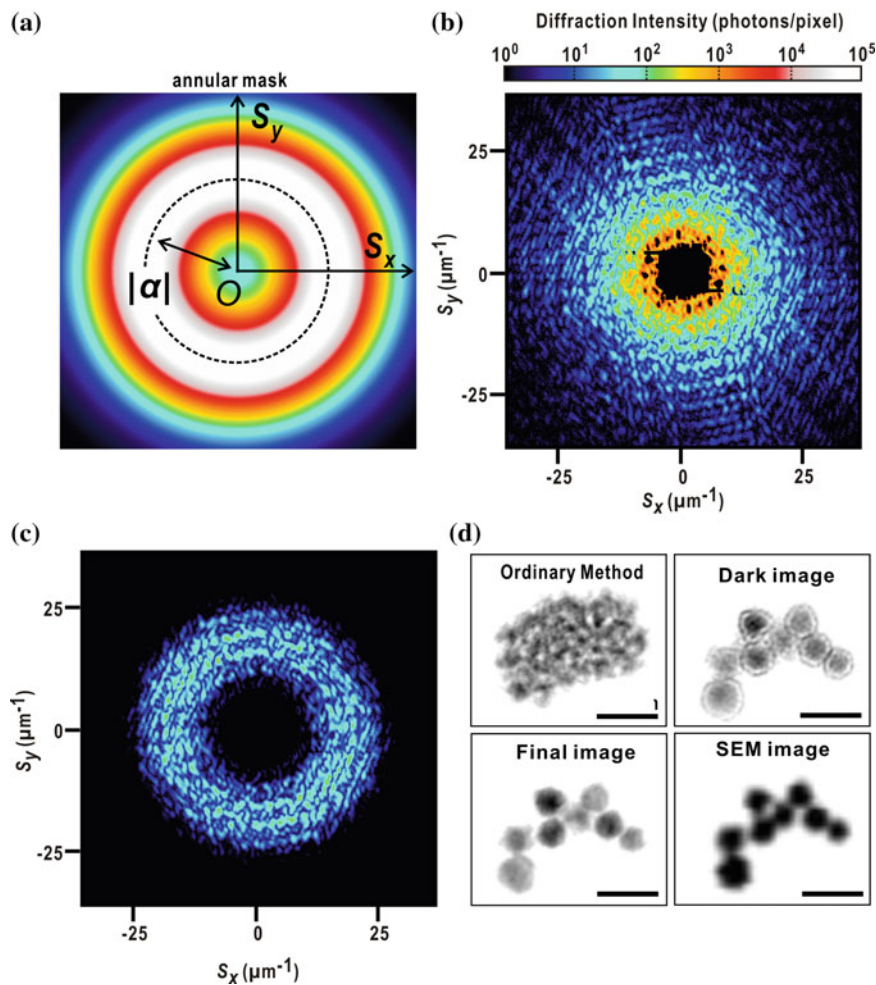
**Fig. 7.6  a** Annular mask defined by (7.14). **b** Diffraction pattern from an aggregate of eight gold colloidal particles recorded by a single shot XFEL pulse at SACLA. Because considerably strong diffractions occur in the small-angle region of $S < 5\ \mu m^{-1}$, almost all the pixels of the MPCCD-Dual detector are saturated. In addition, the central part of the MPCCD-Octal detector misses strong speckle peaks. The $C_{sym}$ value (6.2) of the diffraction pattern is 0.94 up to a resolution of $14\ \mu m^{-1}$. **c** 'Dark-field' diffraction pattern calculated by multiplying an annular mask to the diffraction pattern in panel **b**. In the mask function, the parameter $\alpha$ and the standard deviation of the Gaussian function are $0.2\ \mu m^{-1}$ and $0.13\ \mu m^{-1}$, respectively. **d** Comparison of the PR maps of an aggregate of eight gold colloidal particles and the scanning electron microscopy (SEM) image taken prior to the experiment. The density map labeled 'Ordinary method' is a representative result obtained by HIO/SW calculation. Panels are reused from [25] after modification with permission from The Optical Society

## 7.4.2  Application

The following two-step protocol is implemented in the PR calculations for the diffraction patterns with data missing in the small-angle regions. In the first step, a "dark image" is retrieved using the dark-field PR method with the Friedel centrosymmetry constraint. In the second step, an image is retrieved starting from the dark image by applying the noise-robust HIO and OSS algorithms to all the diffraction patterns.

When diffraction patterns display good signal-to-noise ratios up to resolutions beyond 10 nm, a large area of the small-angle region is frequently missed due to the saturation of the detectors. Figure 7.6b shows a representative diffraction missing the small-angle region up to a resolution of 9 $\mu m^{-1}$. The pattern was taken from an aggregate of gold colloidal particles with a diameter of 250 nm. All PR calculations using the HIO/SW protocol failed.

In contrast, the dark-field calculation (Fig. 7.6c) successfully retrieved the shape of the aggregate. Starting from this shape, an HIO/SW calculation gives a final electron density map. The PR map provided the shapes of clusters found in the dark images as well as structural details with regard to the shape and the variation in the electron density. The size, number, and arrangements of particles were consistent with those observed in the SEM images before X-ray exposure (Fig. 7.6d).

Due to the symmetry constraint, the dark image must be a real number. Subsequently, the possible number of solutions is reduced to half of that in dark-field PR without the symmetry constraint. In fact, PR for real-valued objects is much easier than for complex-valued objects. In addition, the quantity of diffraction data is a major factor contributing to the difference in the efficiency of the PR calculation. A larger annular mask gives dark images with better quality than a small one.

## References

1. J. Drenth, *Principles of Protein X-ray Crystallography* (Springer, Berlin, 2007)
2. J.R. Fienup, Appl. Opt. **21**, 2758 (1982)
3. J. Miao, T. Ishikawa, I.K. Robinson, M.M. Murnane, Science **348**, 530 (2015)
4. M. Nakasako, Rev. Sci. Instrum. **84**, 093705 (2013)
5. A. Kobayashi et al., Rev. Sci. Instrum. **87**, 053109 (2016)
6. T. Kameshima et al., Rev. Sci. Instrum. **85**, 033110 (2014)
7. Y. Sekiguchi et al., J. Synchrotron Rad. **24**, 1024 (2017)
8. Y. Sekiguchi, T. Oroguchi, M. Nakasako, J. Synchrotron Rad. **23**, 312 (2016)
9. M. van Heel, J. Frank, J. Ultramicroscopy **6**, 187 (1981)
10. J. Frank, *Three-Dimensional Electron Microscopy of Macromolecular Assemblies* (Oxford University Press, Oxford, 2006)
11. D.T. Pham, S.S. Dimov, C.D. Nguyen, Proc. Inst. Mech. Eng. C J. Mech. Eng. Sci. **219**, 103 (2005)
12. J. MacQueen, Proc. Fifth Berkeley Symp. Math. Stat. Probab. **1**, 281 (1967)
13. H.N. Chapman et al., J. Opt. Soc. Am. A **23**, 1179 (2006)

14. D.M. Blow, F.H.C. Crick, Acta Crystallogra. **12**, 794 (1959)
15. V.Y. Lunin, M.M. Woolfson, Acta Crystallogra. **D49**, 530 (1993)
16. A. Perrakis, T.K. Sixma, K.S. Wilson, V.S. Lamzin, Acta Crystallogra. **D53**, 448 (1997)
17. P.B. Rosenthal, R. Henderson, J. Mol. Biol. **333**, 721 (2003)
18. Y. Takayama et al., Plant Cell Physiol. **56**, 1272 (2015)
19. D.P. Faith, P.R. Minchin, L. Belbin, Vegetatio **69**, 1 (1987)
20. V. Elser, J. Opt. Soc. Am. A **20**, 40 (2003)
21. S. Marchesini et al., Phys. Rev. B **68**, 140101 (2003)
22. D. Luke, Russel Inverse Problems **21**, 37 (2005)
23. J.A. Rodriguez et al., J. Appl. Cryst. **46**, 312 (2013)
24. A.V. Martin et al., Opt. Express **20**, 13501 (2012)
25. A. Kobayashi et al., Opt. Express **22**, 27892 (2014)

# Chapter 8
# Projection Structures of Biological Cells and Organelles

**Abstract** The diffraction apparatus for X-ray diffraction imaging (XDI) and the specimen preparation methods allow us to collect diffraction patterns from frozen-hydrated noncrystalline biological particles, such as cells and organelles, at 66–80 K. From high-quality diffraction patterns, phase retrieval (PR) calculations reconstruct electron density maps of specimen particles projected along the direction of the incident X-rays. Here, the application of XDI to structural studies of cells and cellular components is presented. Topics in synchrotron XDI include structural analyses of the chloroplasts of spinach and the small eukaryote *Cyanidioschyzon merolae*. In XDI experiments using X-ray free electron laser (XFEL) pulses, the structure of cyanobacteria cells and the chloroplasts of *C. merolae* are investigated. In addition, because XFEL-XDI experiments can provide a large number of diffraction patterns within a short time, the size distribution of targeted particles can be constructed with statistical significance. As examples, the size distributions of cuprous oxide particles, cyanobacteria cells, and amyloid aggregates are presented.

## 8.1 Projection Structures of Biological Particles Visualized by X-Ray Diffraction Imaging Using Synchrotron X-Rays

Since the first demonstration, XDI has been applied to biological specimens to visualize the projection structures of cells and organelles [1]. XDI was first used to visualize the projection structure of *Escherichia coli*, in which histidine-tagged protein was overexpressed in order to concentrate metal ions for the enhancement of the electron density contrast [2]. The XDI experiment was carried out for a dried specimen set in a vacuum chamber using synchrotron X-rays. Regarding the distribution of the tagged proteins in *E. coli*, the retrieved projection electron density maps were consistent with the images obtained by confocal microscopy and X-ray absorption microscopy. The full structure of freeze-dried yeast cells were investigated using X-rays with a wavelength of 1.65 nm [3]. In the PR map, organelles such as the cellular nucleus, vacuole, and membranes were visible at a nominal resolution of

30 nm. The map was consistent with the image obtained by transmission X-ray microscopy with respect to the positions and sizes of the organelles.

These two pioneer studies open the door for the application of XDI to structural analyses of the whole structures of biological specimens, which are opaque to TEM, at resolutions higher than LM. Since these studies, XDI has been applied to visualizing the projection structures of virus and bacterial cells [4–8]. In the preliminary stages of these applications, XDI experiments were carried out for specimens at room temperature and under vacuum conditions. To reduce radiation damage, cryogenic XDI experiments are performed by developing diffraction apparatuses and methods for preparing frozen-hydrated specimens [5, 6, 9, 10].

For cryogenic XDI experiments at BL29XUL [11] of the synchrotron facility SPring-8, frozen-hydrated specimens are prepared using a humidity-controlling chamber and a flash-cooling device (see Sect. 5.3 of Chap. 5 and Fig. 5.5) [12]. The frozen-hydrated specimens are delivered safely using dry shippers to maintain their temperature at 77 K. After tuning the beamline optics, a spatially coherent X-ray beam is produced using a pinhole placed approximately 1.6 m upstream from the specimen position (see Sect. 4.2 of Chap. 4 and Fig. 4.4). Parasitic scattering and background scattering from the upstream optics and the pinhole are reduced significantly by a slit system composed of silicon blades. The diffraction apparatus KOTOBUKI-1 is placed so that the specimen position is within the central peak in the diffraction pattern from the pinhole (see Sect. 4.2 of Chap. 4 and Fig. 4.5). Prior to the collection of diffraction data of biological specimens, diffraction patterns from a cuprous oxide particle with a cuboid shape are recorded in order to examine the flux and coherence of the incident X-ray (Fig. 4.4).

Each frozen-hydrated specimen is mounted on the cryogenic pot connected to the goniometer stage inside of the diffractometer. The temperature of the pot is kept at around 66–80 K by evaporation cooling using liquid nitrogen supplied from a dewar mounted at the top of the apparatus (see Sect. 4.2 of Chap. 4 and Fig. 4.5). Diffraction patterns are recorded by a CCD detector at a distance of 3 m from the specimen position, or a pixel array detector at a distance of 5 m.

Here, the typical diffraction patterns of biological specimens and the metal particle collected at BL29XUL of SPring-8 are shown to demonstrate what kind of structural information is obtainable in cryogenic XDI experiments at SPring-8.

### 8.1.1 Metal Particles as Standard Specimens

The diffraction patterns of metal particles with submicrometer dimensions were collected at ambient temperature in order to quantitatively monitor the flux density and coherence of the incident X-ray beam produced by the pinhole. Two examples are shown in Fig. 8.1.

The first example is the diffraction pattern from an aggregate of nine gold colloidal particles with a diameter of 250 nm [10] (Fig. 8.1a). Diffraction patterns were taken using an X-ray with a wavelength of 0.155 nm. Speckle patterns are
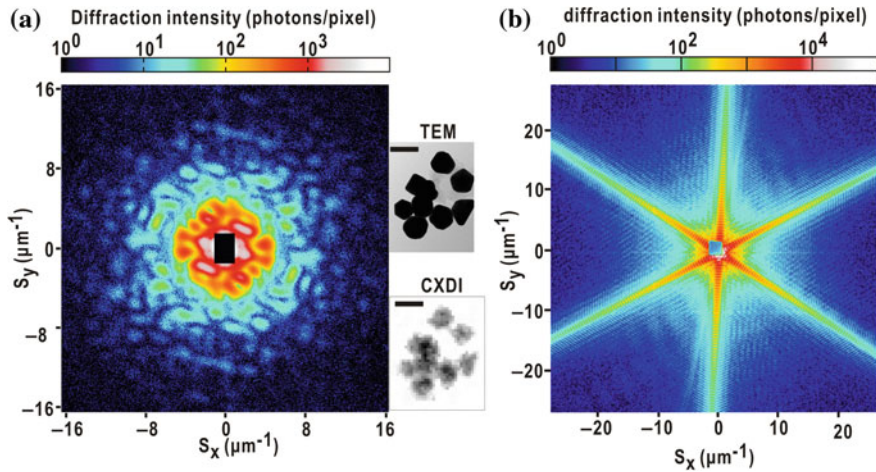
**Fig. 8.1 a** The diffraction pattern from an aggregate of nine gold colloidal particles [10]. The X-ray wavelength was 0.155 nm. A CCD detector was used, and each diffraction pattern was recorded using an accumulation of 2000 exposures of 50 ms each (the total exposure time was 100 s). The TEM image and the PR electron density map are shown on the right. The scale bar is 250 nm. Panels (**a**) is reused with modification from [11] with permission from AIP publishing. **b** The diffraction pattern from a hexagonal ice particle. A pixel array detector was used with an exposure of approximately 60 s. Panel (**b**) is published with kind permission of Masayoshi Nakasako 2017. All Rights Reserved

visible beyond a resolution of 60 nm. Weak diffraction intensities in the valleys between any pair of speckle peaks indicate that good visibility is attained under spatially coherent illumination. The PR electron density map is consistent with a TEM image taken after the XDI experiment. The resolution of the TEM image is significantly higher than that of the electron density map retrieved from the diffraction pattern. However, only the particle shapes are visible, because electrons with an energy of 200 keV cannot penetrate into the specimen due to the thickness. In the electron density map, the internal structures inside the gold colloidal particles are visible because of the penetration power of the X-ray beam with a wavelength of 0.15 nm. This result is a typical example demonstrating the penetration power of X-rays with a short wavelength.

The second example is the diffraction pattern from a hexagonal ice particle, which was accidentally formed during specimen preparation, recorded using an X-ray with a wavelength of 0.225 nm (Fig. 8.1b). The diffraction pattern is approximated as a Fraunhofer diffraction from a hexagonal-shaped aperture. The diffraction intensity in the valleys between any pair of adjacent peaks is ideally zero under spatially coherent illumination. The patterns provide a measure to estimate the coherence of the incident X-rays. In addition, the rough size of the particle can readily be calculated from the intervals of the diffraction peaks. The diffraction

intensity is then useful to estimate the exposure time necessary for biological specimens.

These diffraction patterns from non-biological particles demonstrate that the pinhole placed upstream functions as a source of spatially coherent X-rays with a wavelength of 0.15–0.23 nm. However, because the radius of the pinhole determines the flux density for an area approximated as a plane wave, it is better to carefully calculate the radius suitable for recording diffraction patterns by obtaining the size of the targeted specimen particles before starting the experiments, according to (4.3).

### 8.1.2  Spinach Chloroplasts

As a representative example of a synchrotron XDI experiment for biological specimens, the diffraction pattern from a frozen-hydrated spinach chloroplast is shown in Fig. 8.2 [12]. The area of the chloroplast, approximately 7 μm, was bathed in the spatially coherent area of the Airy disk produced by the pinhole (see Fig. 4.4). Positional fluctuations of the chloroplast relative to the incident X-ray beam were suppressed to ensure that the sample remains within the area of spatially coherent illumination during a long exposure time. The cryogenic pot mounted on the high precision goniometer stage is advantageous for ensuring only small positional fluctuations of the mounted chloroplast particle (see Sect. 4.2.1 of Chap. 4).

For spatially coherent illumination, the optimal position of the chloroplast within the incident beam was searched by iterative scanning of the specimen disk with monitoring Friedel centrosymmetry and diffraction intensity. Due to the cryogenic



**Fig. 8.2** The diffraction pattern from a frozen-hydrated spinach chloroplast kept at 66 K. The PR map is compared to the light microscopy image taken just before the flash-cooling of the chloroplast [12]. Panels are reused with modification from [12] with permission from AIP publishing
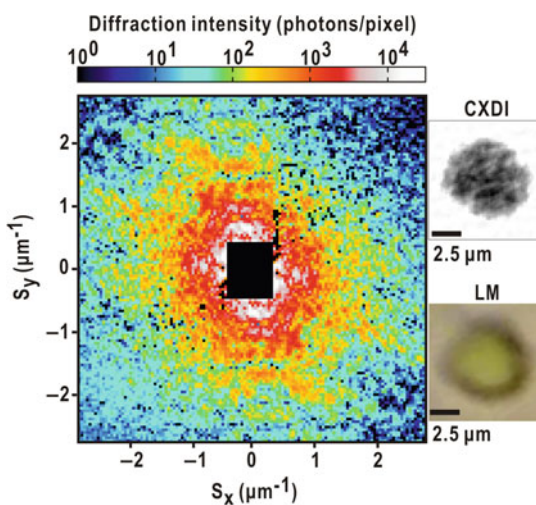
temperature, the chloroplast displayed little radiation damage, as confirmed by comparing the diffraction patterns from the first and last exposures while searching for the optimal position.

The diffraction pattern, visible up to a resolution of 2.8 $\mu m^{-1}$ at the edge (corresponding to a real resolution of 181.6 nm), is composed of speckle peaks with good visibility. For the PR calculation, the missing small-angle region of $21 \times 17$ pixels was initially filled with the Fourier transform modulus of the image taken using LM before flash cooling. The retrieved electron density map is composed of high-density stripes, which probably correspond to internal structures of the chloroplast, such as the granum.

### 8.1.3   Cyanidioschyzon merolae *Cell*

*Cyanidioschyzon merolae* (*C. merolae*) is a small eukaryote that is classified as the origin of eukaryotes [13]. According to the endosymbiotic hypothesis regarding the evolution of eukaryotes, mitochondria and chloroplasts originated through symbioses between different single-celled organisms. *C. merolae* cells are suitable for structural analysis in synchrotron XDI experiments with respect to both their size and total scattering cross-section.

In the preparation of the specimen disk for the diffraction experiment, a single *C. merolae* cell was placed at the center of a window made of a silicon nitride membrane of $1 \times 3$ or $3 \times 3$ mm$^2$ by using a microcapillary mounted on the humidity controlling chamber (Fig. 8.3a). According to the procedure described in Fig. 4.6 of Chap. 4, the flash-cooled specimen disk was mounted on the cryogenic pot so that the membrane plane was normal to the direction of the incident X-ray. A spatially coherent X-ray beam was produced by a pinhole of 38 μm placed approximately 2.0 m upstream from the specimen position. The position of the cell was adjusted to be at the center of the Airy disk by scanning in both the horizontal and vertical directions against the incident X-ray beam. The distance between the specimen position and the pixel array detector was 5 m.

Examples of diffraction patterns taken in a preliminary experiment are depicted in Fig. 8.3. In this case, the flux density of the X-rays with wavelengths of 0.225 nm was $10^8$ photons per $5 \times 5$ μm$^2$ per s at the specimen position. Because the exclusion of parasitic scattering from the upstream optics was insufficient, a beamstop of $3 \times 3$ mm$^2$ was used. For instance, a single *C. merolae* in the G/M phase just before cell division diffracted X-rays beyond a resolution of 20 $\mu m^{-1}$ (corresponding to 100 nm in real space) under one hour exposure (Fig. 8.3b). In addition, a cell in the interphase (G1 phase) diffracted X-rays up to a resolution of 10 $\mu m^{-1}$ (Fig. 8.3c). The clear difference in the highest resolutions between the diffraction patterns of G/M and G1 cells is attributed to the difference in the total scattering cross-section: A cell in the G/M phase has cell components almost twice the amount of those in the G1 phase, i.e., the total scattering cross section is approximately twice that of the G1 phase. In Fig. 8.3c, two diffraction patterns were

**(a)**

**(b)** diffraction intensity (photons/pixel)



**(c)** diffraction intensity (photons/pixel)
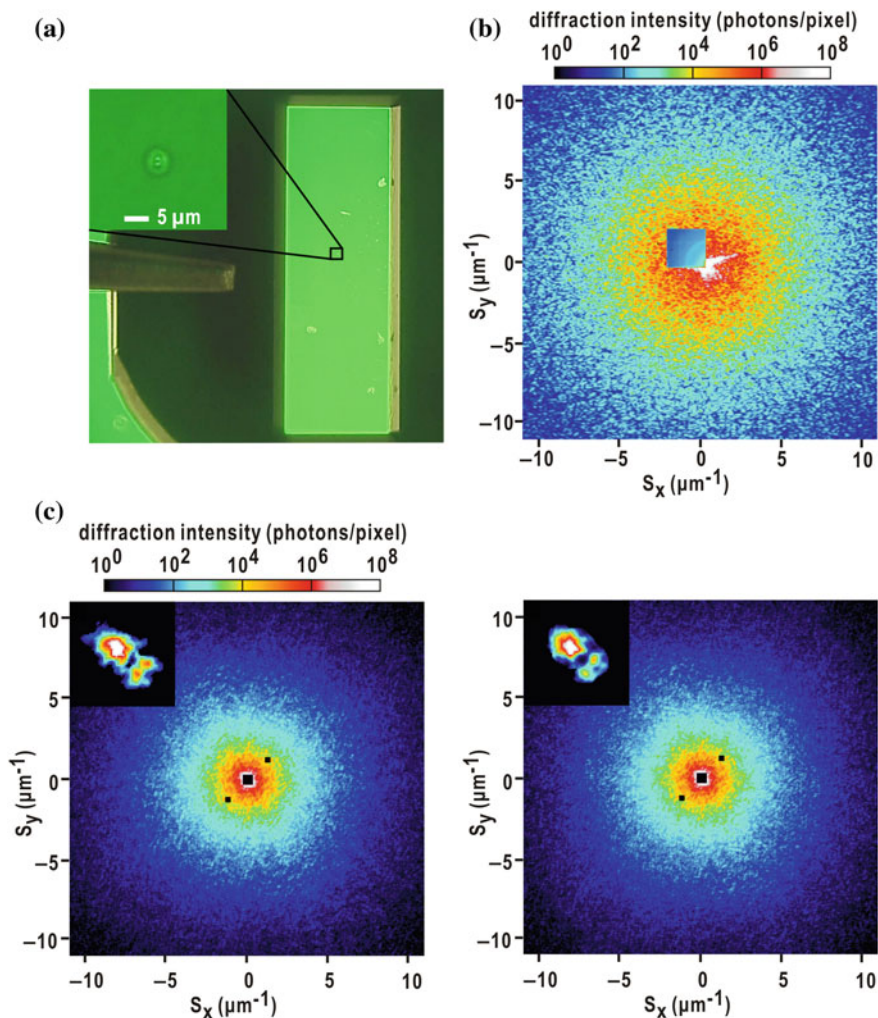


**Fig. 8.3** **a** LM images of a single *C. merolae* cell in the G/M phase (just before cell division) placed on a silicon nitride membrane under the high-humidity condition. The upper left is a magnified view of the cell. **b** The diffraction pattern from a single *C. merolae* cell in the G/M phase with an exposure time of 1000 s. **c** Two diffraction patterns taken from a single *C. merolae* cell in the G1 phase. The diffraction pattern in the upper-left region of the beamstop is generated using Friedel centrosymmetry. The pattern in the right panel was taken with the cell rotated at an angle five degrees from that of the pattern in the left panel. The most probable PR map from each pattern is shown in the upper left. The approximate length of the short axis is 2 μm. Published with kind permission of Masayoshi Nakasako 2017. All Rights Reserved

taken for different orientations of the cell, varied by five degrees with respect to the direction of the incident X-ray. Both of the most probable PR maps appeared as ellipsoidal shapes. Each PR map is comprised of one large and two small density peaks. The similarity of the PR maps with regard to the shapes and peak positions ensures the success in the selection of the correct maps.

By improving the upstream optics, the flux density of the X-rays with a wavelength of 0.225 nm increased to $5 \times 10^9$ photons per $5 \times 5$ μm$^2$ per s at the specimen position. In addition, a modification of the slit system significantly reduced the intensity of parasitic scattering from the upstream optics. Subsequently, a beamstop with a size of $1 \times 1$ mm$^2$ was found to be sufficient to block parasitic scattering and direct the X-ray beam. Under this condition, diffraction patterns from a *C. merolae* cell in the G/M phase were collected. For an exposure time of 45 min, speckle patterns were visible beyond a resolution of 40 μm$^{-1}$ (corresponding to 25 nm in real space) (Fig. 8.4a). Up to a resolution of 10 μm$^{-1}$, speckle patterns were recorded with a very good signal-to-noise ratio (Fig. 8.4b). At a resolution of approximately 23 μm$^{-1}$ (43 nm in real space), the speckle peaks displayed a signal-to-noise ratio far better than 3. In addition, at around 40 μm$^{-1}$ (25 nm in real space), the signal-to-noise ratio was approximately 2–3.

This diffraction pattern suggests the possibility of visualizing the projection density map at a resolution better than 25 nm. At 66–80 K, the secondary process of radiation damage is significantly suppressed. The experimental setup of the diffraction experiment allowed us to successively collect the diffraction patterns in different orientations with respect to the incident X-ray beam direction, as described in Chap. 9.

## 8.2 Projection Structures of Biological Particles Visualized by X-Ray Diffraction Imaging Using X-Ray Free Electron Laser Pulses

XFEL-XDI was first applied to the structural analysis of a mimivirus as large as 1 μm at the Linac Coherent Light Source [14]. Although specimen particles are destroyed at an atomic level by the Coulomb explosion caused by the irradiation of a single XFEL pulse, diffraction from the specimen particles occurs before the destruction (diffraction before destruction) [15, 16]. Owing to the short duration of the X-ray pulses, in the range of several tens of femtoseconds, the structures of specimens are visualized without radiation damage, as demonstrated by the X-ray crystallography of a membrane protein [17].

In XFEL-XDI experiments, fresh specimen particles are introduced into the irradiation area of the XFEL pulses, which are provided at a repetition rate of 30–100 Hz. Three techniques for the delivery of specimen particles are proposed and
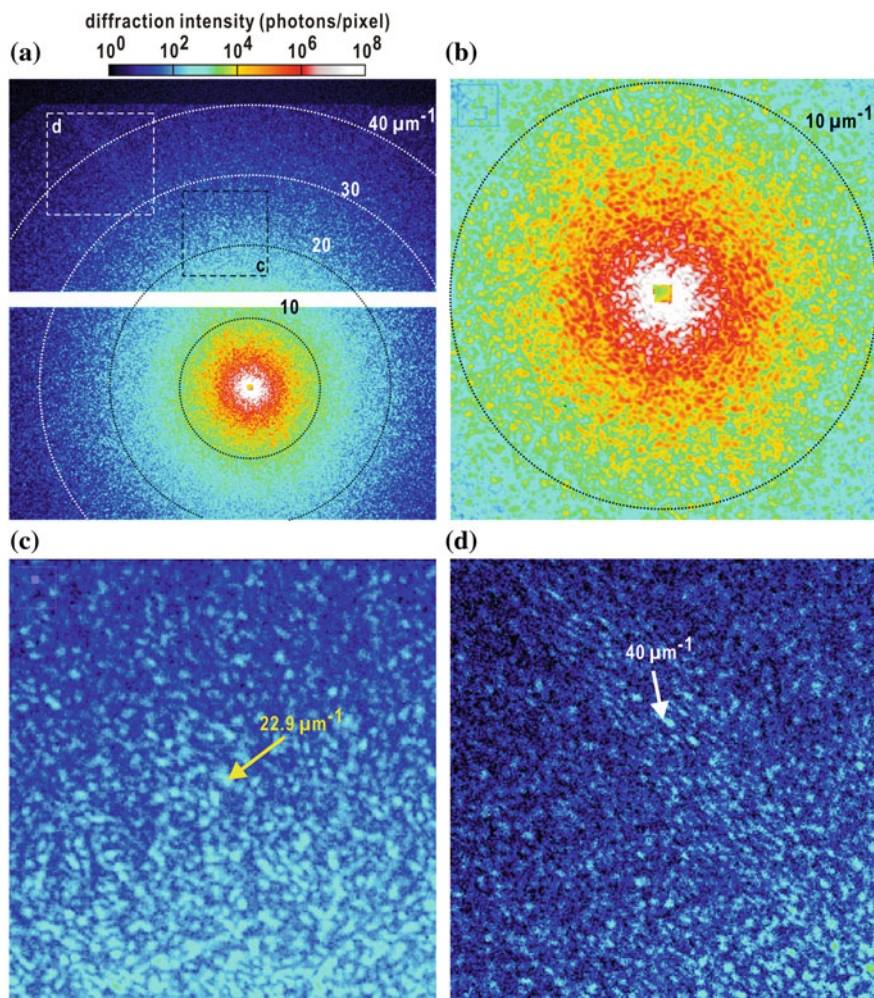
**Fig. 8.4  a** The diffraction pattern from a single *C. merolae* cell in the G/M phase. A beamstop of $1 \times 1$ mm$^2$ was used. Four dotted circles are drawn at resolutions of 10, 20, 30, and 40 µm$^{-1}$. The white stripe is a gap between the detector panels. **b–d** Magnified views of the diffraction pattern in (**a**). The magnified areas are labeled in panel (**a**). Published with kind permission of Masayoshi Nakasako 2017. All Rights Reserved

used for XFEL-XDI experiments. The aerosol method injects specimens surrounded by a small droplet of buffer solution into the irradiation area inside a vacuum chamber. When the small droplet is injected into the vacuum, adiabatic expansion of the cells and organelles, evaporation of water from the buffer solution, and bubbling inside the cells occurs [18–20]. The liquid jet method is developed for macromolecular crystallography using XFEL. When XFEL pulses are incident onto

the interface between the liquid and vacuum, total reflection occurs at the interface. This results in very strong X-ray pulses hitting the detector pixels, which makes it difficult to record diffraction patterns in the small-angle region. The micro-liquid enclosure-array method is developed for XFEL-XDI measurements of biological specimens in an aqueous environment, even in a vacuum chamber [21, 22]. A small amount of the liquid specimen is enclosed in specially designed micro-liquid compartments. Each compartment is destroyed by a single pulse exposure. In addition, the delivery speed of the adjacent cell is in the range of a few Hz. Therefore, this technique makes it difficult to collect a large number of diffraction patterns within a short period of time.

As an alternative approach to all three methods, diffraction data collection from frozen-hydrated biological specimens is proposed, as described in Sect. 4.3 of Chap. 4. For instance, at SACLA, XFEL pulses are provided at a repetition rate of 30 Hz and are focused to yield a density of $10^{10-11}$ photons per $2 \times 2 \mu m^2$ (FWHM) over a duration of 10 fs [23, 24]. In cryogenic XFEL-XDI experiments at SACLA, the TAKASAGO-6 diffraction apparatus [25] allowed us to use more than 30,000 XFEL pulses per hour for diffraction data collection from frozen-hydrated cells and cellular organelles harvested at the desired stages of the cell cycles. Because the average electron density of biological noncrystalline particles is 400–600 e/nm$^3$, small cells and cellular organelles with dimensions of 500–1000 nm are suitable targets for structural analyses at a resolution of several tens of nanometers. In fact, the resolution of the diffraction patterns from such particles occasionally exceeds the resolution limit in fluorescence LM.

The X-ray wavelength used in the experiment was selected by considering the wavelength dependencies of the diffraction intensity, absorption of X-rays by specimens, quantum efficiency of detectors, and the oversampling ratio in diffraction patterns. In the XFEL-XDI experiments described below, an X-ray with a wavelength of approximately 0.225 nm is used. The penetration power is sufficient to visualize the internal structures of specimens with sizes from 0.7 to 1.5 μm. In addition, the diffraction patterns can be approximated by the Fraunhofer diffraction of the real-value object. Stability in the position, profile, and coherence of the focused X-ray pulses is crucial for recording diffraction patterns in very small-angle regions [26].

The intensity and maximum resolution of a diffraction pattern depend predominantly on the relative positions of the specimen particle and the peak position of the X-ray pulse. When an X-ray pulse overlaps with a biological particle with a size of 700–1000 nm, speckle patterns in the diffraction pattern are visible beyond a resolution of 30 nm. However, because of the raster-scan for the membrane with the random dispersion of specimen particles, the probability of obtaining a diffraction pattern worthy of analysis is approximately 2% [27].

In the following subsections, representative examples of diffraction patterns and the projection electron density maps of biological specimens are shown to demonstrate the kind of structural studies that are carried out in XFEL-XDI.

### 8.2.1   Magnetic Bacteria Cell

A magnetic bacterium has a cell size of less than 1 μm and contains a magneto-some, which is an array of iron crystals with a size of several tens of nanometers [28]. The distance between the crystals is less than approximately 100 nm. Therefore, a single magnetic bacterial cell is suitable to address the possible resolution in XFEL-XDI experiments for biological cells.

Figure 8.5 shows a representative small-angle diffraction pattern of a frozen-hydrated magnetic bacterium MO-1 cell [27]. Because the diffraction patterns displayed the centrosymmetry as indicated by the $C_{sym}$ value of 0.77 (6.2), the diffraction patterns are treated as the Fraunhofer diffraction patterns of an object without a large amount of anomalous scatter for incident X-rays with a wavelength of 0.225 nm. The diffraction pattern shows a signal-to-noise ratio greater than 2 up to a resolution of 27 $\mu m^{-1}$.
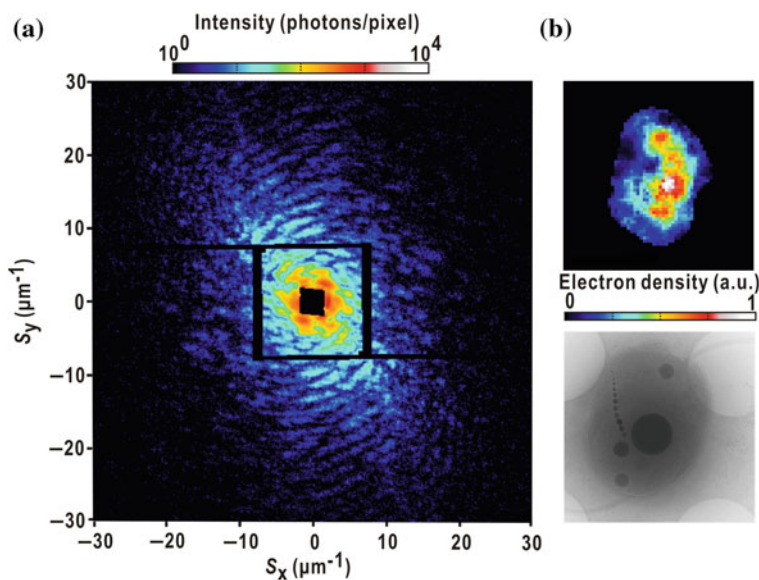


**Fig. 8.5  a** A diffraction pattern from a single magnetic bacterium MO-1 cell [26]. The black square at the center is the shadow of the beamstop. The diffraction patterns are also lost at the gap between the two MPCCD detectors placed at different distances from the specimen. The two black stripes in the horizontal direction are the gaps between the detector panels. The pattern is shown up to a resolution of 30 $\mu m^{-1}$ at the edge, corresponding to a resolution of 33 nm in real space. **b** The upper panel shows a projection electron density map retrieved from a diffraction pattern using the protocol described in Sect. 7.3. The long axis of the cell is approximately 800 nm. The strong density peaks can be assigned as the iron particles in the magnetosome. The lower panel is a TEM image of a single MO-1. Panel (a) is reused from reference [26] with permission from IOP publishing. Published with kind permission of Masayoshi Nakasako 2017. All Rights Reserved

The diffraction pattern consists of layers of speckle peaks arranged into spirals. Some of the spiral layers are in a concentric arrangement, indicating that the frozen-hydrated MO-1 cell maintains its globular shape as observed using TEM. From the spatial frequency along the radial direction in a concentric interference pattern, the MO-1 cell contains high density regions separated by approximately 500 nm.

In the most probable projection electron density map with an effective resolution of 118 nm, the three prominent peaks can be identified as iron particles of the magnetosome in referring to the TEM images. The iron particle size in the retrieved map is somewhat larger than that in the electron microscopic image, probably because of the point-spread effect from the low resolution. While iron particles are resolved in the TEM images in detail, it is still difficult to distinguish each individual iron particle in the XDI at SACLA; this is probably because the incident intensity is limited to $10^{10}$–$10^{11}$ photons per $2 \times 2$ $\mu m^2$ per pulse.

Although the resolution is still low, the electron density map has substantial differences from the TEM image. In the TEM image, the MO-1 cell is almost transparent except for the magnetosome and the borders of the cellular vacuoles. On the other hand, in the electron density map, clusters of densities as high as 50% of the peaks for iron occupy a large area of the cell. Because aged MO-1 is known to have large vacuoles containing phosphate, the high-density region with a size larger than 500 nm can be assigned to be the vacuoles. The TEM images indicate that the scattering cross section of a vacuole with phosphate is not very large. However, TEM allowed us to identify the positions of the vacuoles, and the XDI electron density provided the amount of phosphate inside the vacuoles. The combination of the two imaging techniques is advantageous to specifying the position and amount of materials in cellular components.

## 8.2.2 Chloroplast of Cyanidioschyzon merolae

The cell size of C. merolae ranges from approximately 2 to 4 $\mu m$ in the cell cycle [13], and is larger than the focused beam size currently available at SACLA [29]. On the other hand, chloroplasts completely bathed in the focused beam area are sometimes found in raster scans. The diffraction patterns of small chloroplasts with a diameter of 1 $\mu m$ are selected for analysis of the internal structures.

Figure 8.6a, b show a representative diffraction pattern from a small chloroplast [29]. In these diffraction patterns, the speckle peaks, each of which were recorded by more than $5 \times 5$ pixels, were visible beyond a resolution of 20 $\mu m^{-1}$ (corresponding to a resolution of 50 nm in real space) with signal-to-noise ratios better than 3. The patterns displayed good Friedel centrosymmetry, indicated by the $C_{sym}$ value [see (6.3)] of 0.8 in the resolution range from 5 to 16 $\mu m^{-1}$. In the diffraction pattern shown in Fig. 8.6a, speckle peaks are distributed concentrically with an

**(a)**



**(b)**
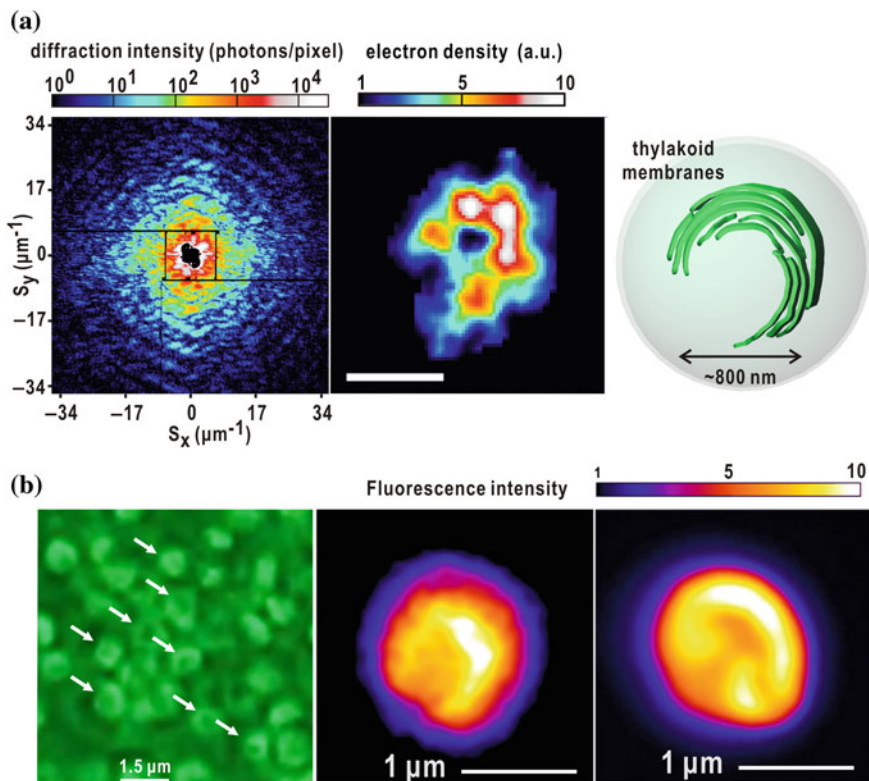


**Fig. 8.6** Structural analysis of a chloroplast of *C. merolae* by the combination of XFEl-XDI and fluorescence LM. **a** The diffraction pattern (left column), PR map (middle), and a putative model explaining the PR map (right) [29]. The scale bar indicates 500 nm. In the model, the green colored sheets represent thylakoid membranes. **b** Three LM images of chloroplasts; (left) a phase-contrast image under a safe green light, (middle) a fluorescence image recorded at 545 nm from a chloroplast stained by fluorescence dye under illumination by a 485 nm excitation light, and (right) a fluorescence image of self-fluorescence from chlorophyll molecules recorded at 670 nm under a illumination by a 570 nm excitation light. The fluorescence intensity decreases in the order white > yellow > orange > red > purple > blue. Panels are reused with modification from [29] with permission from The Plant Cell Physiology, Oxford University Press

approximate interval of 2.5 $\mu m^{-1}$. The concentric pattern indicates the globular shape of the chloroplast particle. In addition, the interval of concentric rings suggests the presence of high-electron-density regions separated by approximately 400 nm. The rough dimension of the chloroplast, projected along the direction of the incident X-ray, is estimated to be approximately 1 $\mu m$ from the reciprocal size of the well-separated speckle peaks (see Fig. 3.1). In the diffraction pattern, the Ewald sphere can be approximated as a plane up to a resolution of 11 nm according to (3.19), if the globular chloroplasts have an approximate diameter of 1 $\mu m$.

The most probable electron density map obtained from the multivariate analysis displayed an effective resolution of 70 nm. In a map averaged over the cluster composed of probable maps (see Fig. 7.3 in Chap. 7), the high density region displayed a C-shape with an approximate size of 600 × 800 nm [29, 30]. The C-shaped structure with high density peaks arranged at rough intervals of 400 nm would predominantly contribute to the concentric interference pattern.

PR maps retrieved at low resolution provide little information on what kind of materials result in the projection electron density. An additional imaging technique is necessary to get chemical information on materials composing the high density peaks. In phase contrast LM, single dark regions appear at the centers of the chloroplasts, suggesting a nonuniform distribution of materials. For instance, thylakoid membranes, a major component of chloroplasts, are comprised of membrane proteins, lipid bi-layers, and chlorophyll molecules. Therefore, the distribution of thylakoid membranes can be identified by measuring the auto-fluorescence from chlorophyll molecules and fluorescence from dye-stained protein molecules (Fig. 8.6b). In a series of confocal LM images sliced along the direction of the optical axis, the high-fluorescence intensity regions appear as a C-shape in the equatorial plane of the chloroplast stained by fluorescence dye with an affinity to proteins. In addition, the region with auto-fluorescence intensity from the chlorophyll molecules appears in a C-shape near the equatorial plane of the chloroplast. Both fluorescence images have diameters of approximately 1 μm and are similar to that observed in the PR map. Therefore, the C-shape in the PR map can be interpreted as an assembly of thylakoid membranes.

The thylakoid membrane, which is composed of protein and lipid molecules, has an average electron density greater than that of vitreous ice. In contrast, when the average electron density of a region is comparable to that of vitreous ice, the structural details are unclear, as the central region is surrounded by the C-shape. In *C. merolae* chloroplasts, the C-shaped structure suggests that the curved and stacked layers of the thylakoid membranes preferentially distribute in the marginal regions rather than the central regions of the cell. This is consistent with the internal structures of chloroplasts visualized by TEM for ultrathin-sectioned specimens after heavy-atom staining and resin fixation [31–34]. The C-shaped stacks of thylakoid membranes would be advantageous for efficient photosynthesis in *C. merolae,* which are rotated randomly and freely by fluid dynamic perturbations in the living medium.

## 8.2.3  Cyanobacteria Cell

According to the endosymbiotic theory of the evolution of eukaryotes, key organelles, such as chloroplasts and mitochondria, originated from symbioses between separate single-celled organisms. For instance, the chloroplast would come from cognates of cyanobacteria. XDI contributes to structural investigations to address the structural similarity between *C. merolae* chloroplasts and cyanobacteria cells.
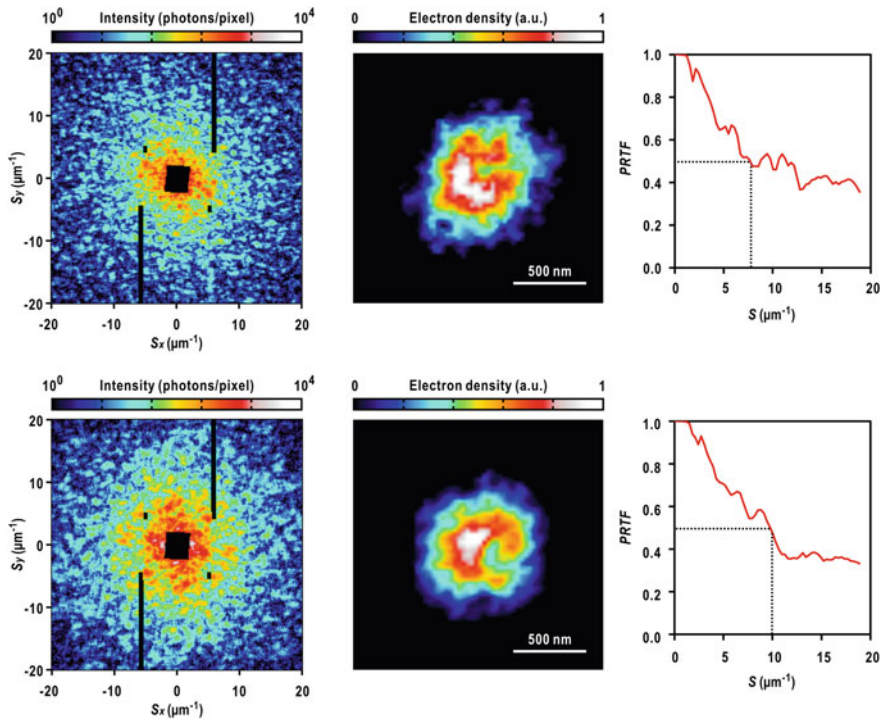
**Fig. 8.7** Two diffraction patterns (left panels) and the most probable PR maps (center panels) of frozen-hydrated single cyanobacterial cells. The effective resolution of each PR map estimated using the PRTF (right panel) was in the range from 100 to 150 nm. Panels are reused from [27, https://doi.org/10.1107/s1600577516007736] after modification with permission from The International Union of Crystallography

Figure 8.7 shows two examples of typical diffraction patterns of cyanobacteria cells obtained in XFEL-XDI experiments. When a single cyanobacteria cell is bathed in a focused X-ray pulse, the maximum resolution of the diffraction pattern reaches 20 $\mu m^{-1}$, corresponding to 50 nm in real space [27]. Speckle peaks with a size of approximately 1.3 $\mu m^{-1}$ were in the range of the reciprocal sizes of cyanobacterial cells measured by DLS. In PR maps, cyanobacterial cells displayed globular shapes with diameters ranging from 700 to 800 nm. Inside the cells, high density regions form a C-shape with an approximate diameter of 500 nm. High density regions appearing inside the cells can be assigned as stacks of thylakoid membranes from comparison with our fluorescence LM observations as well as cryogenic EM tomography of a frozen-hydrated and sectioned cyanobacterial cell [35]. Thylakoid membranes in cyanobacteria are located in the marginal region rather than the central part, as also seen in the chloroplasts of *C. merolae*. The similarity in the structural morphology strongly suggests the symbioses of two organisms.

## 8.3   Size Distribution of Noncrystalline Particles

To study the size distribution of nanoparticles in biology and material sciences, DLS, SAXS, and electron microscopy are used. In DLS, the Stokes radii of particles are estimated from the time-correlation function regarding the Brownian motion of particles in solution [36]. In SAXS, although the range of radii of gyration is estimated for solutions of particles with a size distribution using Fankuchen's plot [37], it is difficult to estimate the size distribution. Only for a monodispersive solution of particles is the radius of gyration determined from Guinier's analysis [38]. While these techniques provide averaged information on the particle sizes in a solution, electron microscopy provides the outer shapes of individual particles at high resolution in vacuum. However, because the penetration depth of electrons into specimen particles is limited by their strong interactions with the atoms, it is difficult to visualize the internal structures of thick particles with dimensions larger than 200 nm.

As the internal structure and size of particles influence the physicochemical properties, it is better for both the size distribution and internal structure of sub-micrometer particles to be simultaneously characterized. XFEL-XDI measurements provide an opportunity to simultaneously measure the size distribution and internal structures of particles. A number of maps retrieved from high-quality diffraction patterns allow us to construct statistically significant size distributions of specimen particles as well as their internal structures [39, 40].

### 8.3.1   Cuprous Oxide Particles

Cuprous oxide particles, which are used as standard specimens to determine the camera parameters in XFEL-XDI experiments, are prepared from a mixture of copper sulfate, sodium dodecyl sulfate solution, sodium ascorbate solution, and sodium hydroxide solutions [41]. The size of particles ranges widely from 200 to 1000 nm, and is difficult to control.

The size distribution of cuprous oxide particles can be constructed from XFEL-XDI experiments. Cuprous oxide particles are dispersed onto silicon nitride membranes at a number density of approximately 5 particles per $10 \times 10 \ \mu m^2$. From raster scans of the membrane, more than 1000 particle images of single particles and aggregates of particles are obtained from diffraction patterns with good signal-to-noise ratios (Fig. 8.8a). Then, the edge lengths of particles are directly measured as the number of pixels in the PR maps. For diffraction patterns from single particles, the edge length of a particle can be determined from the peak-to-peak distance along the axes of the crossed interference pattern.

The size distribution is composed of a major peak located at 300 nm with a half width of 60 nm and an additional sub-peak at 510 nm (Fig. 8.8a) [40]. The
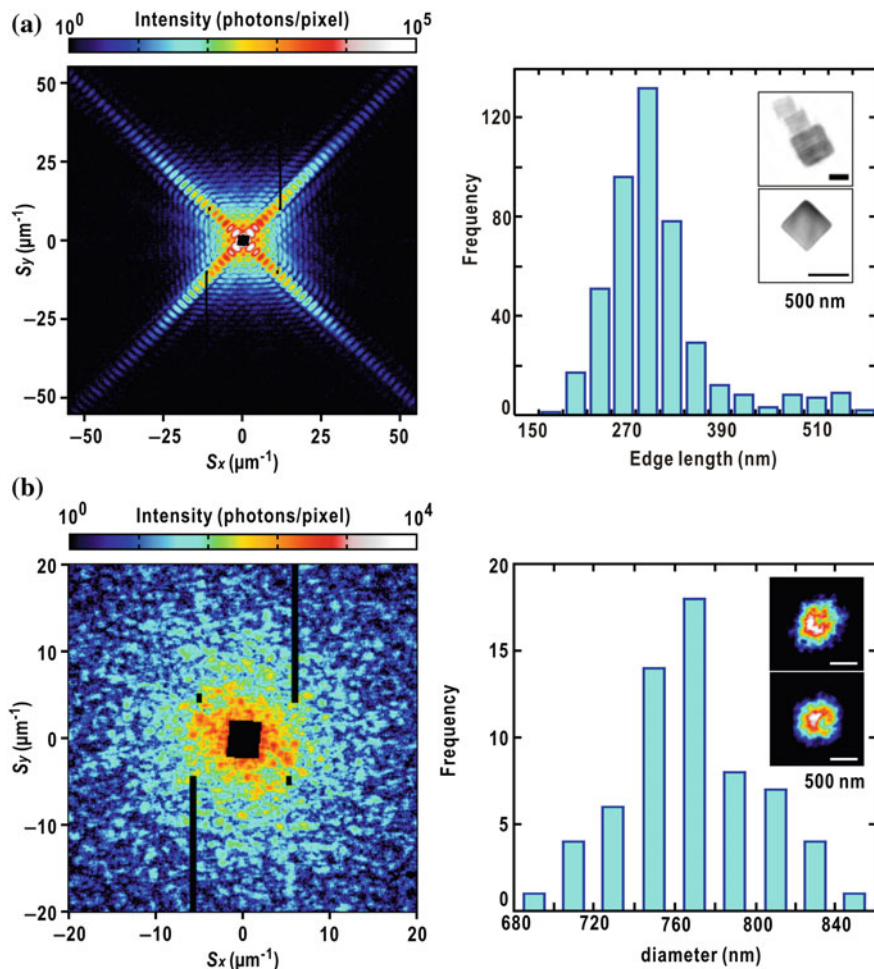
**Fig. 8.8** Diffraction patterns and the size distributions of cuprous oxide particles [40] (**a**) and cyanobacterial cells [27] (**b**). Both panels are reused from [41 (https://doi.org/10.1107/s160057751400343) and [27] (https://doi.org/10.1107/s1600577516007736)] after modification with permission from The International Union of Crystallography

distribution resembles that from SEM images for particles produced at the same time as those used for the XFEL-XDI experiment. The penetration power of the X-rays allows us to visualize the internal structures of particles in XDI. Indeed, most cuprous oxide particles have nonuniform density. Therefore, XFEL-XDI provides opportunities to study both the size distribution and internal structures of synthesized nanoparticles simultaneously.

## 8.3.2   Cyanobacteria Cell

SEM visualizes the surface structures of dried biological specimens under vacuum. TEM provides the sizes of small biological specimens embedded in thin vitreous ice, or sliced and stained specimens. Cryogenic XDI can be applied to measure the size and structure of biological specimens, such as cells and organelles. As demonstrated in Fig. 5.7, the size distribution of cyanobacteria is within the range of that determined from DLS,

Because the cell size is less than 1 μm, cyanobacterial cells are visualized at approximately 5 × 5 pixels of 200 nm at a resolution limit of LM. The small cell size prevents the identification of specific events during the cell cycle. In contrast, the size distribution and PR maps from XDI experiments can be used to define stages in the cell cycle. As an example, the size distribution of cyanobacteria cells is constructed from PR maps from high-quality diffraction patterns. Although the number of PR maps is still small, the size distribution in the range from 700–800 nm is approximated by a Gaussian centered at 780 nm with a half width of approximately 20 nm. In the near future, the size distribution and internal structures of cyanobacteria under different illumination conditions will be studied in order to identify the stage of the cell cycle.

## 8.3.3   Amyloid Aggregate

Amyloid fibrils, insoluble fibrous aggregates of misfolded proteins, are known to cause various neurodegenerative disorders [42]. For instance, the aggregation and deposition of α-synuclein in neuronal cells have recently been demonstrated to have a correlation with the pathogenesis of Parkinson's disease [43]. While the molecular mechanisms regarding the aggregation and fibril formation of α-synuclein have been studied at molecular levels [44], it is still unclear which sizes of aggregates and fibrils display toxicity to cells. Recently, intermediates of α-synuclein formed during fibrillogenesis have been revealed by biological assays to be the most toxic to neuronal cells. Because toxic aggregates of α-synuclein and GroES, a model protein of α-synuclein, have dimensions from 100 to 2000 nm, their sizes and structures can be studied by XFEL-XDI. Toxic aggregates produced by incubation in the presence of a denaturation reagent are dispersed on the silicon nitride membrane and flash cooled for XFEL-XDI experiments [45].

A representative diffraction pattern from an aggregate of GroES was composed of speckle patterns appearing in a small-angle region up to a resolution of 40 $\mu m^{-1}$ (corresponding to 25 nm in real space) and prominent interference patterns with regularly spaced fringes stretched beyond a resolution of 60 $\mu m^{-1}$ (16 nm in real space) (Fig. 8.9a). The most probable PR map has a rectangular shape with dimensions of 800 nm × 400 nm. The dimensions are comparable to those estimated directly from the reciprocal of the speckle size.

**(a)**



**(b)**                                        **(c)**
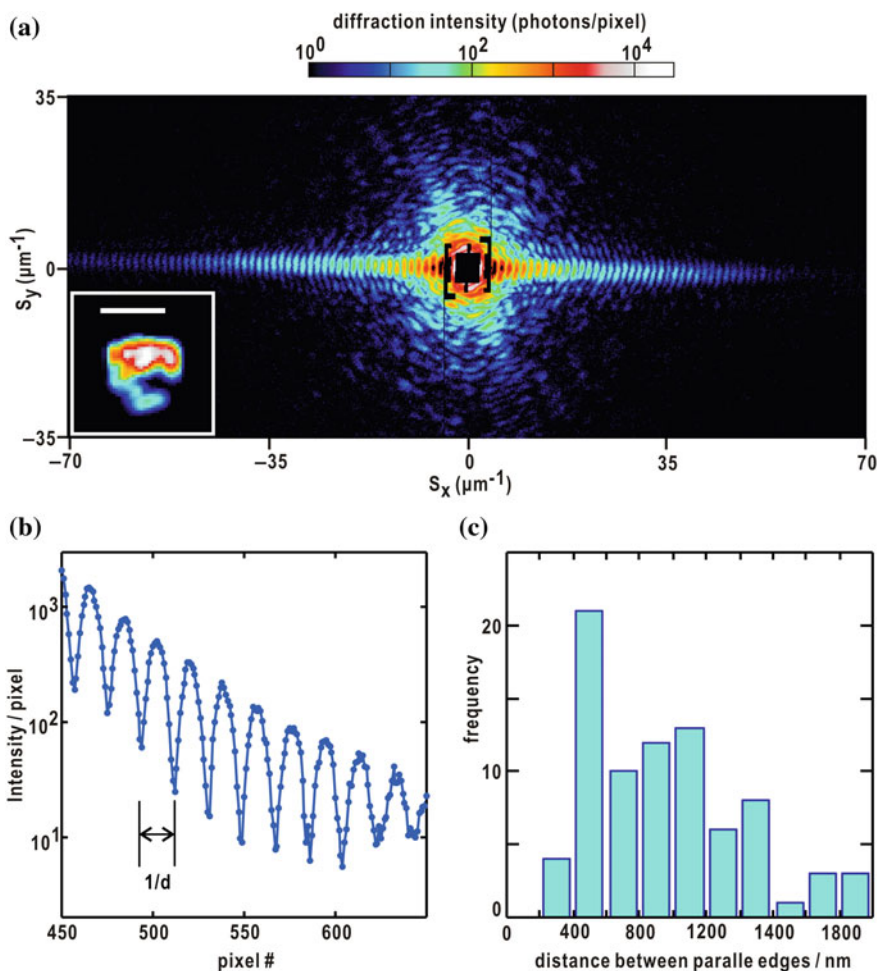


Fig. 8.9  **a** The diffraction pattern from a GroES aggregate. The most probable PR map is shown in the inset with a scale bar of 500 nm. **b** The line profile of the diffraction intensity along the interference pattern in panel (**a**) is plotted against the pixel number. One hundred pixels corresponds to 15.2 μm$^{-1}$. **c** The size distribution of GroES aggregates. Panels are reused from [45] after modification with permission from The Journal of Biochemistry, Oxford University Press

The aggregate contained sharp edges in parallel to each other. The diffraction pattern from a particle with a pair of parallel edges has a series of interference patterns along the direction normal to the edges. In the ideal case, the Fraunhofer diffraction intensity from a pair of edges separated by $2a$ is described by [46]

$$I(S) \propto \left[ \frac{\sin{(2\pi S a)}}{2\pi S a} \right]^2 . \qquad (8.1)$$

By applying this equation, the reciprocal of the period in the fringe pattern gives the edge-to-edge distance of the aggregate, even when PR calculations are failed (Fig. 8.9b).

Under the assumption that the edge-to-edge distances reflect the sizes of toxic aggregates, the distributions of the edge-to-edge distances among aggregates can be constructed from diffraction patterns alone. For instance, the sizes of 138 GroES aggregates are distributed in a wide range from 200 to 1500 nm, suggesting that the parallel edge structures is independent of the aggregate size. In TEM images for stained specimens, parallel edges are difficult to identify, probably because the images of the edges are modified by staining reagents and point spread. On the other hand, diffraction patterns are sensitive to the width and parallelism of the edges of particles. XDI would be more advantageous to address the size distribution than TEM.

Amyloid fibrils are organized into assemblies of β-sheets, which possess parallel edges. By considering the structural characteristics of amyloid fibrils revealed by XDI, it can be seen that assemblies of β-sheets would be one of the structural components forming the parallel edges of aggregates. This idea leads us to speculate on why the aggregates are toxic for cells. Assemblies of β-sheets work as platforms to further extend the β-sheet structures by incorporating proteins onto the surfaces of the aggregates. A number of hydrogen bonds formed between the main chains of polypeptides in the β-strand conformation stabilize the structures. Therefore, the edges of the aggregates probably work as a platform to adsorb β-sheets of other polypeptides and assist the growth of fibril structures.

Toxic aggregates incorporated into cells modify the structures of other proteins by forming hydrogen bonds with the β-sheet structures. If those proteins which are bonded are necessary for cell metabolism, the aggregates will be toxic to the cells. According to this idea, molecules with affinities for β-sheets retard the formation of β-sheet structures between aggregates and other polypeptides, and subsequently reduce the toxicity of aggregates.

# References

1. J. Miao, T. Ishikawa, I.K. Robinson, M.M. Murnane, Science **348**, 530 (2015)
2. J. Miao et al., Proc. Natl. Acad. Sci. U.S.A. **100**, 110 (2003)
3. D. Shapiro et al., Proc. Natl. Acad. Sci. U.S.A. **102**, 15343 (2005)
4. C. Song et al., Phys. Rev. Lett. **101**, 158101 (2008)
5. E. Lima et al., Phys. Rev. Lett. **103**, 198102 (2009)
6. X. Huang et al., Phys. Rev. Lett. **103**, 198101 (2009)
7. D. Nam et al., Phys. Rev. Lett. **110**, 098103 (2013)
8. J. Fan et al., Anal. Chem. **87**, 5849 (2015)
9. E. Lima et al., J. Microsc. **249**, 1 (2013)

10. M. Nakasako et al., Rev. Sci. Instrum. **84**, 093705 (2013)
11. K. Tamasaku et al., Nucl. Instrum. Meth. A **467–468**, 686 (2001)
12. Y. Takayama, M. Nakasako, Rev. Sci. Instrum. **83**, 054301 (2012)
13. Y. Imoto et al., J. Electron Microsc. **60**, S117 (2011)
14. M.M. Seibert et al., Nature **470**, 78 (2011)
15. R. Neutze, Nature **406**, 752 (2000)
16. H.N. Chapman et al., Nat. Phys. **2**, 839 (2006)
17. K. Hirata et al., Nat. Methods **11**, 734 (2014)
18. S. Kassemeyer et al., Opt. Express **20**, 4149 (2012)
19. D. Nam et al., J. Phys. B: At. Mol. Opt. Phys. **49**, 034008 (2016)
20. S. Kassemeyer, Ultrafast coherent diffractive imaging of nanoparticles using X-ray free-electron laser radiation (Doctoral dissertation, Fachbereich Physik der Freien Universität Berlin) (2014)
21. T. Kimura et al., Nat. Commun. **5**, 3052 (2014)
22. R. Yoshida et al., J. Phys. B: At. Mol. Opt. Phys. **48**, 244008 (2015)
23. K. Tono et al., New J. Phys. **15**, 083035 (2013)
24. H. Yumoto et al., Nat. Photon. **7**, 43 (2013)
25. A. Kobayashi et al., Rev. Sci. Instrum. **87**, 053109 (2016)
26. T. Oroguchi et al., J. Phys. B: At. Mol. Opt. Phys. **48**, 184003 (2015)
27. A. Kobayashi et al., J. Synchrotron Rad. **23**, 975–989 (2016)
28. J. Ruan et al., Proc. Natl. Acad. Sci. U.S.A. **109**, 20643 (2012)
29. Y. Takayama et al., Plant Cell Physiol. **56**, 1272 (2015)
30. Y. Sekiguchi, T. Oroguchi, M. Nakasako, J. Synchrotron Rad. **23**, 312 (2016)
31. A.W. McDoWall et al., J. Microsc. **131**, 1 (1983)
32. H.-N. Su et al., Photosynth. Res. **106**, 73 (2010)
33. Y. Yoshida et al., Science **329**, 949 (2010)
34. A. M. L. van de Meene et al., Arch. Microbiol. **184**, 259 (2006)
35. C.S. Ting et al., J. Bacteriol. **189**, 4485 (2007)
36. B.J. Berne, R. Pecora, *Dynamic Light Scattering with Applications to Chemistry, Biology and Physics* (Dover, New York, 2000)
37. M.H. Jellinek, I. Fankuchen, Ind. Eng. Chem. **41**, 2259 (1949)
38. A. Guinier, G. Fournet, *Small-Angle Scattering of X-Rays* (John Wiley, New York, 1955)
39. Y. Takahashi et al., Nano Lett. **13**, 6028 (2013)
40. Y. Sekiguchi, T. Oroguchi, Y. Takayama, M. Nakasako, J. Synchrotron Rad. **21**, 600 (2014)
41. C.H. Kuo, C.H. Chen, M.H. Huang, Adv. Funct. Mater. **17**, 3773 (2007)
42. M. Hashimoto, E. Masliah, Brain Pathol. **9**, 707 (1999)
43. M. Goedert, M. Nat, Rev. Neurosci. **2**, 492 (2001)
44. H.A. Lashuel et al., Mol. Biol. **322**, 1089 (2002)
45. H. Kameda et al., *J. Biochem.* (Tokyo) **161**, 55 (2017)
46. M. Born, E. Wolf, *Principles of Optics* (Cambridge University Press, Cambridge, 1999)

# Chapter 9
# Three-Dimensional Structural Analyses in Cryogenic X-Ray Diffraction Imaging

**Abstract** An electron density map projected along the direction of the incident X-ray is obtained from a single small-angle diffraction pattern. However, most projection maps are difficult to interpret. The final goal of a structural analysis is a visualization of the electron density distribution in three dimensions. In this chapter, the tomography X-ray diffraction imaging (XDI) method is first introduced to visualize three-dimensional (3D) electron density maps of particles in XDI using synchrotron radiation. In XDI experiments using X-ray free electron laser (XFEL) pulses, as the specimen particles are destroyed by single X-ray pulses, tomography experiments are impossible. Under the assumption that the structures of the particles are similar at a low resolution, 3D reconstruction is possible by utilizing the single particle analysis method developed in transmission electron microscopy (TEM). A scheme for 3D reconstruction in XFEL-XDI through simulations for macromolecules and experiments on a cellular organelle is proposed.

## 9.1 Reconstruction of Three-Dimensional Electron Density Map

A single diffraction pattern provides a map of a specimen particle projected along the direction of the incident X-ray, as shown in Chap. 8. However, a single projection image is difficult to interpret, except cases viewed along a particular direction providing representative structures of specimen particles (see Fig. 8.6 in Chap. 8). The reconstruction of 3D electron density maps is necessary to visualize the structures of specimen particles. Two types of 3D reconstruction methods are applied in XDI experiments and simulations.

One is the 3D phase retrieval (PR) calculation for a set of diffraction amplitudes collected to satisfy a 3D OS condition in reciprocal space. Because of the limited beam-time in synchrotron XDI experiments, however, it is difficult to collect

diffraction patterns to satisfy the 3D OS condition. Therefore, the equally sloped tomography with oversampling reconstruction (EST) method is developed for 3D PR of a limited number of diffraction patterns with a insufficient oversampling ratio [1]. 3D PR calculations were applied to the structural analyses of metal particles from material sciences [2] as well as biological cells and cellular components [4−6]. In XFEL-XDI experiments, a number of diffraction patterns are collected from particles oriented randomly against the propagation direction of the XFEL pulses. The collected diffraction patterns are reconstructed as a 3D distribution of diffraction intensity in reciprocal space, under the assumption that the particles are in the same structures and are completely exposed ("naked") to vacuum [7].

The other is the 3D reconstruction method, i.e., the so-called single particle analysis, developed in TEM [8]. In TEM, 3D reconstruction from the projection images of macromolecular assemblies was proposed about 50 years ago [9], and was first applied to specimens with structural symmetry, such as viruses and helical fibrous objects [9, 10]. Owing to the symmetry, the 3D images of those particles could be reconstructed from a limited number of projection images. Later, a strategy was proposed for reconstructing the 3D structure of a single macromolecule without structural order or symmetry [11, 12]. The mathematical principle of the 3D reconstruction method is based on the projection theorem (see below and (3.16) of Chap. 3).

While utilizing the 3D reconstruction method in XDI, care should be taken that there is a large difference between the radii of the Ewald spheres between X-ray diffraction and TEM. In TEM, the wavelength of the electron wave is of the order of a picometer [(1.3) of Chap. 1], and then the Ewald sphere is approximated as a plane intersecting the origin in reciprocal space. In contrast, as the wavelength of the X-rays used in XDI experiments is in the order of 0.1 nm, the Ewald sphere is approximated as a plane only in the small-angle region. Only the structure factor in the small-angle region is assumed to be the Fourier transform of the electron density map projected along the direction of the incident X-ray beam.

In the following subsections, the protocols and examples of applications of single particle analysis combined with PR calculations are described. Prior to these descriptions, the principle of single particle analysis in EM is outlined [8].

### 9.1.1  Projection Theorem

The mathematical background of 3D reconstruction is the projection theorem. We have already mentioned the relevant equation (3.16) in Sect. 3.4 of Chap. 3. The Fourier transform of the density projected along the direction of the incident

beam provides a structure factor on a plane. The plane is normal to the projection direction and intersects the origin of reciprocal space. The direction of projection is arbitrarily defined in any coordinate system in real space by changing the orientation of the specimen with respect to the direction of the incident beam. Therefore, by varying the orientation, the structure factors of the projected electron density maps of a particle at various orientations with respect to the incident beam are collected. When the orientation is finely varied, the 3D structure factor can be reconstructed. The 3D density map of the particle is obtained by taking the Fourier transform of the 3D structure factor. For 3D reconstruction from projection images, several mathematical methods are used. Here, two methods, the back-projection method and the Fourier reconstruction method, are briefly introduced.

## 9.1.2 Back-Projection Method

The structure factor of a particle in the small-angle region is approximated as the Fourier transform of a projection map of the particle. Therefore, small-angle diffraction patterns collected by a series of rotations around an axis perpendicular to the incident X-ray beam yield a set of PR maps (Fig. 9.1). From the set, the 3D map is reconstructed by, for instance, the back-projection method, as a representative method of 3D reconstruction. The weighted back-projection method is an inverse



**Fig. 9.1** Schematics of 3D reconstruction in XDI using the weighted back-projection method. In tomography XDI experiments, diffraction patterns are collected by rotating a specimen particle with respect to the direction of the incident X-ray beam (**a**). From PR maps, the 3D electron density map of the particle is reconstructed by, for instance, the back projection method (**b**). Published with kind permission of Masayoshi Nakasako 2017. All Rights Reserved
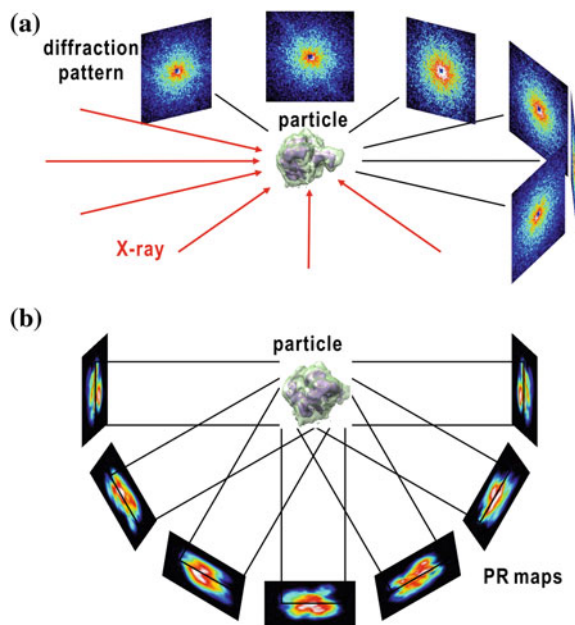
operation of the projection, and prints a projection image onto the 3D volume of an object (Fig. 9.1) [8, 13].

A simple reconstruction of the 3D electron density of an object, $\rho^{3D}(\boldsymbol{r})$, is expressed using $N$ projection maps $\left(\rho_i^{2D}(x, y), \; i = 1, N\right)$ as

$$\rho_{simple}^{3D}(\boldsymbol{r}) = \sum_{i=1}^{N} \rho_i^{2D}(x, y)\, t(z), \qquad (9.1)$$

where $\rho_i^{2D}(x, y)$ is the projection map at the $i$th orientation, and $t(z)$ is a step function that varies as

$$t(z) = \begin{cases} 1 & \text{for} - D/2 \le z \le D/2 \\ 0 & \text{elsewhere} \end{cases} \qquad (9.2)$$

and expands (back-projects) the projection image, where $D$ must be larger than the size of the particle.

In the sampling of the diffraction amplitude in reciprocal space, the sampling points are densely distributed in the small-angle region, but sparse in the high-angle region. This difference causes a blurred 3D density reconstructed by the back-projection method. In practice, to avoid this effect, the weighted back-projection method [8, 13] is used as

$$\rho_{weight}^{3D}(\boldsymbol{r}) = F^{-1}\left[ W(\boldsymbol{S})F\left(\rho_{simple}^{3D}(\boldsymbol{r})\right) \right] \qquad (9.3)$$

The Fourier transform of the weighted density map can be calculated as

$$\begin{aligned} F\left[\rho_{weight}^{3D}(\boldsymbol{r})\right] &= \sum_{i=1}^{N} F\left[\rho_i^{2D}(x, y)\, t(z)\right] \\ &= \sum_{i=1}^{N} F\left[\rho_i^{2D}(x, y)\right] D\frac{\sin(\pi D S_z)}{\pi D S_z}. \end{aligned} \qquad (9.4)$$

By comparing the two equations above, the weight factor $W(\boldsymbol{S})$ can be defined. In practice, there is the possibility that $W(\boldsymbol{S})$ becomes infinitely large. In this case, $W(\boldsymbol{S})$ is replaced with a constant $T$ as

$$W(\boldsymbol{S}) = \begin{cases} \dfrac{1}{\sum_{i=1}^{N} D\frac{\sin(\pi D S_z)}{\pi D S_z}}. \\ T \end{cases} \qquad (9.5)$$

In addition to the weighted back-projection method, the Fourier reconstruction method is used for 3D reconstruction. Then, the 3D map is calculated from the
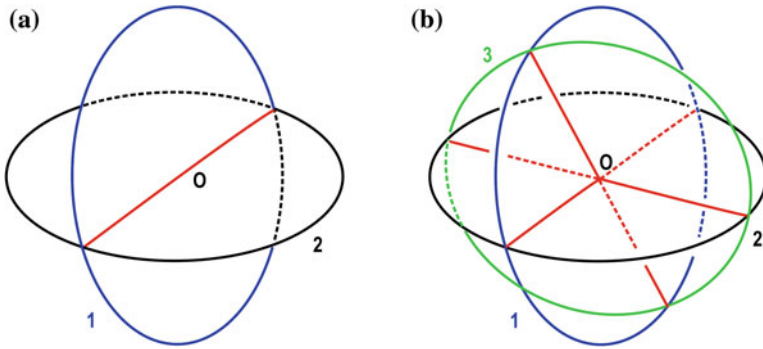
**Fig. 9.2** Illustration of the common line method. The three circles represent diffraction patterns. The red lines are common lines between any pairs of diffraction patterns. **a** A common line between an arbitrary pair of diffraction patterns. Only the relative orientation of the two diffraction patterns (projection maps) is determined. **b** Common lines obtained from the third diffraction pattern fix the rotational arbitrariness in the first pair of diffraction patterns. Published with kind permission of Masayoshi Nakasako 2017. All Rights Reserved

inverse Fourier transform of the 3D structure factor reconstructed in reciprocal space. To conduct the transform, the 3D structure factor of the particle is necessary. In the first step, the structure factors are calculated from each projection map. However, the structure factors on the grid points necessary for the 3D inverse Fourier transform are difficult to calculate. The Whittaker-Shannon interpolation method, for instance, allows us to calculate the structure factors on the grid points from a number of structure factors on planes intersecting the origin in reciprocal space [8]. This procedure gives a set of 3D structure factors necessary for conducting the 3D Fourier transform.

Both the weighted back-projection and Fourier reconstruction method require an estimation of the relative orientation of each projection map to one another. One of the representative algorithms for the estimation is the common line method [12, 14] (Fig. 9.2). According to the projection theorem (see (3.16) of Chap. 3), the diffraction pattern (or structure factor) of any projection map intersects the origin in reciprocal space. Therefore, the diffraction patterns of two arbitrary projection maps both intersect the origin and share intersecting lines running through the origin in reciprocal space. When a diffraction pattern from another projection map is added, the pattern provides two independent common lines. By this procedure, the orientation of the projection maps necessary for 3D reconstruction can be determined.

## 9.1.3   Refinement of Orientation

In the reconstruction of the 3D density map, the estimated relative orientation of each projection map against the reference map is insufficient to yield complete 3D

map, because of the inaccuracy in estimating the relative orientation of particles. Therefore, to accurately visualize the 3D structure of the particle, refinement on the orientation angles of the projection maps is necessary. As an example, the projection matching method is briefly introduced here (Fig. 9.3) [15].

In the first step, a number of projection maps are calculated from the initial 3D map. Then, cross correlation between the calculated maps and an experimental projection map is obtained. Although the orientation of the map is already estimated by, for instance, the common line method, the orientation is reset to that yielding the maximum cross-correlation. The orientation of any experimental projection map is recalculated by this procedure. Then, a new 3D map is reconstructed from a set of projection maps with a new orientation. This procedure is iterated until convergence.

Now, the 3D reconstruction algorithms are implemented in program suits [16–18]. To apply the 3D reconstruction program suite to the XDI structural analyses, the PR maps are treated as TEM images. Recently, a program suite incorporating Bayesian inference has been developed for more reliable refinement of the
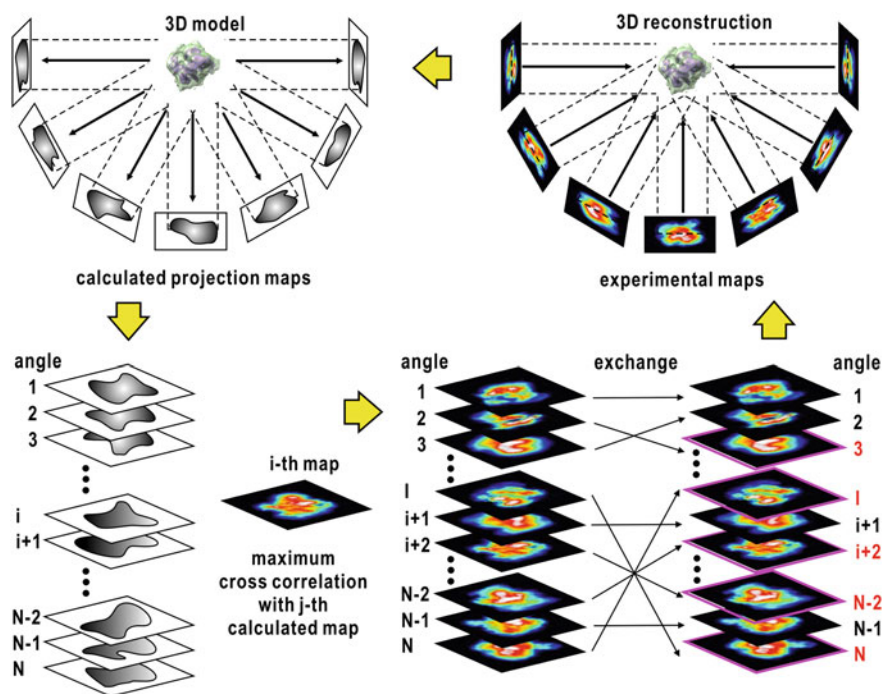


**Fig. 9.3** Schematic of the projection matching method. Published with kind permission of Masayoshi Nakasako 2017. All Rights Reserved

orientation of projection maps without overfitting in 3D models or bias from inaccuracies in experimental data [19, 20].

### 9.1.4   Handedness

For scattering objects without anomalous scatterers, it is, in principle, impossible to determine the absolute structure or handedness of the obtained PR map. In tomography XDI, the handedness of PR maps can be tentatively regularized against a reference map by a series of successive rotations of a specimen particle, although the handedness of the reference map is unknown. In practice, in tomography XDI, the handedness is almost the same among the PR maps, but the possibility of π-rotations must be taken into consideration (see Sect. 9.3.3). In contrast, this regularization of handedness is difficult to apply to PR maps of particles in XFEL-XDI experiments, because the particles are oriented randomly with respect to the direction of the incident XFEL pulses.

### 9.1.5   Fourier Shell Correlation for Estimating the Effective Resolution of the Reconstructed Three-Dimensional Map

The effective resolution of the refined 3D electron density map is evaluated using the Fourier shell correlation (FSC) [12, 21]. FSC for a given resolution shell $S'$ is defined as

$$FSC(S') = \frac{Re \sum_{S \in S'} F_1(S) \cdot F_2^*(S)}{\sqrt{\sum_{S \in S'} |F_1(S)|^2 \sum_{S \in S'} |F_2(S)|^2}}, \tag{9.6}$$

where $F_1(S)$ (or $F_2(S)$) is the structure factor of the reconstructed density from the half-set of the projection images (Fig. 9.4). A Fourier shell correlation of 0.143 corresponds to an FOM of 0.5 in X-ray crystallography [22]. Projection images are divided into two groups at the start of the 3D reconstruction to avoid overfitting in the 3D reconstruction and subsequent refinement. Then, the FSC calculated from two independently obtained 3D structures is designated as the gold standard FSC [23]
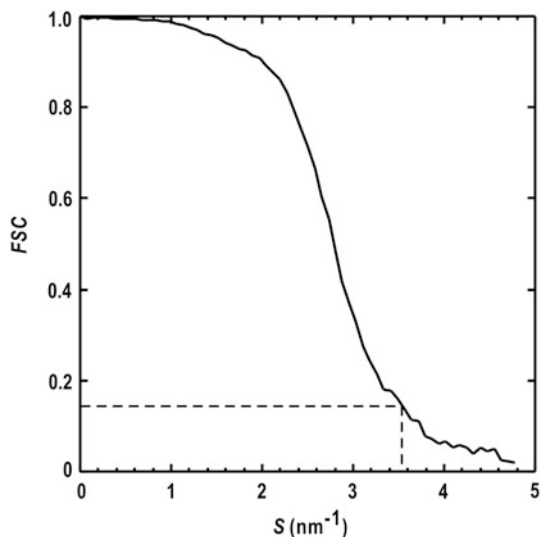
## 9.2  Tomography of Biological Cells by Using Synchrotron X-Rays

In tomography experiments, a series of diffraction patterns is collected by rotating the specimen around an axis perpendicular to the direction of the incident X-ray. From the diffraction pattern, the 3D structure of the specimen particle can be reconstructed. A tomography XDI experiment was first performed for a test specimen at BL29XUL of SPring-8 [24]. The test specimen is composed of two geometrical patterns with the size of $2.5 \times 2.0 \times 0.1$ μm by nickel-deposition onto silicon nitride membranes. The two patterns are separated by 1 μm along the direction of the thickness of the specimen with a mutual rotation. Diffraction patterns are collected in 5° steps in the angular range of 150°. The 3D PR calculation successfully reconstructed the 3D electron density map of the two patterns from the diffraction amplitudes merged in reciprocal space. This experiment demonstrated the advantage of the penetration power of X-rays with short wavelengths. After the demonstration, the tomography XDI method was applied to a quantum dot particle made of gallium nitride [2]. In this experiment, the 3D map was reconstructed from 27 diffraction patterns at a resolution of 17 nm by the EST method [1].

With regard to biological specimens, tomography XDI was applied to a single chromosome of a human HeLa cell [3]. A chromosome particle is set in a vacuum chamber after the deposition onto a silicon nitride membrane. Diffraction patterns were collected in the angular range of 140° with steps of 2.5° or 5°. In the 3D PR map reconstructed at a resolution of 76 nm, the scaffold of the chromosome ran through the four lobes of the chromosome. The 3D map of a chemically fixed spore of budding yeast was reconstructed from 25 diffraction patterns collected in the

angular range of approximately 140° [4]. The organelles inside the yeast cell, such as the nucleus and mitochondrion, are visualized at an approximate resolution of 60 nm. The tomography XDI method was also applied to the chemically fixed and dried cellular nucleus from a mouse [5]. From 29 diffraction patterns, the 3D electron density map was reconstructed at a resolution better than 100 nm.

These tomography XDI experiments demonstrate the potential for revealing the entire structures of cellular organelles with the thickness opaque for TEM at resolutions better than LM. However, unfortunately, the tomography XDI experiments for biological specimens were performed for chemically fixed specimens at room temperature and in vacuum. As it is difficult to deny the possibility of structural damage to the specimen particles by chemical modification, long periods of X-ray exposure, and dehydration, we are hesitant to discuss the implications of these 3D maps.

In the next stage of tomography XDI, the structural damage to cells and cellular organelles must be suppressed as much as possible. The ideal case is diffraction data collection under an aqueous condition. However, the radiation damage is severe because of the long exposure time required to collect a series of diffraction patterns. Therefore, tomography XDI at cryogenic temperatures for frozen-hydrates specimens would be better to visualize the nearly intact structures of biological specimens, under significant reduction of the radiation damage and without chemical modification and dehydration in vacuum.

As described in Chaps. 4 and 5, frozen-hydrated specimens are ideal to withstand radiation damage and dehydration under vacuum condition. Recently, the first example of a tomography XDI experiment for a biological specimen was reported [6]. In the experiment, a protozoan was flash-frozen and set into a cooled nitrogen gas stream, as is done in protein crystallography. From 72 diffraction patterns, the 3D electron density map was reconstructed at a resolution of approximately 100 nm [9].

## 9.3 Tomography of *Cyanidioschyzon merolae* Cell

Here, an example of a tomography XDI experiment is described for a *Cyanidioschyzon merolae* (*C. merolae*) cell in the phase before cell division (G/M phase) [25]. The size of the cell is approximately 5 μm. For the tomography XDI experiment, the KOTOBUKI-1 diffraction apparatus [26] was used at BL29XUL of SPring-8 (see Sect. 4.2 of Chap. 4). In addition to the 2D and 3D structural analyses, the details of the experimental procedure including specimen preparation, production of a spatially coherent X-ray beam, and diffraction data collection are described.

### 9.3.1  Specimen Preparation

*C. merolae* cells were harvested from a synchronous culture by controlling the light/dark period and temperature of incubation. A single cell in the G/M phase, which appeared as a triangular shape in LM, was placed on a $10 \times 10$ mm$^2$ silicon nitride membrane window with a silicon frame of $30 \times 30$ mm$^2$ and a thickness of 0.5 mm. The wide area of the silicon nitride membrane ensures a large rotation angle for the specimen particle against the direction of the incident X-ray. After the droplet containing a single cell was adsorbed on the membrane, any excess amounts of buffer solution were removed by a wick paper. Then, the silicon frame was dropped into a liquid ethane bath.

In referring to the image taken by LM before flash cooling, the specimen disk was placed in such a manner that the *C. merolae* cell is near the incident X-ray beam. Further adjustment of the cell was performed by raster scanning around the initial position at a step size of 1 μm. When the cell was placed in the middle of the incident X-ray beam, the most intense diffraction pattern could be recorded. The sphere of confusion of the rotation stage is less than 10 μm/360°. Therefore, positional adjustment was necessary for every rotation of the specimens for the coherent illumination (see Fig. 4.4 of Chap. 4).

### 9.3.2  Exposure Time and Irradiation Dose

In XDI experiment under spatially coherent irradiation, longer exposure time yields diffraction patterns with higher resolution. The correlation between the maximum resolution in diffraction patterns recorded by a pixel array detector [27] and exposure time was measured for a *C. merolae* cell in the G/M phase. X-rays with a



**Fig. 9.5** Correlation between the resolution limit in a diffraction pattern and the exposure time measured for a *C. merolae* cell in the G/M phase. Here, the resolution limit is defined as the point when the signal-to-noise ratio of the speckle peaks is approximately 3. Published with kind permission of Masayoshi Nakasako 2017. All Rights Reserved
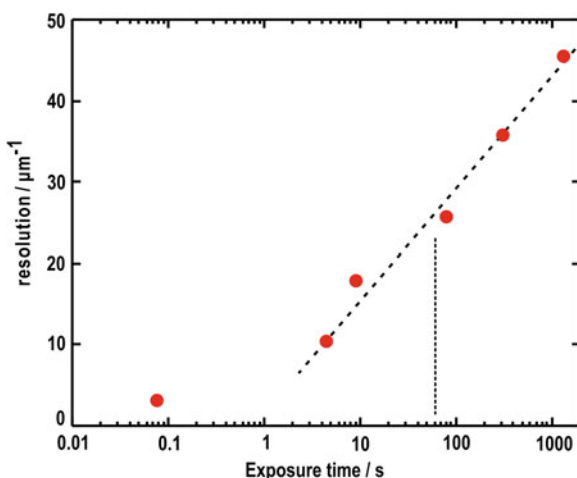
wavelength of 0.225 nm were used, and the photon flux at the specimen position was approximately $3 \times 10^9$ X-ray photons/s. With the exception of the shortest exposure time of the detector, the maximum resolutions in the diffraction patterns recorded by more than a 5 s exposure are correlated with the exposure times as shown in Fig. 9.5. Taking the limited beam-time in the synchrotron experiment into consideration, the exposure time for each diffraction pattern is set at 60 s. Then, diffraction patterns with a maximum resolution better than 25 $\mu m^{-1}$ (40 nm in real space) were expected.

The irradiation dose of the 60 s exposure is estimated using the following equation [5].

$$Dose = \left(\frac{\eta P_T}{A}\right)\left(\frac{\mu}{\rho}\right)E_0 \tag{9.7}$$

where the total number of X-ray photons $P_T$ is calculated by multiplying the photon flux density and the total exposure time. $\eta$ is the fraction of the intensity irradiating the specimen particle; this value is calculated from the particle size and the beam profile from the pinhole at the specimen position (see Fig. 4.4). $A$ is the cross section of the specimen (approximately $5 \times 5$ $\mu m^2$ for *C. melorae* in the G/M state), and $\mu/\rho$ is the mass absorption coefficient of the specimen. For biological cells, the value is set to 1.8 $m^2$/kg [5]. $E_0$ is the energy of an incident X-ray photon and is equal to 5.5 keV. For a 60 s exposure, the irradiation dose is calculated as

$$
\begin{aligned}
Dose &= \frac{0.2 \times 1.5 \times 10^{10}/s \times 60\,s}{25 \times 10^{-12}\,m^2} \times 1.8\,m^2/kg \\
&\quad \times 5.5 \times 10^3 \times 1.6 \times 10^{-19}\,J \\
&= 2.3 \times 10^5\,Gy.
\end{aligned}
$$

Based on a theoretical estimation, the maximum torelable dose for achieving 40 nm resolution is approximately $10^9$ Gy [31]. Therefore, more than 4,000 exposures of 60 s are possible (see Sect. 4.1.2 of Chap. 4).

### 9.3.3  Diffraction Patterns

Subsequently, the diffraction patterns of a single *C. merolae* cell in the G/M phase were recorded in an angular range of 175° with respect to the incident X-ray beam at an angular interval of 1.5°. Before or after recording the diffraction pattern of the cell at every rotation angle, the background diffraction pattern was collected for an area of the silicon nitride membrane far from the cell, because the nominal thickness of the silicon nitride membrane varies against the direction of the incident X-ray.

Figure 9.6 shows a set of diffraction patterns taken at every 1.5° rotation of the specimen. Accompanying the rotation, diffraction patterns in the off-rotation axis
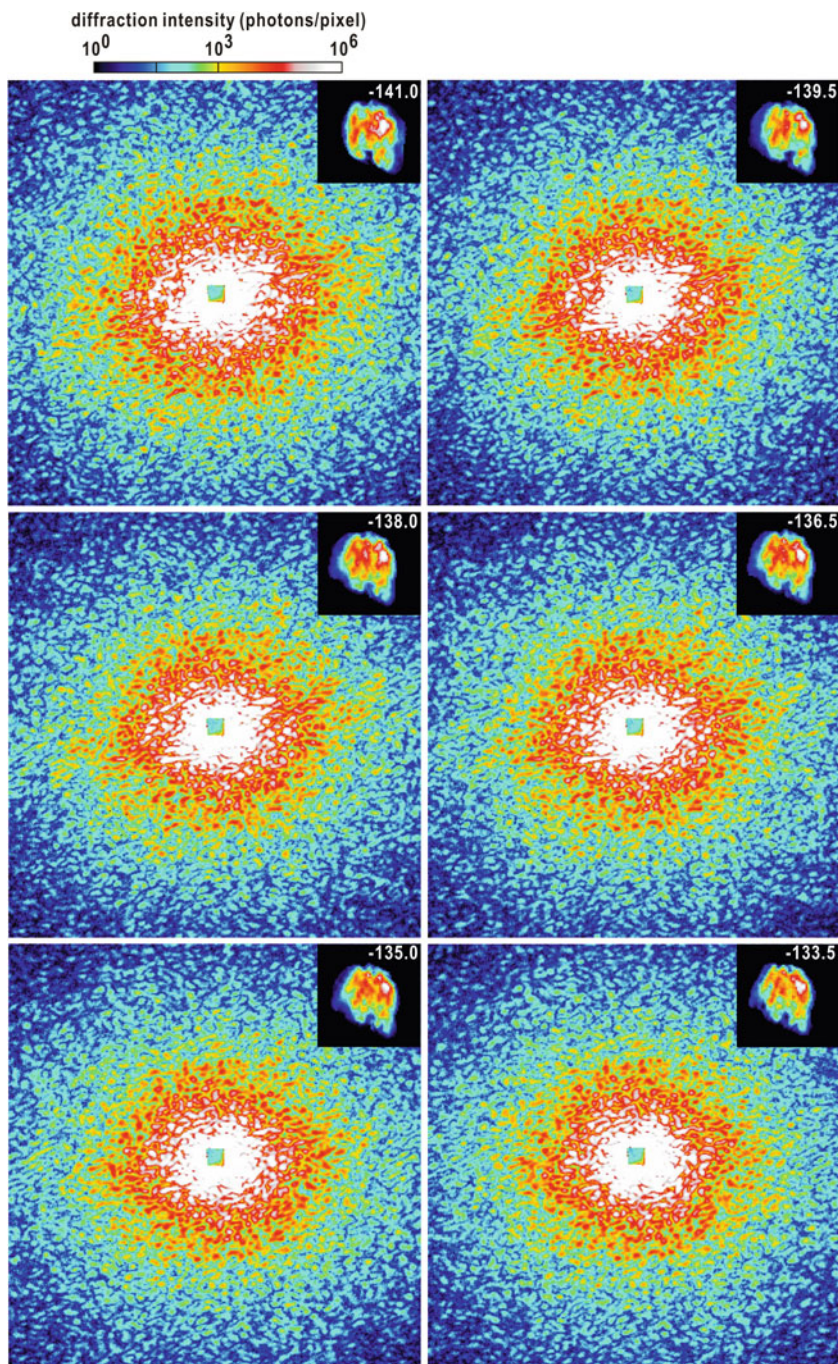
diffraction intensity (photons/pixel)
$10^0$          $10^3$          $10^6$

regions gradually changed because the Ewald sphere intersects the distribution of the diffraction intensity differently. Diffraction patterns along the rotation axis are independent of the rotation angle, due to the small sphere of confusion of the rotation stage in the diffraction apparatus.

In each diffraction pattern, speckle peaks satisfy Friedel centrosymmetry (see (2.20) of Chap. 2 and (6.3) of Chap. 6). The sizes of the speckle peaks are approximately consistent with those expected from the LM image. The signal-to-noise ratios of the speckle peaks were better than 3 up to a resolution of 25 $\mu m^{-1}$. During diffraction data collection, the diffraction patterns degrade little both in the maximum resolution and intensity of speckle peaks observed. This result confirms little radiation adamage in a series of 60-s exposure as estimated in the previous section.

The most probable projection maps were retrieved from diffraction patterns up to a resolution of 7.3 $\mu m^{-1}$ by the structural analysis scheme with multivariate analysis (Fig. 9.6) (see Sect. 7.2 of Chap. 7). In the experiment, to record a portion of the central speckle area overlapping with the incident X-ray beam, a beamstop with a size of $1 \times 1$ mm$^2$ was used. In addition, parasitic scattering from upstream optics including the pinhole was significantly reduced by careful placement of the two silicon slits. By including a portion of the central speckle pattern, the most probable PR map was easily found in the multivariate analysis. The handedness is the same among the PR maps retrieved so far. The arbitrariness regarding the π-rotation in the PR maps is observed. After regularizing the π-rotation to a reference, PR maps in an angular region of approximately 7° display similar shapes and internal structures, indicating the success of the PR calculations. Common characteristics of the PR maps are the presence of a globular body with a concavity. Inside the body, there are two or three lobes of high electron density, assignable as organelles such as chloroplasts and the nucleus.

### 9.3.4  Reconstructed Three-Dimensional Electron Density

In the tomography experiment, 119 diffraction patterns are collected with angular intervals of 1.5° or 3.0° in an angular range of 180°, as illustrated in Fig. 9.7a. The cryogenic pot with a flat top shape enabled us to collect diffraction patterns in this wide angular range (see Fig. 4.5 of Chap. 4).

By applying the weighted back-projection method in the EMAN program suite [17], a preliminary 3D electron density map was reconstructed at an effective
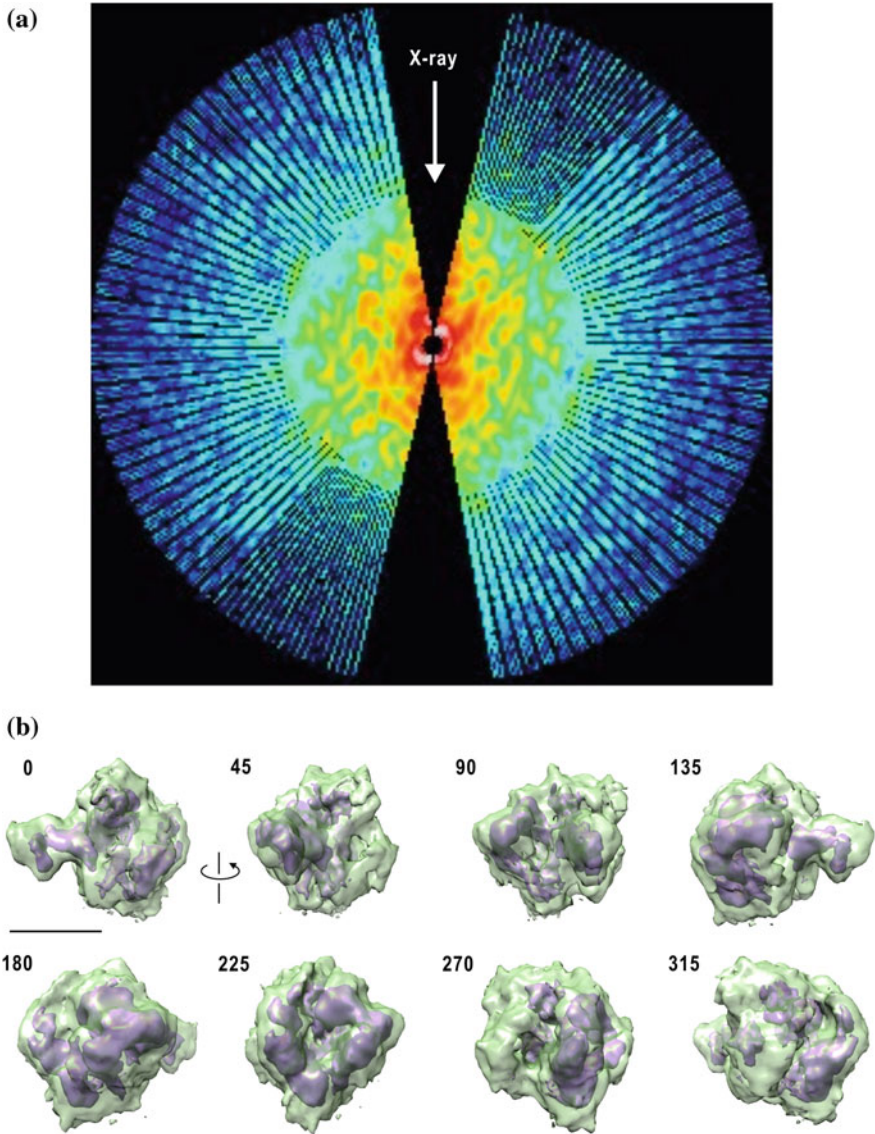
**Fig. 9.7 a** Distribution of the diffraction intensity in a off-equatorial plane normal to the rotation axis of the goniometer. The arrow indicates the direction of the incident X-ray beam. The resolution at the edge is 7.3 $\mu m^{-1}$. **b** Views of the 3D electron density map of a *C. merolae* cell reconstructed from the diffraction data shown in panel (**a**). The nominal angle of each view is labeled. The scale bar indicates 3 $\mu m$. The surfaces colored green and purple are the cell envelop and organelles, respectively. Published with kind permission of Masayoshi Nakasako 2017. All Rights Reserved

resolution of 7 $\mu m^{-1}$, corresponding to 130 nm in real space, as illustrated in Fig. 9.7b. The overall dimensions of the 3D map were approximately $6 \times 5 \times 5$ m$^3$ with an anisotropic shape. The shape is divided into one large lobe and one small lobe. The large lobe has approximate dimensions of $3 \times 5 \times 5$ $\mu m^3$. Inside the lobe, the electron density distribution is nonuniform. Two high density regions with non-globular and curved shapes appear along the envelope. In the small lobe, a stick-shaped high-density region is connected to another high-density region located at the interface of the two lobes.

The structures of *C. merolae* in different steps of the cell cycle are illustrated using fluorescence LM [26]. For instance, a cell in the G/M state appears as two spherical chloroplasts and one spherical nucleus. By comparing the locations of the two lobes and the number of high density peaks in the 3D map with the LM image, the large lobe can be assigned as a region of chloroplasts, and the small lobe as the nucleus. In the two-dimensional LM images, probably due to the point spread, the organelles mostly appear as globular shapes. However, the 3D density map likely provides more detailed shapes of the organelles. By extending the resolution through the refinement of the electron densities in each voxel, further details could be discussed.

The 3D density map obtained from an entire cell without sectioning, staining, or chemical labeling is advantageous for discussing the internal structures of the cells. The resolution of the diffraction patterns depends on the total scattering cross-section of the cell. Cells with an approximate diameter of 5 $\mu m$ would be analyzed at a resolution higher than 50 nm in the near future using undulator radiation.

## 9.4 Simulation of Three-Dimensional Reconstruction in X-Ray Diffraction Imaging Using X-Ray Free Electron Laser Pulses

In XFEL-XDI experiments, only one diffraction pattern is available for each specimen particle, because the specimen particles are destroyed by single-shot XFEL pulses (see Sect. 4.3.1 of Chap. 4). Since the first simulation study for the structural analysis of protein using XFEL pulses [1], a trend in the 3D reconstruction of electron density maps is the application of 3D PR calculations to the 3D distribution of diffraction intensities reconstructed in reciprocal space. The reciprocal-space correlation method has been proposed and applied to the ab initio reconstruction of a 3D image of a single particle, using the diffraction patterns from particles with the same structures but in random orientations [29–31]. If a particle has a special symmetry in its structure, the 3D structure can be retrieved from a single-shot diffraction pattern, as has been demonstrated for a metal particle [32]. In addition, as an attempt to reconstruct the 3D map of a specimen particle from a

single shot diffraction pattern, an algorithm named 'ankylography' has been pro-
posed [33] and is in debate [34].

An alternative approach is 3D reconstruction in real space [35, 36] by using the
single-molecule reconstruction method [12, 17]. Even when the structures of
specimen particles are closely similar, the diffraction patterns, which are sensitive to
small structural differences, prevent a 3D reconstruction of the diffraction intensity
in reciprocal space. In contrast, projection density maps are advantageous for 3D
reconstruction, because they are robust for small structural differences among
specimen particles at a low resolution. In this section, the scheme in the 3D
structural analysis is presented together with the simulation studies for a protein
[35] and macromolecular assembly [36]. The scheme is applied to visualize the 3D
structure of small cells and organelles.

### 9.4.1  Outline of Simulation

Figure 9.8a shows the setup used for the simulation study. In the simulation,
frozen-hydrated biological macromolecules are embedded in thin vitreous ice with
random orientations with respect to the direction of the incident XFEL pulses.
Then, a number of single-shot diffraction patterns of the molecules are collected
using micro-focused XFEL pulses during raster-scanning of the vitreous ice plate
(Fig. 9.8b). For a set of PR maps obtained by applying the HIO-SW algorithm (see
Sect. 3.6 of Chap. 3 and Sect. 6.5 of Chap. 6), the orientation of each particle
yielding the diffraction pattern is determined by the common line method (see
Sect. 9.1.3). Then, the initial 3D density map is reconstructed and refined by the
projection matching method (see Sect. 9.1.4). The effective resolution of the
reconstructed and refined 3D map is estimated using FSC. In this simulation, the
EMAN program suite [17] was used throughout.

The electron density distribution in the irradiation area is written as

$$\rho(\boldsymbol{r}) = \rho_{\mathrm{particle}}(\boldsymbol{r}) + \rho_{\mathrm{v-ice}}(\boldsymbol{r}), \tag{9.8}$$

where $\rho_{\mathrm{particle}}(\boldsymbol{r})$ is the electron density of a single particle. That of the vitreous ice
region is $\rho_{\mathrm{v-ice}}(\boldsymbol{r})$. Because of the interference term between the structure factors of

**Fig. 9.8  a** Schematic of an XFEL-XDI experiment for a thin vitreous ice plate [17]. The raster ▶
scan of the ice plate against the XFEL pulses with a square-shaped cross section. Many diffraction
patterns were collected with the ice plate in different positions before its destruction. **b** In the
XFEL-XDI experiment, fresh particles are provided to the irradiation area pulse-by-pulse. Because
the orientation of each specimen particle is random with respect to the direction of the XFEL pulse,
the orientations of the particles are estimated by the single particle analysis method. **c** 3D density
map can be reconstructed if the orientation of each PR map is determined. Published with kind
permission of Masayoshi Nakasako 2017. All Rights Reserved
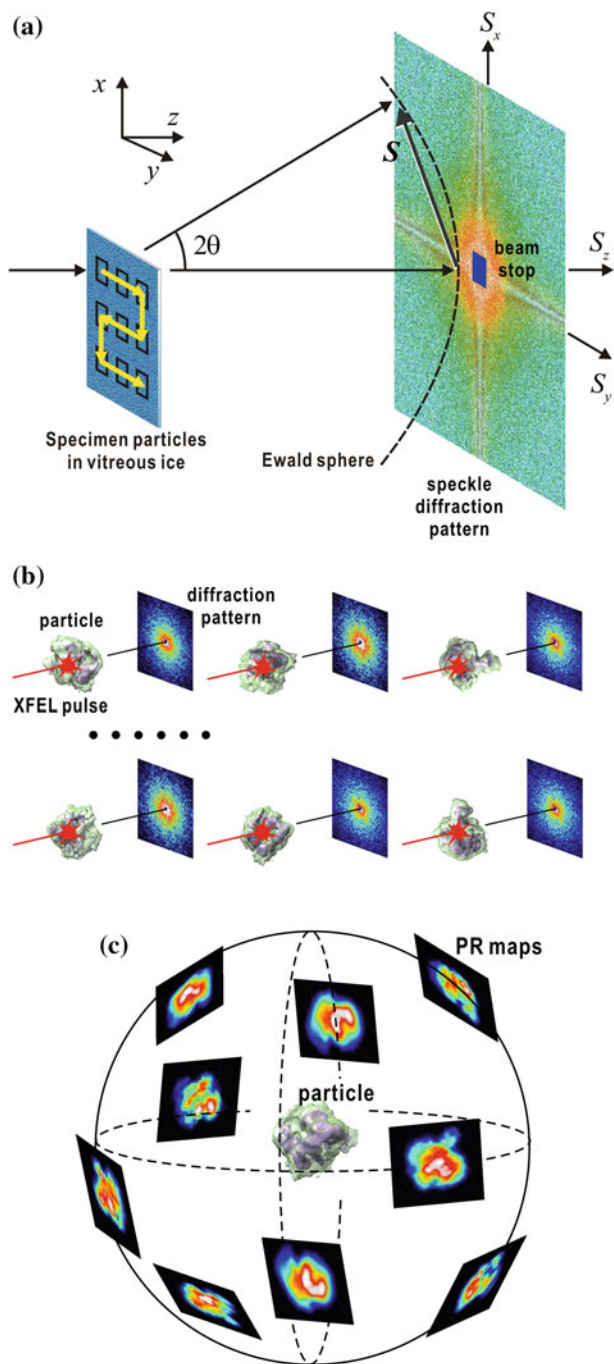
the particle and the vitreous ice region, the diffraction intensity at the scattering vector $S$ is written as

$$
\begin{aligned}
I(\boldsymbol{S}) = K\Big[ & \big|F_{\text{particles}}(\boldsymbol{S})\big|^2 + \big|F_{\text{v–ice}}(\boldsymbol{S})\big|^2 \\
& + F_{\text{particles}}(\boldsymbol{S}) \cdot F_{\text{v–ice}}^*(\boldsymbol{S}) + F_{\text{particles}}^*(\boldsymbol{S}) \cdot F_{\text{v–ice}}(\boldsymbol{S})\Big],
\end{aligned}
\tag{9.9}
$$

where $F_{\text{particles}}(\boldsymbol{S})$ and $F_{\text{v–ice}}(\boldsymbol{S})$ are the structure factors of the particles and vitreous ice in the irradiation area, respectively. $K$ is a constant calculated from the incident intensity, wavelength of the X-ray, OS ratio, specimen size, camera distance, scattering angle, and classical electron radius (see (3.1) of Chap. 3). For instance, the average electron density of water (330 electrons/nm$^3$) decreases the electron density contrast of macromolecules (400–600 electrons/nm$^3$) (see Sect. 5.5 of Chap. 5). For the reconstruction of the 3D map, the contribution from $F_{\text{v–ice}}(\boldsymbol{S})$ must be evaluated. However, the separation of $F_{\text{v–ice}}(\boldsymbol{S})$ from the observed diffraction intensity is difficult because of the third and fourth cross terms in (9.9).

A PR map from a diffraction pattern (9.8) contains the electron densities of both the particles and vitreous ice. The electron density of the particles can be extracted by subtracting the density of vitreous ice from the PR map. In addition, image-processing techniques such as low-pass filtering help to enhance the electron density contrast of the particles [35, 36]. By applying the single molecule analysis method, the initial 3D map is reconstructed at low resolution by determining the relative orientation of particles, and then the 3D map is refined by gradual extension of the resolution.

Experimentally, specimens are embedded in thin vitreous ice plates containing several hundred biomolecules per square micron. XFEL pulses easily hit the target biomolecules randomly located in the ice plate. The 3D electron density map is reconstructed from a number of phase-retrieved projection electron density maps of particles in random orientation. We examined the feasibility of this protocol using simulation studies for biological macromolecules in vitreous ice [35, 36] as described in the following sections.

### 9.4.2   Simulation for the Reconstruction of the Electron Density Map of a Protein in Vitreous Ice

To simplify the interpretation of PR maps, the simulations described in this sub-section assume an X-ray wavelength less than 0.003 nm [35]. This assumption ensures that the diffraction pattern is the square of the Fourier modulus of the

electron density map projected along the direction of the X-ray beam. When the oversampling ratio in one dimension is 2, the radius of the Ewald sphere of an X-ray of wavelength $\lambda$, the maximum resolution regarding the scattering vector length $S_{max}$, and the pixel size $S_{pixel}$ of an area detector in reciprocal space are approximately related as

$$\left(\frac{1}{\lambda^2} + S_{max}^2\right)^{\frac{1}{2}} - \frac{1}{\lambda} \approx \frac{1}{2}\lambda S_{max}^2 < S_{pixel}. \tag{9.10}$$

The molecular model used in the simulation is the crystal structure of protein disulfide isomerase (PDI) [37] (Protein Data Bank accession code: 2B5E), which is comprised of four globular domains with approximate diameters of 2 nm in an asymmetric arrangement (Fig. 9.9a). The asymmetric molecular structure allows us to judge the success and failure of the PR calculations. In the simulation, each XFEL pulse with a cross section of $13.2 \times 13.2$ nm hits a single molecule in vitreous ice with a thickness of 13.2 nm. Molecules are in random orientations and are different from each other. The diffraction pattern was calculated up to a resolution of 0.21 nm for each cube, the plane of which was normal to the direction of the incident X-ray (Fig. 9.9b).

In each projection map retrieved from a diffraction pattern, the molecular boundary of the protein molecule is difficult to define, because of the low electron density contrast between the protein molecule and the vitreous ice region. After subtracting the average electron density of the vitreous ice region from the PR map, a Gaussian low-pass filter is applied to enhance the molecular boundaries of the protein molecules. This calculation is performed using the inverse Fourier transform for a Gaussian-weighted structure factor calculated from the map after the subtraction. The filtered electron density maps allow us to identify the molecular and domain boundaries of the protein (Fig. 9.9c).

The filtered PR maps are classified by, for instance, the K-means clustering method (see (7.2) of Chap. 7), and then averaged. A selected set of images is used to generate an initial 3D density map at a resolution of 1.3 nm. By refining the mutual orientations of the structure models among the projection maps, the final 3D map is obtained along with the gradual extension of the resolution limit. The effective resolution of the final 3D map was estimated at 0.29 nm, where the FSC dropped to 0.143. The final density map fits the crystal structure of the protein well and has a quality suitable for model building (Fig. 9.9d).

While both the side chains and main chains of the amino acid residues are easily modeled in the core regions of the four globular domains, the densities of the long side chains of the amino acid residues are sometimes poor on surface areas. One cause of this poor density is an overestimation of the average density of vitreous ice. The other possible cause is insufficient refinement with regard to the rotation angles defining the orientation. Small errors in the orientation angle can reduce the average electron density of the molecular boundary. The quality of the final density map and the estimated resolution suggest that the protocol for 3D reconstruction in

**(a)**



**(b)**



**(c)**



**(d)**

real space is feasible in XDI for the structural analysis of biological particles immersed in vitreous ice.

This protocol can reduce the number of diffraction patterns necessary for 3D reconstruction. A set of $M$ diffraction patterns of $J \times J$ pixels from particles in different orientations is assumed to be necessary to reconstruct the 3D intensity distribution at an oversampling ratio $\sigma$ for a 3D PR calculation. In the proposed protocol, the support size in the retrieved projection density map is $J/\sigma \times J/\sigma$, and the area outside the support is discarded in the 3D reconstruction in real space. The angular resolution required to define the orientations at the highest resolutions becomes $\sigma$-times lower than that required in the 3D phase-retrieval method.

### 9.4.3 Three-Dimensional Reconstruction of a Number of Macromolecules in a Vitreous Ice Plate

Another simulation study is conducted to examine whether a 3D reconstruction is possible from the diffraction patterns of a thin vitreous ice plate, which contains a few hundreds of macromolecules in the irradiation area [36]. In the thin vitreous ice plate 'container', the macromolecules are dispersed in random orientations without overlap and at a number density of $N_P$ per square-shaped irradiation area $a \times a$. Here, we consider the diffraction pattern from the ice plate irradiated by an X-ray beam with a uniform intensity $I_0$ and a square-shaped cross-section $a \times a$. When the wavelength of the X-ray is $\lambda$, the diffraction intensity $I(\boldsymbol{S})$ at scattering vector $\boldsymbol{S}$ is written as

$$
I(\boldsymbol{S}) = K \left[ \left| \sum_i^{N_p} \sum_j^{N_p} F_{\mathrm{P}i}(\boldsymbol{S})^* F_{\mathrm{P}i}(\boldsymbol{S}) \right|^2 + |F_{\mathrm{v-ice}}(\boldsymbol{S})|^2 \right.
$$
$$
\left. + \left\{ \sum_i^{N_p} F_{\mathrm{P}i}(\boldsymbol{S}) \right\} \cdot F_{\mathrm{v-ice}}(\boldsymbol{S})^* + \left\{ \sum_i^{N_p} F_{\mathrm{P}i}(\boldsymbol{S}) \right\}^* \cdot F_{\mathrm{v-ice}}(\boldsymbol{S}) \right],
$$

(9.11)

where $F_{Pi}(\mathbf{S})$ and $F_{v-ice}(\mathbf{S})$ are the structure factors of the *i*th macromolecule and the irradiated area of the vitreous ice plate, respectively. As in (9.9), it is difficult to extract the first term from the diffraction intensity in reciprocal space; however, the PR map can be divided into macromolecules and the vitreous ice region, as demonstrated in the previous section. Because of the large scattering cross section, the vitreous ice region enhances the diffraction intensity. Subsequently, the resolution of the diffraction pattern from the macromolecules and vitreous ice plate is higher than that from the macromolecules alone.

In a simulation, the 50S ribosomal subunits (Protein Data Bank accession code: 1VQ8 [38]) were randomly dispersed in a vitreous ice plate with dimensions of $500 \times 500 \times 50$ nm$^3$ at a number density of 229 per $500 \times 500$ nm$^2$, corresponding to a concentration of approximately 46 mg/mL, within the possible range of the biochemical specimen preparation. The vitreous ice region is modeled using explicit water molecules, the positions of which were prepared by a molecular dynamics (MD) simulation (Fig. 9.10a). In the calculation of the diffraction patterns, the wavelength of the X-ray was set to 0.06 nm, which is the shortest wavelength available at SACLA. In addition, the cross section of the XFEL pulse was assumed to be $500 \times 500$ nm$^2$. Ideally, if the number density of the macromolecules in the vitreous ice is sufficiently high, the hit rate of the XFEL pulses is 100%.

The maximum resolution in the simulation was set to 0.8 nm, where the structure factor on the Ewald sphere was approximated by the Fourier transform of the electron density of the plate projected along the incident X-ray beam. An X-ray intensity of $5 \times 10^{16}$ photons per pulse per $500 \times 500$ nm$^2$ is necessary to collect diffraction patterns up to the maximum resolution with a good signal-to-noise ratio. Poisson noise was also applied in order to obtain a realistic simulation.

The PR maps from eight ice plates provide more than 1800 projection images of the 50S ribosomal subunits, without redundant orientations. This number of

**Fig. 9.10** Simulated reconstruction of the 3D map of the 50S ribosomal subunit. **a** Specimen ▶ model composed of 229 50S ribosomal subunits (2,086,000 atoms) immersed in 429,590,000 water molecules in a vitreous ice plate with dimensions of $500 \times 500 \times 50$ nm. **b** Simulated diffraction pattern from the model in panel (**a**) up to a resolution of 1.25 nm$^{-1}$ at the edge. The small-angle region magnified up to a resolution of 0.25 nm$^{-1}$ at the edge is displayed on the lower right. **c** PR map retrieved from the diffraction pattern in (**b**). In the magnified view (upper left) of the area indicated by a box, six 50S ribosomal subunits are visible. **d** Upper eight panels are representative maps averaged after the classification. The maps were used to generate the initial model of the 3D map at a resolution of 3.2 nm. The lower eight panels are the electron density maps used for the 3D reconstruction at a resolution of 0.8 nm. **e** Reconstructed 3D maps of the 50S ribosomal subunit (gray-colored and surface-rendered) superimposed on the X-ray crystal structure determined at a resolution of 0.22 nm [38]. The left panel shows a map depicted during the course of refinement with respect to the mutual orientation angles of PR maps. The final map at a resolution of 0.8 nm is illustrated in the right panel. Both density maps are contoured at the level of 1.5 standard deviations from the average. By applying the FSC, the effective resolutions of the left and right maps are 1.6 and 0.8 nm, respectively. Ribosomal RNA is depicted as the orange, cyan, blue, and green tubes, and ribosomal proteins are displayed as magenta ribbons. The characteristic structural regions, such as the ribosomal RNA and proteins, are labeled in the structure shown in the right panel. The panels are reused after a modification from reference [36] with permission from American Physical Society

(a) electron density (e/$A^2$)

(b) diffraction intensity (photons / pixel)

(c)

(d)

(e)

Central protuberance

5S rRNA

Stalk

L5

L11

L7e

L14

L2
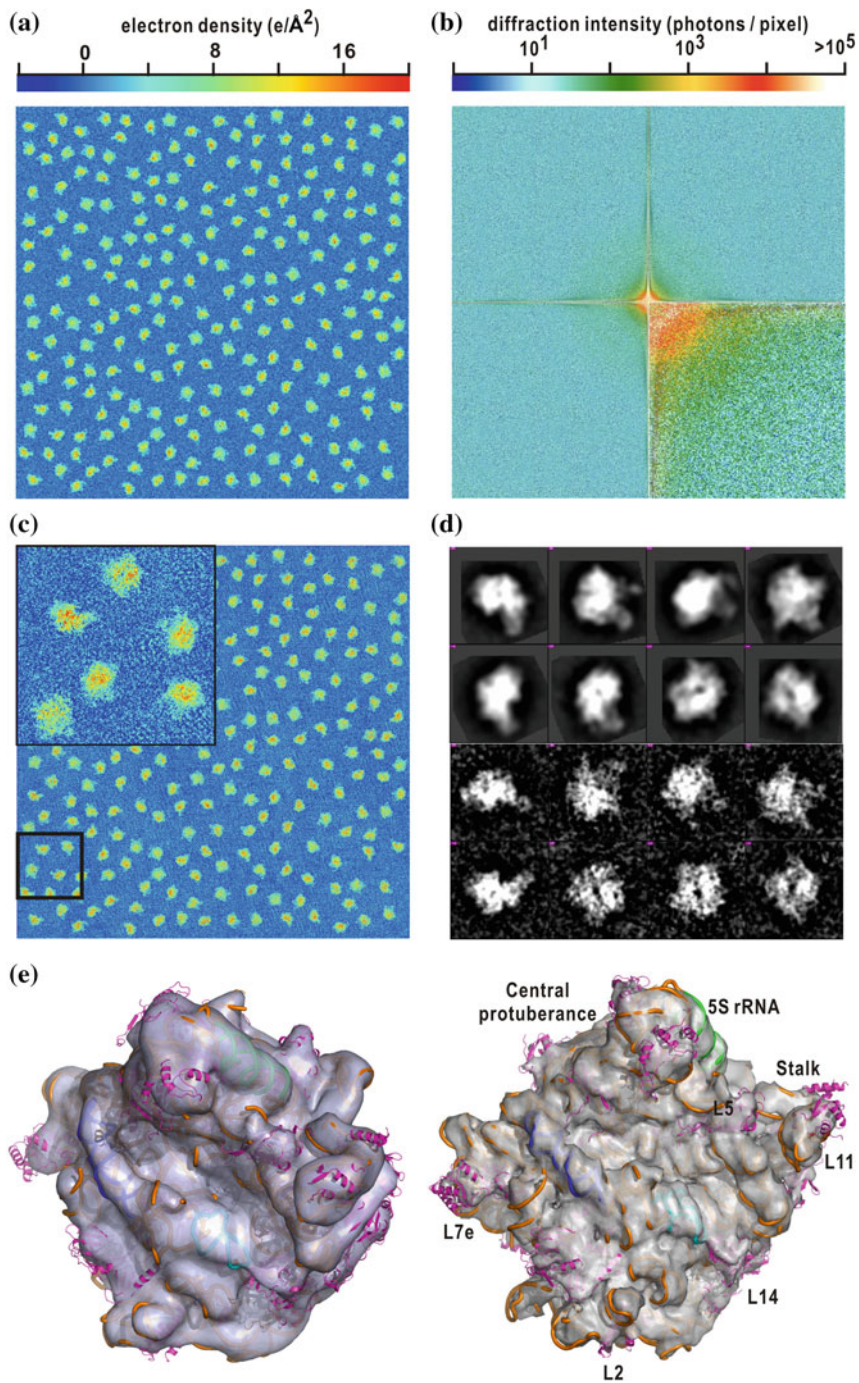
projection images is sufficient to reconstruct the 3D map of the subunit with an approximate diameter of 25 nm [36]. Each diffraction pattern displayed a cross-shaped interference pattern that could be approximated by the Fraunhofer diffraction of a 500-nm-wide square-shaped object (Fig. 9.10b). Although the diffraction pattern at and around the zero-diffraction angle is lost due to the presence of a beamstop in the experiment, the approximation allows us to estimate the size of the irradiated plate and the diffraction pattern at and around the zero-diffraction angle.

Each PR map at a resolution of 0.8 nm had a correlation coefficient of 0.86–0.90 with the electron density maps of the original models. The 3D map of the subunit was reconstructed in real space from 1832 non-redundant projection electron density maps. Before the reconstruction, the averaged projection electron density of vitreous ice was subtracted from the PR maps, and image processing protocols such as low-pass filtering, classification, and averaging were applied, as shown in Fig. 9.10d. An initial 3D model was constructed from the low-pass filtered maps at a resolution of 3.2 nm. Subsequently, the model was refined by gradually extending the resolution to 0.8 nm (Fig. 9.10e).

The overall shape of the reconstructed 3D map was consistent with the crown shape of the 50S ribosomal subunit. In addition, the map displayed a large crevice corresponding to the active-site cleft, a narrow peptide tunnel running from the crevice to the back face, and the double-stranded helices of the 5S ribosomal RNA forming a central protuberance (Fig. 9.10e) On the other hand, the electron density maps of some of the proteins associating with the 50S ribosomal subunit were invisible, probably because of the low electron density contrast of the 50S ribosomal subunits with the vitreous ice region, as also seen in the simulation for PDI (Fig. 9.9d).

## 9.4.4  Poisson Noise and Electron Density Contrast

The simulations in the previous sections demonstrated the feasibility of the protocol in the reconstruction of a 3D map from the PR maps of particles in random orientation against the direction of the incident X-rays. In the simulations, it is possible to assess the influence of the Poisson noise on the reconstructed 3D map. Because Poisson noise is equal to the square root of the detected diffraction intensity, the low-intensity diffraction patterns, particularly those at a high diffraction angle, are modified significantly. Poisson noise has a severe influence on 3D reconstruction. For instance, when the PR maps from diffraction patterns with Poisson noise are averaged and classified, ghost density appears, probably because of the misorientation of the PR maps [35]. According to (9.11), the vitreous ice region increases the diffraction intensity by $10^1$–$10^2$ times of that from a protein alone, and contributes to the reduction of the Poisson noise in the diffraction patterns at high resolution. The quality of the reconstructed 3D maps is correlated with the accuracy in determining the orientation of the particles with respect to the direction of the

incident X-rays. Because of the nature of the Poisson noise, a tenfold difference in the intensity of the incident X-ray beam drastically changes the quality of the 3D reconstructed density model. A diffraction intensity of at least $10^2$ X-ray photons/pixel for the highest resolution is necessary to prevent the loss of structural details in the 3D map.

The quality of the reconstructed 3D maps also depends on the electron density contrast between the particles and vitreous ice, although thicker ice plates can increase the diffraction intensity. It is better to control the thickness of the vitreous ice plate with respect to the projection electron density of the targeted particles. In the case of the simulation for 50S ribosomal subunits [36], even when the diffraction pattern is noiseless, the structural details of some ribosomal proteins on the surface are invisible, probably because of the low contrast between the protein molecules on the surface and the vitreous ice in the projection maps. In the case of a 50-nm-thick ice plate, the projection electron density in the vitreous ice region is within $\pm 500$ electrons/nm$^2$ from the average, while that of the 50S ribosomal subunit is in the range from $-500$ to 1700 electrons/nm$^2$. However, beyond a thickness of 250 nm, the electron density contrast becomes small. As a result, it is difficult to define the borders of the subunits. A series of simulations which increase the thickness of the vitreous ice plate demonstrated that a thickness less than 170 nm provided sufficient contrast in the projection density map for the 50S ribosomal subunits to reconstruct the structural details.

## 9.5   Three-Dimensional Structures of an Organelle and Cell Revealed by X-Ray Diffraction Imaging Using X-Ray Free Electron Laser Pulses

In tomography XDI using synchrotron X-rays, the structures of cells with sizes of 5 μm are visualized at a spatial resolution better than 100 nm (see Fig. 8.4 in Chap. 8). However, because of the limitation in the flux of the incident X-ray beam, the resolution in the diffraction patterns from cells and organelles with sizes of less than 2 μm is limited to 5 μm$^{-1}$ (corresponding to 200 nm in real space). XFEL-XDI experiments provide diffraction patterns for small biological specimens as large as 1 μm better than those from synchrotron XDI in terms of both the resolution and the signal-to-noise ratio.

As an attempt to visualize the 3D structures of biological cells and organelles with dimensions of less than 2 μm, the methods examined in the simulation studies are applied to XFEL-XDI diffraction patterns. Although strong XFEL pulses destroy specimen particles at the atomic level, a large number of diffraction patterns are collected from specimen particles randomly oriented with respect to the incident X-ray pulse by using the TAKASAGO-6 diffraction apparatus [39]. In XFEL-XDI experiments, the cells and organelles must at least be in the same phase of the cell cycle.

The protocol described in the previous sections is applied to the structural analysis of cells and cellular organelles for a number of diffraction patterns. Because the cells are different structures, the 3D reconstruction provides a density map averaged over the cells used in the experiments at low resolution. In an XFEL-XDI experiment, it is difficult to resolve details of the cell, but easy to identify structural features common between a large number of cells. As examples of XFEL-XDI experiments, the structural analyses of a yeast nucleus and cyanobacteria are introduced here.

### 9.5.1  Structure of the Yeast Nucleus

Genomic DNA carries genetic information that implements cellular activity via changes in the hierarchical 3D structures based on the assemblies of chromatins, i.e., complexes of DNA and nucleosome proteins. Genomic DNA also regulates several physiological processes indispensable to the development and reproduction of living organisms, such as gene transcription, recombination, replication, and DNA repair. For these actions, genomic DNA changes the higher-order structures through spatiotemporal and dynamic reorganization, which occurs in the nucleus in eukaryotic cells [40]. However, it is still unclear how genomic DNA is organized and reorganized in the limited space of the nucleus during the cell cycle.

Fluorescence LM can visualize the movements and locations of specific protein molecules labeled with fluorescent proteins, or of nucleic acids labeled with fluorescent dyes (see Sect. 1.2.1 of Chap. 1). For building putative models regarding the distribution of the chromosomes in the nucleus, interaction sites within or between chromosomes in the nucleus are investigated by chromosome conformation capture (3C) and derivative techniques [41]. Despite these techniques, the 3D distribution of the folded genomic DNA is still a subject of much discussion.

XDI has the potential to visualize the distribution of chromosomes in the nucleus. The average electron density of a DNA assembly is more than 1.5 times

**Fig. 9.11** Structural analysis of the nucleus from yeast in the G2/M phase. **a** Schematic of the cell ▶ cycle of yeast. **b** flow cytometry histograms of DNA in asynchronous (red) and G2/M-arrested (blue) yeast cells (right panel). The G2/M-arrested cells, which were prepared in the presence of ith nocodazole, contained twice the amount of DNA (2N) of the cells in interphase (N). On the other hand, the amount of DNA in the asynchronous cell specimens displayed both N and 2 N peaks. **c** Representative diffraction patterns from nuclei in the G2/M phase. These diffraction patterns were composed of speckle peaks with the reciprocal size of the nucleus. Speckle peaks with good signal-to-noise ratios were observed up to a resolution of 20 $\mu m^{-1}$, corresponding to a resolution of 50 nm in real space. **d** PR maps from the diffraction patterns shown in panel (**c**). The scale bar indicates 500 nm. **e** 3D map of the nucleus in the G2/M phase, reconstructed from 424 PR maps. The surfaces of the envelope (E, green), high-density (H1 and H2, red fishnet), and core (C, yellow) regions are contoured at 30, 80, and 120 a.u., respectively. The cross-sectional views 1–4 of the 100 nm steps are shown at the bottom. Published with kind permission of Masayoshi Nakasako 2017. All Rights Reserved
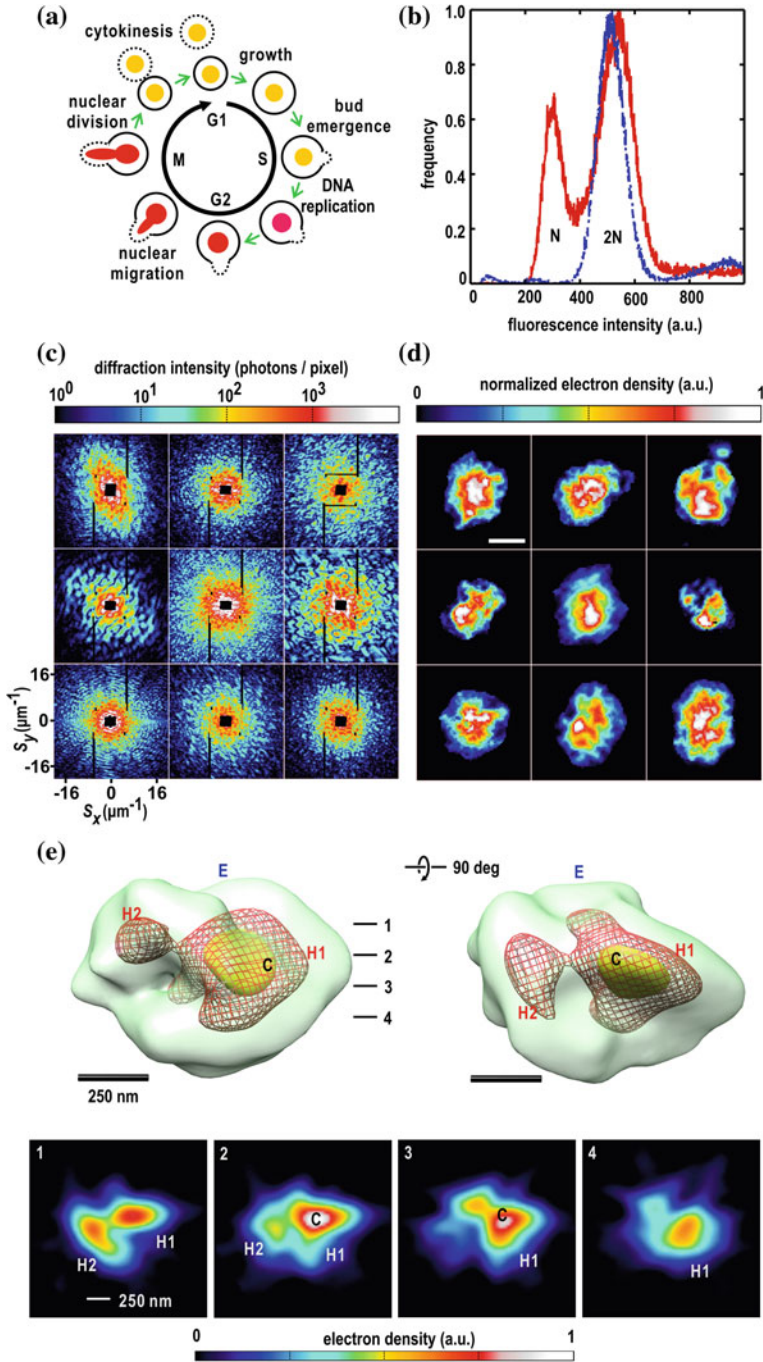
higher than that of a protein, because DNA molecules contain a large number of phosphate groups. Therefore, chromosomes have a significant contribution to the X-ray diffraction of the nucleus. In other words, the high-density regions of the nucleus predominantly reflect the distribution of chromosomes. Based on this idea, the structure of the nucleus isolated from *Saccharomyces cerevisiae* (*S. cerevisiae*; yeast) cell at the G2/M phase (before cell division) of the cell cycle (Fig. 9.1a) was studied by an XFEL-XDI experiment. As the size of the nucleus at this phase is approximately 800 nm, the nucleus can be bathed in focused an X-ray pulse with a cross section of approximately 1.5 μm.

Diffraction patterns from the frozen-hydrated nuclei arrested in the G2/M phase were collected using XFEL pulses provided at a repetition rate of 30 Hz (Fig. 9.11c). The diffraction intensity depended on the relative position of the X-ray pulses relative to the nuclei randomly distributed onto the silicon nitride membrane (see Fig. 5.3 of Chap. 5). By applying data processing (see Chap. 6) and PR protocols (see Sect. 7.1 of Chap. 7) to the collected diffraction patterns, PR maps were obtained from diffraction patterns with good signal-to-noise ratios beyond a resolution of 20 μm$^{-1}$ (Fig. 9.11d). In the PR maps, the images of the nuclei appeared as globular shapes with diameters of less than 1 μm, similar to those seen by LM before flash-cooling of the sample. Subsequently, 424 PR maps were tentatively selected to perform the 3D reconstruction.

The 3D reconstruction was carried out under the assumption that all of the nuclei in the G2/M phase had common structural features, such as overall shape and the distribution of chromosomes, when viewed at low resolution. Therefore, the PR maps were regarded as the projection views of a single nucleus in different orientations with respect to the incident X-ray pulses.

The intensities of the incident X-ray pulses fluctuated within a range of ±10% from the average. In addition, the diffraction intensity depended on the relative position of the nucleus to the X-ray pulse. However, under the assumption that cells all have almost the same structure, each PR map can be normalized so that the sum of the electron densities is equal to a specified value. An initial 3D map was built by applying a single molecular analysis protocol in TEM [2–20, 42, 43]. The PR maps were divided into two groups to prevent overfitting [23]. Then, the initial map was independently refined in each group. The final 3D map was obtained by averaging these independently refined maps using the PRIME program suite [18]. The effective resolution of the final map was estimated to be 171 nm, where the gold-standard FSC value [23] decreased to 0.143. The reliability of the 3D map was validated by the fact that the two sets of PR maps were similar with regard to their overall and internal structures, as well as by the fact that the estimated distribution of the relative orientation of nuclei in the PR maps used in the reconstruction was uniform, without preferential adsorption of nuclei onto the membranes.

The reconstructed 3D map had the shape of a rugby ball, with the long and short axes of approximately 900 and 650 nm, respectively (Fig. 9.11e). The size and shape are consistent with the images of nuclei from LM observations of cells labeled by fluorescence dyes [40]. The 3D map showed a nonuniform distribution of the electron density inside the nucleus. These findings imply that the nuclei used

in the experiment had common structural features when viewed at the effective resolution. Although the G2/M-arrested nucleus contains two copies of genomic DNA, pairs of individual chromosomes are not visible in the 3D map. The different levels of electron density are used to divide the putative nonuniform density into the envelope (designated as "E" in Fig. 9.6a), high-density ("H"), and core ("C") regions, which reflect the packing density of the chromosomes.

The entire volume of the nucleus, which is contoured at a 1.5 standard deviation from the average density, is approximately $1.9 \times 10^8$ nm$^3$. This is large enough to contain the nucleosomes for 24 Mbp of DNA in the G2/M phase, which is estimated to occupy a volume of $1.6 \times 10^8$ nm$^3$. However, because only the regions with good electron density contrast with the vitreous ice surrounding the nuclei contribute significantly to the diffraction patterns of the frozen-hydrated specimens, the size and volume used are lower estimates of the number of measured nuclei.

A large lobe (H1) and small lobe (H2), in which the average electron density in a volume of $3.0 \times 10^7$ nm$^3$ is more than twice that of the E region, are located off-center in the nucleus. The H1 lobe has dimensions of approximately $400 \times 400 \times 500$ nm$^3$. The C region is at the center of the H1 lobe and has a very high density in its volume of $4.9 \times 10^6$ nm$^3$. The approximately triangular H2 lobe has dimensions of $100 \times 100 \times 300$ nm$^3$. The distance between the centers of the two lobes is approximately 400 nm. Chromosomes are expected to have a dense distribution within the H1 and H2 regions. The high-density region C is suspected to be the nucleolus, which is the site of ribosomal DNA transcription into a large assembly of ribosomal RNA. Further accumulation of PR maps may provide 3D maps at higher resolution. This point will be discussed in Chap. 10.

### 9.5.2 Structure of a Cyanobacteria Cell

According to the endosymbiotic hypothesis of the evolution of the eukaryote [44], key organelles such as mitochondria and chloroplasts originated through symbioses between separate single-celled organisms. The cyanobacterium [45], a photosynthetic organism distributing widely in the ocean, is a candidate for the origin of the chloroplasts used to form a eukaryotic cell. It is of interest to determine whether the internal structure of a cyanobacterial cell is similar to that of the chloroplast of *C. merolae*, which has a C-shaped distribution of thylakoid membranes (see Fig. 8.6 of Chap. 8).

In an XFEL-XDI experiment, cyanobacteria were dispersed on a silicon nitride membrane according to the specimen preparation method described in Sect. 5 of Chap. 5. In the experiment, approximately 200,000 XFEL shots were used to stochastically collect diffraction patterns by scanning of the silicon nitride membranes with incident XFEL pulses at a repetition rate of 30 Hz using the TAKASAGO-6 diffraction apparatus [39] (see Fig. 4.7 of Chap. 4). Approximately 149,000 shots are selected for PR calculations by the data processing program (see Chap. 6). Diffraction patterns selected for structural analysis had speckle peaks with
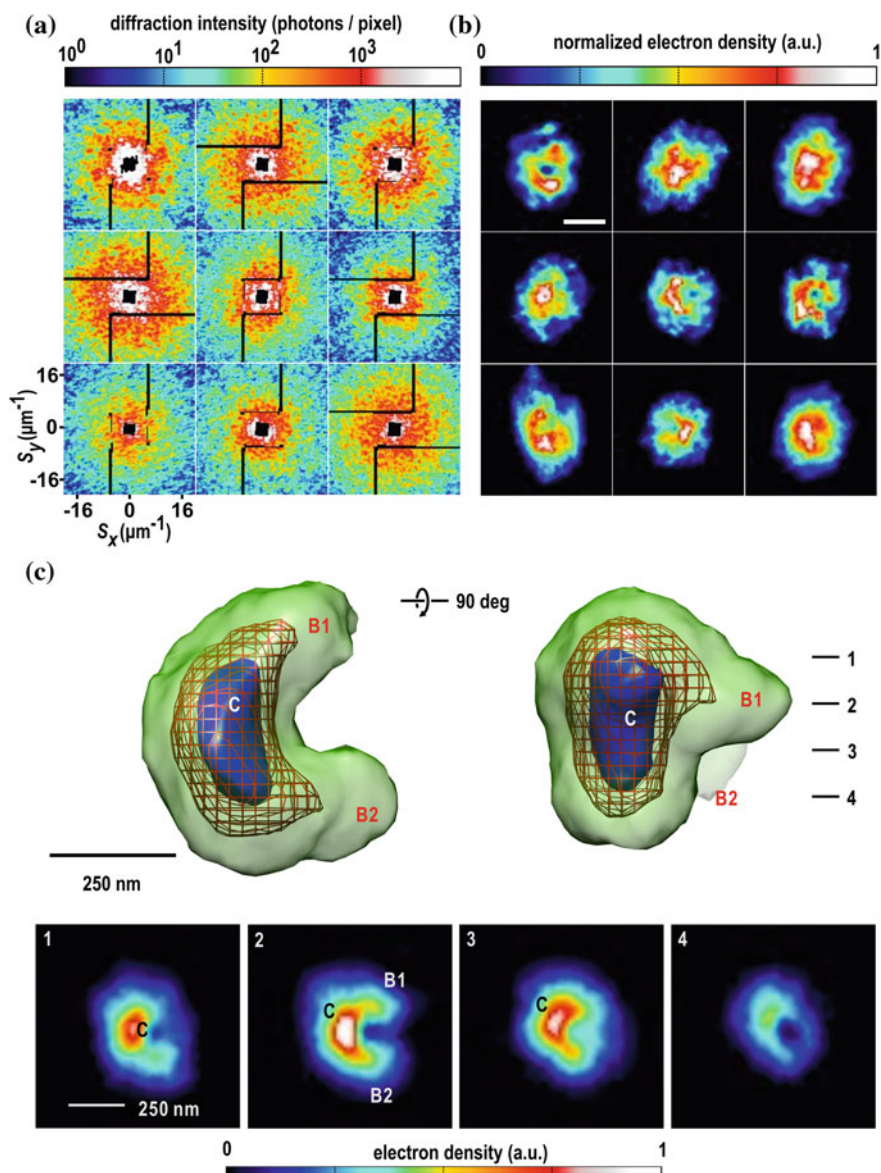
**Fig. 9.12** **a** Representative diffraction patterns from cyanobacteria cells. Speckle peaks with good signal-to-noise ratios were observed up to a resolution of 20 $\mu m^{-1}$, corresponding to a resolution of 50 nm in real space. **b** PR maps from the diffraction patterns shown in panel (**a**). The scale bar indicates 500 nm. **e** 3D map of a cyanobacteria cell reconstructed from projection electron density maps of approximately 800 nm. Only high-density surfaces are rendered, as a high-density envelope with bulges (B1 and B2, green), and core region (C, red fishnet and blue), which are contoured at 30, 80, and 120 a.u., respectively. The cross-sectional views 1–4 of the 100 nm steps are shown at the bottom. Published with kind permission of Masayoshi Nakasako 2017. All Rights Reserved

comparable sizes to the reciprocal of the cell size as viewed by LM (Fig. 9.12a). PR maps from high quality diffraction patterns (Fig. 9.12b) are selected and used for the 3D reconstruction of the electron density map. The effective resolution of the 884 selected PR maps estimated using the PRTF (see Sect. 7.2.2 of Chap. 7) was approximately 120 nm on average.

The 3D map is visualized at an effective resolution of 150 nm (Fig. 9.12c). The reconstructed shape of the cyanobacteria cell, within the low-density envelope, is approximated by a sphere with a diameter of 800 nm. The size is consistent with that expected from the PR maps and DLS measurement (see Fig. 5.7 of Chap. 5). While the overall shape is spherical, the internal structure is nonuniform. A high-density region distributed along the envelope of the cell displays a C-shape with an approximate diameter of 600 nm. The shape can be interpreted as the lamellar structures of thylakoid membranes distributed in the marginal region rather than the central part, as observed in an EM study on a section of chemically stained cyanobacterium [46]. The shape and size of the high-density region are similar to the chloroplast of *C. merolae* described in Chap. 8. This structural similarity confirms that symbiosis with cyanobacteria played a role in the formation of the ancient eukaryotic cell.

# References

1. J. Miao, F. Förster, O. Levi, Phys. Rev. B **72**, 052103 (2005)
2. J. Miao et al., Phys. Rev. Lett. **97**, 215503 (2006)
3. Y. Nishino et al., Phys. Rev. Lett. **102**, 018101 (2009)
4. H. Jiang et al., Proc. Natl. Acad. Sci. U.S.A. **107**, 11234 (2010)
5. C. Song et al., Biophys. J. **107**, 1074 (2014)
6. J.A. Rodriguez et al., IUCrJ **2**, 575 (2015)
7. T. Ekeberg et al., Phys. Rev. Lett. **114**, 098102 (2015)
8. J. Frank, *Three-Dimensional Electron Microscopy of Macromolecular Assemblies* (Oxford University Press, Oxford, 2006)
9. D. DeRosier, A. Klug, Nature **217**, 130 (1968)
10. D. DeRosier, P.B. Moore, J. Mol. Biol. **52**, 355 (1970)
11. W. Hoppe et al., Z. Naturforsch. **A31**, 645 (1986)
12. R.A. Crowther, D.J. DeRosier, A. Klug, Proc. R. Soc. Lond. **317**, 319 (1970)
13. M. Radermacher, J. Electron Microsc. Tech. **9**, 359 (1988)
14. M. Radermacher, in *Electron Tomography*, ed. by J. Frank (Plenum Press, New York, 1992), pp. 91–115
15. S. Lanzavecchia, and P.L. Bellon, J. Vis. Commun. Image Repres. **5**, 255 (1994)
16. M. van Heel, Ultramicroscopy **21**, 111 (1987)
17. P. Penczek, R.A. Grassucci, J. Frank, Ultramicroscopy **40**, 33 (1994)
18. J. Frank et al., J. Struct. Biol. **116**, 190 (1996)
19. S.J. Ludtke, P.R. Baldwin, W. Chiu, J. Struct. Biol. **128**, 82 (1999)
20. H. Elmlund, D. Elmlund, S. Bengio, Structure **21**, 1299 (2013)
21. S.H.W. Scheres, J. Struct. Biol. **180**, 519 (2012)
22. S.H.W. Scheres, J. Mol. Biol. **415**, 406 (2012)
23. M. van Heel, M. Schatz, J. Struct. Biol. **151**, 250 (2005)
24. P.B. Rosenthal, R. Henderson, J. Mol. Biol. **333**, 721 (2003)

25. S.H.W. Scheres, S. Chen, Nat. Methods **9**, 853 (2012)
26. W. Kodama, and M. Nakasako, Phys. Rev. E **84**, 021902 (2011)
27. K. Tamasaku et al., Nucl. Instrum. Meth. A **467–468**, 686 (2001)
28. M. Matsuzaki et al., Nature **428**, 653 (2004)
29. M. Nakasako et al., Rev. Sci. Instrum. **84**, 093705 (2013)
30. A. Casanas et al., Acta Crystallogra. D**72**, 1036 (2016)
31. M.R. Howells et al., J. Electron Spectrosc. Relat. Phenom. **170**, 4 (2009).
32. J. Miao, K.O. Hodgson, and D. Sayre, Proc. Natl. Acad. Sci. USA **98**, 6641 (2001)
33. N.D. Loh, V. Elser, Phys. Rev. E 80, 026705 (2009)
34. N.D. Loh et al., Phys. Rev. Lett. **104**, 225501 (2010)
35. R. Xu et al., Nat. Commun. **5**, 4061 (2014)
36. K.S. Raines et al., Nature **463**, 214 (2010)
37. H. Wei, S. Liu, Phys. Rev. B **86**, 226101 (2012)
38. T. Oroguchi, M. Nakasako, Phys. Rev. E **87**, 022712 (2013)
39. G. Tian et al., Cell **124**, 61 (2006)
40. T.M. Schmeing et al., Mol. Cell **20**, 437 (2005)
41. A. Kobayashi et al., Rev. Sci. Instrum. **87**, 053109 (2016)
42. Q. Bian, A.S. Belmont, Curr. Opin. Cell Biol. **24**, 359 (2012)
43. Z. Duan et al., Nature **465**, 363 (2010)
44. M.W. Gray, J.M. Archibald, in *Genomics of Chloroplasts and Mitochondria*, ed. by R. Bock, V. Knoop (Springer, Dordrecht, 2012), pp. 1–30
45. S.W. Chisholm et al., Arch. Microbiol. **157**, 297 (1992)
46. A.M.L. van de Meene, M.F. Hohmann-Marriott, W.F.J. Vermaas, R.W. Roberson, Arch. Microbiol. **184**, 259 (2006)

# Chapter 10
# Prospects for the Structural Analysis of Biological Specimens by X-Ray Diffraction Imaging

**Abstract** As described in Chap. 9, X-ray diffraction imaging (XDI) has the potential to reconstruct the three-dimensional (3D) electron density maps of biological specimens. The recent XDI structural analyses allow us the opportunity to discuss future prospects for the 3D structural analyses of biological specimens in XDI experiments using either synchrotron X-rays or X-ray free electron laser (XFEL) pulses. Here, we consider the achievable resolution, taking into account the radiation damage in synchrotron XDI experiments and the heterogeneity of specimens in XFEL-XDI experiments.

## 10.1 X-Ray Diffraction Imaging Using Synchrotron X-Rays

In synchrotron tomography XDI using a pixel array detector, the maximum resolution of a diffraction pattern of a specimen particle is proportional to the logarithm of the exposure time (Fig. 9.5 in Chap. 9). Therefore, prolonged exposure allows us to record speckle patterns with good signal-to-noise ratio at high resolution. On the other hand, long exposure causes radiation damage of the specimen particle. Maximum tolerable irradiation dose for a biological particle is theoretically and experimentally investigated ((4.1) in Chap. 4) [1]. In addition, from the reciprocity of the speckle size and the dimension of the specimen particle, 3D reconstruction of a larger specimen particle requires finer angular step.

For instance, to visualize the 3D map of a cell, such as C. merolae in the G/M phase, with the dimension of $5 \times 5 \times 5$ $\mu m^3$ at a resolution of 20 nm (corresponding to 40 $\mu m^{-1}$ in reciprocal space), the tolerable irradiation dose is approximately $2 \times 10^9$ Gy according to the empirically proposed equation [1] total dose (Gy) $= 1.0 \times 10^8 \times$ resolution (nm).

When using the pixel array detector, the exposure time necessary to acquire speckle patterns up to a resolution of 40 $\mu m^{-1}$ is approximately 1000 s. Then, the irradiation dose is calculated to be $3.8 \times 10^6$ Gy per exposure. From the reciprocity between the sizes of the particle and speckle, the maximum angular step necessary

for the 3D reconstruction by using the back-projection method is approximately 0.56°, and then the minimum number of exposures is 320. From the estimation, the total irradiation dose becomes $1.2 \times 10^9$ Gy.

When the theoretical prediction is correct, the maximum resolution achievable in synchrotron tomography XDI would be better than 20 nm. At the resolution, a large protein molecule or macromolecular assembly with the molecular weight of 300 k will be represented as a voxel. However, even when such a tomography XDI experiment provides the 3D electron density map of a cell at a resolution of 10–20 nm, the chemical identification of density peaks are necessary. Therefore, the complementary use of fluorescence LM will provide information toward more detailed visualization of the cell.

## 10.2  X-Ray Diffraction Imaging Using X-Ray Free Electron Laser Pulses

The 3D structural analyses of the nuclei of *Saccharomyces cerevisiae* (Fig. 9.11) and cyanobacteria (Fig. 9.12) give us an opportunity to discuss the method of visualizing the 3D structures of biological specimens using XFEL pulses, and the resulting implications. In a 3D reconstruction using single-particle analysis, the achievable resolution $d$ is roughly estimated by

$$d = \frac{\pi D}{N}, \tag{10.1}$$

where $N$ and $D$ are the number of projection images and the size of the particle, respectively [2]. This equation implies that a larger number of projection images results in better resolution. This equation stands when the particles have nearly the same structures. XFEL-XDI experiments can provide more than 300 PR maps over the course of several hours. Then, according to (10.1), the 3D structure of a particle with a size of 1 μm can be visualized at a resolution of 10 nm.

Even though the resolution of the PR maps is better than 100 nm, the estimated effective resolution of a nucleus is 170 nm. In addition, the effective resolution is nearly independent of the number of PR maps used in the single particle analysis. Therefore, the structural heterogeneity of the nuclei used probably limits the resolution of the reconstructed map. In other words, 3D maps from XFEL-XDI experiments can provide information on structures common among all of the specimen particles, as described in the previous chapter. Therefore, XFEL-XDI is suitable for searching common structures in living cells, in contrast to synchrotron XDI, which reveals the structural details of individual cells at the highest resolution in the resulting diffraction patterns.

To achieve 3D reconstructions at higher resolution in XFEL-XDI experiments, a huge number of diffraction patterns would be necessary in order to obtain redundant PR maps with similar structures. Higher redundancy for similar PR maps may reduce the structural differences and ambiguity. Some classification method is

necessary to obtain sets of similar maps from a huge number of PR maps. One mathematical tool for performing such a classification is the concept of manifold learning (i.e., nonlinear dimensionality reduction). The theory of manifold learning and a simulation examining its feasibility are described in the next section.

## 10.3   Classification of Electron Density Maps by Manifold Learning

Manifold learning was used to classify conformations of macromolecules from heterogeneous data sets in a multidimensional space [3]. For example, a manifold can trace the structural dynamics of a Brownian molecular machine from a large number of snapshots obtained by cryogenic electron microscopy [4]. In addition, the concept has been used to classify conformations in MD simulations [5]. With respect to single-shot XFEL-XDI experiments, the manifold concept can be used for the unsupervised classification of simulated diffraction patterns and for the recovery of conformation sequences of simulated or experimental diffraction patterns from noncrystalline objects which display conformational variation [6, 7]. Therefore, any method based on the manifold concept could be used to classify the electron density maps or diffraction patterns in XFEL-XDI. In this subsection, the concept of manifold learning is first introduced. Then, a simulation study demonstrating how manifold learning is applied to XFEL-XDI data is presented.

### 10.3.1   Concept of Manifold Learning

Figure 10.1 is a schematic illustration of the concept of the manifold learning. When projection images of a protein molecule are visualized using $N_x \times N_y$ pixels, each image is represented as a point in an $(N_x \times N_y)$-dimensional space. The projection electron density $\rho(k, \ell)$ at pixel $(k, \ell)$ is determined uniquely when the Eulerian angles of the protein are specified. Then, all projection images are distributed onto a 3D space, the so-called manifold, in the $(N_x \times N_y)$-dimensional space.

The geometry of the manifold is expressed as a set of geodesic distances $D(i, j)$ between a pair of images. For instance, when the $i$th image on a Swiss-roll-shaped manifold is more similar to $k$th image rather than the $j$th image, $D(i, k) < D(i, j)$. However, their Euclidean distances satisfy the relation $d(i, k) > d(i, j)$. Thus, the geodesic distance is more suitable for illustrating the shape of the manifold than the Euclidian distance.

Here we concern the diffusion map (DM) method [8] of finding a manifold. In the DM method, the distribution of the data points is reduced from a multidimensional space to a low-dimensional space. In addition, a priori knowledge of the number of classes into which the targeted particle images can be classified is not necessary.
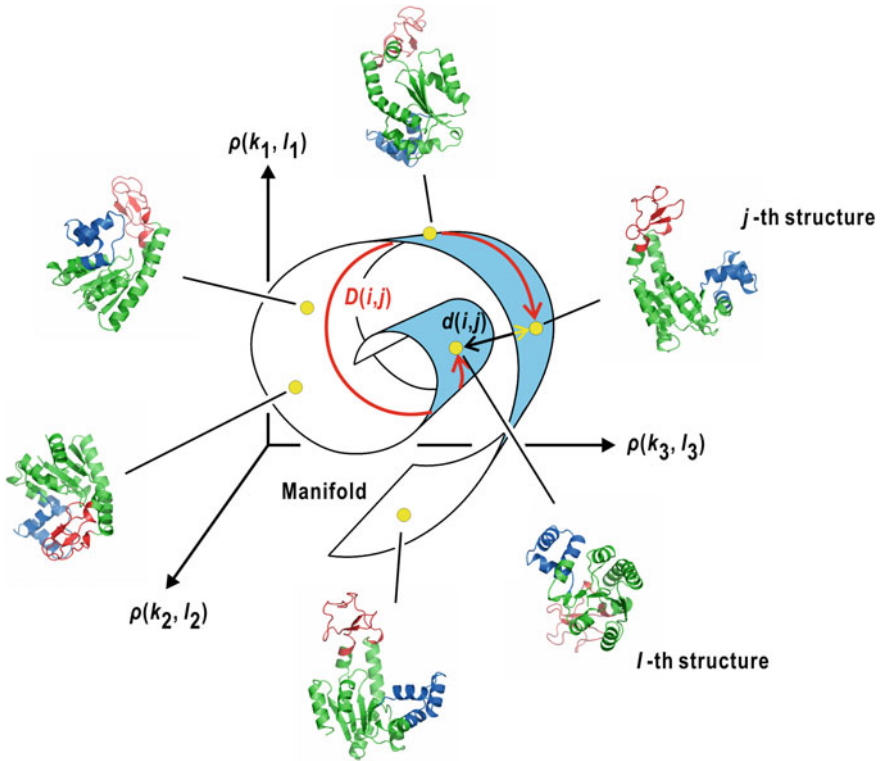
**Fig. 10.1** A schematic illustration of a manifold in a multidimensional image space. Published with kind permission of Masayoshi Nakasako 2017. All Rights Reserved

### 10.3.2 Diffusion Map Method

In the DM method, the shape of the manifold is traced by a random walk among the $M$ image points. The probability of a transition between the $i$th and $j$th points separated by the Euclidean distance $d(i,j)$ during the random walk is calculated using the Gaussian function

$$A(i,j) = \exp\left[-\frac{d(i,j)^2}{\varepsilon}\right] \quad i,j = 1, 2, \ldots, M, \tag{10.2}$$

where $\varepsilon$ is an input parameter that controls the transition probability. Then, matrix **A** is defined to represent the connectivity between all points on the manifold. Because the Gaussian function decreases rapidly when $d(i,j) > \sqrt{\varepsilon}$, transitions predominantly occur between the points for which $d(i,j) \leq \sqrt{\varepsilon}$. Then, $\mathbf{A}^s$ expresses a series of $s$-times transitions on the manifold.

To map the data points, the DM method uses a normalized transition matrix $\mathbf{P} \equiv \mathbf{D}^{-1}\mathbf{A}$, where $\mathbf{D}$ is a diagonal matrix with elements defined as

$$D(i,i) = \sum_{j=1} A(i,j) \quad i = 1, 2, \ldots, M. \tag{10.3}$$

The matrix $\mathbf{P}$ is factorized into $\mathbf{P} = \mathbf{\Phi}\,\mathbf{\Lambda}\,\mathbf{\Psi}^{T}$, where $\mathbf{\Lambda}$ is the diagonal matrix of the eigenvalues of $\mathbf{P}$. $\mathbf{\Phi}$ and $\mathbf{\Psi}$ are the matrices formed by the right-column and left-column eigenvectors of $\mathbf{P}$, respectively, and satisfy $\mathbf{\Psi}^{T}\mathbf{\Phi} = \mathbf{I}$ (where $\mathbf{I}$ is the identity matrix). All eigenvalues $\lambda_i\,(i = 0 \ldots M - 1)$ are positive, $\lambda_0 = 1 \geq \lambda_1 \geq \cdots \geq \lambda_{M-1} \geq 0$. The right-column eigenvector of $\lambda_0$ is equal to $\vec{\mathbf{1}}$, i.e., the all-ones vector. The $i$th image is mapped onto a $k$-dimensional space ($k \ll M$) using the $i$th row of each of the $k$ nontrivial right-column eigenvectors.

In the classification of the PR maps obtained from XDI analysis, the PR maps are normalized so that their total electron densities are the same. In addition, the PR maps are superimposed by taking into account their density centers and the ambiguity in the $0/\pi$-rotation caused by the centrosymmetry of the diffraction patterns. The most probable superimposition is suggested by the correlation function of a pair of maps. After the superimposition, a set of $d(i,j)$ for the PR maps is calculated using

$$d(i,j)^2 = \sum_{k=1}^{N_{px}} \sum_{l=1}^{N_{py}} [\rho_N(i; k, l) - \rho_N(j;\ k + \Delta k_{\mathrm{Max}},\ l + \Delta l_{\mathrm{Max}})]^2, \tag{10.4}$$

where the values of $\Delta k_{\mathrm{Max}}$ and $\Delta l_{\mathrm{Max}}$ correspond to the largest value of $C(i,j; \Delta k, \Delta l)$. Under a given $\varepsilon$, the eigenvalues and eigenvectors of $\mathbf{P}$ are calculated after symmetrizing the matrix as $\tilde{\mathbf{P}} \equiv \mathbf{D}^{1/2}\mathbf{P}\mathbf{D}^{-1/2} = \mathbf{D}^{-1/2}\mathbf{A}\mathbf{D}^{-1/2}$.

### 10.3.3   Simulation Study on Manifold Learning

The feasibility of the DM method was evaluated by a simulated XFEL-XDI experiment for adenylate kinase. Adenylate kinase is an enzyme which develops conformational fluctuations predominantly around its open and closed conformations (Fig. 10.2) [7]. A set of 11,000 structural models were prepared from a molecular dynamics (MD) simulation for the open conformation (5000 models), from another simulation for the closed conformation (5000 models), and from steered MD simulations driving from the open to the closed conformations (1000 models in the in-between conformations). The diffraction pattern of each randomly rotated model was calculated up to a resolution of 0.8 nm. From the diffraction amplitude, a PR map of $32 \times 32$ pixels was calculated at a resolution of 0.8 nm.
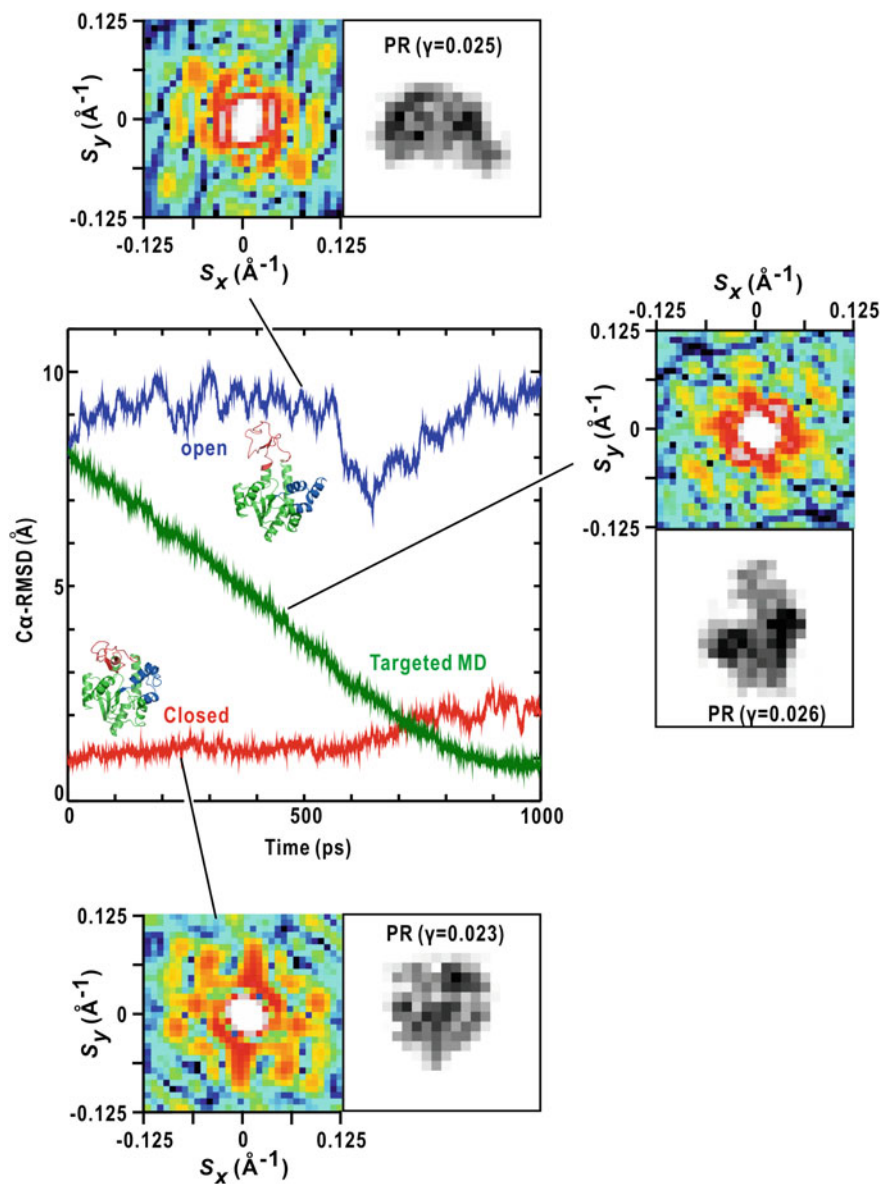
Each PR map is treated as a point in a 1024-dimensional space. The squared distance between the $i$th map and its nearest neighbor, $d(i, i_{\text{Nearest}})^2$ ranges from $5 \times 10^4$ to $3 \times 10^5$ for both the open and closed forms. After inspecting the distribution of $d(i, i_{\text{Nearest}})^2$, the 11,000 PR maps were classified by the DM method in 1024-dimensional space under $\varepsilon = 45 \times 10^3$.

◄**Fig. 10.2** Conformational fluctuations of adenylate kinase during MD simulations were monitored using the root-mean-square-difference (RMSD) of all the α-carbon atoms of the amino acid residues from the crystal structure in the closed form [7]. Blue and red lines are from the mutations for the open and closed conformations, respectively. The green line displays the fluctuation in the stirred simulation. Prior to the calculation of the RMSD, all the conformations are superimposed on the rigid domain of the crystal structure in closed form. Examples of the diffraction patterns calculated from the sampled structure and the PR maps are depicted. In the maps, the γ-values (see 3.27) are indicated. The panels are reused after a modification from [7] with permission from American Physical Society

PR maps projected onto a 3D space spanned by the first three right-column eigenvectors were distributed in a funnel shape (Fig. 10.3). The PR maps from failed calculations were distributed in regions far from the funnel. The PR maps of the open conformation are distributed annularly along the first eigenvector and comprise the main body of the funnel. The PR maps of the closed conformation are concentrated at the bottom of the funnel with the small values of the first eigenvector. Thus, the PR maps of the open and closed conformations were classified on the manifold, and can be distinguished simply by measuring their Euclidean distance from the lowest value of the first eigenvector. The PR maps of the in-between
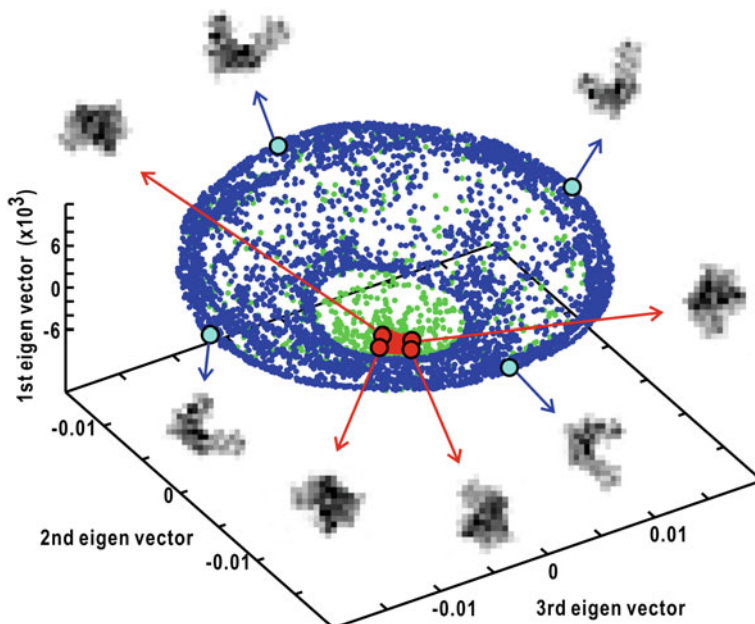


**Fig. 10.3** A view of the manifold projected onto the three major eigenvectors [6]. The blue, red, and green dots indicate the locations of the maps of the open, closed, and in-between conformations, respectively. The locations of some representative PR maps are shown. The panel is reused after a modification from [6] with permission from American Physical Society

conformations are dispersed between the open and closed conformations and penetrate into the regions of the two forms.

Figure 10.3 also illustrates the locations of representative PR maps for the open and closed conformations on the manifold. The locations are correlated with the shape of the electron density maps. For instance, PR maps with compact molecular images are distributed around areas with small values of the first eigenvector. PR maps at the outermost region of the funnel-shaped manifold are similar.

The simulation demonstrates the potential of the DM method to classify low resolution images without prior knowledge regarding the number of classes. Although PR calculations suffer from the lack of a central speckle pattern, the oversampling ratio, and Poisson noise, correct density maps are necessary for the classification. In addition, for the application of the DM method, more than several thousand PR maps are necessary. When applying the DM method to the classification of the PR maps of biological cells and cellular organelles, a large number of PR maps are necessary.

## 10.4   Role of X-Ray Diffraction Imaging in Cell Biology

At present, sophisticated imaging techniques using lenses, such as super resolution fluorescence microscopy (SRFM) [9] and TEM [10], have increased capability to visualize cells and cellular components at higher resolution. SRFM can provide 3D distributions of fluorescence-labeled molecules at a resolution better than 100 nm [11]. TEM provides electrostatic potential maps of noncrystalline supramolecular complexes which can be used to build their atomic models [12]. In addition, X-ray microscopy allows us to view the cellular details at a resolution of several tens of nanometers [13].

XDI is still premature in terms of both experimental procedures and analysis, in comparison to TEM, LM, and X-ray microscopy (see Chap. 1). Owing to the penetration power of short wavelength X-rays, XDI has an advantage in visualizing the structures of noncrystalline particles of micrometer-scale sizes, without staining, chemical labeling, or the use of aberration-causing lenses (Chap. 3). Cryogenic XDI using X-rays from a synchrotron facility has demonstrated the potential to visualize biological cells at resolutions of several tens of nanometers (Chaps. 8 and 9).

XDI for large specimens is also applicable to cellular imaging [14] and can provide the 3D structure of cells as well as those introduced in Chap. 9. The resolution of 3D structures in synchrotron XDI experiments can be improved by the development of a structural analysis algorithm, which would be developed in the near future. Then, the complementary use of XDI alongside sophisticated and established imaging techniques will fill the resolution gap between the cellular biology and structural biology of molecules.

# References

1. M.R. Howells et al., J. Electron Spectrosc. Relat. Phenom. **170**, 4 (2009)
2. J. Frank, *Three-Dimensional Electron Microscopy of Macromolecular Assemblies* (Oxford University Press, Oxford, 2006)
3. P. Schwander, R. Fung, A. Ourmazd, Phil. Trans. R. Soc. B **369**, 20130567 (2014)
4. A. Dashti et al., Proc. Natl. Acad. Sci. U.S.A. **111**, 17492 (2014)
5. M.A. Rohrdanz, W. Zheng, C. Clementi, Ann. Rev. Phys. Chem. **64**, 295 (2013)
6. C.H. Yoon, et al., Opt. Express **22**, 8085 (2014)
7. T. Yoshidome, T. Oroguchi, M. Nakasako, M. Ikeguchi, M. Phys, Rev. E **92**, 032710 (2015)
8. R.R. Coifman et al., Proc. Natl. Acad. Sci. U.S.A. **102**, 7426 (2005)
9. B. Huang, M. Bates, X. Zhuang, Annu. Rev. Biochem. **78**, 993 (2009)
10. S. Subramaniam, W. Kühlbrandtt, R. Henderson, IUCrJ **3**, 3 (2016)
11. B. Huanh, A.A. Jones, B. Brandenburg, X. Zhuang, Nature Meth. **5**, 1047 (2008)
12. I. Gutsche et al., Science **348**, 704 (2015)
13. G. Schneider et al., Nat. Meth. **7**, 985 (2010)
14. A. Diaz et al., J. Struct. Biol. **192**, 461

# Index